



DISSERTATION

**Signal Processing for Ultrahigh
Resolution and Functional
Ophthalmic Optical Coherence
Tomography**

von

Boris Hermann

0027 831

Peter Jordan Str. 121/3/1, 1180 Wien

Wien, April 2006

ausgeführt zum Zwecke der Erlangung des akademischen Grades eines
Doktors der technischen Wissenschaften
unter der Leitung von

Univ. Prof. Karl Unterrainer
Institut für Photonik

und

a.o. Univ. Prof. Wolfgang Drexler
Medizinische Universität Wien
Zentrum für Biomedizinische Technik und Physik

eingereicht an der Technischen Universität Wien
Fakultät für Elektrotechnik

Contents

Summary	iii
Zusammenfassung	iv
I Methods	1
1 Introduction	3
2 Theory and Methods	6
2.1 Optical Properties / Light–tissue interaction	6
2.2 Time Domain – Frequency Domain OCT	14
II Signal Processing	17
3 Two–Dimensional Ophthalmic Ultrahigh Resolution OCT	19
3.1 Dispersion compensation.	19
3.2 Data acquisition	21
3.3 Signal processing	21
3.4 Correlation of histology with ultrahigh resolution OCT in ophthalmic imaging	25
3.4.1 In vitro ultrahigh resolution OCT system	25
3.4.2 Correlation of UHR OCT with histology - pig retina . . .	28
3.4.3 Correlation of UHR OCT with histology - monkey retina	37
3.5 In vivo ophthalmic studies	46
3.5.1 In vivo ultrahigh resolution OCT system	46
3.5.2 Animal study - optic nerve head and retinal nerve fiber analysis in glaucoma	48
3.5.3 Human studies - enhanced visualization of macular pathologies	50
3.5.4 Human studies - assessment of central visual function using UHR OCT	64
3.6 Adaptive optics ultrahigh resolution optical coherence tomography	73

4	Three-Dimensional Ophthalmic Ultrahigh Resolution OCT	80
4.1	Data acquisition	80
4.2	Signal processing	80
5	Segmentation	89
5.1	2-dimensional segmentation in a glaucoma monkey model	91
5.2	3-dimensional segmentation of photoreceptors in humans	93
III	Functional OCT extensions	97
6	Extraction of Depth Resolved Spectroscopic Information	99
6.1	Precision of extraction using spectroscopic OCT	99
6.1.1	Introduction	99
6.1.2	Theory	100
6.1.3	Experiments	102
6.1.4	Results and discussion	104
6.1.5	Conclusion	109
6.2	Water absorption measured by spectroscopic OCT	110
6.3	In vivo qualitative spectroscopic OCT	111
7	Extraction of Depth Resolved Physiologic Information	112
7.1	Optophysiology: depth resolved probing of retinal physiology	112
7.1.1	UHR OCT system	114
7.1.2	Isolated retina sample preparation	114
7.1.3	Data acquisition and processing	115
7.1.4	Results	115
7.1.5	Discussion	120
8	Future Perspectives of Ophthalmic Ultrahigh Resolution OCT	124
	Bibliography	139
	Publications	140
IV	Appendix	146
A	Envelope Generation	147
B	Cross-correlation	149
	Acknowledgement	152
	Curriculum vitae	153

Summary

The eye is the primary sensory organ of human beings. Early diagnosis and treatment of diseases that are affecting the eye and ultimately lead to blindness, can have a significant impact on the quality of life. Ultrahigh resolution optical coherence tomography (UHR OCT) is a valuable diagnostic technique for noninvasive ophthalmic imaging.

Recent technical advances in UHR OCT enforced new signal processing algorithms. From a technical point of view UHR OCT systems are highly sophisticated. Electronics, photonics, mechanics, electromechanics, and optics as well as fiber optics are involved. Software for system control and signal processing is an indispensable key parameter of UHR OCT systems.

This thesis summarizes state of the art UHR OCT signal processing for ophthalmic UHR OCT in *ex vivo* as well as *in vivo* studies. Postprocessing for two- and three-dimensional time domain (TD) and frequency domain (FD) UHR OCT is presented. In the last few years, frequency domain OCT (FDOCT) enabled rasterscanning of three dimensional volumes within a few seconds. Three-dimensional visualization leads to a better perception and understanding of morphological changes caused by retinal diseases, like macular holes or glaucoma. The visualization of volumetric OCT data necessitated new fast representation techniques, which are evaluated in *in vivo* UHR OCT data of healthy and pathologic eyes.

Histology of the eye's retina uses staining techniques for contrast enhancement and enables visualization of the stratification of clearly distinguishable layers. A similar morphology is visualized by ophthalmic UHR OCT, whereas its correspondence to histology is still subject of an ongoing discussion. Two studies are presented in this thesis to solve the discrepancy between OCT and histology.

In OCT axial and transversal resolution are decoupled. Axial resolution is mainly determined by the bandwidth of the light source, whereas transversal resolution depends on the numerical aperture of the imaging optics. Spherical aberrations of the eye's optics blur the spot of the imaging beam in the retina and lead to a decreased transversal resolution. Adaptive optics, individually compensating these aberrations by means of deformable mirrors, was introduced to UHR OCT to correct for these aberrations and improve transversal resolution.

Thicknesses of intraretinal layers can be used for objective diagnosis of disease progression. Therefore segmentation algorithms have been developed for nerve fiber layer and total retinal thickness measurements for use in glaucoma diagnosis. Furthermore a semiautomatic segmentation algorithm was developed and evaluated to produce thickness maps of the photoreceptor layer in humans.

Morphological changes are often related to functional ones and vice versa. Early disease diagnosis could significantly profit from depth resolved functional measurements. First results of optical probing of retinal physiology using OCT are presented.

Spectroscopic OCT (SOCT) is another functional extension of OCT, which represents an additional contrast mechanism and might provide additional valuable diagnostic and metabolic tissue information. Absorption measurements with SOCT were performed on phantoms to evaluate the sensitivity of SOCT. First qualitative results on *in vivo* measurements in retinal pathologies are also presented.

Zusammenfassung

Das Auge ist das primäre Sinnesorgan. Frühzeitige Diagnose und Behandlung von Augenerkrankungen, die langfristig zur Erblindung führen, steigern die Lebensqualität erheblich. Hochauflösende optische Kohärenztomografie (engl: UHR OCT) ist ein bildgebendes, nichtinvasives Verfahren der Ophthalmologie. UHR OCT-Systeme erfordern Expertise in Elektronik, Photonik, Mechanik, Elektromechanik und Optik sowie Faseroptik und sind daher technisch sehr anspruchsvoll. Ebenfalls wichtige Schlüsselparameter sind Computerprogramme zur Kontrolle des Systems und für die Nachbearbeitung der Messdaten.

In dieser Dissertation werden die jüngsten Fortschritte zur Signalverarbeitung von ophthalmischen UHR OCT *ex vivo* und *in vivo* Daten behandelt. Nachbearbeitung von 2- und 3-dimensionalen UHR OCT Daten, ermittelt in Zeit- und Frequenzdomäne, wird präsentiert. Die in den letzten Jahren entwickelte "Frequency Domain" OCT (FD OCT) ermöglicht die volumetrische Erfassung bildgebender Daten innerhalb weniger Sekunden. 3D-Darstellungen verbessern das Verständnis morphologischer Veränderungen, hervorgerufen durch retinale Erkrankungen, wie z.B. Makulalöcher oder Glaukom ("Grüner Star"). 3D-Visualisierung wird exemplarisch anhand von *in vivo* UHR OCT Daten von gesunden und erkrankten Augen gezeigt.

Histologie erreicht eine Kontrasterhöhung durch Einfärbung, wodurch sich bei der Netzhaut des Auges eine klar unterscheidbare Strukturierung in einzelne Schichten zeigt. Eine ähnliche morphologische Information wird mittels UHR OCT erreicht, wobei die Zuordnung zu den histologischen Befunden noch nicht ganz geklärt ist. Zwei Studien, die dieser Klärung der Ungereimtheiten zwischen OCT und Histologie dienen sollen, werden an Schweine- und Affennetzhäuten präsentiert.

Axiale und transversale Auflösung sind in OCT entkoppelt. Die axiale Auflösung wird hauptsächlich durch die Bandbreite des applizierten Lichts bestimmt, während die transversale Auflösung von den optischen Eigenschaften der verwendeten Komponenten abhängt. Sphärische Aberrationen der Optik des Auges verringern die transversale Auflösung. Zur Verbesserung der transversalen Auflösung wurde adaptive Optik, die mittels deformierbarer Spiegel die Aberrationen kompensieren, in das UHR OCT System integriert.

Die objektive Dickenquantifizierung der verschiedenen Netzhautschichten kann zur frühzeitigen Diagnose maßgeblich beitragen. Im Rahmen einer Glaukomstudie wurden Algorithmen zur Vermessung von Nervenfaserschicht und Gesamtdicke der Netzhaut entwickelt. Des Weiteren wurde ein halbautomatischer Algorithmus entwickelt, mit dessen Hilfe Dickenprofile der Photorezeptorschicht des menschlichen Auges erstellt wurden.

Morphologische und funktionelle Änderungen sind üblicherweise eng miteinander verknüpft. Die frühzeitige Diagnostik könnte von tiefenaufgelösten funktionellen Messungen der Netzhaut profitieren. Erste Ergebnisse funktioneller physiologischer OCT (Optophysiology) an der Netzhaut werden vorgestellt. Spektroskopische OCT (SOCT) ist eine funktionelle Erweiterung der OCT, die zusätzliche Kontrastierung bietet und somit möglicherweise wertvolle diagnostische und metabolische Informationen liefern kann. Um die Empfindlichkeit von SOCT zu evaluieren, wurden Absorptionsmessungen mit SOCT an Präparaten durchgeführt. Erste Ergebnisse qualitativer *in vivo* SOCT an retinalen Pathologien werden ebenfalls präsentiert.

Part I
Methods

Chapter 1

Introduction

Advances in biomedical imaging techniques can improve diagnosis of diseases and can help in monitoring during treatment and could therefore lead to a better understanding of pathogenesis. The development of X-ray computed tomography (CT) [1] and magnetic resonance imaging (MRI) [2] allows for three-dimensional insights into the human body and has revolutionized clinical practice. Compared to optical coherence tomography (OCT) these imaging modalities are much more advanced in respect to their commercial availability and their standard clinical use. However, their spatial resolution is limited to the mm-range, wherefore these techniques can not be used for ophthalmic measurements or diagnosis.

Ultrasound was regularly employed in clinical ophthalmic examinations since 1956 [3, 4]. Physical contact with the eye is required, and a depth resolution of typically $150\ \mu\text{m}$ by using a 10 MHz transducer [5, 6] is achieved. With high-frequency ultrasound (50 MHz) the axial resolution is increased to $20\text{--}30\ \mu\text{m}$ [7, 8], but the penetration depth is limited to 4 mm due to the acoustic attenuation. First three-dimensional ophthalmic ultrasound scans were demonstrated in 1992 [9].

In 1979 scanning laser ophthalmoscopy or scanning laser tomography was invented [10–12]. A micron-scale focused laser spot is used for raster scanning of the retina to obtain high-quality, high-contrast en-face fundus images. The axial resolution is limited by the pupil aperture and ocular aberrations and reaches only several hundred microns ($\sim 300\ \mu\text{m}$). With scanning slit confocal microscopy real-time video imaging of the human cornea with submicrometer transversal resolution has been achieved [13, 14].

History. Optical coherence tomography (OCT) is a contact-less imaging technique based on white light or low coherence interferometry (LCI) [15–17] that enables tomographic insights into superficial layers of biological tissue [18]. An optical analogue to ultrasound A-scan was first demonstrated in 1986 with optical ranging measurements, applying femtosecond pulses and LCI [17, 19]. The first *in vivo* tomogram of the human optic disk was reported by Fercher et al. in 1993 [20]. Depth resolution in OCT depends on the bandwidth of the utilized light source and is for standard OCT in the order of several 10 micrometer. With the availability of broad bandwidth laser light sources, the depth resolution

could be shifted to the micrometer [21,22] and sub-micrometer range [23], which makes OCT interesting for cellular imaging, since the size of most cells is in this order. The depth penetration in OCT depends on the scattering properties of the imaged specimen as well as on the central wavelength of the probing beam and is in the range of 0.5 to 1 mm.

Image formation in OCT is based on the coherent backscattering properties of the imaged specimen [24–26]. Several extensions of OCT acting as contrast enhancements have been exploited. In principle, any physical process, which alters the light’s properties of the probing beam, can be used as contrasting information. Birefringent properties of the sample have been measured with polarization-sensitive OCT [27–29] and used for contrast enhancement. In Doppler OCT [30–35] the Doppler shift due to blood flow is measured. In spectroscopic OCT (SOCT) [36–40] tries to extract the spectral properties of the probing beam and therefore to conclude the absorption properties of the sample.

Several statistical methods have been applied for signal processing of OCT data, as deconvolution [41, 42], dispersion compensation [43–45], and speckle reduction methods [46, 47].

Anatomy of the eye. The eye is the organ which represents the most important sense in the mammalian body. Its major imaging components are the cornea, the lens, the vitreous and the retina as the sensory element (see fig. 1.1). Cornea, lens and vitreous are optical transparent and consist mainly of water. Light entering through the cornea is imaged onto the retina. Before it reaches the sensory part, the photoreceptors, which are situated on the back side of the retina, light has to pass six distinct layers: nerve fiber layer (NFL), ganglion cell

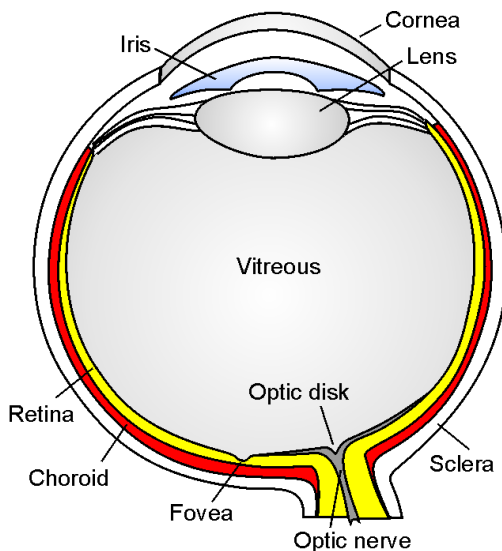


Figure 1.1: Anatomy of the eye. Cornea and lens work as optical imaging system and have their imaging plane at the retina. The spot of best visual acuity is located in the fovea, a cone-dominant region with a characteristic topological depression. The region around the fovea appears yellow in fundus imaging, wherefore this area is called macula or macula lutetia (lat. macula: spot; lutetia: yellow). Optic nerves and vessels leave the eye through the optic nerve head. This is the well known blind spot, since in this region no photoreceptors are present. The choroid is responsible for the blood support. The white sclera is the protective outer coat.

layer (GCL), inner plexiform layer (IPL), inner nuclear layer (INL), outer plexiform layer (OPL) and the outer nuclear layer (ONL) (see fig. 1.2 for anatomical details of the retina). The nuclear layers consist of different cell types (horizontal, bipolar, and amacrine cells), which are responsible for a complex processing of

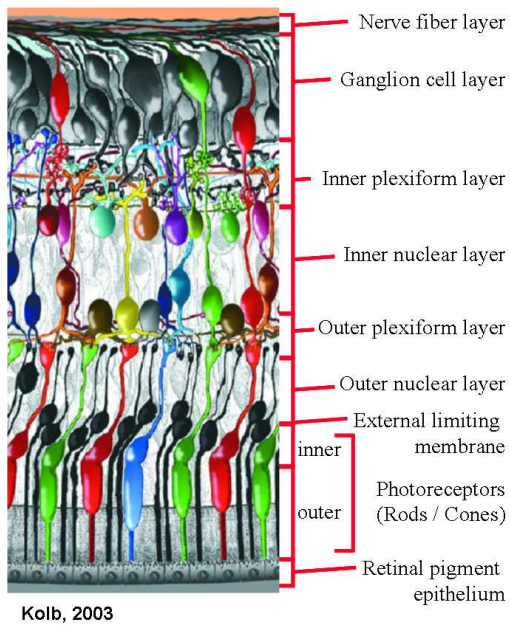


Figure 1.2: Anatomy of the retina. Light is entering the retina from the top and passes the nerve fiber layer, the cell and plexiform layers, before it is detected by the photoreceptors. Nutrition of the photoreceptors is provided by the choroid and the retinal pigment epithelium.

signals originating from the photoreceptors; the GCL contains the ganglion cells, which transform the processed signals into action potentials. These action potentials are guided through their axons, which build up the nerve fiber layer. The bundle of nerve fibers leaves the eye in the optic disk with the optic nerve, which is the cause for the blind spot due to a lack of photoreceptors in that area. The plexiform layers are the dendritic interconnections between the nuclear layers and optical more dense than the nuclear layers.

Chapter 2

Theory and Methods

2.1 Optical Properties / Light–tissue interaction

Light is an electromagnetic (EM) wave and interacts with electric charges, as electrons or molecules with dipole momentum for instance. Depending on the electronic properties of the media surrounding the charged particle and of its specific properties, the EM wave coupling will vary. This determines the way how the energy is transferred from the EM wave to matter and vice versa, i.e. the resonance frequencies, where the energy transfer is maximal. This section discusses the basic properties of EM waves based on [26, 48, 49].

Polarisation. The polarisation \mathbf{P} is the first order approximation answer of the material to the EM-field:

$$\mathbf{P} = \epsilon_0 \boldsymbol{\chi} \mathbf{E}, \quad (2.1)$$

with the dimensionless electric susceptibility tensor $\boldsymbol{\chi}$, which represents the dielectric properties of the media, and ϵ_0 the permittivity of free space. The electric displacement field \mathbf{D} is defined as

$$\mathbf{D} := \epsilon_0 \mathbf{E} + \mathbf{P} = \epsilon_0 (1 + \boldsymbol{\chi}) \mathbf{E} := \epsilon \epsilon_0 \mathbf{E}. \quad (2.2)$$

In biomedical imaging usually the light intensities are low, so there is no need for higher order susceptibilities, which would take nonlinear optical effects into account. However, there are also first attempts to use nonlinear effects for contrast enhancements in OCT [50].

Electromagnetic wave. As a solution of the Maxwell's equations a harmonic function, the wave function, can be derived:

$$\mathbf{E}(\mathbf{x}, t) = \Re \left[\tilde{\mathbf{E}}(\mathbf{k}, \omega) \cdot e^{-j(\mathbf{k} \cdot \mathbf{x} - \omega t)} \right] \quad (2.3)$$

with the complex amplitude $\tilde{\mathbf{E}}(\mathbf{k}, \omega)$ and the wave vector \mathbf{k} , which is related to the frequency $\omega = 2\pi \nu$ via the fundamental dispersion relation:

$$\mathbf{k}^2 = \frac{\omega^2}{c_0^2} \epsilon, \quad (2.4)$$

with c_0 the vacuum speed of light. The velocity of the wave front, which is the phase velocity \mathbf{v}_{ph} , can be calculated by taking the time derivative of the phase term in (2.3):

$$\mathbf{k} \cdot \mathbf{x} - \omega t = \text{const.} \Rightarrow \frac{d}{dt}(\mathbf{k} \cdot \mathbf{x} - \omega t) = 0 \Rightarrow \mathbf{v}_{ph} = \frac{d\mathbf{x}}{dt} = \frac{\omega \mathbf{k}}{k^2} \quad (2.5)$$

The phase velocity vector has the same direction as the wave vector \mathbf{k} and an absolute value of

$$v_{ph} = \frac{\omega}{k} \stackrel{(2.4)}{=} \frac{c_0}{n} \quad (2.6)$$

with the refractive index $n = \sqrt{\epsilon} = \sqrt{1 - \chi}$. This leads with (2.4) to

$$k = \frac{n\omega}{c_0}. \quad (2.7)$$

$k(\omega)$ is in general neither constant nor linear, because n in matter is dependent on ω . The Taylor expansion of k around k_0 leads to

$$k(\omega) = k_0 + \frac{dk}{d\omega}(\omega - \omega_0) + \frac{1}{2} \frac{d^2k}{d\omega^2}(\omega - \omega_0)^2 + \frac{1}{6} \frac{d^3k}{d\omega^3}(\omega - \omega_0)^3 + \dots \quad (2.8)$$

with $\frac{dk}{d\omega}$ the first order dispersion (group delay per unit length) and $\frac{d^2k}{d\omega^2}$ the second-order dispersion (group delay dispersion per unit length). The group delay T_g is defined as the derivative of the phase with respect to the angular frequency ω ; the group delay dispersion is defined as the second derivative of the phase with respect to the angular frequency, accordingly.

In ultrahigh resolution OCT, broad bandwidth light sources with a bandwidth at full width half maximum (FWHM) of up to 300 nm or even more are used. The superposition of EM waves of different frequencies builds wave packets. The individual frequency components have different phase velocities according to (2.6), which raises the question of the velocity of the whole package, the group velocity. The simplest model to determine the group velocity is the superposition of two collinear waves with frequencies $\omega_0 + \Delta\omega$, $\omega_0 - \Delta\omega$, wave numbers $k_0 + \Delta k$, $k_0 - \Delta k$, and equal amplitude. The superposition results in a beating:

$$\begin{aligned} \mathbf{E}(z, t) &= \Re \left\{ \mathbf{E}_0 \underbrace{e^{-j(k_0 z - \omega t)}}_{\cos(k_0 z - \omega t) - j \sin(k_0 z - \omega t)} \underbrace{\left[e^{-j(\Delta k z - \Delta \omega t)} + e^{+j(\Delta k z - \Delta \omega t)} \right]}_{2 \cos(\Delta k z - \Delta \omega t)} \right\} \\ &= 2\mathbf{E}_0 \cos(k_0 z - \omega t) \cdot \cos(\Delta k z - \Delta \omega t) \quad , \end{aligned} \quad (2.9)$$

where the first cosine term represents the carrier with frequency ω , and the second term corresponds to the envelope, which travels with velocity v_g :

$$\Delta k z - \Delta \omega t = \text{const.} \Rightarrow \frac{d}{dt}(\Delta k z - \Delta \omega t) = 0 \Rightarrow v_g = \frac{dz}{dt} = \frac{\Delta \omega}{\Delta k}. \quad (2.10)$$

With the Taylor expansion $\Delta \omega = \frac{d\omega}{dk} \Delta k + \dots$ we obtain

$$v_g = \frac{d\omega}{dk}. \quad (2.11)$$

Refractive Index. An interesting approach to explain the origin of the refractive index n can be found in [51]. The charges are treated as damped one-dimensional oscillators, driven by the external EM field. For a single oscillating charge q_e the equation of motion is:

$$m \left(\frac{d^2x}{dt^2} + \gamma \frac{dx}{dt} + \omega_0^2 x \right) = q_e E_0 e^{j\omega t} \quad (2.12)$$

with the solution

$$x = \frac{q_e E_0}{m (\omega_0^2 - \omega^2 + j\gamma\omega)} e^{j\omega t} . \quad (2.13)$$

The damping coefficient γ and the resonance frequency ω_0 is specific for the material. Integration over a plane of oscillating charges yields for the far field

$$E = -\frac{N\Delta z q_e}{2\epsilon_0 c} \left[j\omega \frac{q_e E_0}{m (\omega_0^2 - \omega^2 + j\gamma\omega)} \right] e^{j\omega(t-z/c)} \quad (2.14)$$

where $N\Delta z$ the number of charges per unit area. If different kinds of oscillators are taken into account with the corresponding densities N_l , resonance frequencies ω_l , and damping γ_l , the formula for the refractive index results in

$$n = 1 + \frac{q_e^2}{2\epsilon_0 m} \sum_l \frac{N_l}{\omega_l - \omega + j\gamma_l \omega} . \quad (2.15)$$

The dependence of the refractive index on the frequency is called dispersion. This frequency dependence leads to the fact that light components with different frequencies have a different phase velocity (see 2.6), which leads to the dispersion of the propagating wave packets. Dispersion is an important parameter in OCT systems and in optics in general, because it degrades resolution.

The refractive index can be separated into a real and an imaginary part: $n = n' - jn''$ where n' and n'' are real numbers:

$$n' \propto \frac{\omega_l^2 - \omega^2}{(\omega_l^2 - \omega^2)^2 + (\gamma_l \omega)^2} \quad \text{and} \quad n'' \propto \frac{\gamma_l \omega}{(\omega_l^2 - \omega^2)^2 + (\gamma_l \omega)^2} . \quad (2.16)$$

According to the exponential term in the complex EM-wave representation (2.3), the real and imaginary part of the refractive index lead to the following effects:

- $-jn''$ results in a exponential decay and describes a decrease of the field's magnitude – energy is absorbed by the material. n'' represents the wavelength dependent attenuation of the EM-wave.
- n' is responsible for a wavelength dependent phase shift which causes dispersion.

Usually the losses are given empirical as exponential expression with the absorption coefficient μ_a and the scattering coefficient μ_s :

$$I = I_0 e^{-[\mu_a(\lambda) + \mu_s(\lambda)]z} , \quad (2.17)$$

where I_0 is the initial intensity, I the intensity of the light after passing the distance z through the absorber. This formulation is known as Beer-Lambert's law¹.

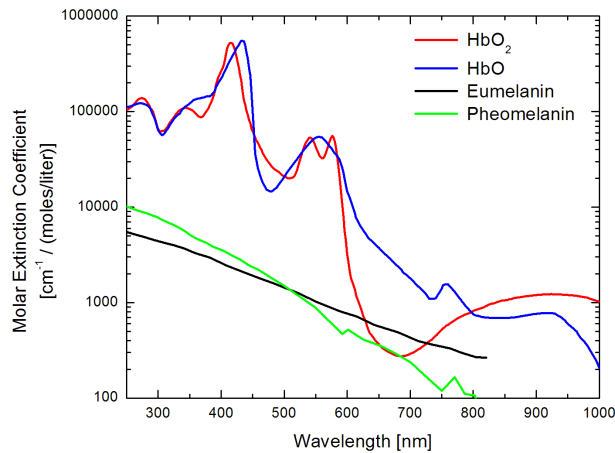


Figure 2.1: Absorption profiles for melanin, oxy- and deoxy-hemoglobin. Eumelanin is present in human black hair and in the retina, pheomelanin can be found in red hair. The iron containing hemoglobin is contained in red cells of the blood in mammals and responsible for the oxygen transport. The absorption property of hemoglobin strongly depends on the oxygenation state. The point at 800 nm, where the absorption of oxy- and deoxy-hemoglobin is equal, is called isosbestic point.

Biological tissue is highly inhomogeneous. Different kinds of tissue can be classified by the distribution of scatterers, i.e. cell types, cell size, and their different absorption behavior. The absence or presence of certain chromophores, e.g. melanin also helps for tissue classification. Changes in the chromophore distribution are usually attributed to certain pathologies.

The molar extinction coefficient is a measure, how much light is absorbed by a certain absorber. It is normalized by the amount of moles per volume (unit: $\text{cm}^{-1}/(\text{moles/liter})$). fig. 2.1 shows the molar extinction coefficients [52] of melanin, oxy- and deoxy-hemoglobin². Around 800 nm the absorption profiles of the hemoglobin derivatives have a crossing point, where below 800 nm the HbO absorption is dominant, whilst above 800 nm HbO₂ absorption dominates. Measuring blood absorption at wavelength covering the isosbestic point will enable conclusions concerning the oxygenation level.

Another important chromophore in biological tissue is melanin, which has a relatively linear absorption and is more absorbent at shorter wavelength. Melanin plays an important role in the pathogenesis of cancer, hence a biomedical imaging tool for qualitative or quantitative detection of melanin distribution might have an important impact for early cancer diagnosis.

¹The effect of light absorption was first described by Pierre Bouguer in 1729, than rediscovered by Lambert (1760) and Beer (1852).

²Hemoglobin with an oxygenation level of 100 % is referred to as oxy-hemoglobin; hemoglobin with an oxygenation level of 0 % is named deoxy-hemoglobin. hemoglobin

Coherence. Interference between waves only takes place, if their phases have a fixed relation and if their polarisation matches. The degree of phase relation is called coherence and defined as the correlation between two fields. We distinguish between spatial and temporal coherence. Spatial coherence denotes the phase relation of the field at different positions in the beam profile. Lasers usually have a very high spatial coherence. Temporal coherence describes the phase relation of fields at the same fixed position at different times. The cross-correlation of two complex analytical signals³

$$\Gamma_{RS}(\tau) := \langle E_R(t) E_S^*(t + \tau) \rangle, \quad (2.18)$$

can be normalized with their auto-correlation terms at $\tau = 0$, $\Gamma_{RR}(0) = I_R$ and $\Gamma_{SS}(0) = I_S$:

$$\gamma_{RS} := \frac{\langle E_R(t) E_S^*(t + \tau) \rangle}{\sqrt{I_R I_S}} = \frac{\Gamma_{RS}(\tau)}{\sqrt{I_R I_S}} \quad (2.19)$$

γ_{RS} is called the normalized complex degree of coherence. The Fourier transform of the auto-correlation function (ACF) $\Gamma(\tau) := \Gamma_{SS}(\tau)$ of the field

$$S(\omega) = \frac{1}{\pi} \int_{-\infty}^{\infty} \Gamma(\tau) e^{-j\omega\tau} d\tau \quad \Leftrightarrow \quad \Gamma(\tau) = \frac{1}{\pi} \int_{-\infty}^{\infty} S(\omega) e^{j\omega\tau} d\omega \quad (2.20)$$

equals the power spectrum of the light source. This relation is called Wiener-Khinchin-theorem and is the base of Fourier spectroscopy. The width of the ACF is proportional to the coherence time τ_{coh} and the spectral width $\Delta\omega$ and the coherence time are connected as [48]:

$$\tau_{coh} \Delta\omega \approx 2\pi. \quad (2.21)$$

With $\omega = 2\pi \frac{c_0}{\lambda}$ and $\frac{\Delta\omega}{\Delta\lambda} \approx -2\pi \frac{c_0}{\lambda_0^2}$ (2.21) the coherence length l_{coh} is

$$l_{coh} = c_0 \tau_{coh} \approx \frac{\lambda_0^2}{\Delta\lambda_0}. \quad (2.22)$$

Interferometry. OCT is based upon a Michelson interferometer with a detector unit at the interferometer exit, where a time average of the light intensity I is measured. The averaging times T are usually in the range of 10^{-6} to 10^{-9} s, which is several orders of magnitude above the cycle duration of visible light ($\approx 10^{-14}$ s).

In the interferometer (fig. 2.2), the incoming complex plane light wave $\mathbf{E}(\omega, t) = E_0 e^{i(kz - \omega t)}$ is split into two waves: the reference wave \mathbf{E}_R , which is back reflected by a mirror, and the sample wave \mathbf{E}_S , which is altered by the sample and partly back reflected. The alteration effects of the waves can be described by complex transfer functions $H_R(\omega)$ and $H_S(\omega)$ of the reference and sample arm, respectively. With $S(\omega)$ the power spectral density of the light source we obtain for the waves from the reference and sample arm:

$$|\mathbf{E}_{R,S}(\omega)| = S(\omega) H_{R,S}(\omega) \quad (2.23)$$

³Where $\langle \cdot \rangle = \lim_{T \rightarrow \infty} \frac{1}{T} \int_{-T}^T \cdot dt$ denotes the time average, assuming ergodic processes. The time average is equal to the ensemble average.

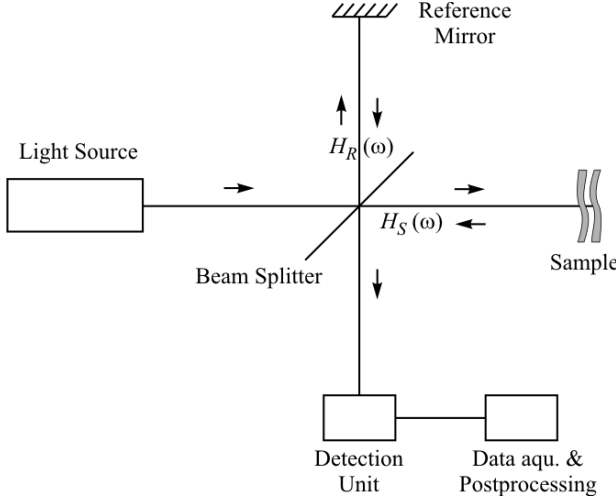


Figure 2.2: Michelson interferometer. Light is split in the reference and the sample wave. The back reflected light interferes in the beam splitter and is measured by the detection unit followed by filtering, data acquisition and postprocessing. $H_R(\omega)$ and $H_S(\omega)$ are the transfer functions of the reference arm and the sample arm respectively.

The back reflected waves of the two arms are recombined for interference. The intensity depends on the optical path difference the waves traveled in the two interferometer arms and can be expressed as a function of the zero delay τ :

$$\begin{aligned} I(\tau) &= \langle [\mathbf{E}_R(t) + \mathbf{E}_S(t + \tau)]^2 \rangle \\ &= \langle \mathbf{E}_R(t)^2 \rangle + \langle \mathbf{E}_S(t + \tau)^2 \rangle + 2 \Re \langle \mathbf{E}_R(t) \mathbf{E}_S^*(t + \tau) \rangle \end{aligned} \quad (2.24)$$

$$= I_R + I_S + 2 \Re[\Gamma_{RS}(\tau)], \quad (2.25)$$

where \Re denotes the real part of the complex argument. The first two terms contribute to the dc-component of the measured intensity; the latter is the interference term and denotes the cross correlation between the reference and the sample wave. In OCT signals this interference term is referred to as fringes.

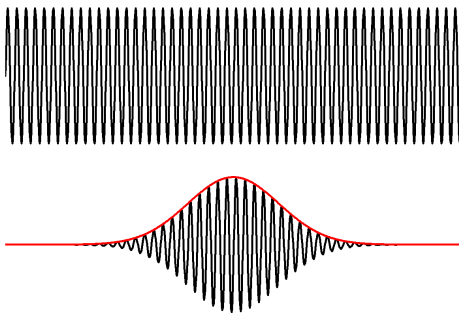
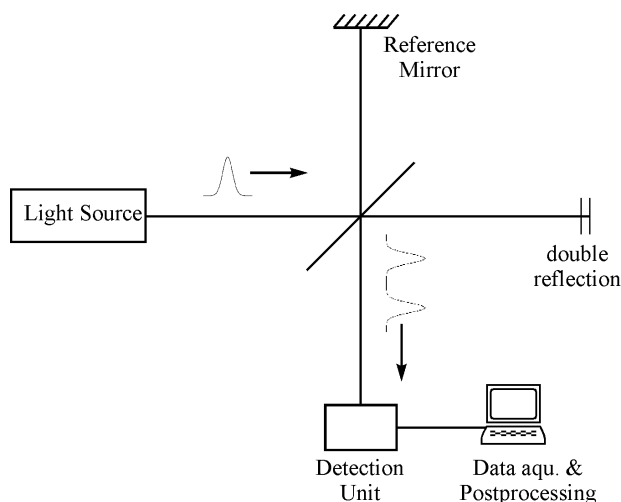


Figure 2.3: Interference fringes for different coherence length. Top: long coherence lengths, corresponding to a small bandwidth; bottom: short coherence length, corresponding to a large bandwidth. The envelope (red) is a measure for the the backscattered light intensity, which is coupled to structural changes of the imaged specimen. The intensity changes are visualized in standard OCT tomograms.

Time domain OCT principle. In OCT light with short coherence length (see fig. 2.3) is used. By changing the time delay, therefore the path difference of the two interferometer arms, the fringe pattern will move correspondingly. The envelope of the fringe pattern can be seen as an ‘echo’ from the sample, therefore OCT can be considered as the optical analogue to ultrasound. In the case of two reflective layers in the sample arm, there will be two ‘echoes’ (see fig. 2.4).

Figure 2.4: Time domain OCT principle. The two back reflections, originating from interfaces that separate areas of different refractive index, experience a different time delay. In time domain OCT (TDOCT) the reference mirror is actively scanned, in frequency domain OCT (FDOCT) the reference mirror is fixed in one position.

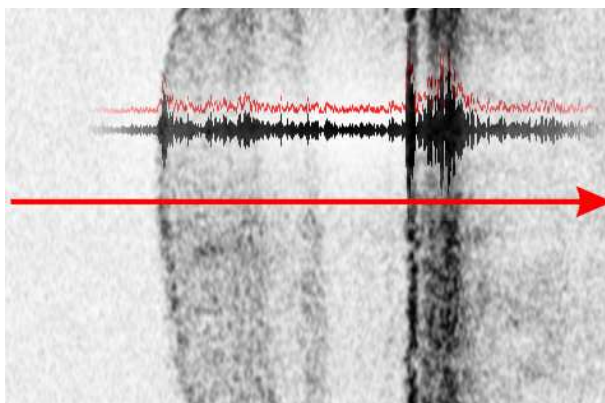


The detected intensity as a function of delay time is proportional to the back reflected light intensity as a function of sample depth. One such scan is called an A-scan according to ultrasound. Neighbored A-scans build up a tomogram, also called B-scan (see fig. 2.5). Back reflections from within the sample are caused by refractive index changes, small enough to be detectable by the system sensitivity. The changes of refractive index OCT is sensitive to are in the order of 10^{-5} , corresponding to a sensitivity of 100 dB⁴ [53].

Resolution. In OCT the transversal and axial resolution are decoupled. The first is given by the numerical aperture of the imaging optics as in conventional microscopy. The latter is determined by the coherence length of the light source. For a Gaussian spectrum with central wavelength λ_0 and bandwidth $\Delta\lambda$ the

⁴For dielectric media and perpendicular incidence the reflectivity from different depends on the square of the change in refractive index Δn .

Figure 2.5: OCT tomogram generation. The red arrow shows the direction of the incident light and therefore an A-scan, respectively. The corresponding fringe data (black) and the envelope (red) of an A-scan are overlaid. The B-scan is generated of consecutive A-scans at neighboring positions. The envelope covers only half of the dynamic range of the fringe signal.



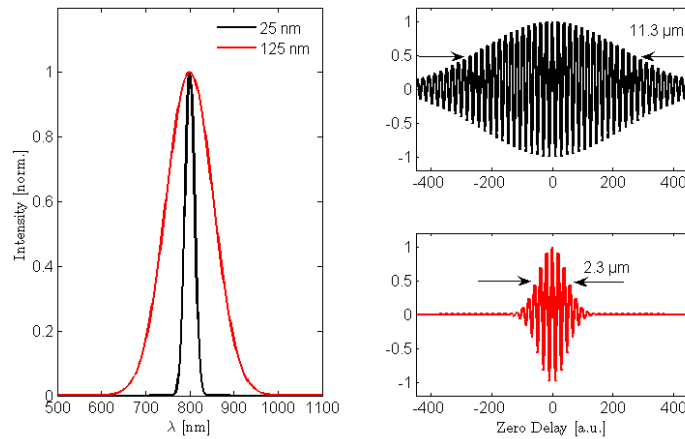


Figure 2.6: Bandwidth dependence of the resolution. On the left are two Gaussian spectra with 25 nm (black) and 125 nm (red) optical bandwidth; on the right are the corresponding fringes showing 11.3 μm (black, top) and 2.3 μm (red, bottom) theoretical resolution.

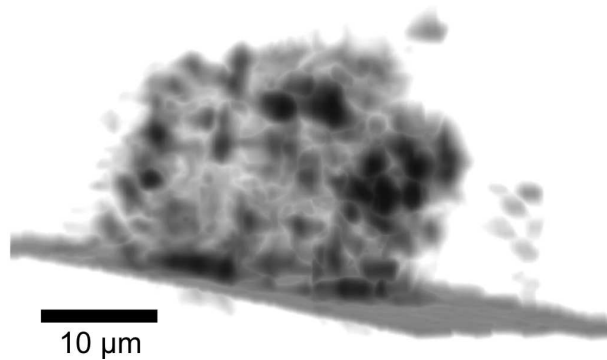


Figure 2.7: Sub-micrometer axial resolution with TD-OCT. The figure shows a 3D-representation of tomograms of an accumulation of human HT-29 cells (colon cancer cells) *in vitro*. Sub-micrometer resolution ($0.5 \mu\text{m}$) was achieved by utilizing a broadband emission spectrum (325 nm at full width half maximum), centered at 725 nm with a laser based on a photonic crystal fiber. The three-dimensional tomogram reveals highly scattering subcellular structure such as nucleoli (black dots). The image was filtered and then rendered with ImageJ.

coherence length in air is [54, 55]:

$$l_c = \frac{4 \ln 2}{\pi} \frac{\lambda_0^2}{\Delta\lambda}. \quad (2.26)$$

Fig. 2.6 shows the corresponding fringe patterns, as they would be measured with OCT for two different optical bandwidth (25 nm, black and 125 nm, red). The axial resolution is given by the full width at half maximum (FWHM) of the envelope. This example shows that with bandwidth as they are provided by state of the art lasers, resolutions in the micrometer regime can be achieved. Actually, fig. 2.7 shows submicrometer resolution OCT of in vitro human colorectal adenocarcinoma cells HT-29 [23]. The axial resolution was $0.7 \mu\text{m}$ in air and $0.5 \mu\text{m}$ in tissue, achieved with a laser based on a photonic crystal fiber (PCF) light source, providing a bandwidth of 325 nm, centered at 725 nm.

2.2 Time Domain – Frequency Domain OCT

The detection unit in fig. 2.2 can either be a detector based on photodiodes (time domain, TD), or a spectrometer with a CCD⁵ array (frequency domain⁶, FD). The main difference between these two detection schemes is, that in TD an integration of all optical frequencies is measured, whereas in FD the optical frequencies of the spectrum are measured separately. This can be done in parallel by dispersing and measuring the light using a spectrometer (spatially encoded FDOCT), or by sweeping the frequencies and measuring them sequential in time (time encoded FDOCT).

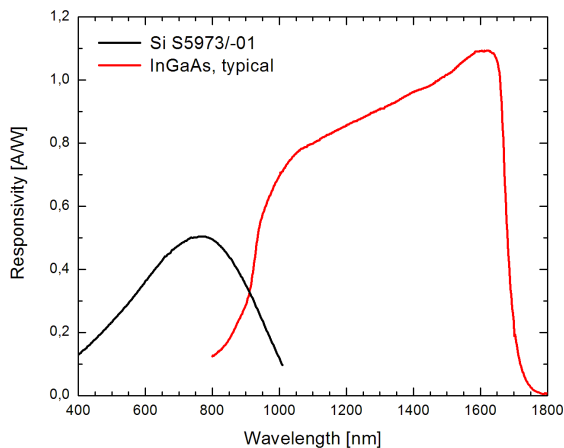


Figure 2.8: Detector sensitivities. In the visible range Si-detectors are used, which have a maximum sensitivity around 800 nm. In the infrared range InGaAs-detectors are used, for instance.

Dual balanced detection. In TD, a photo current $i_{det} \propto I$ (2.25) is measured, while moving the reference mirror back and forth. I is the light intensity at the

⁵CCD is the abbreviation for Charged Coupled Device, invented in 1969 by Boyle and Smith at the Bell Labs. [56]

⁶In the literature the terms “fourier domain” and “spectral domain” are often used as synonyms.

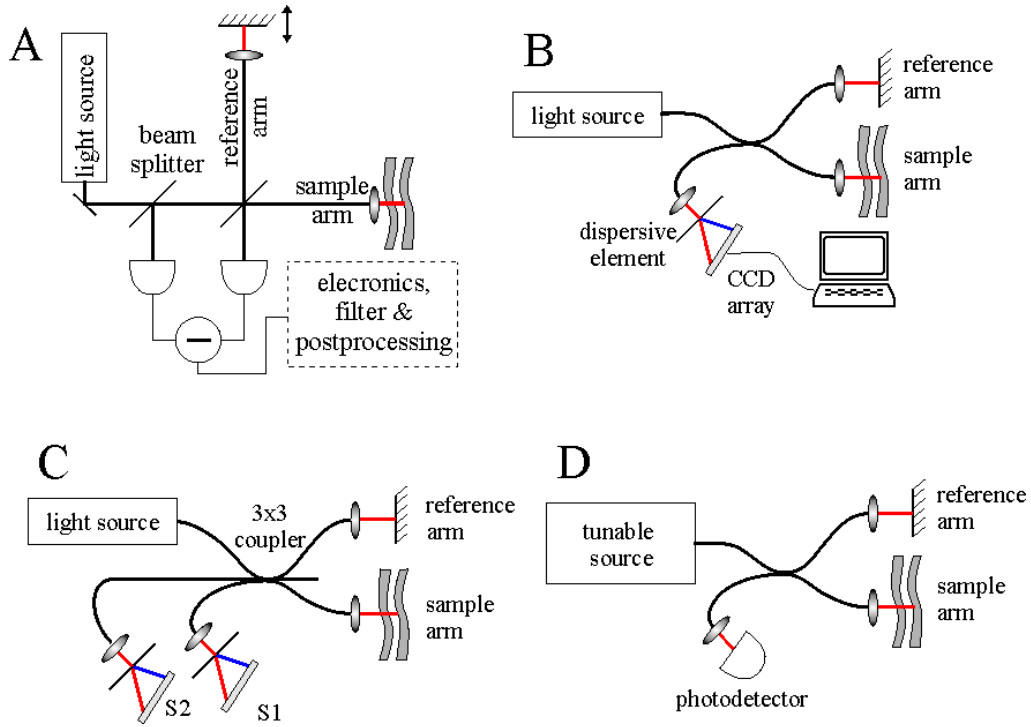


Figure 2.9: Detection schemes in OCT. Dual balanced detection (left) in time domain OCT; frequency domain OCT (right).

detector, which is determined by integration of the optical frequencies in the spectrum. Dependent on the central wavelength of the light source, either Si-detectors or InGaAs-detectors are used (see fig. 2.8).

Because high sensitivity is needed, dual balanced detection [57] is utilized (see fig. 2.9A). One detector unit consists of two photodiodes, where one detects the incoming field intensities with a phase shift of π in respect to the other detector. The signals of the two photodiodes are subtracted electronically. This leads to a cancellation of excess noise, which is prominent at both detectors, and of the dc-component. The signal height is doubled. The combined effect of signal doubling and noise cancellation leads to a gain in signal-to-noise of more than 3 dB. As scanning device for the reference arm galvo or piezo scanners are utilized. Since mechanical scanning has always a limited linearity, phase instabilities of the OCT-signal are inherent in TD.

Frequency domain. FD-OCT uses a different detection scheme. The reference mirror stays at a fixed position and instead of measuring a spectral integrated photo current, the interfering fields are dispersed and imaged onto a CCD array (see fig. 2.9B). Every pixel collects a photoelectron charge instead of a photo current, which is an integration over the spectral range incident on the individual pixel, and is only a small part of the whole spectrum.

Because phase instabilities are omitted due to the motionless measurement, FD has a very high potential for OCT extensions like Doppler or spectroscopic

measurements [39, 58]. From the obtained spectrogram the spatial information is gained by applying a Fourier transform. Since the measured signal is real, the Fourier transform will result in an even function, producing mirror images in the negative frequency range. A way to suppress mirror images is the measurement of complex signals with a phase modulator [29, 33] or by using a different interferometer design employing a 3x3 coupler and measuring two spectrograms (see fig. 2.9C) [59].

The finite pixel width of the camera results in the convolution of the spectrogram with a rectangular function. The associated amplitude in time domain therefore has to be multiplied with a sinc function, resulting in a 4 dB loss at the half depth range [60] - a fact that does not happen in time domain. On the other hand in frequency domain a significant shot noise reduction is achieved [61].

An alternative frequency domain technique represents swept source OCT: instead of dispersing the spectrum onto an array (spatial encoded FD OCT), a swept laser light source illuminates the sample, and a PIN-diode is used for detection (time encoded FDOCT, see fig. 2.9D) [62].

Part II

Signal Processing for Ophthalmic Ultrahigh Resolution OCT

Chapter 3

Two-Dimensional Ophthalmic Ultrahigh Resolution OCT

3.1 Dispersion compensation.

In order to achieve ultrahigh resolution as given by the bandwidth of the light source, there are two main issues that have to be fulfilled. First, the optics used in the system has to support the full bandwidth of the laser, since a reduction of the bandwidth as well as chromatic aberrations will result in a loss of resolution according to (2.26). Second, the dispersion in both arms of the OCT interferometer has to be matched, otherwise the fringe pattern will be broadened and the resolution will be degraded. Fig. 3.1 shows the fringe pattern for a Gaus-

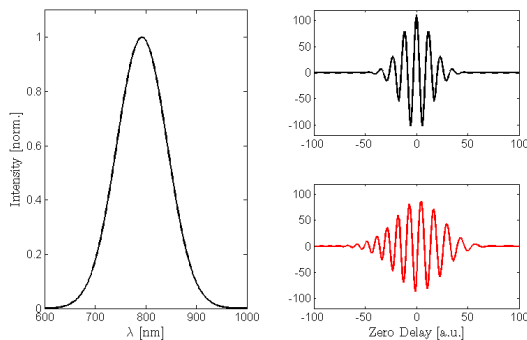


Figure 3.1: Dispersion mismatch. Gaussian spectrum (left) and the corresponding fringes for dispersion matched (right, top), and the unmatched case (right, bottom).

sian spectrum in the matched (top) as well as the unmatched (bottom) case. In the unmatched case the fringe pattern is broadened and has less peak intensity, therefore the axial resolution will decrease as well as the signal-to-noise-ratio (SNR). The best way to match the dispersion is to use the materials with the same optical properties in both interferometer arms. Due to the fact that most biological tissues have a high water content, the dispersion of water has to be considered for OCT. For imaging the retina at the rear part of the eye, for example, a 25 mm cell of water is placed in the reference arm to match the dispersion of the vitreous, which mainly consists of water.

In order to optimize an UHR OCT-system a dispersion control program was

developed, which allows for online SNR- and dispersion measurement¹. SNR in OCT is defined as

$$\text{SNR} = 10 \cdot \log_{10} \frac{I^2}{\sigma}, \quad (3.1)$$

where I is the maximum intensity of a signal produced by a mirror in the sample arm, and $\sigma = 1/N \sum_N (x_n - x_0)^2$ is the variance of the noise.

The panel shows four graphs: the measured fringe (upper left), the amplitude spectrum calculated from the fringe via Fourier transform (upper right), the group delay (lower left), which is obtained by differentiation of the phase spectrum, and the group delay dispersion (lower right), which is the second derivative of the phase spectrum. If the first order dispersion in the two interferometer arms is not matched, the group delay as a function of wavelength will have a slope

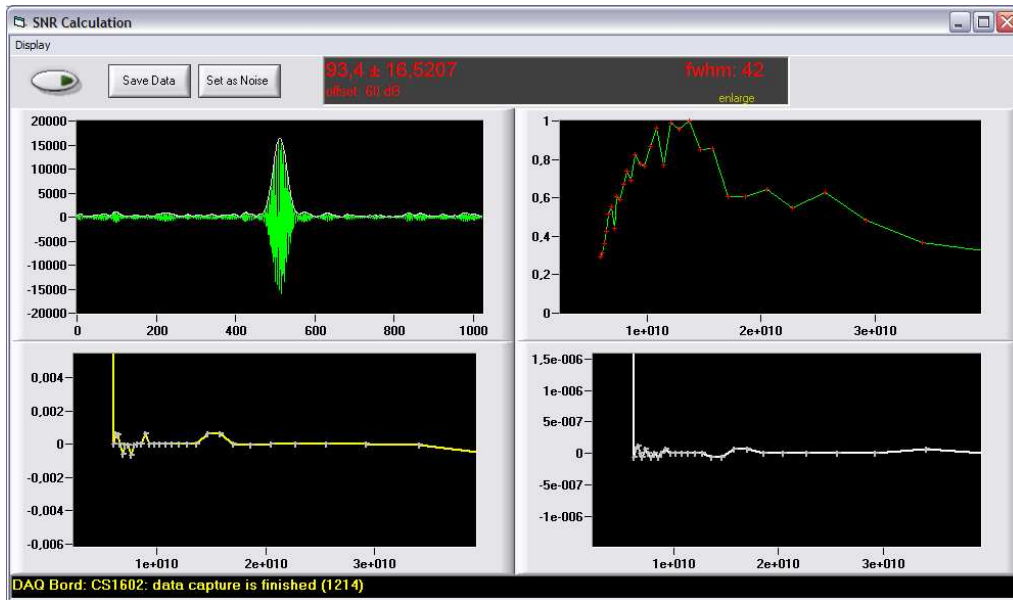


Figure 3.2: Dispersion control program. top left: fringes; top right: spectrum as calculated from the fringes; bottom left: group delay, calculated as first derivative of the phase spectrum; bottom right: group delay dispersion, 2nd derivative of the phase spectrum.

different from zero. By adjusting the amount of dispersive material in the reference arm the dispersion can be matched online. The second order dispersion mismatch of the interferometer arms can be examined with the group delay dispersion panel. For both, first and second order dispersion matched, group delay and group delay dispersion have a flat appearance within the spectral range as shown in fig. 3.2.

¹Visual Basic 6, Visual Studio, Microsoft Corp.

3.2 Data acquisition

In TD the coherence gate is scanned through the sample by changing the time delay in the reference arm. Scanning in UHR OCT is performed with up to 250 Hz. One depth scan is called an A-scan (see fig. 3.3, top), consecutive A-scans build up a tomogram (B-scan) with the A-scan's intensity mapped to a gray- or colorscale. The phase of the A-scan contains additional information about the imaged specimen. In order to obtain the full-fringe interferometric data, a high speed, 10 Ms/s (10^6 samples per second), 16 bit PCI data acquisition board was utilized², which allows for full fringe detection with 10-times oversampling. The typical depth sampling spacing in tissue is in the range of 30 nm, which is necessary for the spectroscopic evaluation of the fringe data. Due to the oversampling aliasing effects are suppressed. The dynamic range is $20 \cdot \log_{10} 2^{16} \approx 96$ dB.

Since the depth resolution for *in vivo* ophthalmic UHR OCT is typical $3 \mu\text{m}$, for visualization of the backscattering intensity it is not necessary to display every sample point. Therefore, downsampling by a factor of 50 was applied prior visualization, which leads to a depth spacing of $1.5 \mu\text{m}$ (half the depth resolution).

Compared to standard resolution OCT, measurements acquired with ultra-high resolution OCT and full fringe detection require ten times the data storage. The data acquisition program saved the data in variant format, which automatically stores information about length and data format in the header of each scan. The data storing policy was to directly keep the raw data without any post processing. The advantage is the conservation of the complete information content. On the other hand the amount of data to be stored is much higher and displaying needs always postprocessing prior to visualization.

3.3 Signal processing

Envelope generation. For displaying the intensity information the envelope was generated and downsampled, to reduce the amount of data. Envelope generation was realized by shifting the interferogram to baseband. This can be done by filtering (electronically or by software), which has the draw back, that the filter smears out the signal. A better way is to calculate the spectrum $S(\omega)$ from the measured signal $s(t)$ with a fast fourier transform (FFT), shift $S(\omega)$ to baseband in frequency space ($\hat{S}(\omega)$), and to obtain the envelope signal $\hat{s}(t)$ with the inverse FFT (see figure 3.3):

$$S(\omega) = \int_{-\infty}^{\infty} s(t)e^{-j\omega t} dt \xrightarrow{S \rightarrow \hat{S}} \hat{s}(t) = \frac{1}{2\pi} \int_{-\infty}^{\infty} \hat{S}(\omega)e^{j\omega t} d\omega \quad (3.2)$$

A matlab³ implementation of this envelope generation can be found in appendix A. Another way is the use of the Hilbert transform \mathcal{H} . The envelope $\hat{s}(t)$ is

²CompuScope 1602 from GaGe Applied Technologies, Inc., Canada.

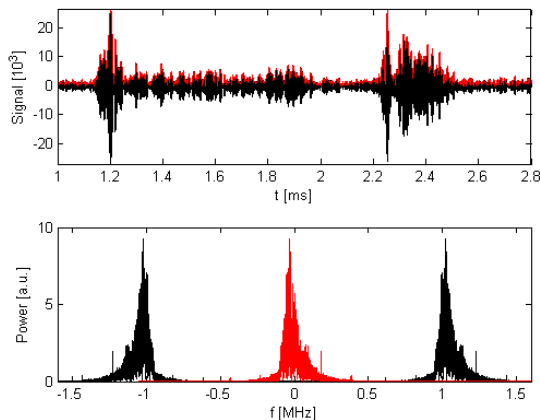
³matlab release 14, Service Pack 1, student version, Mathworks.

gained by analytic continuation of the measured signal intensity $S(t)$:

$$\hat{s}(t) = |S(t) + j\mathcal{H}\{S(t)\}|. \quad (3.3)$$

The envelope generation reduces inherent the dynamic range of the signal. If

Figure 3.3: The top row shows typical fringe data (A-scan, black) and the corresponding envelope (red), which is calculated by shifting the spectrogram (bottom row, black) from 1 MHz to zero frequency (bottom, red), followed by the inverse FFT.



the fringe data is sampled with 16 bit, the envelope will have only 15 bit (half of the original range). The maximal achievable dynamic range for data acquisition including envelope generation is $20 \cdot \log_{10} 2^{15}$, which is close to 90 dB. The dynamic range in ophthalmic UHR OCT images is ~ 42 dB, depending on the transparency of the ocular media. In case of cataract, a disease in which the lens becomes opaque, the dynamic in the tomogram is dramatically decreased.

If the movement of the reference arm is not linear within the scanning range, the carrier frequency of the interferometric signal will change during a single scan. This will result in a partial compression of the envelope signal, and in a change of the phase of the fringe data. This phase instability will produce artifacts, when the phase information is used like in Doppler flow or spectroscopic OCT.

Motion artifacts. In vivo measurements in TD are usually impaired by motion artifacts. In ophthalmology, these motions can be related to head movements, eye movements (tremor, drifts, and microsaccades) [63], and pulsation (see fig. 3.4A). Since the measurement time differs significantly in TD and FD, motion artifacts have to be handled separately.

In TD a cross-correlation of the intensities of neighbored scans is used and individual A-scans are shifted to the position, where the cross-correlation is maximal. Correlation of only one neighbored scan leads to a “walk off” in the correlated tomogram (see fig. 3.5). This is due to the random distribution of digitization points along the envelope. With a correlation that takes 20 neighboring scans into account, the resulting image is straightened (see fig. 3.4).

The algorithm starts at the left side and correlates the first two scans. After shifting, the third scan is correlated with the first two, and so on.

The drawback of the cross-correlation is, that the natural topology is not preserved - the individual A-scans are always aligned with respect to the highest

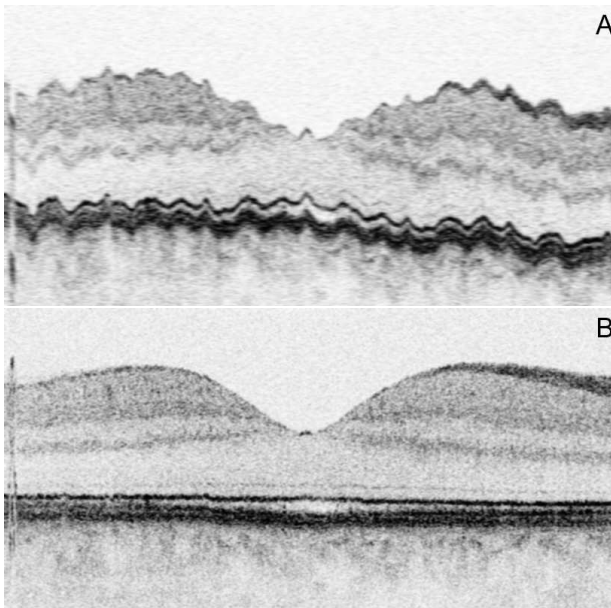


Figure 3.4: Cross-correlation. (A) Image distorted due to motion artifacts; (B) shows the same tomogram after applying the cross-correlation algorithm. All A-scans are aligned with respect to the highest signal, originating in the junction of the inner and outer segments of the photoreceptor layer.

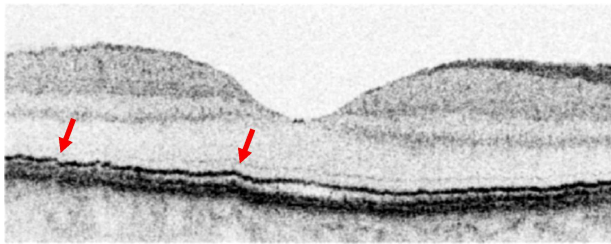


Figure 3.5: Cross-correlation of only two A-scans at a time. The original distortion is no longer visible, but small irregularities (red arrows) are still visible.

signal. In ophthalmic OCT of the retina this is usually the signal originating from the RPE or the PR IS/OS junction. From fig. 3.4A it is clear, that the real topologic structure is not reproduced in the B-scan due to motion artifacts. A matlab implementation for the cross-correlation can be found in appendix B.

Data display For displaying tomographic data a data viewer (see fig. 3.6) has been developed⁴. Batch processing for different data formats (TD and FD OCT) is implemented as well as postprocessing (envelope generation, cross-correlation, filter), different mappings (color map, look up table) and the possibility to store the images in bitmap format for further image processing.

Noise in tomograms. In OCT tomograms noise with high spatial frequency, which extends only over one to three pixels, is apparent. Since this dimension is below the axial resolution of ophthalmic OCT systems ($\sim 3 \mu\text{m}$), it does not represent real structure and is usually filtered with a low-pass filter (3 pixels) during image postprocessing. The direct comparison of an unfiltered (fig. 3.8A) and a filtered tomogram (fig. 3.8B) shows the smoothing effect.

Another kind of noise results from speckles. Speckle noise appears as a local varying stripe pattern within the tomogram. Its origin is the interference of

⁴Visual C++ 6.0, Visual Studio, Microsoft Corp.

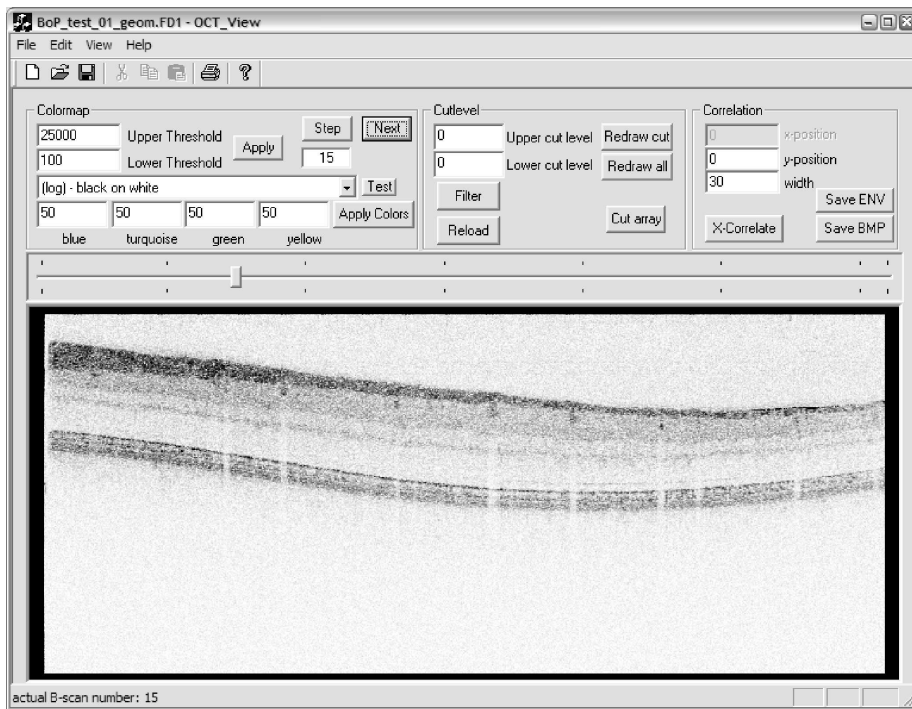


Figure 3.6: Data Viewer. Example FD tomogram showing the retinal layers from the parafoveal region of a healthy volunteer.

backscattered electric fields from different scatterers within the coherence volume - the larger the volume is, i.e. the smaller the bandwidth of the light source, the more speckle are produced. To eliminate speckle noise despite the use of broad bandwidth, a motion blur filter was applied in orthogonal directions whenever necessary. This filter essentially overlays copies of the image, shifted in a given direction and adjusting the transparency to keep the intensity constant.

Intensity mapping. To enhance the visibility of small signals, a logarithmic scale is used to display the data. The sensitivity of the eye and the image perception plays an important role in image visualization. For black and white

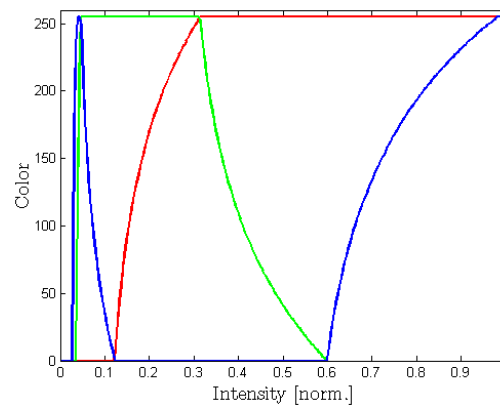


Figure 3.7: Pseudo Colormap. The figure shows the mapping from the intensity to different colors in RGB color space. This colormap is used as a standard in ophthalmic OCT (see fig. 3.8D).

maps it depends on the preferences of the individual observer, if higher signals are mapped to black (black on white, fig. 3.8 B) or the other way around (white on black, see fig. 3.8C). A custom designed pseudo color map (fig. 3.7) based on [64] has been used to maximize the image perception and to visualize small differences in signal intensity (see fig. 3.8D). Small signals are mapped to a color gradient from black over blue to green. Medium to high intensities are displayed in gradients from yellow over red to white (see colormap on the right of fig. 3.8D).

3.4 Correlation of histology with ultrahigh resolution OCT in ophthalmic imaging

There are still ongoing discussions about the correspondence of intraretinal layers as visualized with OCT and retinal anatomy known by histopathology. As already mentioned, in OCT changes in the optical properties, i.e. refractive index changes, are detected. The question is how these local variations of the optical properties can be correlated to the color achieved with H&E staining⁵, a method that stains the cytoplasmic material, cell membranes as well as some extracellular structures in pink (eosin), and the nuclei in blue-violet (haemotoxylin).

Several studies using either animal [65,66] or human cadaver [67] retinas have been conducted to compare OCT tomograms with histology in order to gain a better understanding and interpretation of OCT images. However, the exact correlation of OCT tomograms with retinal morphology has been a long-standing controversy. One of the limiting factors was insufficient axial resolution of about 10–15 μm as given by the bandwidth of the employed light source, usually a superluminescent diode, and therefore reduced visualization of intraretinal layers.

Correlation of histology and UHR OCT images in two retinal animal models (monkey and pig retina) was performed in two studies in collaboration with the Department of Physiology, Medical University of Vienna. Histology was performed by E.M. Anger (pig retina) and M. Glösmann (monkey retina). C. Schubert prepared the retinas for imaging. Scientific input and interpretation of the data was assisted by P. Ahnelt. Tissue shrinkage due to histological processing have been evaluated with a morphing procedure.

3.4.1 In vitro ultrahigh resolution OCT system

A new generation of a compact ultrahigh-resolution OCT system was developed and used. The system consists of a scanning unit (up to 250 Hz, 400 mm s^{-1}) integrated in a fiber optic-based Michelson interferometer using a compact, user-friendly, state-of-the-art sub-10-femtosecond titanium:sapphire laser (800 nm center wavelength, up to 170 nm (FWHM), optical bandwidth, 400 mW output power; Compact Pro; Femtosource, Vienna, Austria). The interferometer was interfaced to a microscope delivery system. Both the fiber-optic interferometer and the optical components of the microscope were designed to support the

⁵H&E is a standard histological staining technique for contrast enhancement based on haematoxylin and eosin.

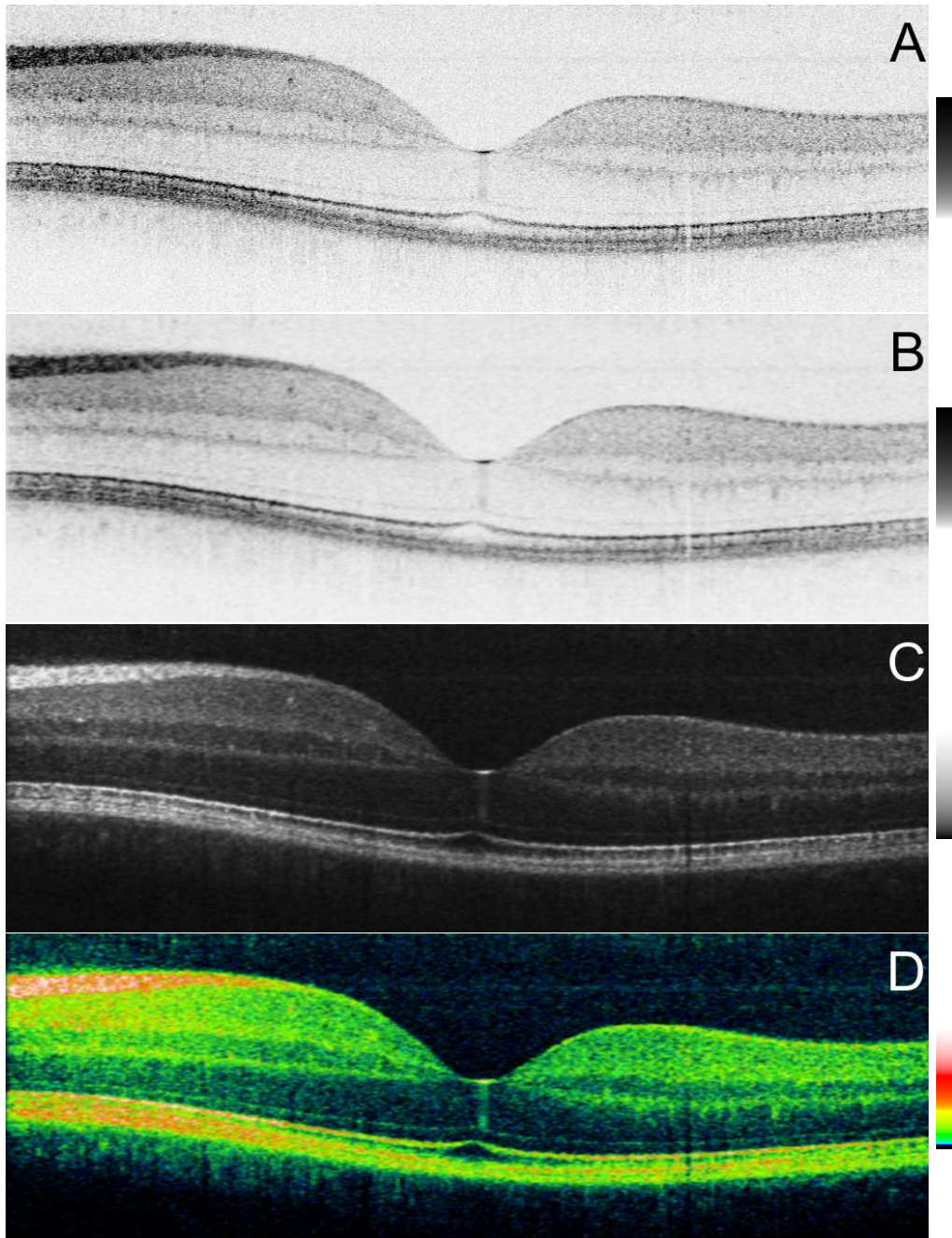


Figure 3.8: Different colormaps. A: unfiltered logscale black-on-white tomogram; B: same mapping as A but low-pass filtered (3 pixel); C: white on black logscale, low-pass filtered; D: custom designed color map to enhance the visibility of small signals close to the noise level.

propagation of very broad bandwidth light throughout the OCT system and to compensate for any polarization and dispersion mismatch between the sample and reference arms of the interferometer [68].

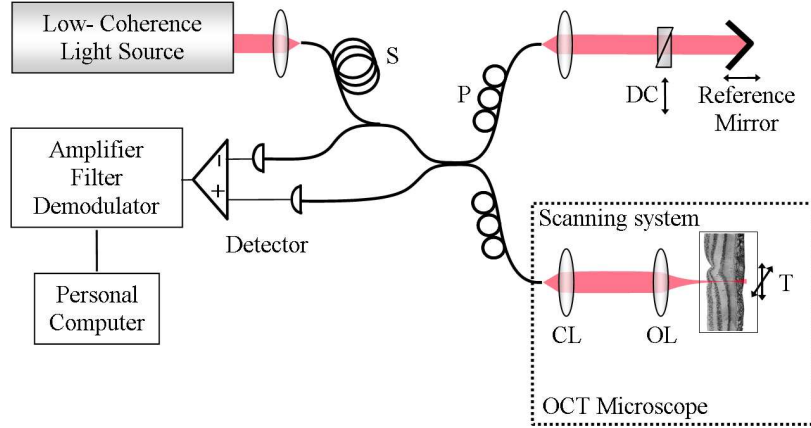


Figure 3.9: UHR OCT microscope system. S: pulse stretcher; P: polarization control; DC: dispersion compensation; CL: collimating lens; OL: objective lens; T: X-Y-translation stage.

To achieve high transverse resolution, a specially designed achromatic objective with 10 mm focal length and a numerical aperture of 0.30 was used, achieving $3\ \mu\text{m}$ free-space transverse resolution, resulting in a confocal parameter of approximately $40\text{--}60\ \mu\text{m}$ in air, degrading the OCT image outside the focused zone. To overcome the depth of field limitation and to maintain high transverse resolution at various depths through the image, a zone focus and image fusion technique was used [68]. Separate images with different focal depths of the optics were recorded, while maintaining the same interferometer delay depth (2 mm). These tomograms were then fused together. This technique is similar to C-mode scanning used in ultrasound imaging [69]. Up to $80\text{--}100\ \mu\text{m}$ imaging depth was obtained without significant image degradation. This image fusion technique would not be necessary in case of *in vivo* ultrahigh-resolution OCT imaging. Due to ocular aberration the best transverse resolution possible in the living human retina is limited to $10\text{--}15\ \mu\text{m}$, resulting in a more than $500\ \mu\text{m}$ depth of focus to cover the whole retinal thickness.

Special single-mode fibers (570 nm cutoff wavelength) and special broad band, wavelength-flattened, 3 dB fiber couplers were used to maintain ultrabroad bandwidth and singlemode propagation. Applying laser light centered at 800 nm with up to a 170 nm bandwidth (FWHM), axial resolution of $2.0\ \mu\text{m}$ in air, corresponding to $1.4\ \mu\text{m}$ in biological tissue, was achieved with this system. A signal-to-noise ratio of 105 dB was achieved at 1 MHz carrier frequency by using an incident power of 5 mW, using dual-balanced detection. Although applied in *ex vivo* tissue, retinal exposure must be taken into account in studies using the ultrabroad-bandwidth light generated by a titanium:sapphire laser. The American National Standards Institute (ANSI) standards for retinal exposure account for wavelength, exposure duration, and multiple exposures of the same spot of

the retina. Because the laser source generates femtosecond pulses, the laser output was coupled into a 100-m-long optic fiber that was used to provide dispersive stretching of the pulse duration to hundreds of picoseconds. This reduces the peak pulse intensities by several orders of magnitude and, because the laser operates at an 80 MHz repetition rate, the output can be treated as a continuous wave. Persistent illumination of the retina with laser light centered around 800 nm with 500 μ W is allowed for only 20 seconds. Therefore the microscope OCT system has been designed to avoid direct illumination of the focused beam into the eye. Full interference fringe signal OCT data were digitized with a high-speed (10 megasamples/s) and high-resolution (16-bit) analog-to-digital (A/D) converter followed by software demodulation.

During OCT imaging, real-time imaging display enabled simultaneous, immediate cross-sectional visualization of the imaged area. Using a scanning frequency of up to 130 Hz resulted in a measurement time of approximately 16 seconds for an OCT tomogram consisting of 2000 A-scans. Except for image fusion, no other technique was used to generate OCT tomograms. Position, orientation, and length of OCT scanned cross sections were recorded on the digital fundus micrographs and used to achieve matching orientation of specimens in subsequent histologic sectioning.

3.4.2 Correlation of UHR OCT with histology - pig retina

The goal of this study was to compare cross-sectional images of the retina obtained by ultrahigh resolution OCT with light microscopy in order to identify the morphology visualized in OCT tomograms. We here demonstrate that ultrahigh resolution OCT will provide a powerful tool for ophthalmic diagnosis by enabling optical biopsy of the retina, i.e. the visualization of retinal microarchitecture, which previously has only been possible with histopathology.

Materials and methods. Because human retinal tissue quickly loses histological and optical quality post mortem, pig tissue was chosen for the present study. The pig eye is increasingly used as a model in vision studies and is readily available for experimentation. Besides its size, several features are similar to those of the human eye. The domestic pig has two areas lateral to the main medial ascending vessels as evidenced by density peaks of ganglion cells [70, 71], cones, and spectral cone types [72, 73]. Cone densities remain high in peripheral retina, indicating good overall adaptation to diurnal activities. Pig cone inner segments reveal paraboloidal morphology similar to human perifoveal and peripheral cone inner segments, thus allowing to infer similar optical properties. Finally, the pig retina is holangiomatic. The prominent vascular architecture provides suitable landmarks to precisely align ultrahigh resolution OCT images with histological sections.

Ocular tissue. All handling of animals was carried out in accordance with the Association for Research in Vision and Ophthalmology Statement for the Use of Animals in Ophthalmic Research. Eyes were enucleated from domestic pigs

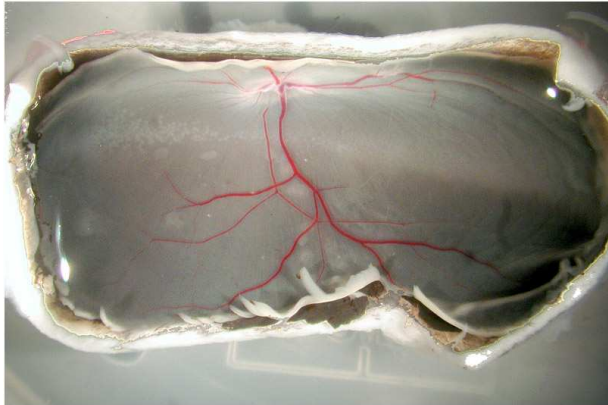


Figure 3.10: Porcine retina, one hour post mortem. The prominent vessels can be used as landmarks for histology following UHR OCT imaging.

that were used for unrelated experiments, either shortly before or immediately after sacrificing the animals. Following immersion in cooled oxygenated 0.01M phosphate buffered saline (PBS, pH 7.4), eyes were transferred to the lab within 30 minutes, and the cornea, lens, and vitreous were removed. The reason for removing the anterior eye segment and the vitreous was to obtain high transverse resolution, that would be limited by ocular aberration in case of using the intact eye. From the eyecup, a horizontal strip including the optic disc was prepared, the remaining vitreous removed, and the fundus digitally photographed prior to transferring the sample to the ultrahigh resolution OCT setup.

Histological preparation. OCT-imaged tissue was fixed in 4% paraformaldehyde / 0.1 M PBS (pH 7.4) for 12 to 72 h, cryoprotected in ascending series of sucrose / PBS, infiltrated in 20% sucrose / PBS (two parts) and O.C.T. medium (one part; Miles, Elkhart, IN) for 18 h, flash frozen, and mounted to receive vertical sections matching the plane of the OCT scans. Series of 12 μm frozen sections were collected onto chrome-alum gelatine-coated slides, air dried and stained with cresyl violet or left unstained for differential interference contrast (DIC) microscopy.

Data analysis. Sections matching the position of OCT scans were identified using blood vessels as landmarks and photographed with a Photometrics NU-200 CCD camera attached to a Nikon Eclipse 600 microscope. Using Adobe Photoshop 5.5 (Adobe Systems, San Jose, CA) micrographs were linearly scaled to correct for volume changes of the tissue that occurred in the course of histological processing and overlaid to OCT images in order to evaluate their correlation. OCT image enhancement was applied when appropriate and included gradient subtraction, and noise or median filtering (Image Processing Tool Kit, Reindeer Graphics Inc., Asheville, NC). Shadow extending from blood vessels and nerve fiber bundles was reduced by orientational FFT-masking (Digital Micrograph, Gatan Inc., Warrendale, PA). To obtain averaged density profiles, pixel-line projections were performed along the radial axis of OCT images in Image SXM (NIH, Bethesda, MD).

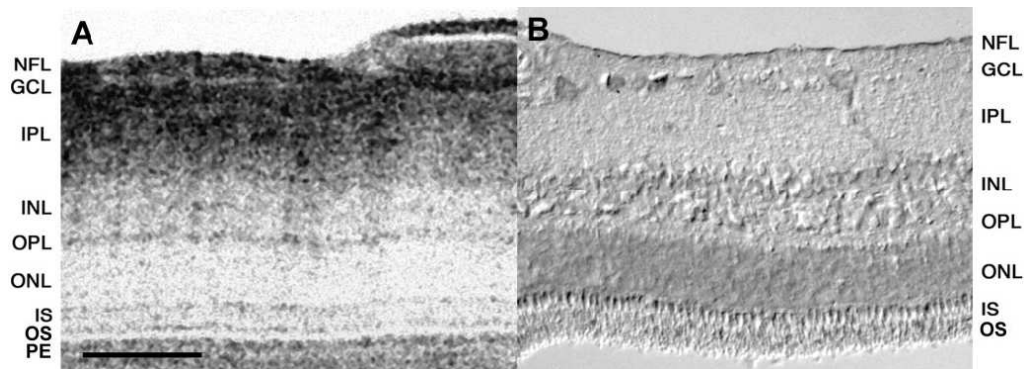


Figure 3.11: Comparison of in vitro ultrahigh resolution OCT imaging with histology in the pig retina. (A) Cross-sectional OCT image with $1.4\ \mu\text{m}$ axial \times $3\ \mu\text{m}$ radial resolution of an area of $330 \times 410\ \mu\text{m}$ consisting of 6600×410 pixels. (B) Differential interference contrast (DIC) micrograph of a frozen section obtained from the matching retinal position. From the proximal (top) to the distal (bottom) retina, alternate dark/light bands of signal in the OCT image directly correlate with the retinal layers, nerve fiber layer (NFL), ganglion cell layer (GCL), inner plexiform layer (IPL), inner nuclear layer (INL), and outer plexiform layer (OPL). Distal to a band attributable to the outer nuclear layer (ONL), a more delicate bright ribbon is likely to represent both the external limiting membrane and the myoid portion of the cone inner segments. The adjacent dark and stippled signal is in alignment with the cone ellipsoids prominently seen using DIC optics. A distal dark band is possibly associated with the cone outer segment tips and, finally, a dark/light banding is attributable to the pigment epithelium/choriocapillaris complex. In B, due to histological processing, the retinal pigment epithelium is detached and the photoreceptor layer slightly bent. Scale bar for A and B: $100\ \mu\text{m}$.

Correlation of OCT images with histology. Profiles of blood vessels and their relative positions proved to be reliable landmarks to identify matching histological sections at almost micrometer precision. Ultrahigh resolution OCT clearly delineated the inner retinal border with the attached major vascularization and resolved the different cross-sectional status of both arteries and veins (figs. 3.11, 3.12, 3.14). This precise positional and cytoarchitectural information of OCT images was used to fit micrographs obtained from matching histological sections to their respective tomograms, by simply performing a linear scaling manipulation. As a result, we identified a close correspondence of at least 8 bands of OCT signal with specific retinal layers (3.14). We found no significant evidence that volume changes occurring in the course of tissue processing differently affected different retinal layers, and thus would have interfered with our approach. Mismatch encountered when superimposing histological and OCT images was found to be due to artefact arising from tissue handling, such as different grades of retinal detachment and collapse of blood vessels (figs. 3.11B, 3.14C), or to slight deviations of the sectioning plane from the plane of the scan. Further, due to the high resolution of structural detail in the deeper retina, positional noise did not complicate the straight-forward correlation of OCT signal patterns with retinal structure. This was particularly evident for the retinal layers between internal and external limiting membrane, and for the retinal pigment epithelium and the

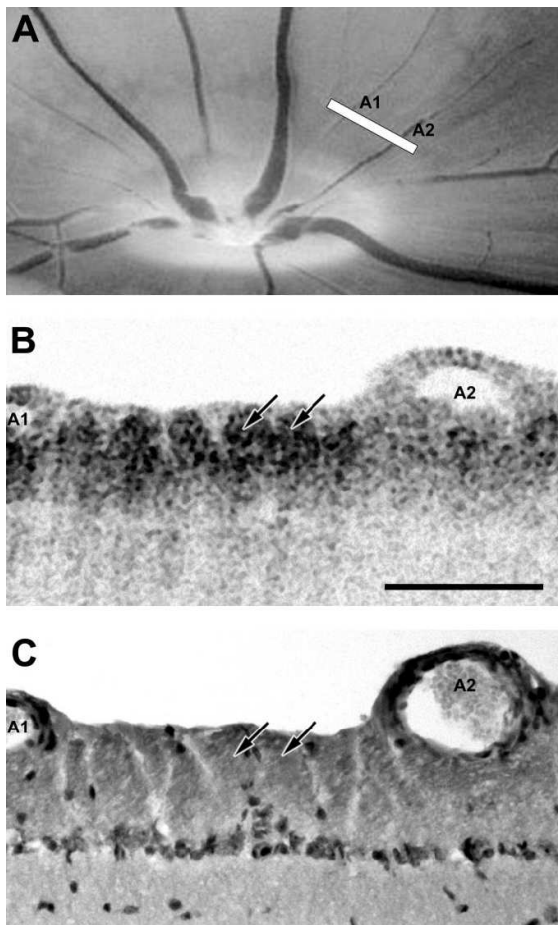


Figure 3.12: Peripapillary ganglion cell layer. (A) Photograph of the in vitro fundus showing the papilla and major blood vessels. White bar indicates the orientation of the OCT scan. (B) Ultrahigh resolution OCT image as obtained by focusing on the proximal retinal layers with $1.4 \mu\text{m}$ axial \times $3 \mu\text{m}$ transverse resolution of an area of $220 \mu\text{m} \times 390 \mu\text{m}$ consisting of 4400×390 pixels. (C) Micrograph of the matching radial frozen section stained with cresyl violet. The dark nerve fiber layer (NFL) is well distinguishable from the bright band of the underlying ganglion cell layer (GCL). Towards the inner retinal border, bundles of ganglion cell axons (B, C, arrows) are separated by Müller cell endfeet. Scale bar for B, C: $100 \mu\text{m}$.

choroid.

OCT of proximal retinal layers. Ultrahigh resolution OCT identified the nerve fiber layer by the strongest signal (fig. 3.11). In scans carried out perpendicular to the papillary radiation, individual axon bundles were easily distinguished between Müller cell columns (fig. 3.12B, C; arrows). Distally, a band of lower signal precisely corresponded to the ganglion cell layer (figs. 3.11, 3.12). Both shape and thickness of the band changed with retinal eccentricity and was found to strictly correspond to the number of ganglion cell somata rows present (fig. 3.12B, C). The adjacent highly reflective band, at both its proximal and distal border, precisely correlated with the location and extension of the inner plexiform layer as revealed by either DIC or brightfield microscopy (figs. 3.11, 3.12). We noticed numerous patches of higher signal (dark spots) within this inhomogeneous band (fig. 3.11A) but were unable to confirm their correspondence to profiles of intraretinal capillaries. Two further distinct bands of low and high signal, respectively, were corresponding to the inner nuclear layer and the outer plexiform layer (figs. 3.11, 3.13).

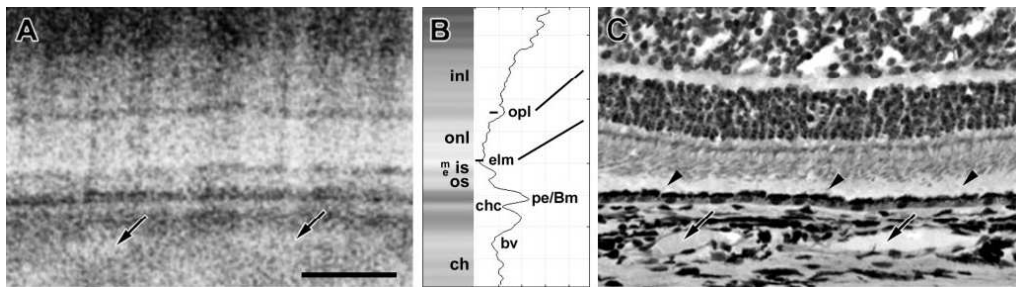


Figure 3.13: Distal retina and choroid. (A) Ultrahigh resolution OCT image with $1.4\ \mu\text{m}$ axial x $3\ \mu\text{m}$ transverse resolution of an area of $240 \times 360\ \mu\text{m}$ consisting of 4800×360 pixels. (B) Left: noise reduction profile obtained by performing median density projection on the OCT image along the x-axis. Right: density plot. (C) Micrograph of the matching frozen section stained with cresyl violet. Distal to the outer nuclear layer signal (onl), a light band corresponds to the position of the external limiting membrane (elm) and the proximal parts (myoids, m) of the photoreceptor inner segments (is). An adjacent band of dark signal presumably results from the specific light guiding properties of the paraboloidal cone ellipsoids (e) and is followed by a light band corresponding to the (predominately rod) photoreceptor outer segments (os). Adjacent to the distinct signal of the pigment epithelium (pe) a band of light signal corresponds to the choriocapillary lumen (cc). Diffuse dark signal within the choroid (ch) is locally lightened by the profiles of the major blood vessels (arrows). Tissue processing caused detachment of the retina (C, arrowheads). Scale bar for A, C: $100\ \mu\text{m}$.

OCT of distal retinal layers. The adjacent band of lower signal largely corresponded to the outer nuclear layer. However, its outermost aspect was not unequivocally attributable to the position of the external limiting membrane (figs. 3.11, 3.13). Densitometric profiling confirmed sublayering and discriminated a wider proximal portion of higher signal from a slender distal portion of lower signal ('m' in fig. 3.13B). A further high signal band of speckled appearance was found in correlation with the location of the cone ellipsoids (figs. 3.11, 3.13). Beyond the photoreceptor layer, a distinct band of high signal corresponded to the retinal pigment epithelium (PE, figs. 3.11A, 3.13, 3.14). Densitometric profiling (fig. 3.13B) confirmed that the signal intensity was the most prominent in the outer retina and this was particularly evident in OCT images focused on the distal retina (figs. 3.13A, C). Distally to the PE layer, a thin light band corresponded to the position of the choriocapillary layer, and diffuse high signal interspersed with patches of low signal closely correlated with the pigmented choroidal stroma and the lumina of larger blood vessels (figs. 3.13A, C, arrows). Recording of local retinal detachment

In a series of OCT scans the initiation of a retinal detachment event was monitored within a time frame of 30 minutes (fig. 3.14). Ultrahigh resolution OCT visualized a focal elevation of the neural retina concomitant with an increase in subretinal space (fig. 3.14A, arrow). Fifteen minutes later, alterations were observed within the monolayered band of the PE signal. While still continuous, the PE signal appeared triple-layered at the initial locus of detachment, with a stripe of bright signal framed by two darker bands (fig. 3.14B, arrowheads).

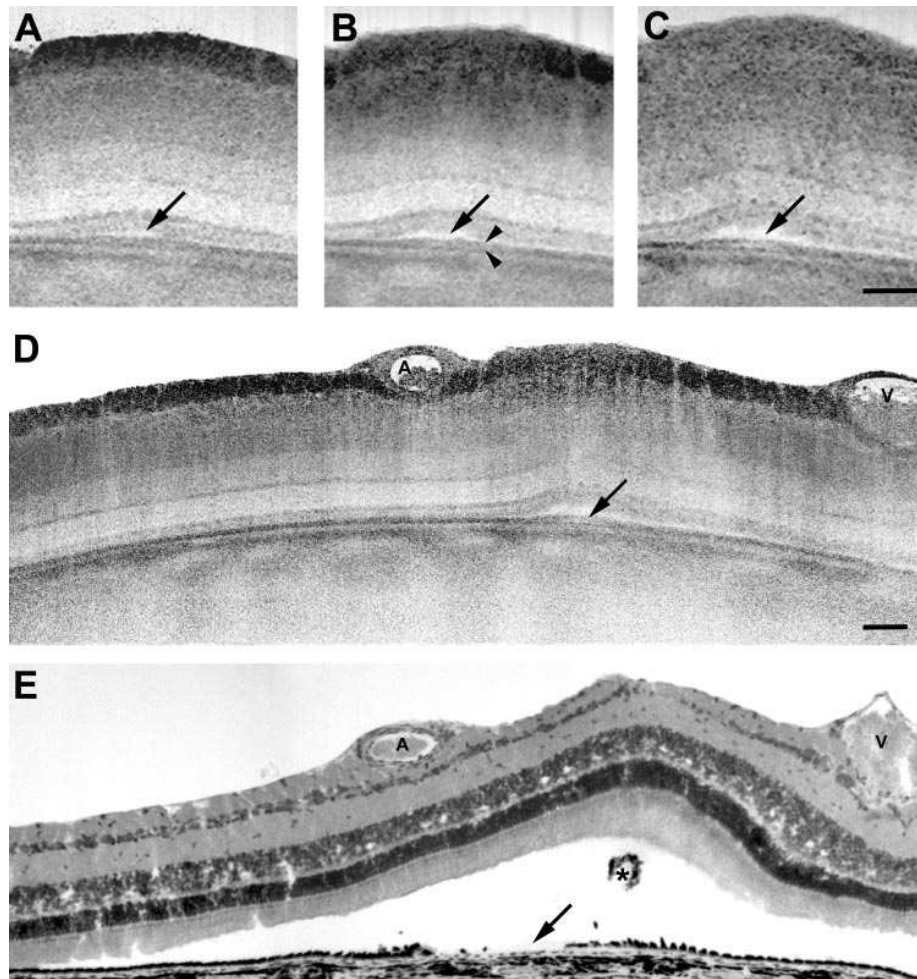


Figure 3.14: Time lapse sequence of retinal detachment during in vitro ultrahigh resolution OCT imaging with $1.4 \mu\text{m}$ axial \times $3 \mu\text{m}$ transverse resolution. (A, B, C) Enlarged image portions of the detachment zone covering an area of $0.5 \times 0.5 \text{ mm}$ consisting of 10000×500 pixels, FFT-filtered for reduction of radial shadowing effects. Time intervals between these images is 15 minutes. In the aligned micrographs, progressive bending and swelling of tissue is evident. (A) All photoreceptor sublayers have begun to bend proximally resulting in a subretinal lumen. (B) The subretinal blebs have significantly increased. Underneath the detachment zone the dark band of signal corresponding to the pigment epithelium/Bruch's membrane complex is still continuous (arrowheads) but locally triple-layered, as indicated by a bright inclusion (arrow). (C) The innermost aspect of the triple-banded signal appears interrupted (arrow). (D) Full OCT image of an area of $0.7 \times 2 \text{ mm}$ consisting of 14000×2000 pixels. (E) Corresponding histological section. Tissue processing has led to more extended retinal detachment. Debris from the damaged pigment epithelium (arrow) is present in the subretinal space (*). All scale bars: $100 \mu\text{m}$.

After additional fifteen minutes, all retinal layers were found bent inwards and measurements of their relative thicknesses (not shown) indicated increased thickness of the proximal retinal layers. In the PE signal, the bright inclusion had increased while the innermost aspect of the signal appeared eroded (fig. 3.14C and D, arrow). Histological examination of the matching retinal position demonstrated a significantly extended region of detachment (fig. 3.14E). The pigment epithelium was found lesioned at the initial locus of detachment and fragments of tissue were dislocated into the subretinal lumen (fig. 3.14E, asterisk).

Discussion. Ultrahigh resolution OCT and optical properties of retinal sublayers The present study demonstrates that in vitro ultrahigh resolution OCT imaging reveals retinal microarchitecture with unprecedented detail. By using histological sections precisely matching the plane and retinal position of cross-sectional OCT scans for comparison, we have chosen an approach that enabled us to directly correlate the various components of the OCT image to histology. Despite the enhanced axial resolution, however, caution is imperative when assigning specific bands of OCT signal to specific retinal layers. OCT images are determined by the optical properties of the tissue. As a consequence, tissue components that give strong contrast in histological staining may appear fairly inconspicuous in the tomogram. Sample characteristics that strongly modulate the signal include thickness, absorption, and refractive index. OCT signal arising from the different retinal sublayers results from the averaged refractive indices of both intracellular and extracellular components. Differences in histological architecture lead to differences in scatter, reflection or guidance of light. Absorption and reflection profiles similar to that obtained by light microscopy are evident in the hemoglobin of blood vessels (figs. 3.11, 3.12, 3.13) and melanin which is present in the retinal pigment epithelium and choroid (figs. 3.11, 3.13, 3.14). The tight packing of lipid membranes in bundles of the ganglion cell axons, axo-dendritic layers, and in subcellular components such as ellipsoidal mitochondria, outer segment discs, microvilli and calycal processes is associated with loci of higher refractive indices. Therefore, scatter phenomena differ between cell body layers and axo-dendritic layers and contribute to the different signal from these regions. Several factors further complicate the correlation of structural detail with OCT images. Inherent to optical imaging techniques is the degradation of signal contrast with distance from the focus level. We could partly compensate for this by combining multiple scans acquired at different focal levels. Mismatch between histology and OCT images results from the limits of precision in selecting sections closest to the OCT plane from an entire series, possible deviations from perpendicular orientations of both OCT images and histological sections and volume changes in the tissue after scanning and during histological processing. A particular problem is the frequent detachment along the PE/PR border with subsequent upfolding of the retina. With the enhanced resolution of ultrahigh resolution OCT, however, positional mismatch between histology and OCT signal provides a source of information to evaluate artefactual modification of the tissue in the course of histological processing. In histological preparations, epiretinal blood vessels are observed to protrude into the vitreous (fig. 3.14D).

They appear smoothly embedded into the inner retinal surface in the OCT tomograms (fig. 3.14C). Choroidal lacunae are clearly visible in OCT scans (figs. 3.13, 3.14), while in the course of tissue processing they frequently collapse. This further helps to discriminate procedural artifacts from pathologic alterations.

Assignment of signal to the inner retinal layers. Taking into account the above limitations, our approach allows to reliably correlate all main retinal layers with specific bands of the OCT signal. Ultrahigh resolution OCT imaging precisely distinguishes the nerve fiber layer from the ganglion cell layer. OCT scans carried out perpendicular to the papillary radiation allow to evaluate the full cross-sectional status of nerve fiber bundles (fig. 3.12A, B). We did not resolve individual ganglion cell somata, although the size of the large alpha ganglion cells is well within the range of resolution of the technique. Unequivocal confirmation of the representation of individual somata in an ultrahigh resolution OCT tomogram requires correlation at the cytological level and was beyond the scope of this study. The inhomogeneous appearance of OCT signal corresponding to the inner plexiform (IPL) and the inner nuclear layer (INL) implies that with further refinements of image acquisition and post processing, substructures within both layers (IPL sublayers, capillaries) will become identifiable.

Assignment of signal to the photoreceptor/pigment epithelium/choroid complex. The detailed evaluation of the photoreceptor layer, the pigment epithelium, and the choroid is of prime interest for clinical diagnosis. Ultrahigh resolution OCT distinguishes these layers. The most intense signal deriving from the outer retina can be safely correlated with the position of the pigment epithelium, thus providing a landmark for the delineation of the retina versus the choroidal layers. This is confirmed by our record of progressive retinal detachment. While the neural retina increasingly detaches, additional alterations affect the pigment epithelium signal which splits at the site of detachment with a brighter cleft of about 5–8 μm framed by two darker bands. While the present data do not suffice to resolve the cytological equivalent of the cleft, i.e. whether the pigment epithelium is lesioned between villous processes and cell bodies or at Bruch's membrane, the observation demonstrates the resolving power of the technique.

To assign substructures within the photoreceptor layer at a micrometer scale is challenging. Artefactual alterations of fragile photoreceptor outer segments in the course of tissue processing interferes with direct alignment and it is likely that disproportionate vertical representation due to refractive index variation further complicates the assignment of signal. Apparently, the complex structural subtiering of the photoreceptor layer is not reflected by an equivalent number of bands in the OCT tomogram. For example, in the myoid portion of the cone inner segments cresyl violet contrasts a rich Nissl substance, the light microscopic equivalent of the endoplasmic reticulum at the electron microscope level (fig. 3.13B) [74]. This zone appears to have no OCT correlate. Therefore, in an attempt to assign observed bands of OCT signal to specific components of the photoreceptors we considered their optical properties. The outer nuclear layer

(ONL) comprises 2-4 rows of rod somata and a monolayer of cone cell bodies [75], located proximal to the external limiting membrane (ELM). The regular arrays of cone somata and the tight association of photoreceptor myoids and microvillious processes of Müller cells adjacent to the proximal and distal border of the external limiting membrane, respectively, may provide for enhanced transparency and similar refractive properties of the tissue and therefore be represented as the delicate light band discernible at the outermost aspect of the outer nuclear layer (figs. 3.11, 3.13). This interpretation is supported by DIC microscopy. Proximal and distal to the ELM, corresponding to the location of cone cell somata and the photoreceptor inner segment myoid portion, respectively, DIC microscopy identifies two bands of high transparency but low relief (fig. 3.11B) indicating a region of similar transmissive and refractive properties. Evidently, the light signal band would then include the external limiting membrane which seems to give no separate signal ('elm' in fig. 3.13B). An alternative interpretation would correlate the borderline between high and low signal to the ELM. However, this would leave a very small radial representation of the ONL. We consider this unlikely for both optical and morphological reasons.

Using DIC optics, the ellipsoid portions of the cone inner segments are clearly distinguished by their high relief (fig. 3.11A). OCT imaging identified this zone as a high signal band. In pig, cone inner segment ellipsoids comprise ca. 70% of the cross-sectional light capture area [76]. Their paraboloidal morphology and their high refractive index may result in periodical alterations of reflectivity within this zone, which is consistent with the speckled appearance of the OCT signal.

Photoreceptors attain specific shapes beyond their myoid portion (rod IS and OS: cylindrical, cone OS: conical, cone IS ellipsoids: paraboloidal) [77]. They are supposed to constitute individual optical elements with refractive indices n of 1,4 separating them from the surrounding interphotoreceptor matrix ($n \approx 1,34$). Under physiological conditions, particularly the cone ellipsoids are guiding light towards the photopigments located in the outer segments [78]. Further, photoreceptor outer segments consisting of densely stacked disc membranes have high refractive indices [79]. The transition zone to the outer segments appears to produce a reflective signal which appears more prominent in the all-cone foveal photoreceptor layer. Interestingly, in macaque fovea approximately 20 tapering calycal processes arise from the ellipsoid surrounding the cone outer segment base as a dense collar [80, 81]. The processes are supposed to provide structural support or semi-occluded periciliary compartmentation. These processes are less numerous around the base of the longer rod outer segments. It is possible that cone calycal processes contribute to the optical properties of the IS/OS transition zone. In pig and human retina, the photoreceptor layer is tiered with fat short cone inner segments collecting major portions of the incoming light at the basal aperture [82]. The cone outer segments are tapered and possibly distribute non-absorbed light from their shorter tips to the surrounding rods [76, 77]. Cone inner segments are shorter than rod inner segments, and their short tapered outer segments (OS) lead to the positioning of cone OS tips just above the rod inner/outer segment transition.

Together, this suggests that interactions of the OCT beam with the outer

retina are less homogeneous than in the proximal retina. The interpretation proposed here attempts a coarse correlation of photoreceptor subtypes with the OCT image. Further studies will be needed to clarify how the various subcellular components of the photoreceptors contribute to the OCT signal. We may expect that, beyond the external limiting membrane, OCT signal patterns are different in cone prominent retinas (as studied here), rod dominant retinas, and the fovea with its homogeneous array of elongated cones. Evaluation of these differences may allow the interpretation of pathological conditions such as congenital or progressive cone dystrophies.

Although the pig retina may well approximate the human peripheral and extrafoveal retina, caution has to be taken in directly transferring the layering assignment to the human fovea. In the fovea, rods are lacking. Both cone inner and outer segments have 'rod-like' morphology [81]. The refractive index of the elongated foveal outer segments has been estimated ($n=1,419$) to be higher than in peripheral retina [77]. Finally, foveal cones have been reported to exert a spatial-frequency-filter effect [83] for coherent light with wavelengths from 410 to 654 nm (where two waveguide modes are carried) and a flat response for wavelengths greater than 654 nm (the single-mode region). Together, the specific morphological and optical properties of the foveal receptors may significantly alter the banding pattern of OCT signal particularly at the level of their inner and outer segments, and our layering assignment may need specific adaptation in order to reliably interpret ultrahigh resolution OCT images of the normal and pathologic fovea.

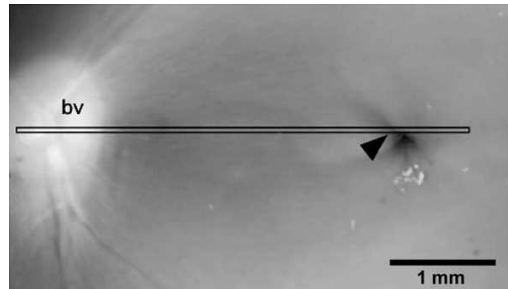
3.4.3 Correlation of UHR OCT with histology - monkey retina

The goal of the present study was to obtain cross-sectional UHR OCT scans of optimally preserved primate retina and compare it with the elements in corresponding semithin sections. The retina was fixed by perfusion fixation to avoid the effects of post mortem degenerative changes. In order to provide the optimal correlation of histological and imaging data, we used morphing algorithms for the correction of tissue artifacts in the processed retinal tissue. Morphing is a geometric procedure able to compensate distortions such as differential shrinkage of sublayers depending on their cytoskeletal constitution and aqueous content. We here demonstrate that ultrahigh resolution OCT does provide a powerful tool for ophthalmic diagnosis by enabling "optical biopsy" of the retina, i.e. the detailed visualization of retinal microarchitecture, which has so far only been possible with histological sectioning.

Animals and tissue processing. Eyes were obtained from adult *Macaca fascicularis* monkeys used for experiments not related to ocular tissue. All procedures were in compliance with the NIH Health Guide for the Care of Animals in Ophthalmic and Vision research and approved by the Animal Care and Use Committee of the University Oxford. Animals were killed by an anesthetic overdose and perfused with saline followed by 4% paraformaldehyde in phosphate-buffer (0,1 M, pH 7,4). Eyes were removed and immersed in fixative overnight. After

washing in buffer, a square shaped piece of central retina was immersed in a chamber with the proximal border facing the OCT measurement beam.

Figure 3.15: *Macaca fascicularis*. Central fundus of fixed retina. Papilla (left) and macula (right) after OCT scanning. Shrinkage artifacts are notable at the fovea despite of perfusion (empty blood vessels, BV). The position and orientation of the UHR OCT scan and of subsequent semithin serial sectioning is indicated.



Histology and Data display. Orientation and extent of scans were mapped on fundus micrographs (fig. 3.15). OCT scans were subjected to noise reduction filtering (3 x 3 Rank) and contrast enhancement and shading correction using the Image Processing Tool Kit (Reindeer Graphics) for Adobe Photoshop. Retina samples from 8 different monkeys have been imaged with UHR OCT. Assessment of retinal quality in the UHR OCT profiles led to the selection of two samples for histological processing. The correlation between OCT and histology was comparable for both samples. The tissue blocks including the macula and papilla were dehydrated and embedded in Spurr's epoxy resin. To obtain precise alignments with UHR OCT tomograms major blood vessels were used as orientation markers. 300 serial semithin sections of ca. 4 mm length were made with the Histo-Jumbo-diamond knife and stained with Methylene blue. From the sections that matched the OCT scans most closely, high resolution montages were created from 1300 x 1050 pixel micrographs taken with 20 x lens on a Zeiss Axiovert microscope.

Morphing. Non-linear distortions (dehydration, sectioning stress) limits direct overlay of histological details onto corresponding UHR OCT locations. Therefore correlation was further improved by feature based image metamorphosis with MorphX software⁶ on an Apple computer. First both the OCT and the semithin section images were set to the same horizontal scale and imported into the editing windows. Fiducial points were then set on the histology micrograph at well-defined positions such as blood vessels or along unequivocal border lines including the inner limiting membrane (fig. 3.16a). Correlated points, created by the software, were then placed on corresponding structures on the UHR OCT scan (fig. 3.16b). Based on this data grid the semithin micrograph was remapped by geometric interpolation to achieve extensive correspondence with tissue proportions on the OCT scan (fig. 3.17).

General features and limitations of UHR OCT imaging. Retinal layering is identifiable in both, the OCT scan (fig. 3.17a) and the semithin micrograph

⁶<http://www.orcsoftware.com/martin/Morph.html>

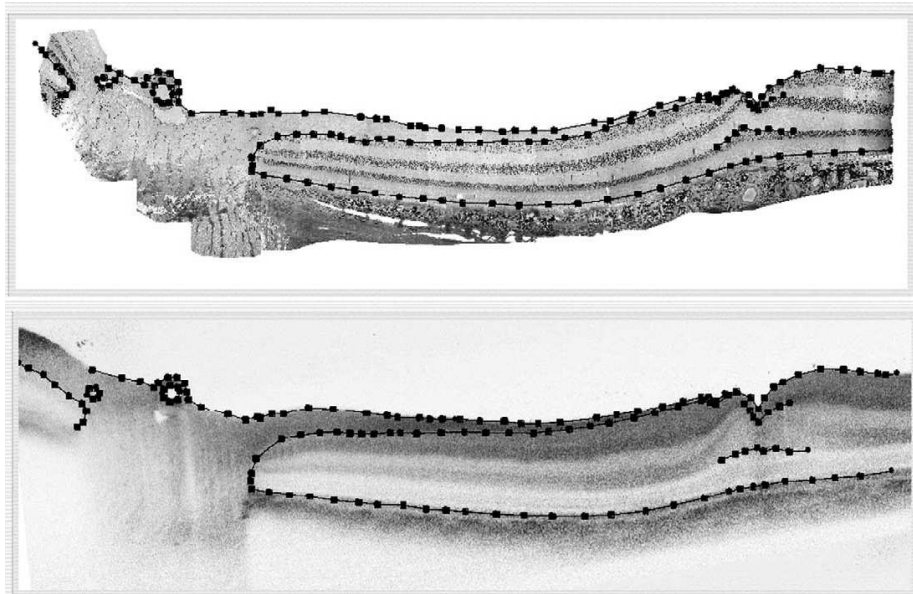


Figure 3.16: Screenshot of morphing procedure. On the semithin section (upper image) fiducial points were set on landmarks (papilla, foveal floor, pigment epithelium, inner limiting membrane) and corresponding points created by the software were adjusted to related locations along the UHR OCT transect.

(fig. 3.17b) although the OCT banding differs from that seen in the semithin sections with Methylene blue staining. Both profiles show the characteristic elements of primate macular region: the foveal depression, the perifoveal maximum and the papilla where some major blood vessels are discernible. However, even with the horizontal scale adjusted, the section is still notably thinner and the tissue has undergone convex deformation as a consequence of histological processing.

Horizontal straightening and radial thickening of the semithin section were produced by geometric normalization (fig. 3.17c) based on the proportions of the OCT scan. The agreement between retinal layers in the sections and OCT scans was improved by this method but artefactual tissue distortion remained apparent when the tissue was viewed at higher resolution (fig. 3.18 and 3.19). Because only 3–5 horizontal borders had been marked for the adjustment via morphing, the intermediate sublayers were interpolated without further correction. Also a non-perfect horizontal alignment of corresponding points does induce some artefactual discrepancies in dimensions, elongated cell bodies and waviness of outer segments. Within these limits however the procedure allows detailed comparison of UHR OCT and semithin section profiles at resolutions that approach the cellular level.

Foveal shape. The differential sensitivity of foveal components to fixation and dehydration made it difficult to preserve the normal foveal shape. Inspection of the fundus from 8 perfusion fixed eyes did not identify a single specimen without changes along the foveal slope. Slight distortion of the foveal slope was seen in all 8 perfusion fixed retina. An example of the artefactual notches associated with

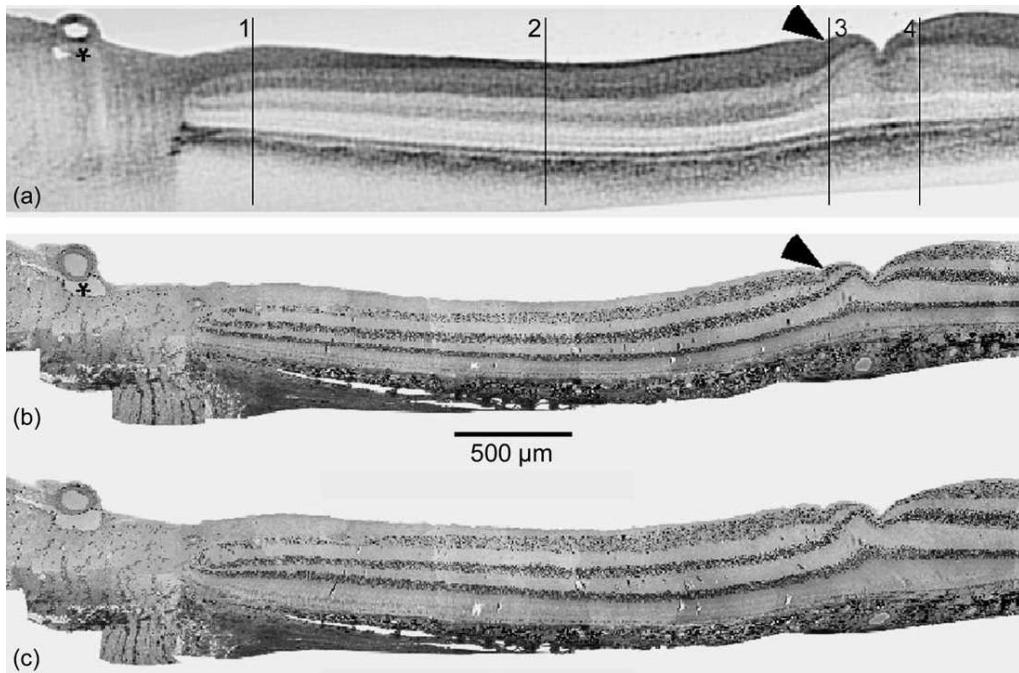


Figure 3.17: Original and corrected image data. (a) UHR OCT scan. Many retinal sublayers are identifiable including their specific course and changing proportions along the foveal slope.

(b) Correlated semithin section. Close correspondence is confirmed by landmarks: Papillary blood vessels (asterisks) and foveal artefactual notch (arrowheads, corresponds to folds visible in fig. 3.15) but bending and unequal shrinkage prevents direct overlay.

(c) Section corrected by morphing. Bending is relaxed and overall thickness as well as sublayer proportions are adjusted to the UHR OCT.

this distortion is shown in figs. 3.17a and 3.17b. When required, these points were used for the exact identification of the corresponding sections within the series.

The main proximal layers of standard retinal histology correspond well to prominent signal bands from ultrahigh resolution OCT and the correction performed by the morphing procedure was relatively minor (fig. 3.17a and 3.17b). The UHR OCT scans however display an increased number of sublayers characterized by their average grey levels as well as by specific speckle patterns (fig. 3.18b). The signals result from local combinations of tissue related scatter and absorption at the particular wavelength of the laser. As a first step in correlating OCT banding with histological structures, the most characteristic retinal layers were first identified.

Distal and Proximal Retinal Border. The retinal pigment epithelial layer (PE) gives rise to a prominent component of the OCT signal. In the OCT section, the intensity of the signal varies which corresponds to the variation in the distribution in RPE melanosomes (fig. 3.18a and 3.19a). Interestingly the radial extension of the PE signal appears stronger and more diffuse at the

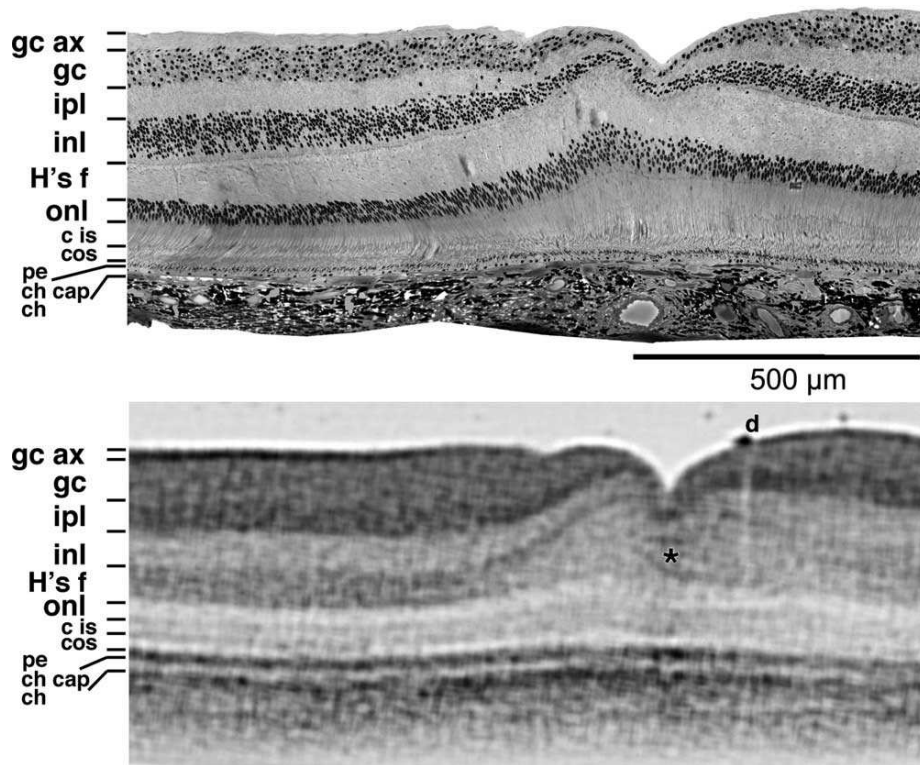


Figure 3.18: Foveal portion of corresponding semithin section and UHR OCT transect. All major retinal sublayers are distinguishable and can be adjoined. gc ax: ganglion cell axon layer, gc: ganglion cells, ipl: inner plexiform layer, inl: inner nuclear layer, Hf: fibers of Henle, onl: Outer nuclear layer, cis/cos: cone inner/outer segments, pe: Pigment epithelial layer, ch cap: choriocapillaris, ch: choroid, asterisk: darker faults in foveal floor indicative of foveal strain, d: epi-retinal debris producing negative shadow.

particular wavelength used, than what is actually present in the semithin section. It suggests that a scatter component is also present. In scans obtained with infrared wavelengths where absorption by melanin is reduced the PE signal is smaller and has higher contrast [84]. The same studies, which achieved greater penetration beyond the PE by using a source with wavelength 1300 nm, have confirmed that the brighter components represent the venous choroidal plexus. With wavelengths around 800 nm as used in the present study, the choroid (CH) is largely masked by the PE. It produces only diffuse gradients representing the lacunar organization as clearly seen in the micrograph (fig. 3.18a). In the UHR OCT scan the two pigmented layers are separated by a delicate bright (= transparent) band. It consists in its major part of the choriocapillaris (CHC) and Bruch's membrane. It is also likely to include the pigment epithelial cell bodies, which are shown to be largely free of melanosomes in this particular sample (fig. 3.18a and 3.19b).

At the opposite retinal border a strong signal is also present arising from the ganglion cell axon layer. This layer gains in thickness towards the papilla but is also present at the fovea since the scan is not crossing exactly in the foveal

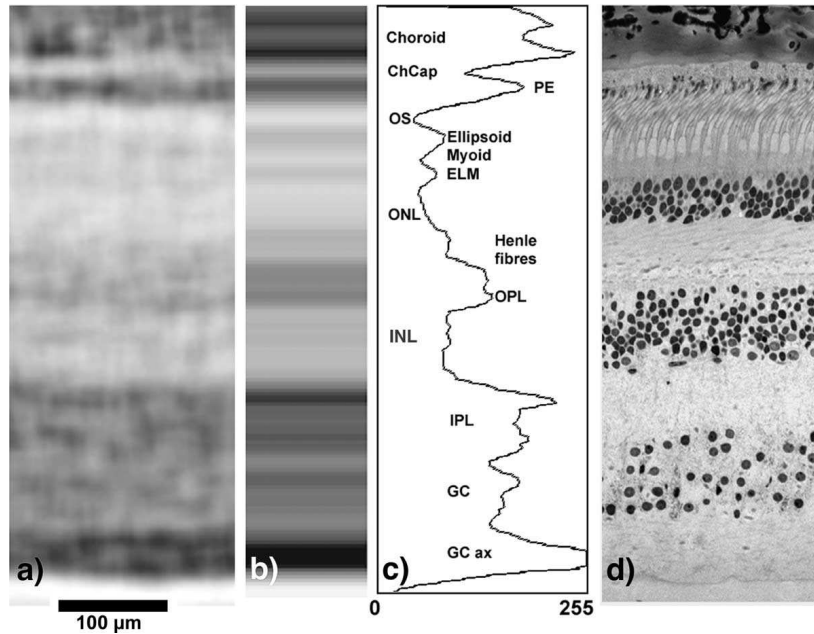


Figure 3.19: High resolution comparison of corresponding peripheral profiles at ca. 2,5 mm nasal eccentricity. Same abbreviations as in fig. 3.18.

a: UHR OCT scan. Dark proximal and distal bands representing ganglion cell axon fiber layer and pigment epithelium. Note delicate but distinct triple sublayering distal to the light band of the outer nuclear layer (ONL).

b: Density profile averaged horizontally from the central portion of fig. 3.19a. The layer of obliquely radiating cone axons (Henle fibers) creates a prominent sublayer not present in peripheral retina.

c: Gray level densitogram (inverted) along fig. 3.19b. Inner and outer nuclear layers (INL, ONL), photoreceptor inner and outer segments (IS, OS) and Choriocapillaris sublayer are below mean signal density, proximal portion of the pigment epithelium (PE) and ganglion cell (GC) axons are above.

d: Semithin section allows the identification of cytological details of sublayers including the presence of prominent cone photoreceptors. Myoid, ellipsoid and outer segments correspond to triple band in 5a. Melanin granules are concentrated in pigment epithelial processes while cell bodies are transparent.

center (fig. 3.15). The strong signal from this fibrous tissue type is apparently the result of high scattering rather than from absorption as in the PE. Scatter is produced by the densely packed axons running approximately orthogonal to the scanning beams. Between these two dark landmark layers several further layers are distinguishable yet by lesser contrast.

Photoreceptors. At the photoreceptor level correspondence has been difficult and ambiguous in standard resolution OCT. Adjacent to the PE there is a triple band (bright-medium-bright). By overlay with histology it is identified as outer and inner segments and cell bodies of photoreceptors. The last layer after the dark PE band is the brightest and apparently represents the portion of the outer segments that is free of pigmented PE processes. This outer segment zone decreases substantially from the foveal center to the papilla (50–30 μm). The transition to the inner segment band is smooth in the fovea where rod-like cones have inner and outer segments with similar diameters (fig. 3.18). In the periphery however (fig. 3.19) where cone inner segments shorten (60–40 μm) but increase in diameter and taper towards the slender outer segment these bands appear to be separated by a delicate darker lining. In the periphery additional sub-banding is discernible within the inner segment strip (fig. 3.19c and 3.19d). Analogous to what has been found in *in vitro* pig retinal scans [85] a darker distal sub-tier possibly represents the highly refractive ellipsoid and a brighter strip the myoid regions respectively. The external limiting membrane itself does not seem to produce a specific signal although a delicate and discontinuous border appears at the transition to the next slightly darker component representing the inner segment sub-tier. It is followed proximal by the bright cone cell body sublayer (ONL). As the cone somata accumulate around the foveola the ONL becomes V-shaped. A continuous outer plexiform layer has to be expected outside of the foveola only and does not appear as a distinct signal. In the foveal OCT scan the OPL must rather be considered to be represented by the proximal border of the most voluminous component: the photoreceptor axon layer and its surrounding Müller cells, the Henle fiber layer (Hf).

Henle fibers - effects of orientation on OCT signal. The photoreceptor-axons (Hf) are an additional band characteristic of the foveal profile. The layer has its maximum extension (170 μm) at the foveal rim with bundles of axons descending from the multitiered somata of foveal cones and radiating with lengths of up to 400 μm towards the macaque OPL [86, 87]. In the UHR OCT scans of this layer changing signal intensities are discernable (fig. 3.18b). The foveal floor region is a "transparent" area consisting of strands of voluminous Müller cells sheathing only few remaining photoreceptor axons and interneurons [88]. Fixation-induced distortions present in the specimen appear as corresponding faults (asterisk in fig. 3.18b). Outside the foveal center a thin dark band along the proximal border of the HF layer widens and the entire layer changes towards a darker signal. The maximum signal density - reached at approximately 500 eccentricity (fig. 3.18b) - represents the zone with tightly bundled cone axon fibers running obliquely towards the periphery [89–91]. The OCT signal density

decreases again beyond ca. 2 mm where the axons (including increasing numbers of thinner rod fibers) are less tightly organized, shortening and gradually turning to a radial course (fig. 3.16a). At the papilla the layer ($\sim 30 \mu\text{m}$) represents little more than the OPL. The inner nuclear layer (INL, $45\text{--}80 \mu\text{m}$) consisting mostly of bipolar cells, amacrine and horizontal cell bodies then is more transparent again.

The inner plexiform layer (IPL, $60\text{--}40 \mu\text{m}$) consisting mostly of tightly interwoven axo-dendritic processes leads to high scatter and a dark signal in the UHR OCT profile. As in the Henle fiber layer, foveal IPL regions appear darker than those closer to the papilla. The effect is probably related to the course of centrifugally oriented foveal IPL elements versus more radial components the peripheral IPL. As seen in the densitogram (fig. 3.19d) the OCT signal from the ganglion cell body layer (GC, $33\text{--}75 \mu\text{m}$) is only slightly brighter than the axonal layer. Lacking in the foveal center the GC layer steeply rises to a maximum at $\sim 200 \mu\text{m}$ eccentricity and decreases in a gradient approximately reciprocal to its own axon layer.

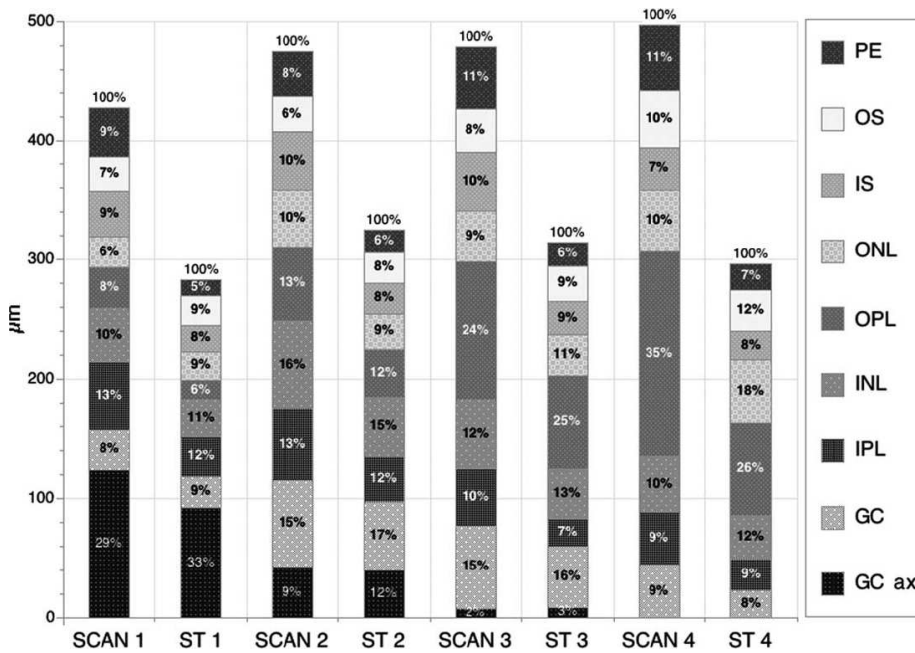


Figure 3.20: Nonlinear shrinkage along central retinal profiles during histology preparation. Absolute and relative dimensions of retinal sublayers along four locations indicated in fig. 3.17a in UHR OCT (SCAN) and in corresponding uncorrected semithin section (ST). Shrinkage resulting from histological processing is most prominent in the Henle fibers (Hf) and other photoreceptor sublayers. Ordinate: absolute thickness of profiles; values at columns indicate relative percentages of retinal sublayers. Abbreviations as in fig. 3.18 and 3.19.

Papilla and blood vessels. The present work was not focusing on papillary morphology but the UHR OCT shows many details with unprecedented clarity.

At the margin of the optic disc the distal retinal layers are thinning substantially (ca. 60%) in the UHR OCT scan (fig. 3.17 and 3.20). Due to the accumulating ganglion cell axons this is however nearly compensated so that the overall radial dimensions is nearly maintained (85% of the foveal rim). A slight convex bend, visible where the nerve fibres fan out into the papilla (fig. 3.17a) had been lost in the semithin section and was restored by the morphing procedure (fig. 3.17c). The axon fibers become brighter in the prelaminar zone of the papillary head. After bending into the papilla radial bundling is discernible before and at the level of the lamina cribrosa.

At the optic nerve disc a superficial arteriole and an underlying venule (asterisk in fig. 3.17a and 3b) are recognizable in both the scan and the section. The arteriole with its more rigid wall creates a shadow artifact, the thinner-walled venule appears more collapsed or sectioned at a different orientation. However, it is notable that smaller capillaries such as one right below the retinal margin (fig. 3.17b) are not resolved.

Discussion. The present study aims to answer the question of how the wealth of details delivered by ultrahigh resolution optical coherence tomography can be reliably linked to distinct retinal elements. Adaptive geometric correction of corresponding sections allows more precise correlation of features in retinal ultrahigh OCT imaging, even along the changing profiles of foveal sublayers. This allows the extraction of structural information of high clinical relevance in *in vivo* ultrahigh resolution ophthalmic OCT tomograms and has reduced major ambiguities allowing correlation of more than 10 sublayers to corresponding signals in UHR OCT profiles. Since this is not based on *in vivo* imaging we cannot rule out changes in the tissue itself prior to and as a consequence of fixation. Comparison with *in vitro* data from pig retina (see section 3.4.2) which shares many characteristics with primate retinal periphery suggests that in living retina signals are indeed expected to be similar for the same sublayers. It is also likely that the scaling of the OCT signal is not completely linear along the retinal profile. Since the signal in part depends on the refractive index certain sublayers rich in lipids such as the inner segment ellipsoids [92,93] may be represented at a different scale than others with higher aqueous proportions. For photoreceptors it has been determined that tissue components rich in lipids such as the ellipsoid region have higher refraction [79] and furthermore the optical fiber properties will change at increasing eccentricities with changes in shape, alignment and orientation of inner/outer segments as well as with varying proportions of rods and cones [82,94].

The reproducibility of the normal retinal radial density profile suggests that the signals from sublayers appear to have characteristic relative strength, resulting from sum of absorptive and scattering components (fig. 3.19b). Interestingly the signal appears sensitive to anisotropies from tightly packed oriented elements such as the ganglion cell fibers and the fibers of Henle (Hf). Along the Hf sublayer differing signal intensities appear linked with changing fiber orientation. In pathological conditions such changes may indicate twisting and deformation of tissue as is also apparent in the foveal floor of the sample (fig. 3.18). Why the

ganglion cell body layer too produces a relatively strong signal may be linked to their specific cytoskeleton but this needs further investigation.

The scans also show small horizontal variation of signals within sublayers (see fig. 3.19c). It comes from internal reflections appearing as speckle patterns [95] but most likely parts of it also depend on elements within the UHR OCT resolution range but are yet unidentifiable. In the case of pigment epithelial the origin of "bumpiness" appears evident from melanin densities but in other layers the source is less clear. Speckle apparently also arises from local inhomogeneities, which may include capillary layers, ascending vessels and other differences in refractive power by radial (Mueller cells) and horizontal (dendritic strata) components. The use of more elaborate Morphing software (allowing zooming, semi-automatic edge detection etc.) could further improve the alignment and restitution of sections allowing more precise detection of OCT correlates for such elements.

Pre-retinal optics and recording stability may lead to fuzzier signals in patient scans but identification of *in vivo* structures can be put on firmer grounds based on studies under controlled conditions such as the present. It remains to be shown whether similar sequences of signals are also distinguishable in OCT scans from living tissue although it is to be expected from *in vitro* data so far. It will be necessary to close the gap to *in vivo* imaging by obtaining OCT scans from primate eyes or freshly enucleated donor eyes prior to histology and *in vitro* scanning. Preliminary data further indicate that achieving three-dimensional information from serial UHR OCT profiles should be possible. Thus UHR OCT should be of benefit for enhancing the precision in various fields including pathologic conditions [96], treatment effects, aging/developmental studies or tracking of animal models with degenerative diseases.

3.5 In vivo ophthalmic studies

3.5.1 In vivo ultrahigh resolution OCT system

The axial resolution of OCT is mainly determined by the optical bandwidth of the low coherence light source used for imaging. In particular, the coherence length, and therefore the axial OCT resolution is inversely proportional to the optical bandwidth of the imaging light source. Standard resolution, commercially available ophthalmic OCT systems use superluminescent diodes emitting light with 20-30 nm bandwidths centered at 830 nm, resulting in a 10–15 μm axial image resolution. In the present study, a compact, robust, commercially available Titanium-sapphire laser (Compact Pro, FEMTOLASERS) with up to 165 nm bandwidth at 800 nm center wavelength was used for imaging. This ultrahigh resolution OCT system is based on a commercially available OCT system (OCT 1) that was provided by Carl Zeiss Ophthalmic Systems, Inc. Both the fiber-optic interferometer and the optical components of the OCT system were redesigned to support the very broad bandwidth light necessary to achieve ultrahigh resolution and to compensate for any polarization and dispersion mismatch between the sample and reference arms of the interferometer. The major limiting



Figure 3.21: Prototype of the clinical UHR OCT system. A ultrabroad bandwidth titanium:sapphire laser (up to 170 nm bandwidth full width half maximum, 800 nm central wavelength.) is interfaced to a fundus camera (Zeiss OCT 1, Zeiss Meditec, Dublin, CA). The fiberbased interferometer and the optics of the fundus camera were designed to support the whole bandwidth of the laser.

factor in achieving high dynamic range and sensitivity imaging is that the maximum allowed illumination power is limited by retinal exposure considerations. This requires the design of extremely high sensitivity and low noise detection electronics.

For these studies, the retinal exposure must account for the ultra-broad bandwidth light generated by the laser. The ANSI standards for retinal exposure account for wavelength, exposure duration, and multiple exposures of the same spot of the retina. Because the laser source generates femtosecond pulses, the laser output was coupled into a 100 meter long optic fiber which was used provide dispersive stretching of the pulse duration to hundreds of picoseconds. This reduces the peak pulse intensities by several orders of magnitude and since the

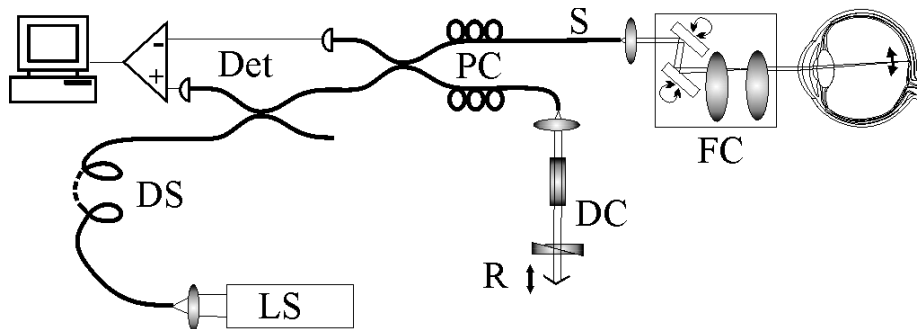


Figure 3.22: In vivo system. LS: Light source; DS: dispersive stretcher; PC: polarization control; S: sample arm; R: reference arm; DC: dispersion compensation; FC: fundus camera; DET: dual balanced detection.

laser operates at an 80 MHz repetition rate, the output can be treated as continuous wave. OCT imaging was performed with axial scan rates ranging between 125 Hz to 250 Hz. Assuming 30 consecutive scans at 125 Hz scanning rate (the slowest rate used in this study) as a conservative limit, a maximum permissible exposure of 1 mW (for 700 nm center wavelength) and 1.54 mW (for 800 nm center wavelength) was calculated using the ANSI standard [97]. OCT imaging

was performed using 500 to 800 μW incident optical power in the scanning OCT beam, well below the ANSI exposure limits. All of the investigations followed the tenets of the Helsinki agreement, written informed consent was obtained from all subjects in this study after the nature and possible consequences of the study had been explained. The study was approved by the ethics committee of the Vienna University, School of Medicine. All of the ultrahigh resolution OCT tomograms in the present study were acquired in a similar manner, with $\sim 3 \mu\text{m}$ axial and 15–20 μm transverse resolution and consisted of 600 transverse and about 3000 axial pixels, covering an area determined by the pathology of about 1–2 mm in depth and 2–4 mm transverse direction. Using this incident power in combination with a 2.8 mm scan depth, a sensitivity of 95 dB or greater could be achieved for all scanning conditions. The full interference fringe signal OCT data was digitized with a high speed (10 Msample/s) and high resolution (16 bit) A/D converter. The OCT signal was extracted by software digital demodulation.

3.5.2 Animal study - optic nerve head and retinal nerve fiber analysis in glaucoma

For early glaucoma diagnosis, UHR OCT might enable significantly improved visualization of the retinal nerve fiber layer, especially of its posterior surface, quantification of its circumpapillary thickness distribution as well as topographic information of the optical nerve head. Hence UHR OCT might be a powerful technique to track subtle intraretinal morphology changes associated in early stages of this disease. Figure 3.23 depicts *in vivo* horizontal UHR OCT tomograms of the optic nerve head in a non-human primate glaucoma model (cynomolgous monkey; this study has been conducted in collaboration with Novartis Institutes for Biomedical Research, by E. Polska and A. Doelemeyer). Cross-sections are depicted at baseline (top), 20 days (middle, left), 34 days (middle, right), 48 (bottom, left) as well as 179 days (bottom, right) after induction of unilateral ocular hypertension at approximately the same retinal location. The retinal nerve fiber layer in the circumpapillary region is clearly visualized despite its atrophy due to increased ocular pressure. Furthermore the lamina cribrosa is clearly visualized at baseline (top, red arrows), which might also be used for detecting early glaucomatous changes. In the advanced stages, the lamina cribrosa is severely thinned or even absent (middle, bottom) and vessels appear prominent caused by significant cupping of the optic nerve head due to increased intraocular pressure. The time course of the intraocular pressure is shown in fig. 3.24.

These preliminary results demonstrate that UHR OCT enables unprecedented visualization of intraretinal morphology, which had previously only been possible with histopathology and therefore provides a powerful tool for the clinical diagnosis of glaucoma. Furthermore, it provides a tool to investigate the impairment of the foveal ganglion cell layer in early stages of glaucomatous damage. Due to increased accuracy and with recent efforts in significantly improving scanning speed while maintaining image resolution and sensitivity [45, 98] this technique may allow three-dimensional detection of topographic as well as intraretinal morphological changes, that might significantly improve the sensitivity and specificity

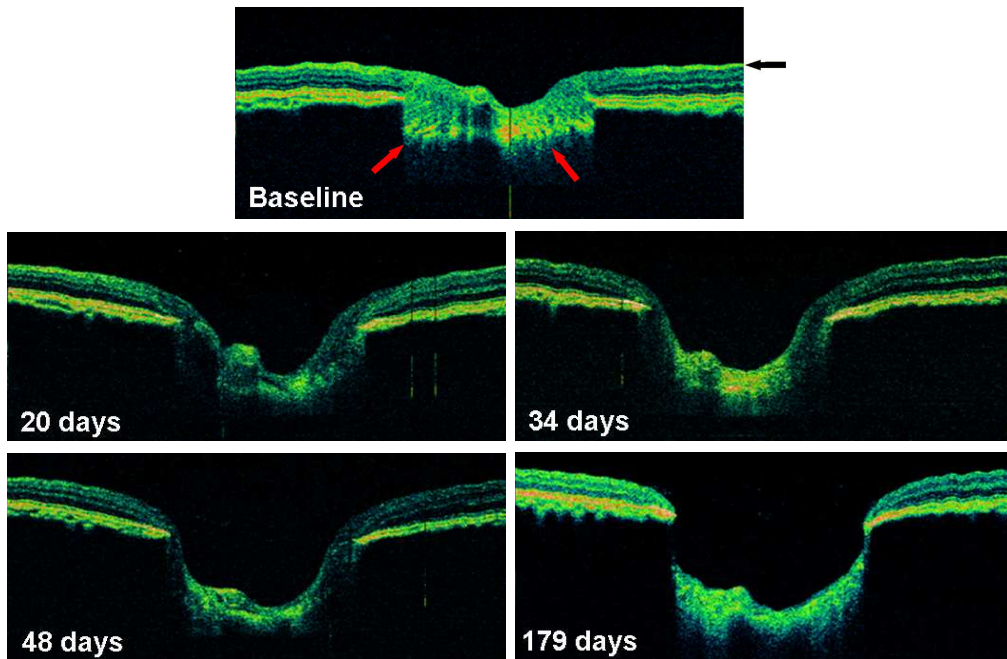


Figure 3.23: Monitoring disease progression in an animal model for glaucoma. Severe atrophy of the nerve fiber layer (black arrow) and clear topographic depression of the optic nerve head as well as thinning of the lamina cribrosa (red arrows) during disease progression is clearly visualized.

of glaucoma diagnosis.

Standard resolution, commercially available ophthalmic OCT systems use superluminescent diodes emitting light with 20- to 30-nm bandwidths centered at 830 nm, resulting in a 10- to 15- μm axial image resolution. In the present study, a recently developed, compact, cost-effective (i.e., two to three times cheaper than other commercially available comparable lasers), titanium-sapphire laser (Femto-lasers Produktions GmbH, Vienna, Austria), with up to a 176-nm bandwidth at an 800-nm center wavelength was used for imaging [99]. This UHR-OCT system is based on a commercially available OCT system (OCT 1) that was provided by Carl Zeiss Meditec, Inc. (Dublin, CA) [96].

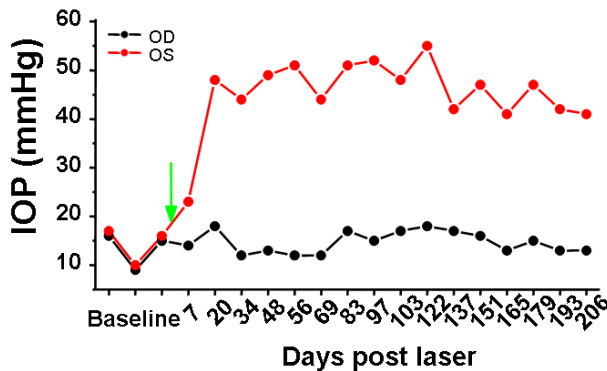


Figure 3.24: Intraocular pressure as a function of time.

3.5.3 Human studies - enhanced visualization of macular pathologies

Novel medical imaging technologies can improve not only diagnosis and clinical management, but also the understanding of disease pathogenesis and therefore promise to have a significant impact in medical research as well as clinical practice. A and B scan ultrasonography require physical contact with the eye and are routinely used in ophthalmic diagnosis with a typical longitudinal resolution of $150\ \mu\text{m}$ [5, 6]. In the last decade, advances in optics, fiber optics as well as laser technology have led to the development of a non-contact, high resolution optical biomedical imaging technology, called optical coherence tomography (OCT) [17, 18, 24, 100]. Analogous to ultrasonic pulse-echo imaging, OCT achieves two- or three-dimensional cross sectional imaging of tissue by measuring the echo delay and intensity of back reflected infrared light from internal tissue structures. Employing a classical optical measurement technique known as low coherence interferometry (LCI) [15, 16] in combination with special broad bandwidth light, OCT achieves high resolution, cross sectional visualization of tissue morphology at depths significantly greater than the penetration depth offered by conventional bright field and confocal microscopy.

Ocular media are essentially transparent, transmitting light with only minimal optical attenuation and scattering and also provide easy optical access to the retina. For these reasons, ophthalmic diagnosis represents one of the most clinically developed OCT applications.

With $10\text{--}15\ \mu\text{m}$ axial resolution, standard ophthalmic OCT provides more detailed structural information than any other ophthalmic diagnostic technique. Despite the promising and clinically valuable results of these OCT studies, the axial resolution and performance of standard clinical ophthalmic OCT technology can be significantly improved. Many of the early pathologic changes associated with disease are still below the resolution limit of standard OCT. Intraretinal structures, such as the ganglion cell layer, the photoreceptor layer, and the retinal pigment epithelium, are often involved in early stages of ocular diseases, but cannot not be resolved with standard OCT. One of the most powerful approaches for obtaining ultrahigh resolution is the use of femtosecond laser light sources for OCT imaging. Ultrahigh resolution OCT imaging employing a laboratory prototype femtosecond Titanium-sapphire laser light source has recently been demonstrated to achieve an axial resolution of $1\text{--}3\ \mu\text{m}$ in non-transparent and transparent tissue, enabling unprecedented in vivo sub-cellular [21] as well as intraretinal [22, 68] visualization.

In this study, we describe a clinically viable ultrahigh resolution ophthalmic optical coherence tomography system based on a commercially available Titanium-sapphire laser (Femtosource Compact Pro, FEMTOLASERS). This system can be used in a clinical setting, enabling in vivo cross-sectional imaging of macular pathologies with unprecedented axial resolution of $\sim 3\ \mu\text{m}$. We perform the first ultrahigh resolution imaging studies of macular pathologies and demonstrate that ultrahigh resolution OCT permits visualization of all principal intraretinal layers, including the ganglion cell layer, inner and outer plexiform,

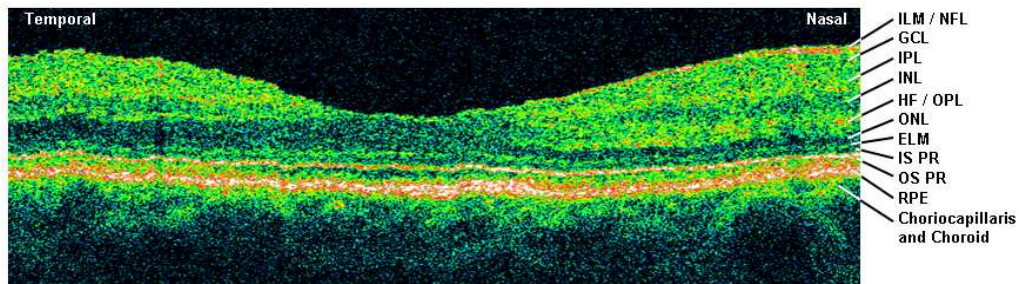


Figure 3.25: Horizontal ultrahigh resolution OCT image of a normal human macula. Labeling of intraretinal layers according to subjective correlation of with intraretinal anatomy: ILM: internal limiting membrane; NFL: nerve fiber layer; GCL: ganglion cell layer; IPL, OPL: inner and outer plexiform layer; INL, ONL: inner and outer nuclear layer; HF: Henle's fiber layer; ELM: external limiting membrane; IS, OS PR: inner and outer segment of photoreceptor layer; RPE: retinal pigment epithelium; BM: Bruch's membrane.

nuclear layers, external limiting membrane, and the inner and outer segments of the photoreceptor layer in selected macular pathologies. This study establishes a baseline for the interpretation of ultrahigh resolution OCT images of macular pathology.

Results. Figure 3.25 shows a typical horizontal in vivo cross-sectional ultrahigh resolution OCT image of a normal human macula, demonstrating the potential for in vivo visualization of all major intraretinal layers. These layers were subjectively correlated to the well know foveal anatomy. Layers which consist of nerve fibers or plexiform layers are optically backscattering, while nuclear layers are less backscattering. The internal limiting membrane (ILM), has previously only been visible with electron microscopy and is not resolved with OCT. The obliquely running photoreceptor axons are sometimes considered as a separate layer in the outer plexiform layer (OPL), known as Henle's fiber layer (HF), and are highly backscattering.

The ELM as well as the junction between the inner and outer segments of the photoreceptors (IS PR, OS PR) could be visualized. This structure is not a physical membrane, but an alignment of junctional complexes between Müller cells and photoreceptor cells. The retinal pigment epithelium (RPE), which contains melanin, is a very strongly backscattering layer. The distance between the RPE and the inner and outer segment junction of the photoreceptors increases significantly in the foveal region, consistent with the well-known increase in length of the outer cone segments in this region. Bruch's membrane, which is only 2–5 μm thick [101], could not be visualized since it is included in the bright reflecting broad band of the RPE appearance, except in patients with RPE atrophy or AMD (cf. fig. 3.30D-F, 3.31A-C, 3.32B). In general, light in the 800 nm wavelength region is strongly reflected and absorbed by the melanin contained in the RPE. In addition, because the choriocapillaris and choroid are highly vascular, causing strong absorption by hemoglobin as well as increased multiple scattering, the

penetration of light in this wavelength region is limited and only the superficial choroidal layers can be visualized.

Clinical ultrahigh resolution ophthalmic OCT imaging was performed in collaboration with the Department of Ophthalmology, General Hospital of Vienna (M. Stur, C. Scholda, M. Wirtitsch, and E. Ergun) in 56 eyes of 40 patients with the following macular diseases: central serous chorioretinopathy (6 eyes), macular edema (8 eyes), age-related macular degeneration (11 eyes), macular hole (18 eyes), epiretinal membranes, detachment of pigment epithelium and sensory retina (13 eyes).

Selected case reports:

Central Serous Chorioretinopathy. Patient 1. This case describes a 42-year-old man with recurrent central serous chorioretinopathy (CSC) in his left eye and a visual acuity of 20/25. For comparison purposes, Figure 3.26A shows a typical vertical cross-sectional ultrahigh resolution OCT image of a normal human macula. Figure 3.26B depicts a vertical cross-sectional ultrahigh resolution OCT image of the CSC patient. Figure 3.26D indicates the corresponding scan on a fluorescein angiography (FA) fundus photo during the late phase. No clinically significant leakage or staining of subretinal fluid was evident using FA, there were only small window defects superior to the fovea. The ultrahigh resolution OCT image indicates a normal appearing NFL, GCL as well as inner and outer nuclear and plexiform layer. In the slightly elevated foveola region, ultrahigh resolution OCT imaging reveals a clear impairment of the ELM-IS/OS photoreceptor layer complex. The ELM appears to be intact. The inner PR segments are moderately swollen and slightly detached from the RPE. Due to the enhanced axial resolution of OCT, the optically clear subretinal serous fluid accumulation, an optically empty space under the retina is clearly visualized, causing thickened neurosensory retina above this serous detachment and therefore the foveal pit is slightly distorted. The ultrahigh resolution OCT image indicates that the RPE layer is not detached. Figure 3.26C shows a vertical scan at approximately the same location of the same patients eye 2 months later. Ultrahigh resolution OCT reveals complete recovery and disappearance of the intraretinal fluid as well as no signs of scarring. The external limiting membrane, the inner as well as outer photoreceptor segment are properly aligned and show normal appearance in the foveola region, comparable to the foveal appearance of the age-matched normal subject (Figure 3.26A).

Patient 2. This case describes a 52-year-old man with chronic recurrent central serous chorioretinopathy in his left eye with a visual acuity of 20/25in both eyes. Figures 3.27A-D depict horizontal cross-sectional ultrahigh resolution OCT images through the foveal region of the left eye, which has visual acuity of 20/25. Figures 3.27E and F indicate scan positions corresponding from top to bottom to scans A-D on early (3E) and late (3F) phase fluorescein angiography fundus photos, respectively. Ultrahigh resolution OCT images indicate normal appearance of the NFL, GCL, inner and outer plexiform layers as well as the inner

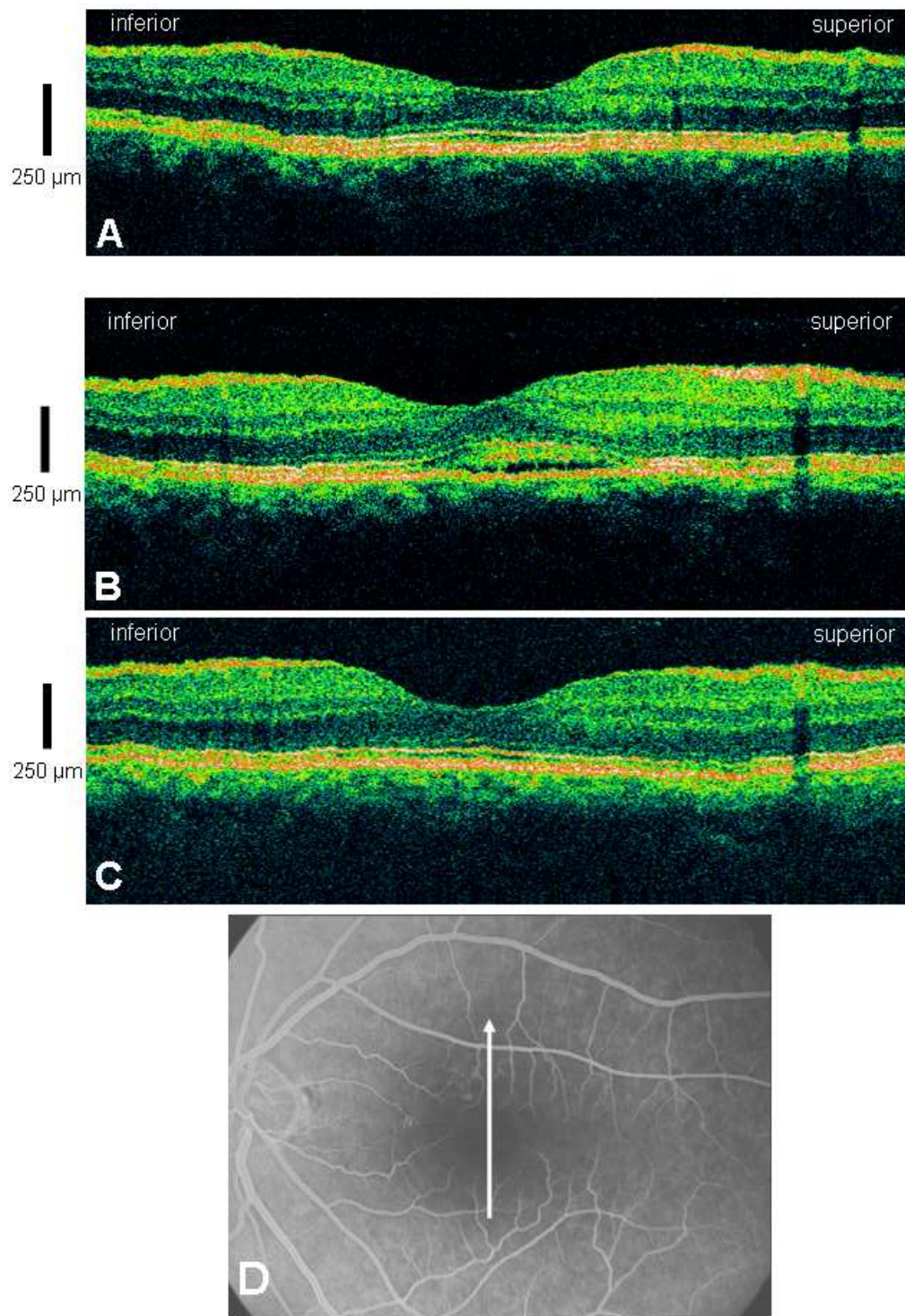


Figure 3.26: Patient 1. A: Vertical ultrahigh resolution OCT image of a normal human macula; B: ultrahigh resolution OCT image of a patient with recurrent central serous chorioretinopathy; C: vertical scan approximately at the same location of the same eye 2 months later D: corresponding scan on a fluorescein angiography.

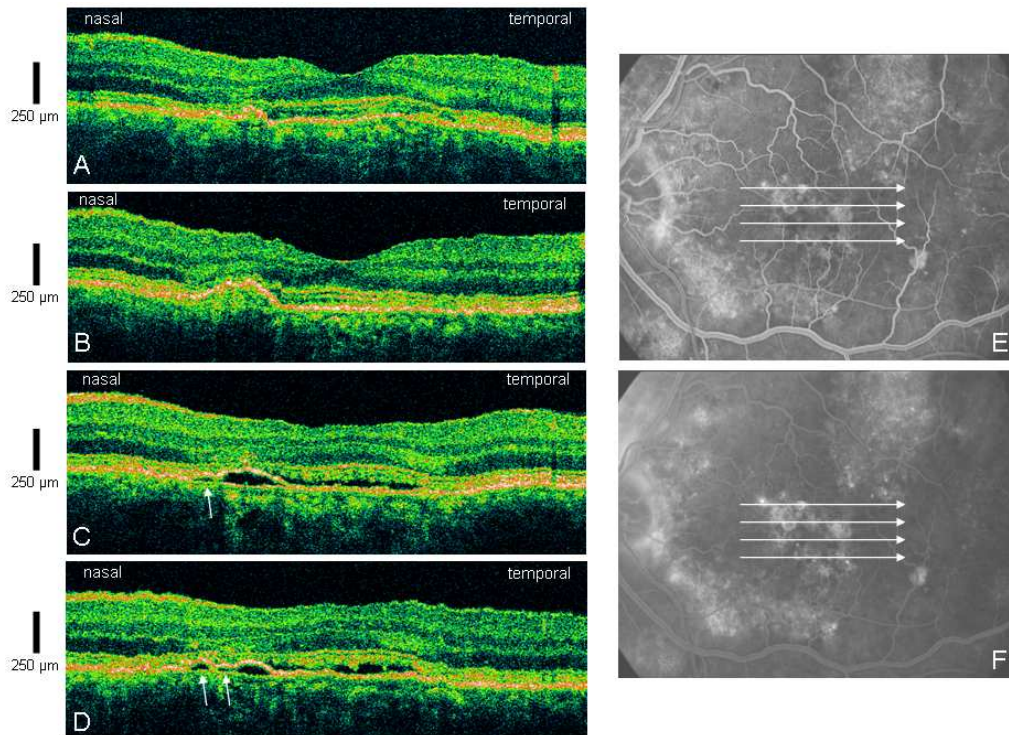


Figure 3.27: Patient 2. Patient with chronic recurrent central serous chorioretinopathy. A–D: ultrahigh resolution OCT images through the foveal region. 3E and 3F: scan position on early (E) and late phase (F) fluorescein angiography fundus photos. Arrows indicate subtle RPE detachments.

nuclear layer. In the foveal nasal region, ultrahigh resolution OCT enables visualization of several subtle serous RPE detachments seen as leakage in the FA of about 10–15 μm (cf. arrows fig. 3.27C, D). In the upper scans (cf. Figure 3.27A, B) there is higher reflectivity within the space of the RPE detachments due to some optically backscattering deposits, whereas the lower scans (cf. Figure 3.27 C, D) show optical empty space within the RPE detachments, maybe indicating different stages of the disease. The photoreceptor IS and OS are similarly affected in this region as in the non-chronic case (cf. fig. 3.26B), indicating serous detachment of sensory retina caused by optically clear subretinal fluid. In all four cross-sectional images a compressed photoreceptor layer is depicted by ultrahigh resolution OCT, especially in areas of RPE detachments.

Macular Edema. Patient 3. This case describes a 61-year-old woman with macular branch vein occlusion and cystoid macular edema in her left eye with visual acuity of 20/25. Figures 3.28A–D show horizontal cross-sectional ultrahigh resolution OCT images through the foveal region. Figure 3.28E–G indicate corresponding scan positions corresponding from top to bottom to scans A–D on an infrared, early and late phase fluorescein angiography fundus photos, respectively. Ultrahigh resolution OCT images show a clear thickening of the retina,

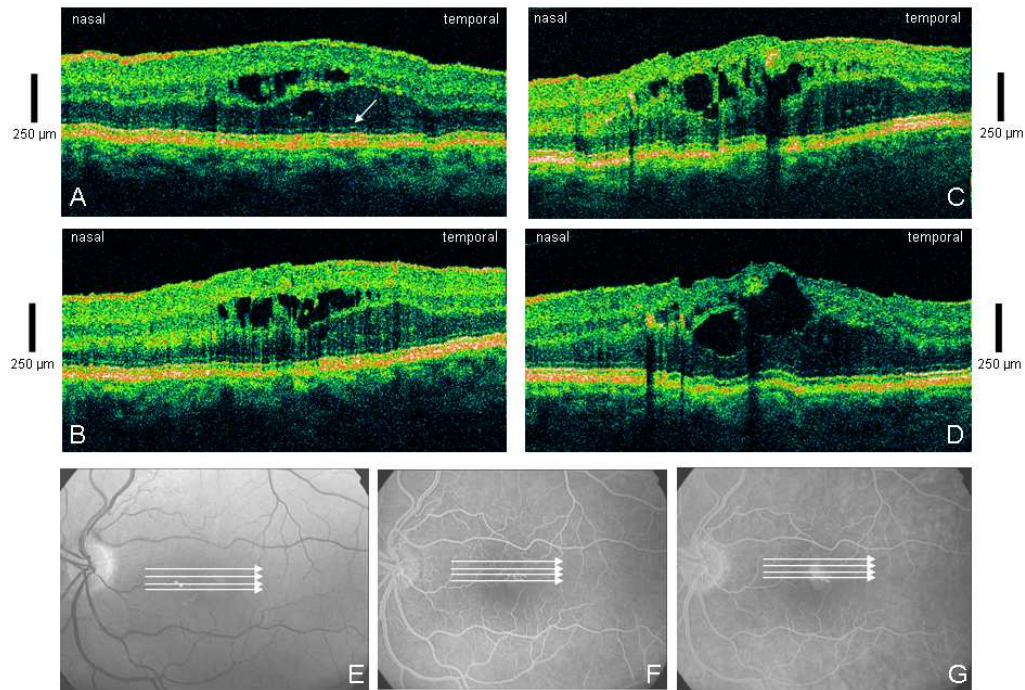


Figure 3.28: Patient 3. Patient with macular branch vein occlusion with cystoid macular edema. A–D: ultrahigh resolution OCT images through the foveal region. 4E: corresponding scan positions on an infrared fundus photo, F and G: early and late phase fluorescein angiography fundus photos. Arrow indicates intact external limiting membrane.

mainly caused by intraretinal cystoid spaces, that mainly originates in the inner nuclear and outer nuclear layer parafoveal (4A and 4B). Their intraretinal location varies according to the distance of the scans from the foveolar center. The cystic spaces in the Henle fiber layer are enlarged. (4C and 4D). Intraretinal hard exudates cause high optical backscattering and shadowing artifacts (cf. fig. 3.28C and D). Ultrahigh resolution OCT images also reveal the intact ELM (cf. arrow), photoreceptor inner and outer segments, and RPE layer.

Age-related Macular Degeneration. Patient 4. This case describes a 52-year-old man with massive cystoid degeneration of the macula and visual acuity of 20/400. Figures 3.29A–C depict horizontal cross-sectional ultrahigh resolution OCT images through the inferior-foveal region. Figures 3.29D–F indicate corresponding scan positions corresponding from top to bottom to scans A–C on a fundus photo and infrared and late fluorescein angiography photos, respectively. Inferior to the fovea, the cystoid appearance is mainly located in the inner nuclear layer (cf. fig. 3.29C). The ELM is not visible, indicating damage to and partial loss of the photoreceptor layer. In addition, the photoreceptor inner and outer segments as well as the RPE are strongly atrophied in this region. Close to the fovea (cf. fig. 3.29B), inner and outer nuclear and outer plexiform layers show large cystoid spaces. The inner retinal layers, such as the NFL, GCL and

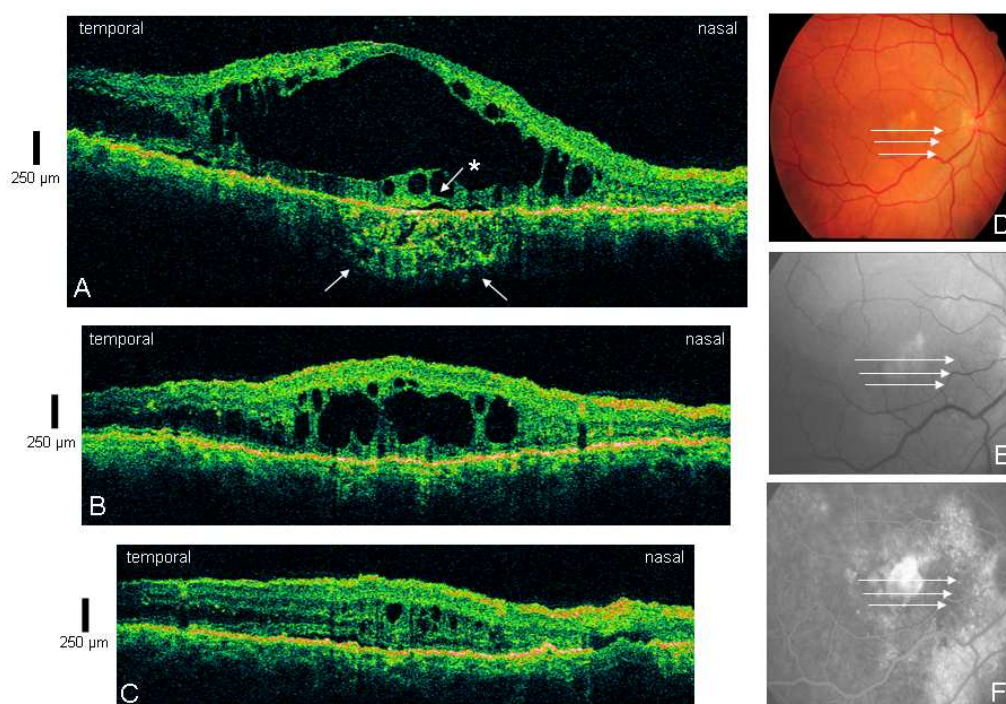


Figure 3.29: Patient 4. Patient with cystoid macular edema with subretinal fibrosis and serous detachment of sensory retina. A–C: ultrahigh resolution OCT images through the inferior-foveal region. D: corresponding scan positions on fundus photo, F and G: red-free and late fluorescein angiography fundus photos. In A, the arrow with asterisk depicts the subtle photoreceptor layer detachment. The arrows indicate the subretinal fibrosis.

IPL seem to be less affected. In the central foveal region (cf. fig. 3.29A) the cysts ruptured and all the intraretinal layers are affected. Subtle photoreceptor layer detachment (cf. arrow with asterisk fig. 3.29A), and subretinal fibrosis as well as RPE and choriocapillaris atrophy (cf. arrows fig. 3.29A) can be visualized. Nasal to this region, the OCT scans show normal appearance of intraretinal layers.

Patient 5. This case describes a 60-year-old woman with age-related macular degeneration with minimal classic neovascularization and vascularized RPE detachment in her right eye and an inactive plakoid occult CNV in her left eye with a visual acuity of 20/40. Figures 3.30A–D depict several horizontal cross-sectional ultrahigh resolution OCT images through the foveal region providing three-dimensional information about the morphology of the retinal changes. Figure 3.30E–G indicate corresponding scan positions corresponding from top to bottom to scans A–F on fundus photo as well as early and late phase fluorescein angiography photos, respectively. Ultrahigh resolution OCT images reveal an increased retinal thickness, especially in the parafoveal region (3.30A and B), with normal appearance of the inner retinal layers, the NFL and GCL. Similar to the case of macular edema (cf. case 3, fig. 3.28), the IPL layer is mainly affected in the region outside of the fovea. Furthermore the ONL, photoreceptor inner and outer segments as well as the RPE/BM/choriocapillaris interface are severely affected.

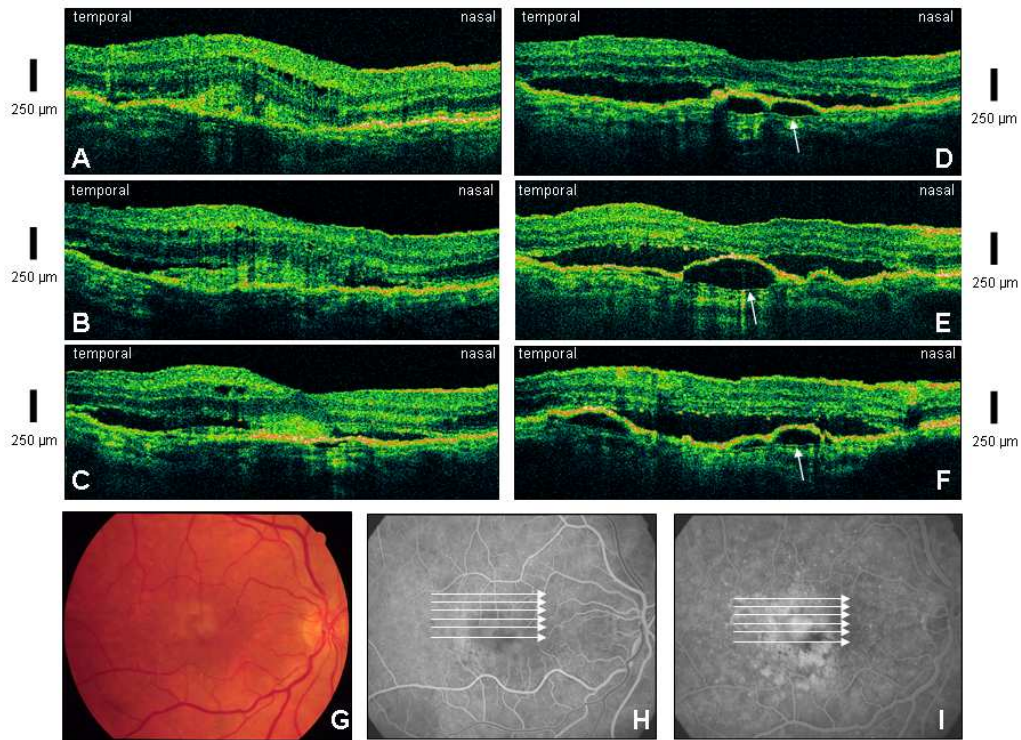


Figure 3.30: Patient 5. Patient with age-related macular degeneration with minimal classic neovascularization and vascularized RPE detachment. A–D: ultrahigh resolution OCT images through the foveal region providing three-dimensional information about the morphology of the retinal changes. 6E: corresponding scan positions on fundus photo, F and G: early and late fluorescein angiography photos. Arrows in D–F indicate Bruch’s membrane underneath the RPE detachment.

Ultrahigh resolution OCT seems to reveal a classic CNV component above the RPE in the fovea visualizing a thickened RPE-CC layer and serous detachment of the RPE and of sensory retina in the fovea and the parafoveal region (cf. fig. 3.30C to F). It is interesting to note that ultrahigh resolution OCT shows a normal appearance of NFL, GCL, IPL and INL despite the existing RPE and retinal detachment (cf. fig. 3.30D–F). The ultrahigh axial image resolution of the OCT system enabled the visualization of another thin layer, possibly corresponding to Bruch’s membrane underneath the RPE detachment in some locations (cf. fig. 3.30D to F, arrows) as well as parts of the detached RPE pigmentation.

Similar appearances are encountered in the left eye of the same patient having regressing drusen with placoid occult without classic CNV with a visual acuity of 20/20. Figures 3.31A–C depict three horizontal cross-sectional ultrahigh resolution OCT images through the foveal region. Figure 3.31D indicates corresponding scans corresponding from top to bottom to scans A–C in a late phase fluorescein angiography fundus photo. In addition to a normal appearance of the NFL, GCL and IPL and INL, the photoreceptor layer is strongly comprised, due to a serous detachment. Ultrahigh resolution OCT enables visualization of the occult membrane underneath the RPE as well as the outer membrane of Bruch’s

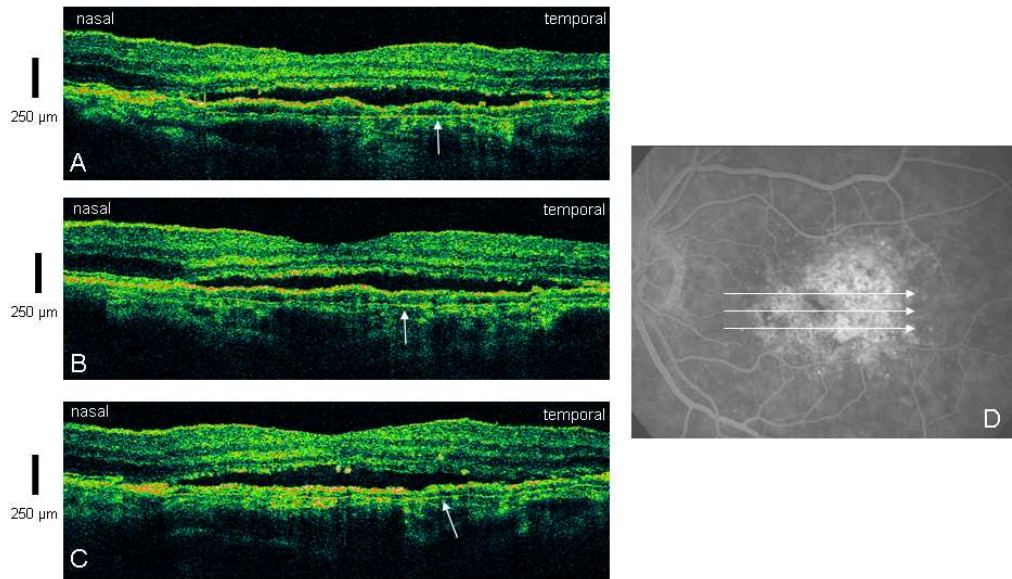


Figure 3.31: Patient 5. Patient with regressing drusen and occult classic neovascularisation. A–C: three horizontal cross-sectional ultrahigh resolution OCT images through the foveal region. D: corresponding scans in a late phase fluorescein angiography fundus photo. Arrows indicate thin layer, possibly corresponding to Bruch’s membrane underneath the RPE detachment.

membrane, indicating intra-Bruch’s CNV for the first time (cf. arrows fig. 3.31A–C). In all three cross-sections highly reflective particles in the level of the outer photoreceptor layer which could be isolated RP cells or damaged photoreceptors could be differentiated by ultrahigh resolution OCT.

Patient 6. This case describes a 63-year-old woman with an adult-onset pseudovitelliform macular dystrophy in her right eye with a visual acuity of 20/32. Figure 3.32A depicts a vertical cross-sectional ultrahigh resolution OCT images through the foveal region of the right eye. Figures 3.32B and C indicate corresponding scans in the fundus photo and the late phase fluorescein angiography fundus photo. OCT reveals a normal appearance of the inner retinal layers, such as the NFL, GCL and IPL and INL. The RPE layer is affected by drusen in the parafoveal region, resulting in a modulated appearance of the RPE contour maybe due to protein deposits. In the central foveal region, . There is a thickening of the RPE-choriocapillary complex, perhaps indicating a subretinal deposit. A well circumscribed elevation of the sensory retina above the thickened RPE is clearly visualized by OCT, characteristic for a vitelliform lesion. The ELM as well as inner and outer segments of the PR are affected in the central region, and the photoreceptor layer is therefore strongly compressed.

The same patient’s left eye has areolar atrophy of a vitelliform lesion associated with age-related macular degeneration with a visual acuity of 20/160. Figure 3.32D shows a horizontal cross-sectional ultrahigh resolution OCT image through the foveal region of her left eye. Figure 3.32E and F indicates corresponding scans in the fundus photos and late phase fluorescein angiography fundus photo. OCT

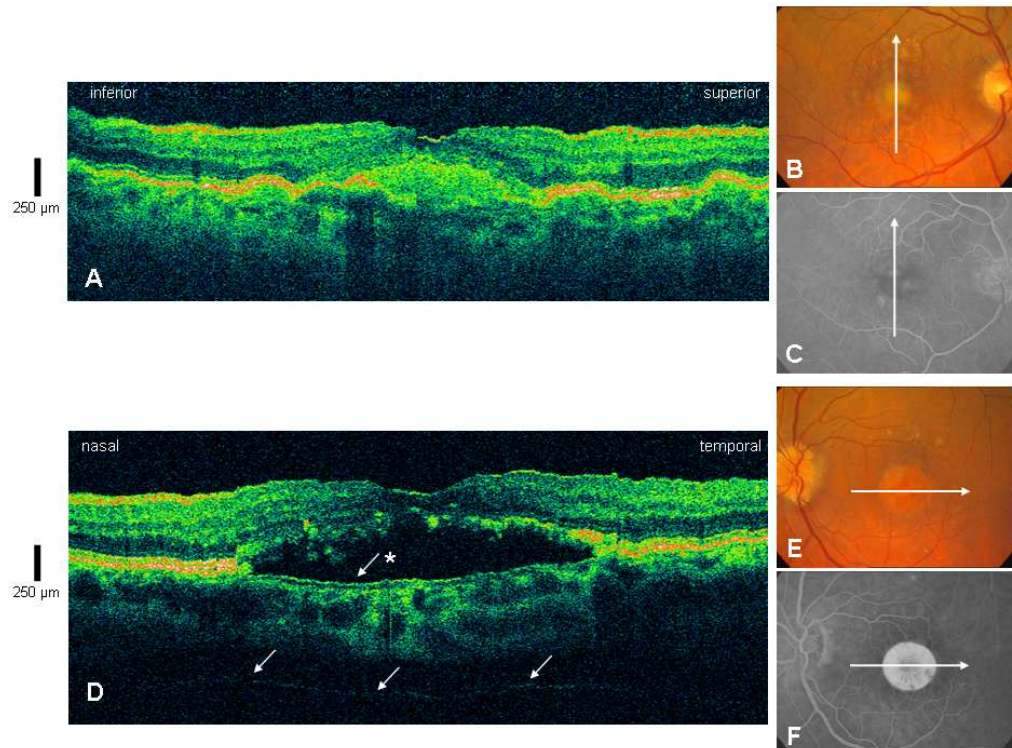


Figure 3.32: Patient 6. Patient with a vitelliform lesion of age-related macular degeneration and drusen on the right eye. A: vertical cross-sectional ultrahigh resolution OCT images through the foveal region. B: corresponding scan in the fundus photos, C: late phase fluorescein angiography fundus photo. Left eye of the same patient with an areolar atrophy after a vitelliform lesion of age-related macular degeneration on the left eye. D: horizontal cross-sectional ultrahigh resolution OCT images through the foveal region. E: corresponding scan in the fundus photos, F: late phase fluorescein angiography fundus photo. Second layer of Bruch's membrane (arrow with asterisk), as well as a very weak reflection of the choroidal-scleral interface, allowing the visualization and thickness quantification of the choroidal (arrows) are indicated.

reveals a normal appearance of the inner retinal layers, such as the NFL, GCL, IPL and INL. The RPE layer is affected by atrophy in the central foveal region, resulting in a damaged PR layer. There is a serous detachment of sensory retina, most likely presenting a late stage vitelliform lesion. Due to RPE atrophy and, therefore, reduced backscattering and absorption, the ultrahigh resolution of this OCT system enables the visualization of choroidal vessels, the second layer of Bruch's membrane (arrow with asterisk), as well as a very weak reflection of the choroidal-scleral interface. This enabled the choroid to be quantitatively measured in vivo for the first time (arrows). The measured optical thickness was $\sim 740 \mu\text{m}$, corresponding to a geometrical thickness of $\sim 528 \mu\text{m}$, assuming a group refractive index of 1.4. This is in good agreement with previously reported choroidal thickness results [102].

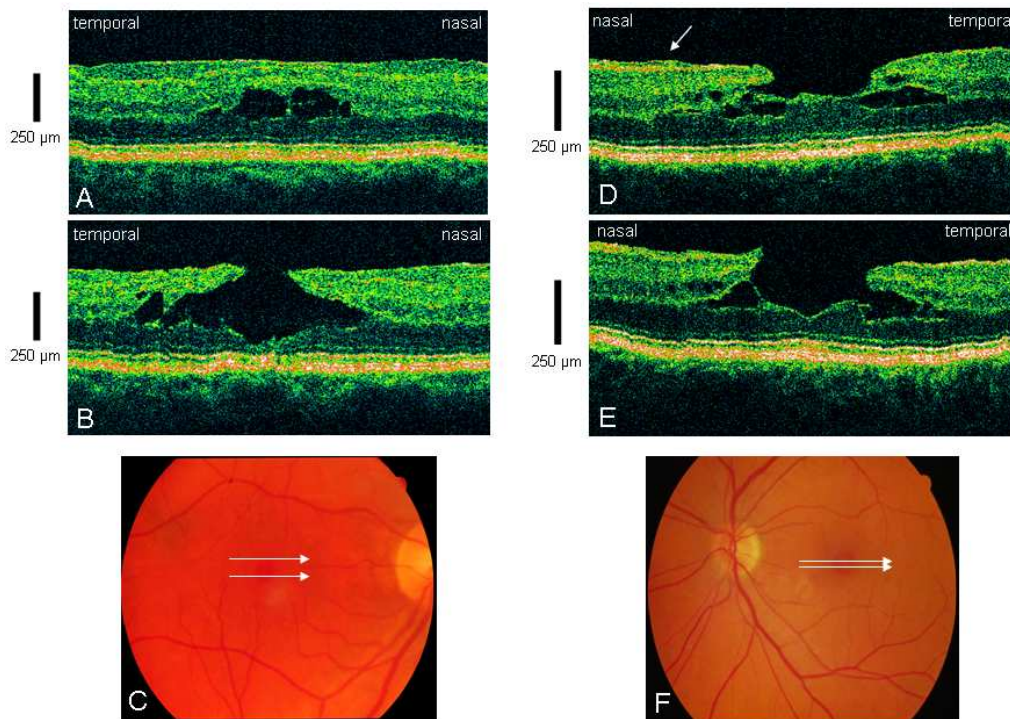


Figure 3.33: Patient 7. Patient with lamellar macular hole (stage 2). A and B: horizontal cross-sectional ultrahigh resolution OCT images through the foveal region providing three-dimensional information about the morphology of the macular hole. C: corresponding scans in the fundus photos. Patient 8. Patient with macular hole stage 3A. D and E: horizontal cross-sectional ultrahigh resolution OCT images through the foveal region providing three-dimensional information on the morphology of the macular hole. F: corresponding scans in the fundus photos. Arrow in D indicates epiretinal membrane.

Macular Hole. Patient 7. This case describes a 66-year-old woman with a lamellar macular hole in her right eye with a visual acuity of 0.5 and Watzke Allen-Sign negative. Figures 3.33A and B depict horizontal cross-sectional ultrahigh resolution OCT images through the foveal region providing three-dimensional information about the morphologic development of the retinal hole. Ultrahigh resolution OCT reveals a lamellar or partial thickness macular hole. Figure 3.33C indicates corresponding scans corresponding from top to bottom to scans A-B in the fundus photo. The foveal contour (cf. fig. 3.33 B) indicates a rupture of central intraretinal cysts (cf. fig. 3.33A). All retinal layers can be differentiated. Ultrahigh resolution OCT imaging enabled the outer nuclear layer, the inner and outer segment of the PR layer as well as the ELM to be clearly visualized and will enable their morphology to be used as criteria for diagnosis and therapeutic decision making for the first time.

Patient 8. This case describes a 56-year-old woman with a lamellar macular hole in her left eye. Visual acuity was reduced to 0.5, Watzke Allen-Sign negative. Figures 3.33D and E depict horizontal cross-sectional ultrahigh resolution OCT images through the foveal region providing three-dimensional information

about the morphologic appearance of the macular hole. Figure 3.33F indicates the corresponding scans corresponding from top to bottom to scans D-E on the fundus photo. Ultrahigh resolution OCT reveals an inner lamellar macular hole. The enhanced resolution of ultrahigh resolution OCT enables the condition of the outer nuclear layer, the inner and outer segment of the PR layer as well as the ELM to be clearly visualized. In this case, the fine connections of the ONL and inner outer segment complex to the edges of the hole can clearly be seen. Ultrahigh resolution also enables the visualization of epiretinal membranes (arrow). Diagnosis of macular holes based on the morphology of the PR layer and ELM should provide the ophthalmologist with significantly improved information for surgical and treatment planning.

Patient 9. This case describes a 77-year-old woman with an idiopathic full thickness macular hole in her left eye. Visual acuity was reduced to 0.16, Watzke Allen-Sign positive. Figures 3.34A to D depict horizontal cross-sectional ultrahigh resolution OCT images through the foveal region providing three-dimensional information about the morphologic development of the retinal hole. Figure 3.34E indicates corresponding scans corresponding from top to bottom to scans A-D in the fundus photo. Ultrahigh resolution OCT reveals a full thickness stage 3 macular hole according to Gass [103,104], with complete loss of retinal tissue in the fovea extending to the RPE. As in the case of macular edema (cf. case 3 and fig. 3.28), the IPL layer is affected first in the region outside of the fovea, causing retinal edema (cf. fig. 3.34A-D). In this case the GCL is also affected (cf. fig. 3.34A and B). A remaining (Pseudo-) operculum as well as an epiretinal membrane at the edge of the hole (cf. Fig 3.34D) can be visualized by the ultrahigh resolution OCT. In this case, the photoreceptor layer is completely gone and therefore the ELM is also not visible.

Discussion. Use of state of the art femtosecond laser technology enables unprecedented axial resolution for ophthalmic OCT imaging. Studies were performed using a compact, robust, user-friendly commercially available Ti:sapphire laser (Femtosource Compact Pro, FEMTOLASERS) instead of a large footprint, laboratory prototype laser. A clinically viable ultrahigh resolution ophthalmic OCT system, based on a commercially available system (OCT 1; Carl Zeiss Ophthalmic Systems, Inc.) has been developed which is well engineered for use in the clinic. Ultrahigh resolution OCT has been applied to image macular disease pathology for the first time. This novel, third generation OCT system achieves an unprecedented axial image resolution of $\sim 3 \mu\text{m}$ and enables optical biopsy of the human retina, i.e. visualization of intraretinal morphology in retinal pathologies approaching the level of that achieved with histopathology.

The novel ultrahigh resolution OCT system used in this study was designed to acquire full fringe interference signals, compared to the envelope of the fringe signal, which is typically detected in standard ophthalmic OCT systems. The digital detection of the full interference signal enables the simultaneous acquisition of ultrahigh resolution structural images, spatially resolved Doppler flow as well as spectroscopic imaging for detection of different biochemical chromophores by using special post processing digital algorithms. Since this novel ultrahigh resolu-

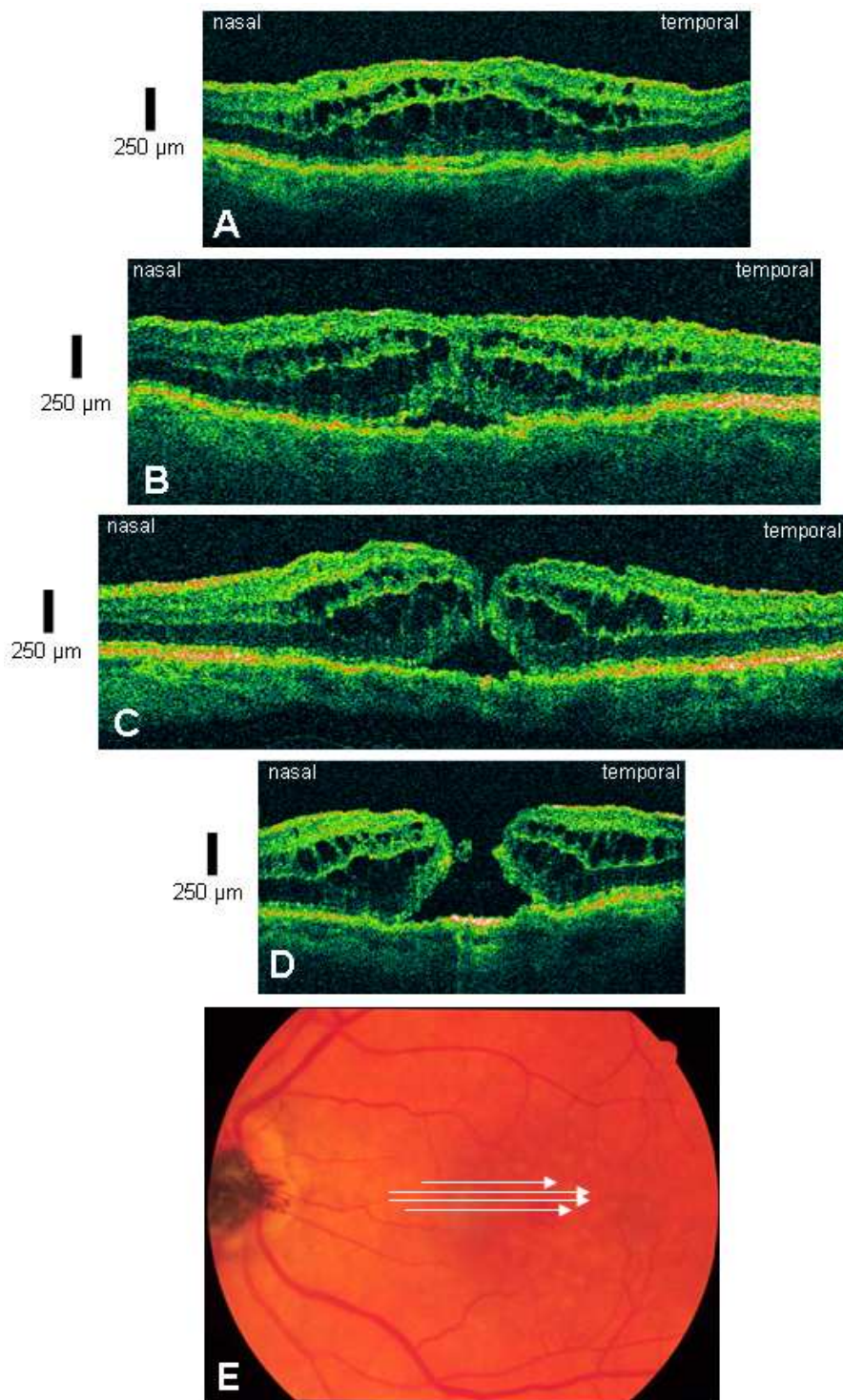


Figure 3.34: Patient 9. Patient with an idiopathic macular hole stage 4. A–D: ultrahigh resolution OCT images through the foveal region providing three-dimensional information on the morphology of the macular hole. E: indicates corresponding scans in the fundus photos.

tion OCT system is based on a commercially available OCT 1 system (Carl Zeiss Meditec Inc.) and employs a compact commercially available Ti:sapphire laser, a clinically viable system can be developed and used for imaging patients. The current OCT system has a maximum axial scan rate of 250 Hz. To further reduce the effects of patient eye motion during OCT image acquisition, a further increase to 500 Hz-600 Hz is envisaged in the near future, yielding image acquisition times of 1 second for a 600 transverse pixel image. The ultimate availability of this ultrahigh resolution OCT technology will depend on the availability of ultrabroad bandwidth light sources which are suitable for OCT applications. The principal disadvantage of current femtosecond laser technology is its extremely high cost. With continuing research, more compact and less expensive light sources for ultrahigh resolution OCT imaging can be expected in the near future.

Ultrahigh resolution OCT enabled all of the major intraretinal layers to be visualized noninvasively in vivo for the first time and images had excellent correlation with known retinal morphology (cf. fig. 3.25). A recent study investigated ultrahigh resolution OCT images from the porcine retina immediately post mortem and preformed detailed correlations with histology³³. This study permits a more accurate interpretation of the region between the outer nuclear layer and the retinal pigment epithelium / choriocapillaris interface than in earlier studies. This correlation and interpretation of OCT imaging has also been confirmed by the findings of this study, where well-known anatomical intraretinal changes could be visualized by ultrahigh resolution OCT and confirmed with other standard ophthalmic diagnostic techniques. It is especially interesting to note that ultrahigh resolution OCT is able to visualize the external limiting membrane as well as the inner and outer segment of the photoreceptor layer. The high reflection of the interface between inner and outer photoreceptor segment is not fully understood yet, but has been identified by correlating ultrahigh resolution OCT images with histology [85] and might be due to the waveguide characteristics and the different shapes of these two photoreceptor segments [83]. Photoreceptor segments beyond the distal myoid attain specific shapes (cylindrical: rod IS and OS, conical: cone OS, paraboloidal: cone IS) and are thought to represent individual optical elements with refractive indices greater of equal to 1.4, separating them from the surrounding interphotoreceptor matrix ($n \approx 1.34$). Under physiological illumination conditions, the cone ellipsoids guide light towards the photopigments in the outer segments [78]. The outer segments that contain densely stacked disc membranes have high refractive indices [79].

This clear visualization and delineation of all major intraretinal layers, enabled the determination of which intraretinal layers are involved in different types of retinal pathology and promises to significantly improve the understanding of ocular pathogenesis as well as enable more sensitive and specific diagnosis. In macular edema (cf. fig. 3.28), AMD (cf. fig. 3.30) as well as macular holes (cf. fig. 3.34), ultrahigh resolution OCT revealed that the inner nuclear layer seems to be significantly affected. Enhanced visualization of inner and outer segments of the photoreceptor layer, their thickness changes as well as their displacement (cf. fig. 3.26, 3.27) enabled the evaluation of condition of the photoreceptors for the first time. The ability to directly visualize these features might have a significant

impact not only in the early diagnosis, but also in treatment planning and follow up. Despite their advanced progression, clear delineation of the photoreceptor inner and outer segment of pathology could be visualized in different cases with inner lamellar macular holes (cf. fig. 3.33). This promises to improve the investigation of hole progression as well as treatment planning and post operative follow up. To our knowledge, this is also the first time that occult neovascular subretinal membranes (cf. fig. 3.30 and 3.31) and the outer lamella of Bruch's membrane (cf. fig. 3.32) could be visualized in patients with age-related macular degeneration and occult CNV. In addition, clear localization of CNV above the RPE was possible using ultrahigh resolution OCT (cf. fig. 3.30C). There has been a longstanding controversy about the exact location of the CNV with respect to the RPE. Ultrahigh resolution OCT promises to significantly contribute to the diagnosis and understanding of the pathogenesis of AMD. The enhanced visualization of inner and outer segment of the photoreceptors, external limiting membrane as well as the RPE might also facilitate the investigation of morphological changes after photodynamic therapy and transpupillary thermotherapy in AMD or ILM peeling in diabetic retinopathy. In addition, the choroidal thickness could be imaged and quantitatively measured for the first time (cf. fig. 3.32 D) in patients with RPE atrophy. This condition reduces the high backscattering and absorption of infrared light at this interface, enabling deeper image penetration into subretinal layers. Enhanced visualization of retinal alterations in CSC patients (cf. fig. 3.26, 3.27) was also possible. Subtle RPE detachments (cf. fig. 3.27, 3.29) as well as serous detachments of sensory retina (cf. fig. 3.27) could be visualized with ultrahigh resolution OCT. Photoreceptor misalignments and thinning (cf. fig. 3.26, 3.31) as well as subtle serous detachment could be detected in a patient with recurrent CSC (cf. fig. 3.26).

In summary, the clear visualization of all the major intraretinal layers and the ability to assess changes of retinal morphology associated with retinal pathologies, especially in the inner outer segment of photoreceptors / external limiting membrane / retinal pigment epithelium complex, promises to have a significant impact on the diagnosis, investigation of pathogenesis as well as the evaluation of therapy of a variety of macular diseases. Therefore ultrahigh resolution OCT has the potential to become an important and powerful adjunct to standard ophthalmic diagnostic methods.

3.5.4 Human studies - assessment of central visual function using UHR OCT

Stargardt's disease and fundus flavimaculatus are variants of the same hereditary disease that affects the retinal pigment epithelium (RPE) and photoreceptor layer [105–108]. Because the faulty gene involved has a central role in photoreceptor function, these diseases manifest themselves clinically in the retina. The general course of Stargardt's disease and fundus flavimaculatus is a slow loss of central vision, resulting in central atrophy and thus loss of central visual function [109–114]. Loss of visual acuity (VA) depends on the patients' age at first presentation of disease. The likelihood of severe visual loss is considerably less in older patients

[109, 110]. Some have noted a more pernicious course of fundus flavimaculatus [111].

It is generally accepted that mutations in the photoreceptors lead to Stargardt's disease/fundus flavimaculatus, in addition to a pathologic RPE. Thus, from a clinical viewpoint, one of the most important clinical aspects of the disease, besides the RPE, is the assessment of photoreceptor function as a parameter of the patient's central visual function. The latter is particularly important in performing everyday tasks, such as reading and writing, independently. As in age-related macular degeneration, the handicap of these functions can have a significant effect on quality of life [115]. Also, it is an indirect indicator of the patient's prognosis.

Fundus autofluorescence is generally accepted as the most effective method for ascertaining Stargardt's disease— in particular, the extent of the condition [116–118]. Conventional studies with fluorescein angiography, visual field, and ERG have been performed and can provide additional useful information [119–123]. As for other imaging techniques, microperimetry [124] and OCT have been used in various macular dystrophies [125–128].

Ultrahigh-resolution optical coherence tomography (UHR-OCT) is a recent development of the well-established OCT technology. It is noted for its superior axial resolution ($3\ \mu\text{m}$) over standard-resolution $10\text{--}15\ \mu\text{m}$ OCT technology [22, 85, 96]. Although some macular dystrophies have been examined with conventional OCT [125–128], to our knowledge, there have been no studies published investigating patients with Stargardt's disease. The purpose of this study was to examine whether UHR-OCT can visualize and quantify transverse photoreceptor loss, in particular focal loss, and compare this with the patient's VA. It is already known that OCT images correlate well with histologic cross sections of the retina in animal experiments [22, 85, 96, 129].

Methods. Fourteen patients (nine women, five men; average age, 39 ± 8 years; range, 27–53) with Stargardt's disease participated in the study. In all cases, the disease had been diagnosed within the past 3 years at the Medical Retina Department of the Medical University of Vienna's Department of Ophthalmology, and was confirmed with electroretinography (to rule out other potential dystrophies). One patient had had laser treatment for choroidal neovascularization in her left eye 3 years ago. This eye was therefore not included in the study. All the investigations followed the tenets of the Declaration of Helsinki, and written informed consent was obtained from all subjects in the study after the nature and possible consequences of the study had been explained. The ethics committee of the Vienna University School of Medicine approved the study.

All patients had a full ophthalmic examination, including bestcorrected Snellen VA, biomicroscopy, applanation tonometry, and funduscopy. Furthermore, for fundus autofluorescence, a confocal scanning laser ophthalmoscope (Heidelberg Retina Angiograph [HRA]; Heidelberg Engineering GmbH, Heidelberg, Germany) was used. An argon blue laser (488 nm) was used to excite lipofuscin, and macular autofluorescence was detected in a spectrum above 500 nm. The maximum transverse diameters of the autofluorescent area were measured

with HRA standard software.

Digital fluorescein angiograms were performed in all patients. The maximum transverse diameter of atrophy seen on fluorescein angiography was calculated. This was performed with a scale that was obtained with a Gullstrand-type model eye with laser-etched scale of concentric half circles in the center of an artificial fundus [130]. The innermost half-circle had a true diameter of 4 mm. Thus, having measured the value of this innermost half-circle on the computer screen (the 4-mm diameter had a value of 10 mm on the screen), we calculated the maximum transverse amount of atrophy.

UHR-OCT scans were performed with a set grid of B-scans covering the whole foveal region. The cross section with minimal retinal thickness was assumed as the central UHR-OCT scan so that scan acquisition was independent of patients' fixation. The assumption that the minimal retinal thickness is at the fovea may introduce a slight error in patients with Stargardt's disease, because atrophy of the macula may not affect all areas equally. Central foveal thickness was obtained by measurement of the amount of pixels in depth and multiplying it with $1.38 \mu\text{m}/\text{pixel}$ (i.e., the spacing of depth-sampling points), assuming a group refractive index of the human retina of 1.4 for conversion of optical to geometric thicknesses.²⁵⁻²⁸ The extent of transverse photoreceptor loss in the UHR-OCT images was measured in each patient on the same horizontal scan through the center of the fovea that was used for central foveal thickness measurements, employing a freeware medical imaging software program created at the University of Geneva (OSIRIS, ver. 4.18; available at www.idoimaging.com) [131]. The transverse extent of PR loss was measured manually. The system calculated the number of pixels, which then had to be normalized, since transverse UHR-OCT scanning pattern sizes varied among the different patients. These normalized pixel values were multiplied by the transverse pixel spacing of $10 \mu\text{m}$ (6-mm transverse OCT scans with 600 A-scans), to obtain the absolute transverse extent of photoreceptor loss (table 3.1).

Statistical calculations were performed on computer (SPSS for Windows, ver. 11.5.0; SPSS Sciences, Chicago, IL). The Spearman ρ rank correlation test and a logistic regression analysis of covariance (ANCOVA) was used to assess the influence of photoreceptor loss on VA. Of the 14 patients, 10 had central atrophy, and the results of these patients were correlated with VA, transverse photoreceptor loss, and maximum transverse diameter of autofluorescence. All probabilities are results of two-tailed tests. The chosen level of statistical significance was $P \leq 0.05$.

Results. The median VA was Snellen 0.4 (20/50; range, 0.05–1.25 [20/400–20/15]) for the right and 0.4 (20/50; range, 0.02–1.25 [20/1000–20/15]) for the left eye. Table 3.1 shows VAs, the amount of transverse PR loss, and central foveal thickness in each patient examined. The mean transverse PR loss was $4390 \pm 2270 \mu\text{m}$ (range, 530–9240).

Angiographically, 4 patients had hyperfluorescent pisciform lesions (flecks) without central atrophy. Ten patients had a central atrophy of various sizes or bull's-eye lesions and flecks. The choroid remained dark in all patients with

Name	Sex	Age	VA RE	VA LE	Transverse PR loss RE (in μm)	Transverse PR loss LE (in μm)	Central foveal thickness RE (in μm)	Central foveal thickness LE (in μm)
MA	m	32	20/50	20/50	4320	4710	69	41
CB	f	33	20/100	20/100	5300	4940	62	38
DD	m	53	20/400	20/100	6060	8550	135	91
BF	f	47	20/20	20/1000	530	not performed ¹	280	not performed ¹
JH	m	44	20/25	20/20	2310	3200	158	192
SK	f	42	20/100	20/50	5650	5490	63	78
AK	f	31	20/15	20/15	1020	1700	248	234
SP	f	29	20/22	20/33	4110	3900	114	93
EP	f	28	20/200	20/100	2900	6300	58	49
RR	m	41	20/200	20/20	4380	3440	62	70
ER	f	42	20/20	20/20	1280	1070	242	262
RS	m	50	20/100	20/40	5320	8400	97	107
PS	f	27	20/22	20/25	4420	4090	77	72
RW	f	46	20/28	20/125	5980	9240	72	96

Table 3.1: Visual acuity, transverse photoreceptor loss and central foveal thickness in patients with Stargardt's disease (SD) fundus flavimaculatus (FF).: ¹laser treatment for CNV

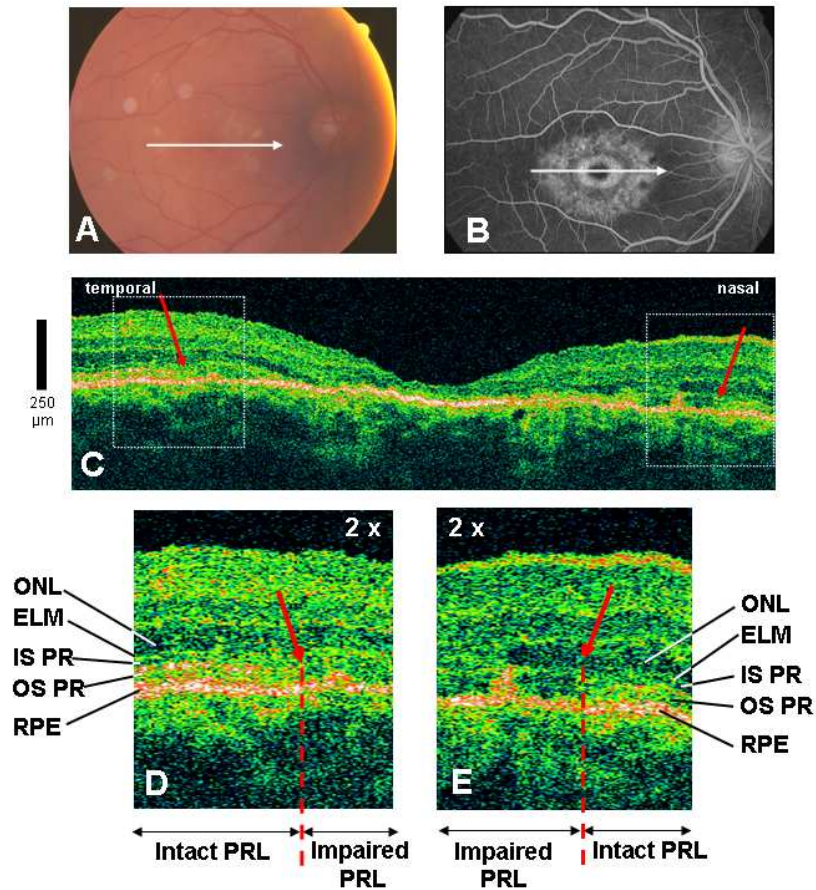


Figure 3.35: Patient with Stargardt's disease: A, colour fundus photograph; B, Ultrahigh-resolution optical coherence (UHR OCT) tomographic image; C, Late phase fluorescein angiogram indicating UHR OCT scan direction (arrow); D, E, 2-fold magnification of framed part of A show interface of intact and impaired photoreceptor layer area (red arrows). Transverse PR loss is $4320 \mu\text{m}$ resulting in 0.4 (20/50) VA. Central foveal thickness is $69 \mu\text{m}$. ONL: outer nuclear layer; ELM: external limiting membrane; IS PR: inner segment, photoreceptor layer; OS PR: outer segment, photoreceptor layer; RPE: retinal pigment epithelium.

Stargardt disease, as seen in fluorescein angiography (Figs. 3.35, 3.36). The mean extent of transverse atrophy seen on fluorescein angiography was $2985 \pm 1097 \mu\text{m}$ (median, 2800; range, 1100–4600). As for autofluorescence, the mean transverse diameter was $2118 \pm 1708 \mu\text{m}$ (median, 2285).

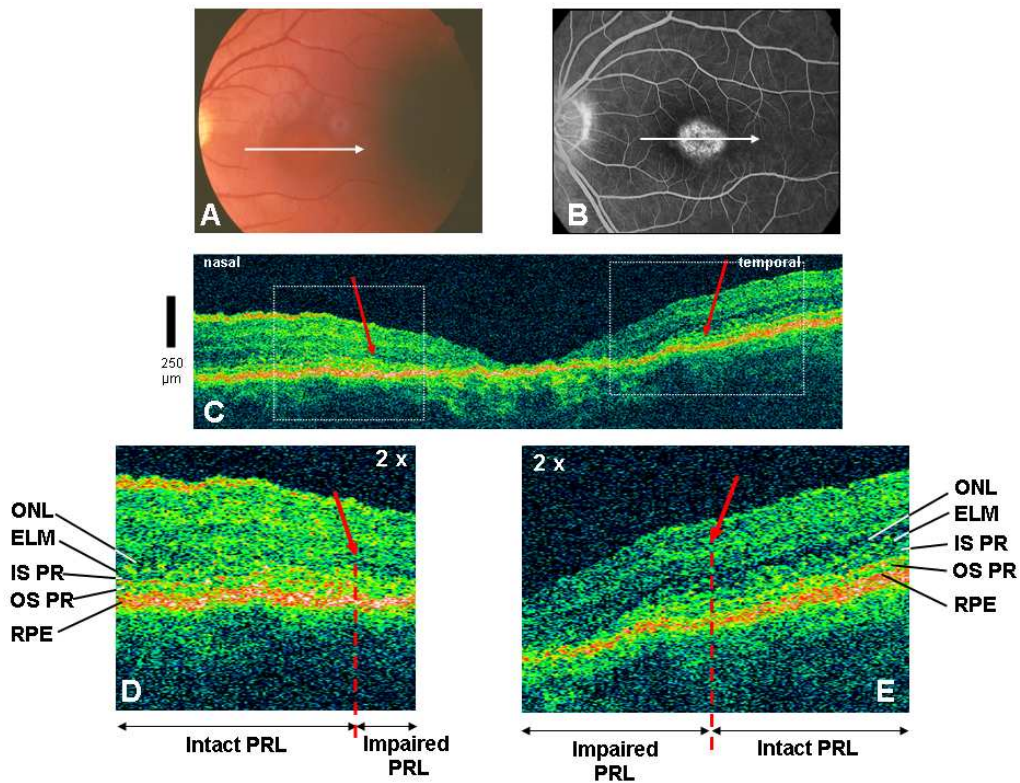


Figure 3.36: Patient with Stargardt's disease: A, colour fundus photograph; B, Ultrahigh-resolution optical coherence (UHR OCT) tomographic image; C, Late phase fluorescein angiogram indicating UHR OCT scan direction (arrow); D, E, 2-fold magnification of framed part of A show interface of intact and impaired photoreceptor layer area (red arrows). Transverse PR loss is $4940 \mu\text{m}$ resulting in 0.2 (20/100) VA. Central foveal thickness is $38 \mu\text{m}$. ONL: outer nuclear layer; ELM: external limiting membrane; IS PR: inner segment, photoreceptor layer; OS PR: outer segment, photoreceptor layer; RPE: retinal pigment epithelium.

UHR-OCT showed an excellent visualization of all major intraretinal layers—in particular, of the inner and outer segments of the photoreceptor layer - and thus, the extent of transverse photoreceptor loss. Figure 3.35C depicts a horizontal, cross-sectional, foveal UHR-OCT tomogram of the right eye of a 32-year-old patient with Stargardt's disease. Figures 3.35C and 3.35B indicate the location of the performed scan on the corresponding color fundus photograph and fluorescein angiogram. UHROCT revealed a large central transverse defect in the photoreceptor layer (defined by red arrows) and a general atrophy of all intraretinal layers. Figures 3.35D and 3.35E show two-fold enlarged views of the interface of the intact and impaired photoreceptor layer, clearly depicting the discontinuation of the signal bands corresponding to the inner (IS PR) and outer (OS PR)

photoreceptor segments. The mean transverse defect in this case was $432\ \mu\text{m}$, Snellen VA of 0.4 (20/50). Central foveal thickness was measured by UHR-OCT at $69\ \mu\text{m}$.

Figure 3.36C shows a horizontal, cross-sectional UHR-OCT tomogram of the left eye of a 33-year-old patient with Stargardt's disease. Figures 3.36A and 3.36B indicate the location of the performed scan on a color fundus photograph and fluorescein angiogram. Figures 3.36D and 3.36E show enlarged views of the interface of the intact and impaired photoreceptor layers. UHROCT clearly visualized significant atrophy of the intraretinal layers (comparable to Figure 3.35C), with a central foveal thickness of $38\ \mu\text{m}$. The transverse PR loss was more pronounced ($4940\ \mu\text{m}$), however, and the corresponding VA was worse (0.2 [20/100]).

Patients without central atrophy had an intact central PR layer, but had parafoveal defects. Figure depicts a horizontal, cross-sectional UHR-OCT tomogram of the right eye of a 42-year-old patient. Figures 3.37C 3.37A and 3.37B

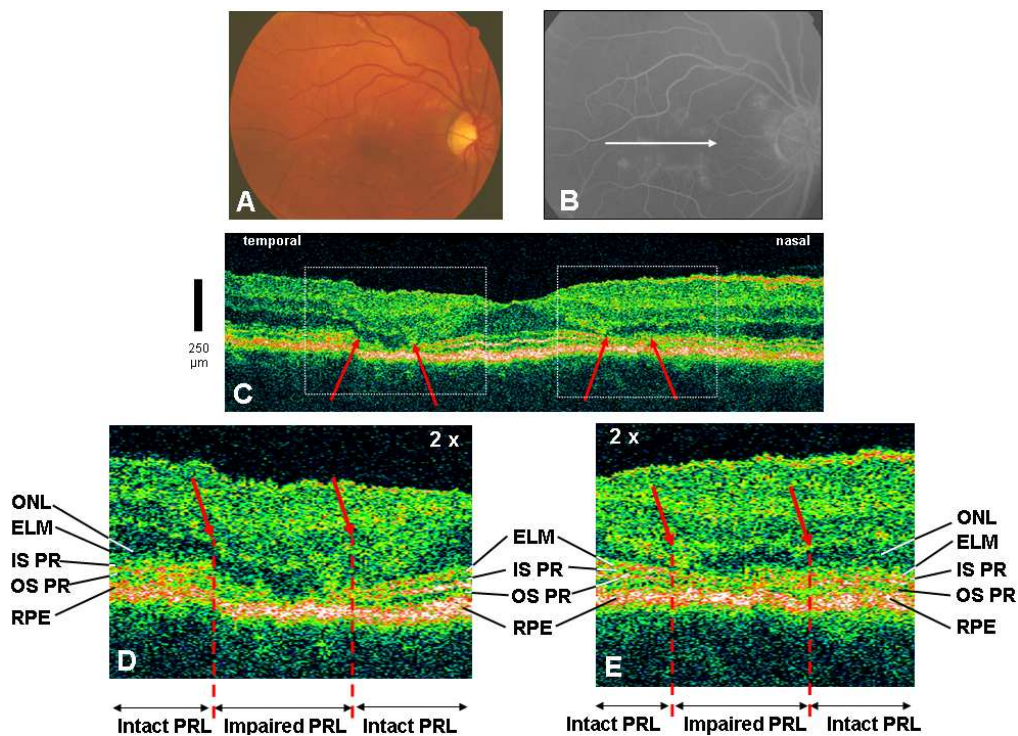


Figure 3.37: Patient with Stargardt's disease without central atrophy: A, A, colour fundus photograph; B, Ultrahigh-resolution optical coherence (UHR OCT) tomographic image; C, Late phase fluorescein angiogram indicating UHR OCT scan direction (arrow); D, E, 2-fold magnification of framed part of A show areas of focal transverse photoreceptor layer losses (red arrows). Total transverse PR loss is $1280\ \mu\text{m}$ resulting in 1.0 (20/20) VA. Central foveal thickness is $242\ \mu\text{m}$. ONL: outer nuclear layer; ELM: external limiting membrane; IS PR: inner segment, photoreceptor layer; OS PR: outer segment, photoreceptor layer; RPE: retinal pigment epithelium.

indicate the location of the performed scan on a color fundus photograph and

fluorescein angiogram. UHR-OCT visualizes intact intraretinal layers, and a corresponding central foveal thickness of $242 \mu\text{m}$, with 1.0 (20/20) VA. Parafoveally, UHR-OCT reveals two areas with focal transverse PR losses (fig. 3.37C, defined by arrows). Figures 3.37D and 3.37E show enlarged views of areas of focal transverse photoreceptor layer loss. The total transverse PR loss was $1280 \mu\text{m}$. The corresponding angiogram showed typical pisciform lesions corresponding to fundus flavimaculatus (fig. 3.37B).

Statistically, a correlation was seen between VA and transverse photoreceptor loss in patients with Stargardt's disease (Spearman $\rho = -0.60$, $P = 0.03$). A linear regression model for VA and photoreceptor loss showed a highly significant result ($R^2 = 0.49$, $P = 0.0001$; fig. 3.38). There was also a statistically significant correlation between VA and the amount of atrophy seen in fluorescein angiography (Spearman $\rho = -0.51$, $P = 0.007$) as well as with the transverse diameter of fundus autofluorescence (Spearman $\rho = -0.72$, $P = 0.008$).

The mean central foveal thickness was markedly reduced ($85 \pm 40 \mu\text{m}$) in patients with Stargardt's disease. Central foveal thickness did not correlate with transverse PR loss (Spearman $\rho = -0.23$, $P \gg 0.05$) but did correlate with VA (Spearman $\rho = 0.43$, $P = 0.04$). Linear regression analysis, however, showed a statistically significant association between central foveal thickness and VA ($R^2 = 0.51$, $P = 0.0001$). There were no correlations with the amount of atrophy or with the extent of fundus autofluorescence ($P \gg 0.05$); but, on linear regression, there was a statistically significant association ($R^2 = 0.32$, $P = 0.005$; $R^2 = 0.37$, $P = 0.05$).

Transverse photoreceptor loss correlated highly with central atrophy on fluorescein angiography (Spearman $\rho = 0.77$, $P = 0.0001$) and with the extent of fundus autofluorescence (Spearman $\rho = 0.77$, $P = 0.003$).

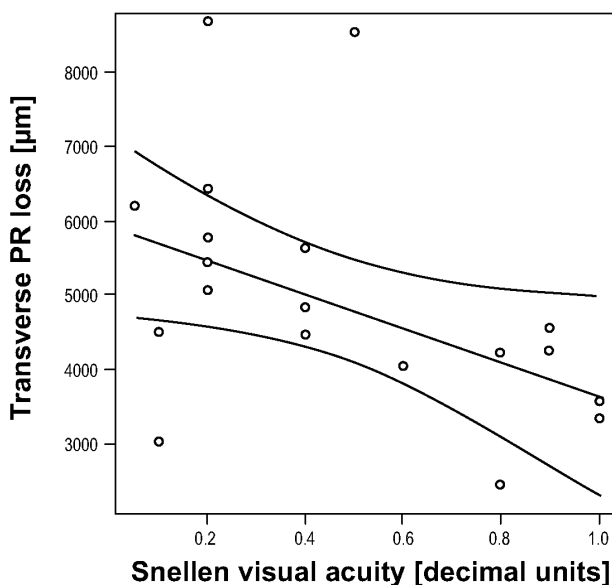


Figure 3.38: Linear regression graph with 95% confidence intervals between visual acuity and transverse photoreceptor loss.

Discussion. This study demonstrates, for the first time, in vivo visualization and quantification of the photoreceptor layer and correlation of transverse PR loss with VA. using UHR-OCT. Thus, this represents a novel approach in the assessment of central visual function.

The amount of PR loss correlated negatively with the patients' VAs. It did not, however, correlate with foveal thickness. In our opinion, this implies that, even with severe intraretinal layer atrophy, VA could be relatively well preserved with an intact photoreceptor layer. Possibly, the lack of correlation is also the result of Stargardt's disease patients who have clinically end-stage disease and thus very little foveal thickness (which has a finite value – i.e., can only be reduced to an absolute minimum), but still large defects in the PR layer. However, there is a significant correlation of PR loss with the extent of fundus autofluorescence and atrophy on fluorescein angiography, which would confirm the intimate relation between pigment epithelial and photoreceptor changes.

Among the macular dystrophies, Stargardt's disease, first described in 1909 by Karl Stargardt [105], is considered to be the most common. Some investigators believe that it makes up to 7% of all macular dystrophies [132]. Generally, patients have a slow loss of VA that usually bottoms out at 20/200, although the amount of visual loss depends on the initial time of presentation of the patient [110, 112]. Although it is morphologically different, it is generally accepted that fundus flavimaculatus, first described by Franchesetti [107] and Stargardt's disease have a joint genetic background. Stargardt's disease is generally autosomal recessive and is caused by changes within the ABCA4 gene [133]. This gene is found in both cone and rod outer segments, and acts as a flippase enzyme for Nretinylidene phosphatidylethanolamine (N-RPE), which acts as a precursor for A2E. This in turn is a precursor of lipofuscin. The ABCA4 gene is highly polymorphic and occurs in both recessive and dominant forms [134]. Not all sequence changes necessarily lead to the disease, but various phenotypes are possible, and clinical expression varies [131, 134, 135]. UHR-OCT offers a novel, noninvasive approach to visualizing and quantifying the photoreceptor layer objectively in real time. Image acquisition is quick and causes no discomfort to the patient, which represents an important clinical advantage. Furthermore, the advantage of the UHR-OCT system, in comparison to conventional OCT systems, is its superior axial resolution of $3\ \mu\text{m}$, in comparison to commercially available OCT systems with $10\ \mu\text{m}$ (StratusOCT; Carl Zeiss Meditec). The quality of the imaging is comparable to conventional histopathology [22, 85, 129]. Obviously, from a pathophysiological viewpoint, a more detailed assessment of the RPE would be very relevant in treating this disease; however, this requires a further increase in axial resolution not available now.

In conclusion, UHR-OCT allows quantitative in vivo assessment of the photoreceptor layer in patients with Stargardt's disease and correlates it with VA. UHR-OCT can also be of use in elucidating the health of the photoreceptor layer in Stargardt's disease, based on the extent of transverse PR loss, particularly in those cases where central atrophy is absent. This is of particular relevance, because as seen in this study, changes in autofluorescence (i.e., RPE changes) do not necessarily reflect on photoreceptor health immediately. Therefore, in the

future, UHR-OCT could provide important, adjunct diagnostic information to assess the prognosis of a patient with Stargardt's disease.

3.6 Adaptive optics ultrahigh resolution optical coherence tomography

The axial resolution in OCT is given by the bandwidth of the light source. The lateral resolution is determined by the numerical aperture (NA) of the imaging

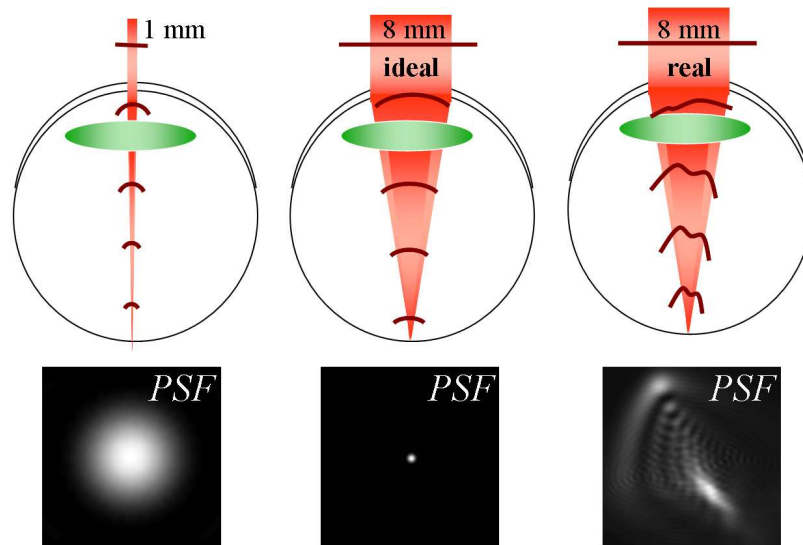


Figure 3.39: Point spread functions for different beam diameters. Left: Diameter of the probing beam is 1 mm. Aberrations of the eye have nearly no influence to the wave front, wherefore the point spread function in the retina is little affected. Middle: In an ideal eye without spherical aberrations a 8 mm probing beam diameter would result in a $1.5 \mu\text{m}$ spot in the retina, leading to higher transverse resolution. Right: In the real case the aberrations of the eye affect the wave front of the probing beam, resulting in a distorted point spread function.

optics. In the case of ophthalmic measurements, cornea, and lens are part of the imaging optics and therefore their aberrations to the wave front of the probing beam have to be considered. In ophthalmic UHR OCT measurements the transverse resolution is typical $\sim 15\text{--}20 \mu\text{m}$, corresponding to a beam diameter of 1 mm entering the eye. In a diffraction-limited eye, a 8-mm-diameter beam (with a center wavelength of 800 nm) would produce a theoretical spot size of $1.5 \mu\text{m}$. However, in practice, for large pupil diameters, monochromatic aberrations of the eye [136] blur the retinal images (see fig. 3.39). Although the axial resolution of ophthalmic OCT has been improved dramatically, the transverse resolution is still limited to $\sim 15 - 20 \mu\text{m}$ in retinal UHR OCT tomograms because of the small beam diameter (1 mm) used so far.

A way to overcome this limitation is the use of adaptive optics (AO) [137–141]. The basic idea is to measure the aberrations of the wave front and to correct for them with a correcting device as a deformable mirror, which compensates

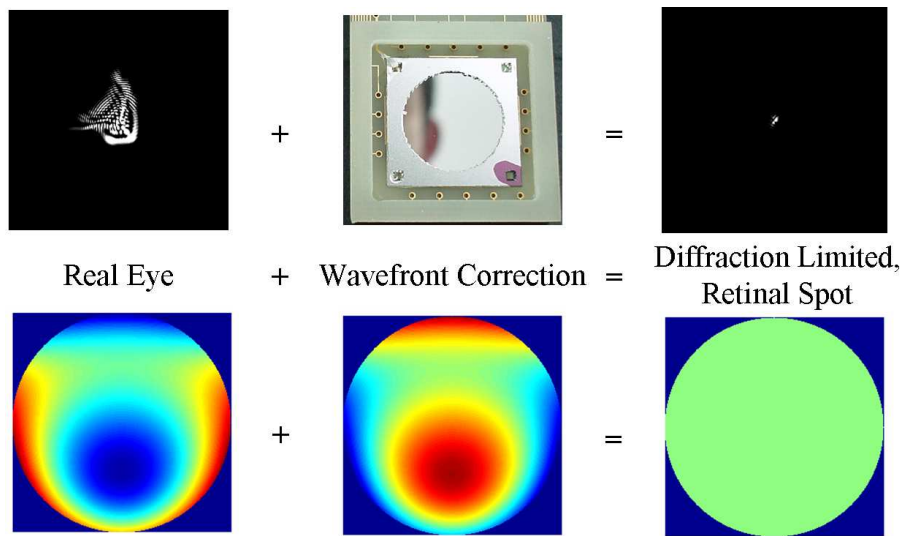


Figure 3.40: Principle of wave front correction. The aberrations of the eye are corrected with a deformable mirror by introducing the opposite aberrations, resulting in a near diffraction limited spot.

the spherical aberrations of the beam by introducing the opposite aberrations (see fig. 3.40). This technique has originally been applied in astronomy for the compensation of aberrations introduced by turbulences in the earth's atmosphere. The wave front is measured with a Hartmann-Shack sensor [142], which consists essentially of a microlens array with a camera located in the focal plane. A plane wave will produce a regular dot matrix pattern in the camera. In the presence of aberrations the dots will shift to different positions. From the shifted dot matrix the aberration of the wave front can be calculated, naturally in terms of Zernike polynomials⁷ [143].

In order to test the usability of AO in combination with OCT, an AO system was interfaced with an ophthalmic UHR OCT setup. The work was performed in collaboration with the University of Murcia, Spain, with the coworkers P. Artal and E.J. Fernández.

A compact (300x300mm) closed-loop adaptive optics system [144], shown in figs. 3.41 and 3.42, based on a real-time Hartmann-Shack (HS) wave front sensor operating at 30 Hz and a 37-element low-cost micromachined membrane deformable mirror (OKO Technologies, Holland), was interfaced to a fiber optic, time domain UHR OCT system. The OCT system itself was based on a commercially available OCT 1 instrument (Carl Zeiss Meditec Inc., Dublin, Calif.), employing a compact Titanium:sapphire laser (Femtolasers Produktion GmbH, Vienna, Austria) with 130-nm optical bandwidth (at FWHM) centered at 800 nm. Both the fiber-optic interferometer and the optical components (L, fig. 3.42) of the AO and OCT system were designed to support the propagation of ultrabroad bandwidth light necessary to achieve ultrahigh resolution and to compensate for any polarization (PC, fig. 3.42) and dispersion mismatch (DC, fig. 3.42) between

⁷Zernike polynomials are a complete orthonormal base.

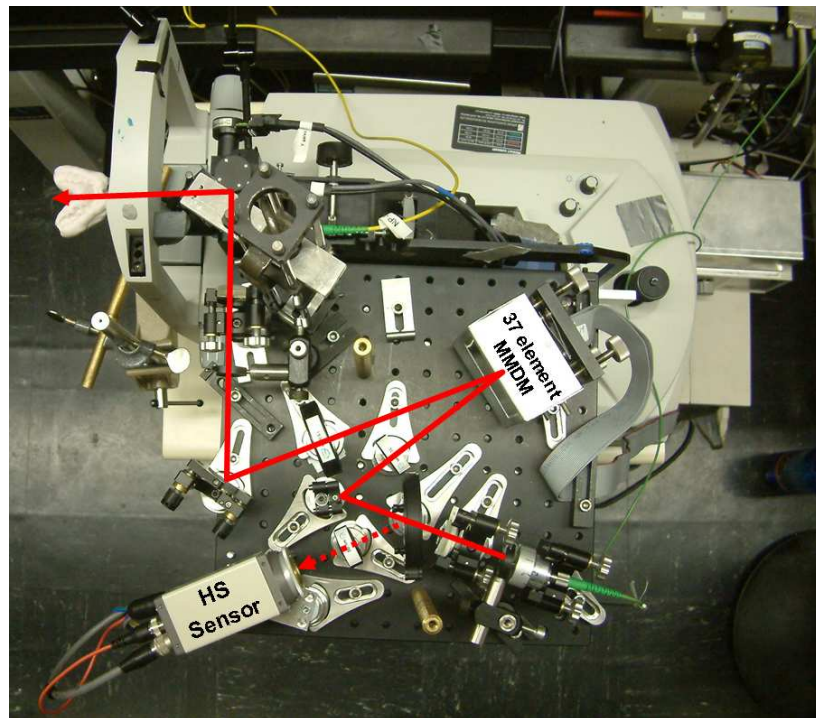


Figure 3.41: AO set-up. A bread board with a footprint of 30x30 cm was connected to an OCT fundus camera. The red line depicts the beam path.

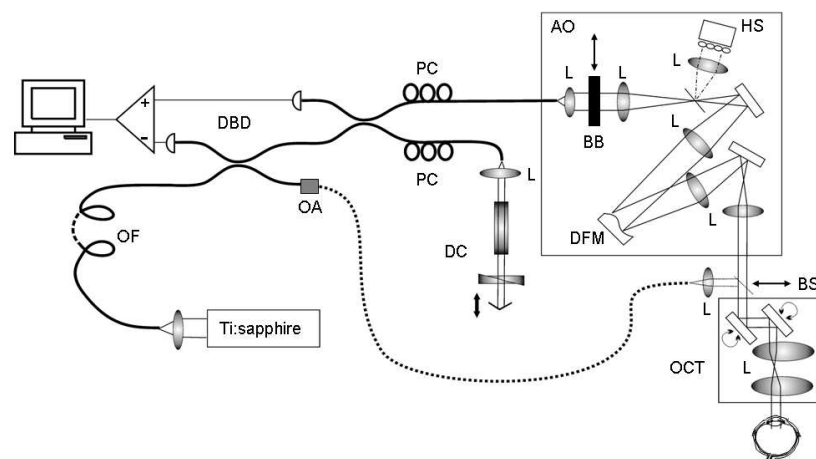


Figure 3.42: Adaptive optics ultrahigh resolution OCT system: AO: adaptive optics system, OCT: OCT system; Ti:sapphire: Titanium:sapphire laser; DBD: dual balanced detection; PC: polarization controller; OA: optical attenuator; OF: 100 meters optical fiber; DC: dispersion compensation; L: achromatic doublet lenses; BB: removable beam blocker; HS: Hartmann-Shack-sensor; DFM: deformable mirror; BS: removable beam splitter.

the sample arm - including AO and OCT system - and the reference arm of the interferometer.

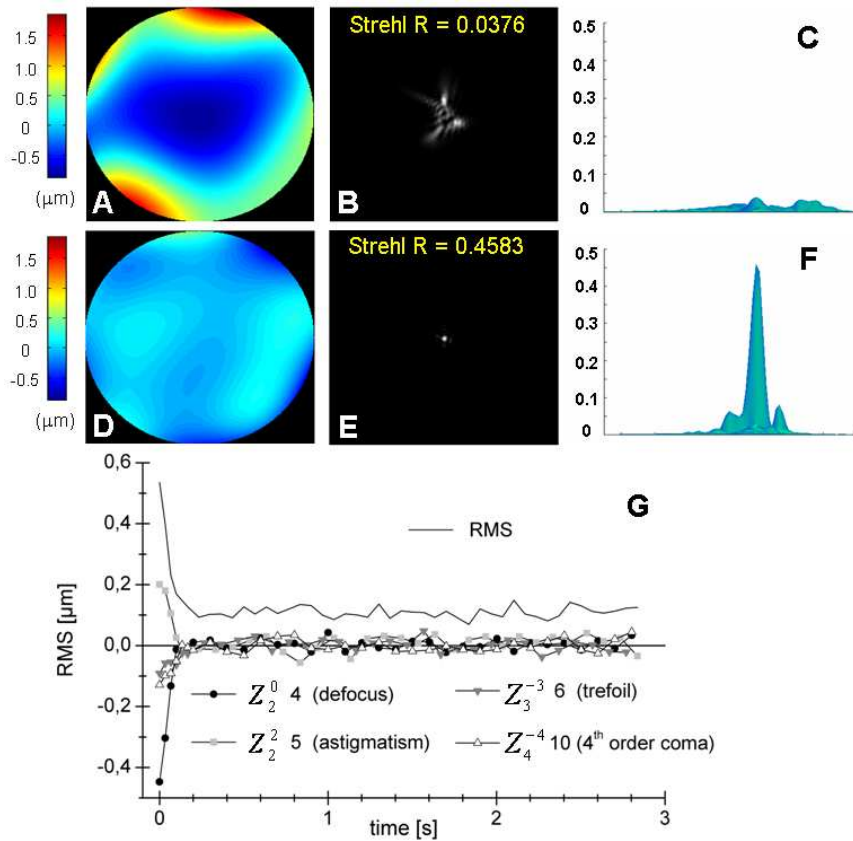


Figure 3.43: Wave front for the uncorrected (A) and corrected (D) case and the associated point spread functions (PSF) for the uncorrected (B, C) and corrected (E, F) cases are indicated. Evolution of the rms error (top, black squares) of the corrected wave front and representative Zernike coefficients as a function of time for the same subject (G). A residual uncorrected wave front of $\sim 0.1 \mu\text{m}$ for a 3.68 mm pupil diameter as well as a more than ten times improvement of Strehl ratio is achieved although employing broad bandwidth (130 nm) light.

The AO system was designed to conjugate the exit pupil of the eye onto the deformable mirror, into the Hartmann-Shack sensor, and into the fiber. The diameter of the measurement beam entering the eye was increased from 1 mm to 3.68 mm by changing the optical magnification of the OCT system. To keep the imaging planes during the measurement and correction of ocular aberrations, the distance of the investigated eye to the exit lens of the OCT was set properly and kept constant during the entire measurement procedure. Accommodation was paralyzed with tropicamide (mydriacyl, Mydriaticum Agepha). Since the OCT system uses an off-center illumination geometry, there were no back reflections from the lenses of the OCT system. To prevent back reflections from lenses of the AO into the Hartmann-Shack sensor, an attenuated probing beam that delivered $5 \mu\text{W}$ onto the eye was introduced at the entrance of the OCT system with

a removable beam splitter while the OCT-beam was blocked with a removable beam blocker. In this mode both the aberrations of the eye and those of the imaging optics were measured by the Hartmann-Shack sensor and corrected in a 30 Hz closed loop with the 37 element micro-machined deformable mirror. When the correction was achieved, the system was switched to the UHR OCT imaging mode by removing the beam blocker and the beam splitter. UHR OCT tomograms were acquired with corrected as well as uncorrected wavefronts with axial scan rates ranging between 125 Hz to 250 Hz using up to $800 \mu\text{W}$ incident optical power in the scanning OCT beam, well below the American National Standards Institute exposure limits.

Figure 3.43 shows a closed-loop correction of the aberrations in a normal subject using the AO UHR OCT system employing light centered at 800 nm with 130 nm optical bandwidth (FWHM) for the first time. The system was first set to compensate for refractive error of the subject. The wave front for the uncorrected (fig. 3.43A) and corrected (fig. 3.43D) situation and the associated point spread functions (PSFs) for the uncorrected (Figs. 3.43B and 3.43C) and corrected (Figs. 3.43E and 3.43F) case are indicated; aberrations were corrected up to the fifth order. Figure 3.43G depicts the evolution of the RMS error as well as exemplary aberrations (Z_2^0 , defocus; Z_2^2 , astigmatism; Z_3^{-3} , trefoil; Z_4^{-4} , 4th order coma aberration) as a function of time for the same subject [145]. These results show effective measurement and correction of lower and higher order aberrations despite the use of ultrabroad bandwidth light, with a residual uncorrected wave front of $\sim 0.1 \mu\text{m}$ for a 3.68 mm pupil diameter (see Figs. 3.43A and 3.43D). Strehl ratio improvements of a factor of more than 10 (Figs. 3.43B and reffig:InVivoAO02E) were achieved resulting in a significantly improved PSF profile (Figs. 3.43C and 3.43F).

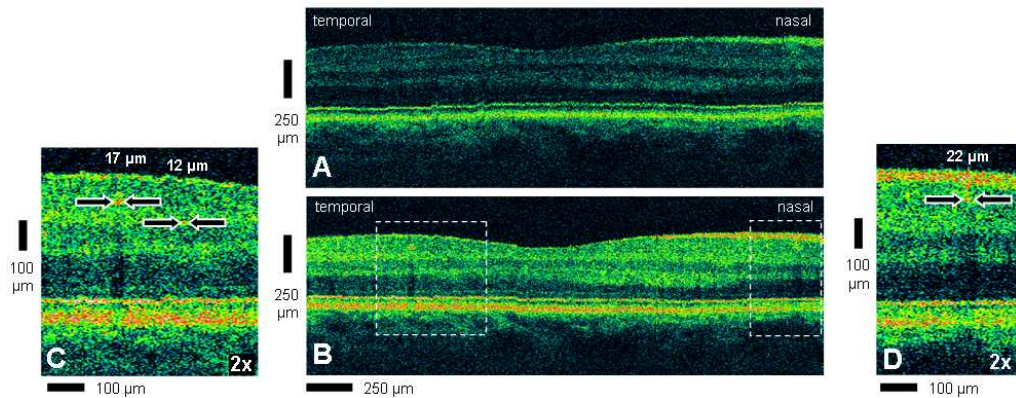


Figure 3.44: In vivo adaptive optics ultrahigh resolution OCT tomograms of a normal human eye in the foveal region for the uncorrected (A) as well as corrected (B) case (600 A-scans over a line of 2.8 mm, transverse sampling rate $\sim 5 \mu\text{m}$). Signal-to-noise improvement of up to 9 dB as well as $5\text{--}10 \mu\text{m}$ transversal in addition to $3 \mu\text{m}$ axial resolution could be achieved by wave front corrections introduced by a 3.68 mm diameter beam (B). Small features within the ganglion cell layer as well as inner plexiform layer, that might correspond to vessels with 12 to $22 \mu\text{m}$ diameter are clearly visualized in twofold enlargements (C, D).

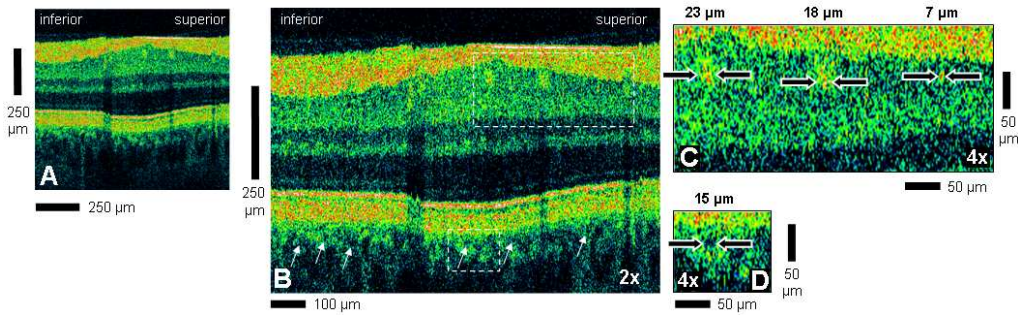


Figure 3.45: 4. Aberration corrected vertical adaptive optics ultrahigh resolution tomogram of a normal human eye in the parafoveal region across a line of 1.125 mm (600 A-scans, transverse sampling rate $\sim 2 \mu\text{m}$) The same proportions as used in Figure 3.44 A; (B) is a twofold enlargement of A. Intraretinal features probably corresponding to vessels with 7 to $23 \mu\text{m}$ diameter as well as $15 \mu\text{m}$ are clearly visualized in the ganglion cell and inner plexiform layer (fourfold enlargement, C) as well as in the choroid (D and arrows in B) indicating a transverse resolution in the order of 5–10 μm .

Figure 3.44 illustrates the effect of aberration correction in UHR OCT, depicting cross-sectional AO UHR OCT tomograms of a normal human eye in the foveal region across a transverse line of 2.8 mm (600 A-scans, lateral spacing $\sim 5 \mu\text{m}$) for the uncorrected (fig. 3.44A) as well as corrected (fig. 3.44B) case. Small features within the ganglion cell as well as inner plexiform layer that might correspond to vessels with 12–22 μm diameter are clearly visualized in the twofold enlarged views (Figs. 3.44C and 3.44D). A significant improvement in the signal-to-noise-ratio (SNR) of up to 9 dB is clearly visible, yielding a slightly better sensitivity (44 dB in the tomogram) as achieved with standard UHR OCT (42 dB). The clear visualization of all major intraretinal layers indicates that the axial imaging resolution of 3 μm could be preserved.

In Figure 3.45 an aberration corrected vertical AO UHR OCT tomogram in the parafoveal region across a line of 1.125 mm (600 A-scans, transverse sampling rate $\sim 2 \mu\text{m}$) is depicted. The proportions in Figure 3.45A are the same as in Figure 3.44A; Figure 3.45B shows a twofold enlargement. Intraretinal features probably corresponding to vessels with 7–23 μm as well as $15 \mu\text{m}$ are clearly visualized in the ganglion cell and inner plexiform layer (see fourfold enlargement in Figure 3.45C) as well as in the choroid (see Figure 3.45D and arrows in Figure 3.45B). These results clearly indicate an achieved transverse resolution of 5–10 μm . This is an improvement of two to three times compared with the UHR OCT systems used so far that employed a 1-mm beam diameter without AO [22]. The uncorrected tomograms should not be compared to tomograms obtained with standard UHR OCT systems, i.e. systems without AO, because the diameter of the beam entering the eye is about four times larger in the present study, and therefore the aberrations of the eye decrease UHR OCT image quality. Assuming a Gaussian beam profile, 5–10 μm transverse resolution at 800 nm central wavelength should theoretically result in ~ 50 –200 μm depth of field, defined as two times the Rayleigh range. In practice, the actual depth of field useful in OCT tomograms is larger than this theoretical value [21].

In conclusion, we demonstrated that AO can be interfaced to UHR OCT, based on broad bandwidth (130 nm FWHM) state-of-the-art laser technology, by maintaining the performance of both techniques compared with using them as stand alones. Therefore in vivo AO UHR OCT imaging of the normal human retina could be demonstrated with $3\ \mu\text{m}$ axial and $5\text{--}10\ \mu\text{m}$ transverse resolution. In addition to improved visualization capabilities, significant UHR OCT tomogram SNR improvements could be obtained. Further improvements of transversal resolution are limited by the approach of the present study to employ a relatively low-cost 37 element micromachined membrane deformable mirror. On the basis of the presented results of this study, however, three-dimensional visualization of retinal features, such as photoreceptors, ganglion cells, or capillaries, by interfacing ultrahigh resolution OCT to AO using corrector devices with improved performance.

Chapter 4

Three-Dimensional Ophthalmic Ultrahigh Resolution OCT

4.1 Data acquisition

In FD the reference mirror stays at a fixed position. The whole A-scan is performed in a single measurement using a CCD camera. This allows for faster scanning of the whole tomogram compared to TD OCT and avoids non-linearities. State-of-the-art CCD cameras allow for line read out rates - equivalent to OCT scanning rates - of 30 kHz and more. This faster scanning ability on one hand allows for three-dimensional measurements with almost no motion artifacts within one B-scan. On the other hand the amount of data which has to be stored is multiplied - the data set for one three-dimensional tomogram is in the range of 250 Mb. Without recent development towards fast and large hard disk drives the data handling would have been impossible.

For data storage of three dimensional data, a custom binary data format was utilized. Prior to the data a 40 byte header contains information about the size of each frame, and the data format. The data itself is stored sequentially. The storage policy was the same as in the TD case - the read out data from the spectrometer was directly stored without any processing.

The envelope generation in FD is quite different to TD. After a remapping of the spectrogram to equidistant frequencies, subtraction of the background, a fourier transform is applied in order to obtain the spatial information of the imaged specimen.

4.2 Signal processing

Remapping The FDOCT data post processing involves a Fourier transform to obtain the spatial information of the scatterer's locations in the sample under investigation, which is encoded in the spectrogram. The relation between frequency

and wavelength depends on the geometrical properties of the spectrometer. In the ideal case the wavelength scale is linear.

An algorithm was written in matlab to calculate an approximate remapping $\lambda \rightarrow \nu$, which is based on energy minimization with a dynamic threshold (“flood algorithm”). As energy term an image sharpness value is calculated, which es-

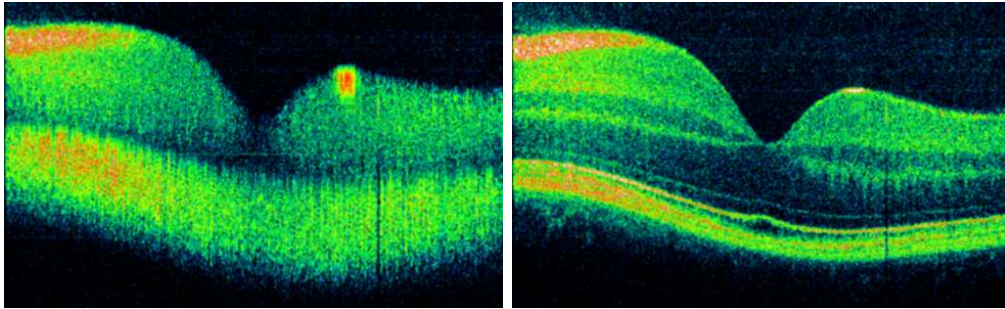


Figure 4.1: Fourier transformation of the spectrometer data: without (left) and with remapping (right).

entially is the negative maximum value in the image divided by the standard deviation. This method maximizes the highest value in the tomogram and simultaneously minimizes the standard deviation. This is appropriate for images, which contain sharp features, as they are present in OCT images.

The starting assignment is stochastically varied, followed by energy evaluation of the tomogram, obtained with the new assigned parameters. If the new calculated energy is within a permitted range, the new set of parameters is used for the next iteration, otherwise it is dismissed. Figure 4.1 shows the macula of a healthy subject without remapping (left), and with remapping (right) as calculated by the algorithm. Without remapping the spatial information is broadened and the intraretinal layers can not be distinguished.

Motion artifacts In FD the measurement time for one B-scan is several milliseconds; the main motion artifact appear as a positional offset between B-scans. To account for this artifact, the choroid-RPE order as a relatively easy detectable boundary has to be identified within all B-scans of the volume, whereon the B-scans are shifted accordingly. Figure 4.2 shows an example of axial displaced tomograms as measured from a patient with serous RPE detachment. The top row shows three exemplary tomograms with a spacing of approximately $250 \mu\text{m}$, taken out of a volume data set consisting of 60 tomograms. The red line indicates the detected boundary. As a measure of the positional offset between the B-scans the median for each boundary is calculated. The bottom row shows the same tomograms after axial shifting by the calculated offsets, clearly showing an improved axial alignment among the B-scans.

3D Rendering Three-dimensional imaging requires a proper visualization of the data to enable a clear insight of the investigated tissue. 3D rendering requires a lot of computing power and very specialized programming knowledge. Existing

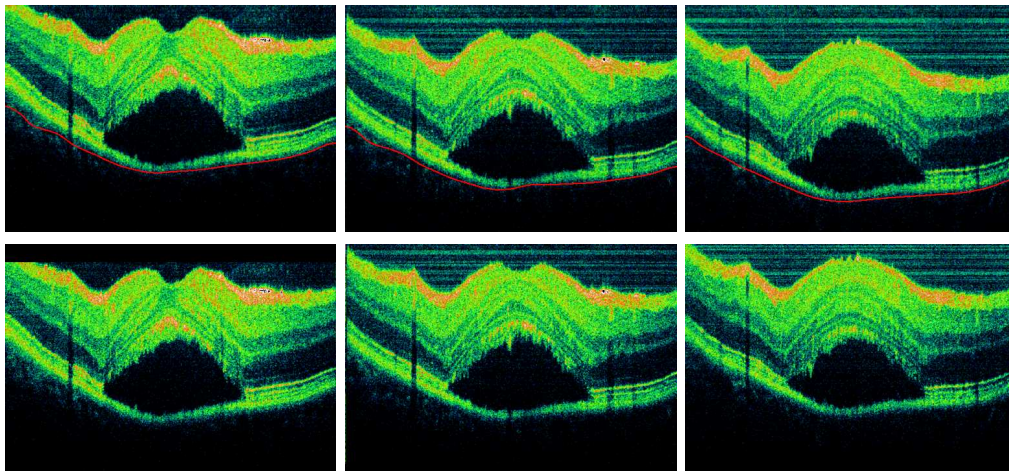


Figure 4.2: Motion artifacts in FDOCT measurements. The figure shows the detection of the approximate RPE in a tomograms taken from a patient with serous RPE detachment. Top: tomograms with a spacing of $\sim 250 \mu\text{m}$ show a clear axial shift. The red line indicates the RPE boundary detected by the algorithm. Bottom: same tomograms after axial sift according to the median of the detected red line.

3D-rendering software is available, partly free, partly commercial. In the medical environment ImageJ is a common public domain software tool, written in the Java language and therefore mostly independent of the operating system, distributed by the NIH¹. It contains a wide range of image processing functions, including basic 3D render routines. Its usability for processing of 3D UHR OCT was evaluated [146].

The user interface is relatively simply, but with some practice easy to operate. There are two major drawbacks:

- Rendered animations can be rotated around only one axis. For visualization of 3D features a free adjustable rotation is desirable.
- The rendered surface looks very dim, because a possibility to apply spotlights is not realized.

On the other hand, ImageJ is very powerful in working with stacks of images, i.e. reslicing stacks or calculating projections in x , y or z direction with arbitrary pixel spacing, calculating profiles for lines or areas within an image etc. ImageJ is a powerful tool for analyzing images, despite the limitations in 3D rendering.

Much better results were obtained with Cinema4D², a commercial rendering software (see fig. 4.3). The usability of this program for visualization of 3D UHR OCT data was evaluated and customized routines for image processing using Cinema4D were developed in collaboration with S. Binder and C. Glittenberg from the Ludwig Boltzmann Institute for Retinology and Bm. Laser Surgery,

¹National Institutes of Health, USA, <http://rsb.info.nih.gov/ij>.

²Cinema 4D R9, Maxon Computer GmbH, Friedrichsdorf, Germany.

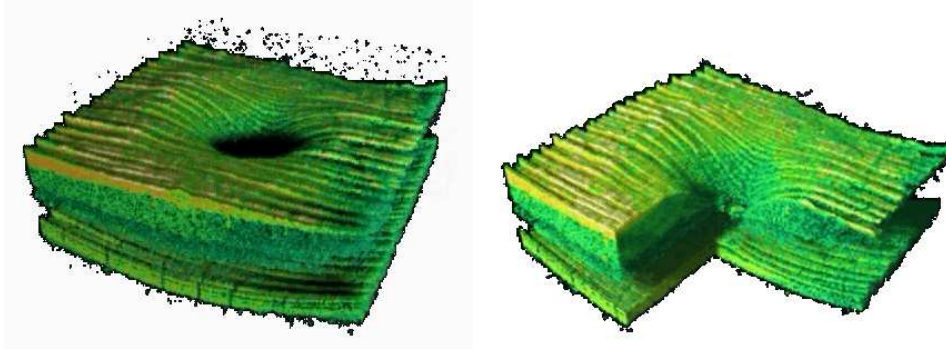


Figure 4.3: Two rendering examples produced with Cinema 4D of a normal and healthy human fovea. Left: Visualization of a complete data set (60 B-scans, each consisting of 1024×1024 points), covering an volume of $3 \times 3 \times 0.5 \text{ mm}^3$. Right: The same data set with an area cut out, allowing insights into the internal structure of the retina.

Rudolfstiftung, Vienna, Austria. Cinema4D allows free animation of all rendering parameters such as light, camera path, and arbitrary cuts, which has a great potential for interactive work in future developments.

Figure 4.4 shows a comparison of the render results obtained with ImageJ (B) and Cinema4D (D) on the example of a normal human fovea.

The major intraretinal layers are clearly visualized in the tomograms (fig. 4.4A) and also in the 3D rendering (fig. 4.4D). Compared to the two dimensional visualization a much better perception is obtained. The volume consists of 60 B-scans, each 1024×1024 points, covering a volume of $3 \times 3 \times 0.5 \text{ mm}^3$. Measuring time was 3 s . The separation between the B-scans is $50 \mu\text{m}$, whereas the pixel separation in axial and transversal direction within one B-scans is $3 \mu\text{m}$, leading to a detailed reproduction of the retinal morphology within single B-scans. A scanning protocol with 256 tomograms, each 256×1024 pixels, would lead to a more isotropic sampling, but the image quality would suffer from the decreased transversal pixel spacing. The chosen scanning protocol was a trade-off between imaging time, visualization detail within one B-scan and spacing between B-Scans. Intraretinal layers are resolved with ultrahigh resolution while the imaging time for patients was kept acceptable. Irregularities in the surface in figs. 4.3 and 4.4D are originating from the scanning mirrors.

Figure 4.4C depicts the projection of the whole stack of images into the z -direction (calculated with ImageJ), leading to an OCT fundus image. Any arbitrary cut in the 3D reconstruction can be correlated with the exact position in the fundus image due to the one-to-one correspondence.

Figure 4.5 shows isotropic sampled en-face reconstructions from a stack of $512 \times 512 \times 1024$ pixels, produced with ImageJ. The measurement time of 10 s is unacceptable for patients, because motion artifacts will be dominant and the patient will not be able to fixate. This scanning protocol was only used on healthy subjects. In fig. 4.5A-C the central foveal depression, nerve fiber layer (white arrows in fig. 4.5A), as well as the vascular structure (white arrows in fig. 4.5C)

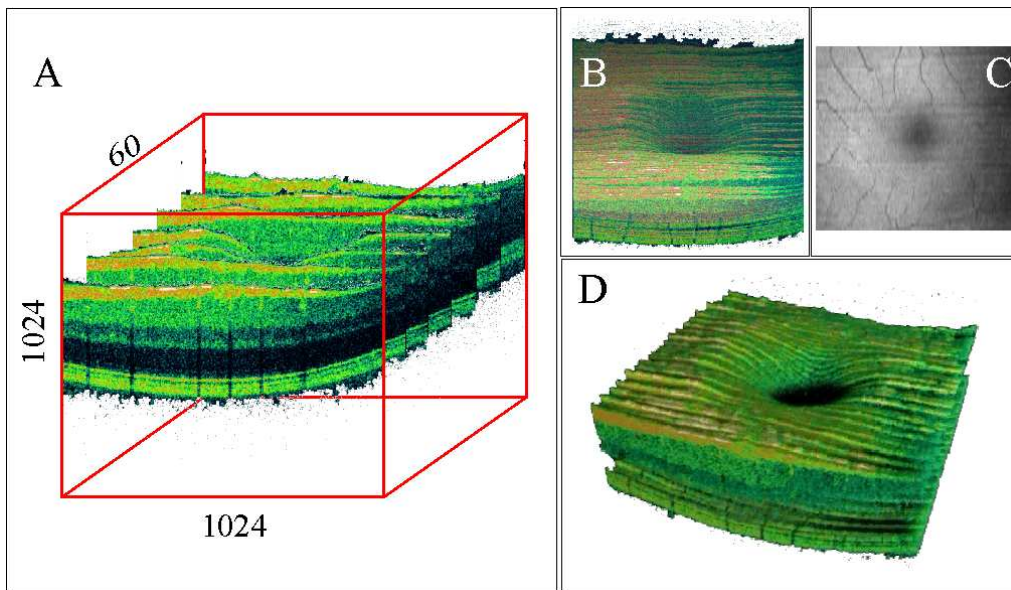


Figure 4.4: Imaging protocol for 3D UHR OCT. (A) The imaged stack consists of 60 tomograms with 1024x1024 pixels; (B) 3D rendering with ImageJ; (C) OCT fundus image produced with ImageJ by summarizing the intensity values in axial direction; (D) 3D rendering with Cinema4D.

are visible. In fig. 4.5D-F the very weak scattering ELM is depicted. Figure 4.5F-I shows the junction of the inner and outer photoreceptor layer (ISPR/OSPR in fig. 4.5F), the photoreceptor outer segments (OSPR in fig. 4.5F), and the retinal pigmented epithelium (RPE in fig. 4.5G). The white arrow in fig. 4.5H indicates shadowing due to vessels.

An example for a macular hole is shown in Fig. 4.6. The hole is formed by a detachment of the vitreous from the retina, resulting in a tractional force and following hole formation. The detached part of the central fovea is still connected to the vitreous and visible above the hole. The inner nuclear layer shows cystic changes (white arrows). Red arrows depict the impairment of the photoreceptors in the central foveal region.

Figure 4.7 demonstrates 3D UHR OCT in the foveal region composed from 60 tomograms, each consisting of 1024 A-scans with 1024 data points. Three-dimensional representation of the macular region is presented at different angled views (fig. 4.7A and B) with simultaneous fly through of B-scans (upper left corner) depicting the topography of the foveal depression as well as parafoveal. A virtual C-Scan system enables arbitrary horizontal removal of different retinal layers revealing morphologic information from inside the scanned volume at the level of the ganglion cell layer (fig. 4.7C), external limiting membrane level (fig. 4.7D), inner outer photoreceptor junction level (fig. 4.7E) as well as the retinal pigment epithelium level (fig. 4.7F). The latter one also reveals the visualization of the pattern of the retinal vasculature without the use of fluorescent markers.

Figure 4.8 depicts different 3D views of a patient with pathology of the vit-

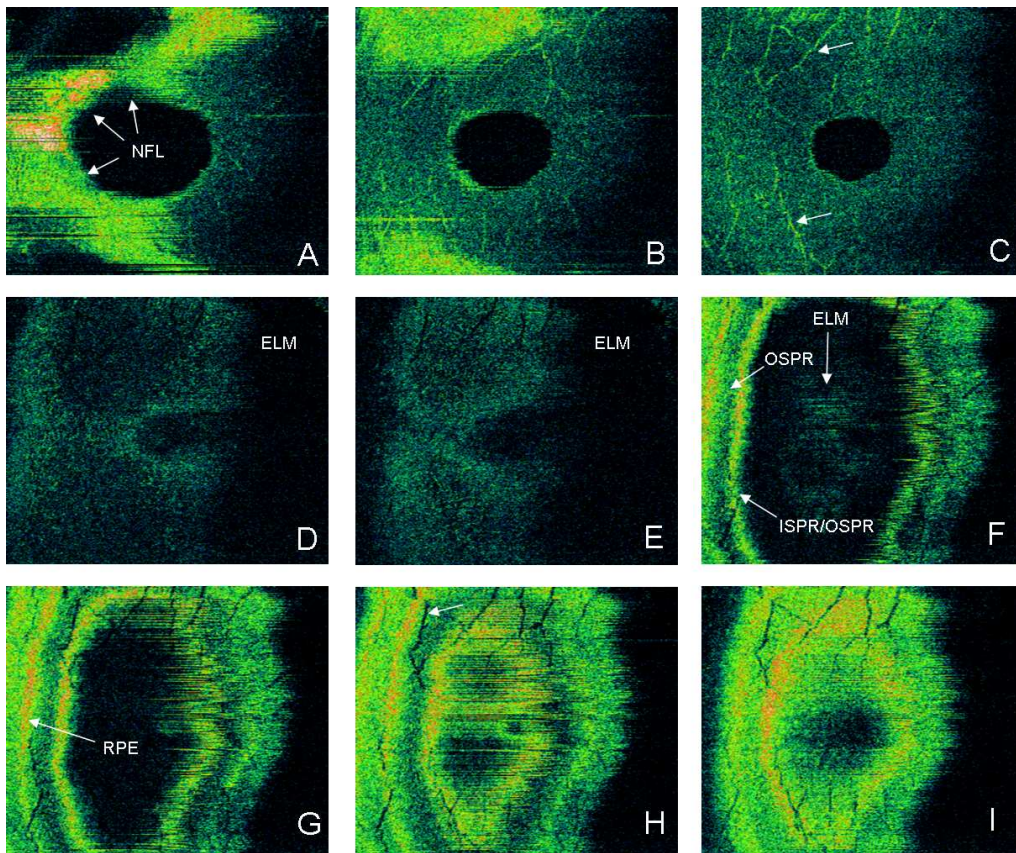


Figure 4.5: Isotropic sampling. Nine selected C-scans extracted from 3D UHR OCT consisting of $512 \times 512 \times 1024$ pixels over a $3 \times 3 \times 1$ mm volume of a normal human retina (measurement time: 10 s). A: nerve fiber layer (NFL); B: ganglion cell and inner plexiform layer; C: capillaries; D, E: external limiting membrane (ELM); F, G, H, I: external limiting membrane, junction of IS and OS of the photoreceptors (ISPR, OSPR) and retinal pigment epithelium (RPE).

reomacular interface in the macular area that exerts traction in vertical as well as in axial direction and leads to distortion of the retinal layers and loss of the foveal depression. The alteration of the retinal surface is easily identified in the 3D overview by the 3D UHR OCT. An analysis of the simultaneously displayed single B-scans (upper left corner) adds substantial information regarding the distribution of the traction forces and the resulting effects on intraretinal organization.

Vitreomacular traction in an axial direction leads to a macular hole formation and therefore to a completely different appearance of the three-dimensional ultrastructure of the retina. The 3D overview depicted in Figure 4.9A illustrates a loss of the foveal contour and a distinct central elevation of the retinal surface. A virtual biopsy system allows the user to excise any given shape from the probe in order to visualize intraretinal morphology inside the acquired volume (fig. 4.9B–F). In the extrafoveal region, no traction is seen, however, cystic changes are

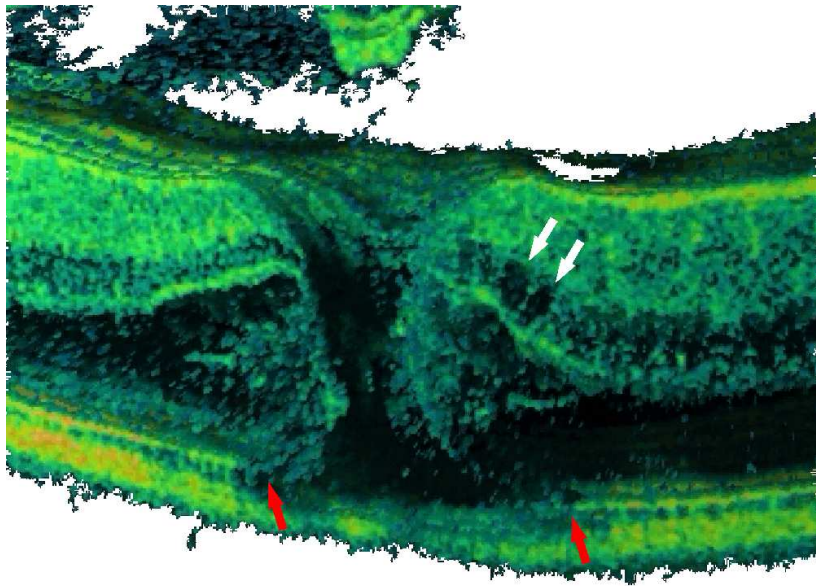


Figure 4.6: Macular hole. Cystic changes in the inner nuclear layer (white arrows) and a disruption of the photoreceptor layer in the foveal region (red arrows) is visualized.

located in the superior portion of the retina mostly within the ganglion cell layer and inner nuclear layer. In the juxtafoveal area the localized attachment of the posterior hyaloid membrane is clearly identified as well as the resulting distortion of the intraretinal layers throughout the entire thickness of the retina. The foveolar site of focal traction on the ILM leads to a rupture of the central retina with formation of a small, but full- thickness macular hole. Superior to the fovea and outside of the defect, the retina demonstrates massive cystic changes most intensively within the deeper portion of the retina including the outer nuclear layer and, to a lesser extent, within the superficial layers.

Figure 4.10 presents 3D UHR OCT of a patient with retinal pigment epithelium dystrophy (Bull's Eye Dystrophy). In addition to the topography of the retina as well as information about intraretinal morphology, 3D UHR OCT also enables the detection of localized RPE atrophy, resulting in signal coming from choroidal layers underneath the RPE in a circular pattern. Again the virtual biopsy feature allows the user to excise and remove any given layer or part of the retinal volume in order to visualize intraretinal morphology inside the acquired tissue.

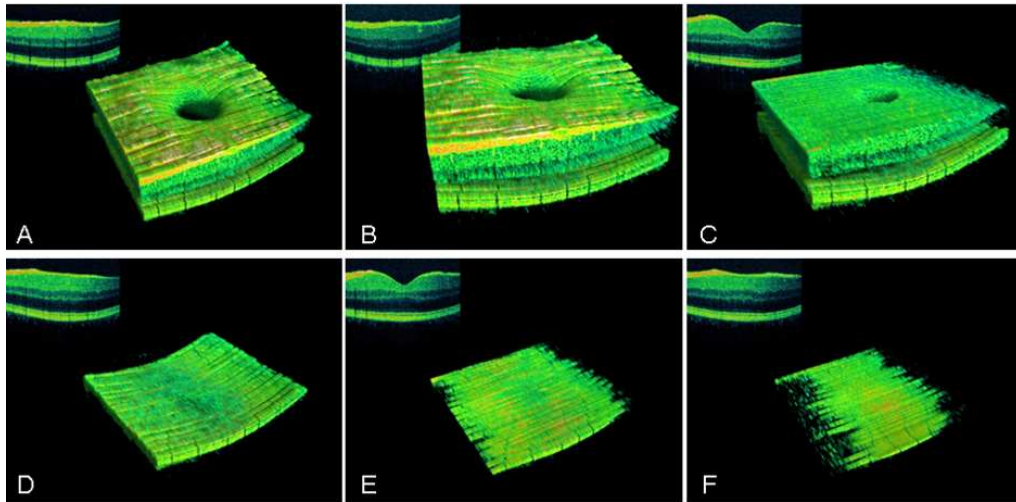


Figure 4.7: 3D UHR OCT of the foveal region at different views (A,B) with simultaneous fly through B-scans of the whole volume (upper left corner). Virtual C-scans system (C-F) enables arbitrary horizontal removal of different retinal layers revealing morphologic information inside the scanned volume.

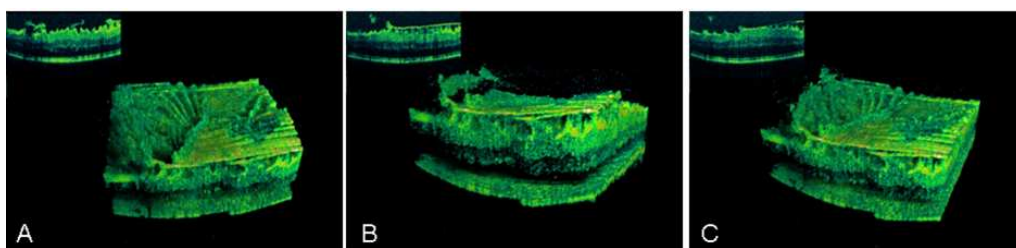


Figure 4.8: 3D UHR OCT of a patient with pathology at the vitreomacular interface at different views with simultaneous fly through B-scans of the whole volume (upper left corner).

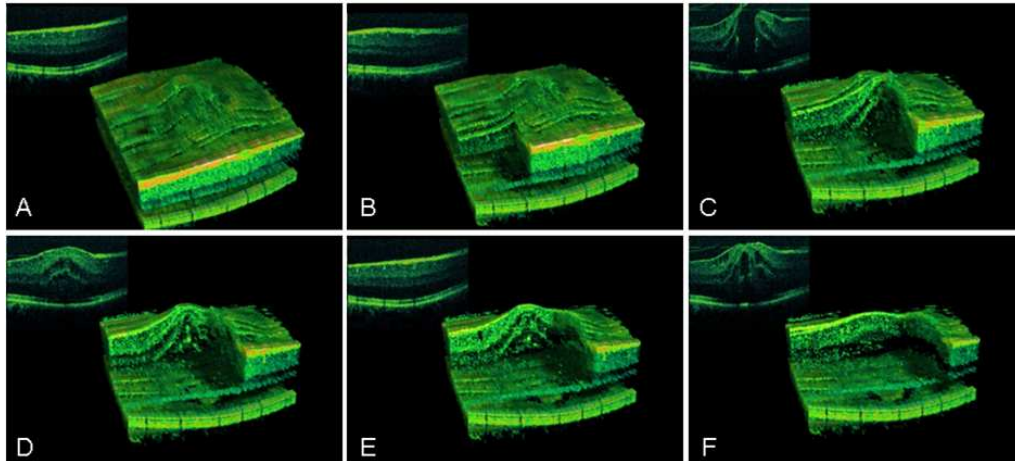


Figure 4.9: 3D UHR OCT of a patient with macular hole (A) with simultaneous fly through B-scans of the whole volume (upper left corner). A virtual biopsy system allows the user to excise any given shape from the probe in order to visualize intraretinal morphology inside the acquired volume (B-F).

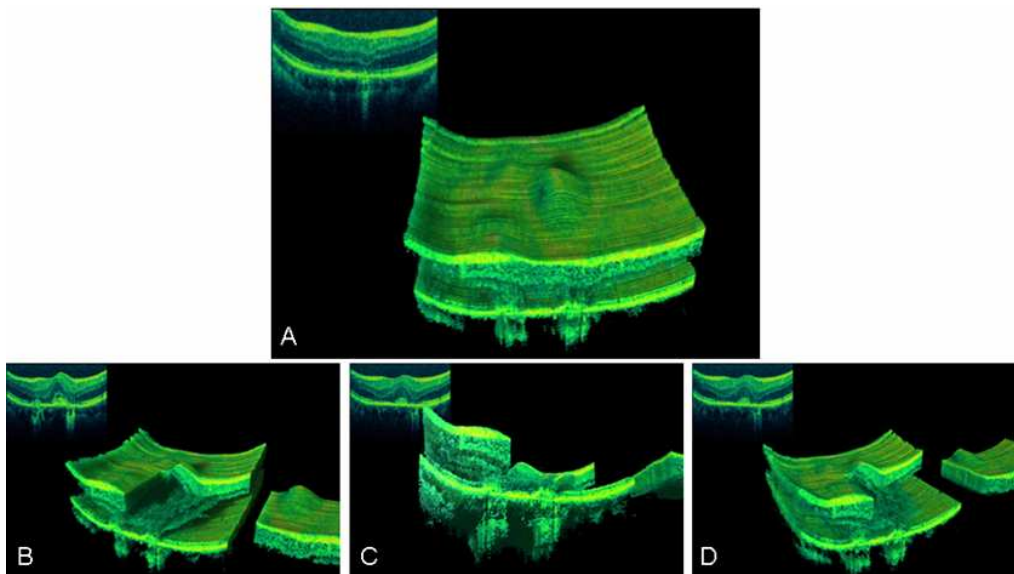


Figure 4.10: 3D UHR OCT of a patient with Bull's Eye Dystrophy (A). The virtual biopsy feature allows the user to excise and remove any given layer or part of the retinal volume.

Chapter 5

Segmentation in Ophthalmic Ultrahigh Resolution OCT

Segmentation in biomedical imaging is an absolute necessary step towards quantification and objective diagnosis. The human eye can very easily distinguish different structures and layers in tomograms. However, trying to recreate this ability with computer based automated segmentation is very challenging. Segmentation appears to be a very complex task and much work has been done in the field of segmentation, feature detection, and pattern recognition in biomedical imaging.

A variety of methods was examined for feature detection and extraction in fluorescence microscopy [147]. Active contours balance an internal force against the image gradient [148]. Neural networks have been applied for segmentation in Magnetic Resonance Imaging (MRI) [149]. But these algorithms are designed for MRI data, which is multimodal and their usability for OCT images has not yet been explored. Neural networks try to mimic the functionality of the brain, which is, as already mentioned, very good in image segmentation. From that point of view neural networks might have a high potential for OCT image segmentation.

Tomograms acquired with ultrasound are from the point of view of their noise and speckle statistics, as well as from their signal characteristics more comparable to OCT data than MRI. Different neural networks have been compared for ultrasound image segmentation [150]. Ashton and Parker [151] applied a probabilistic segmentation algorithm, which assumed only a limited number of classes of tissue within an image. However, their algorithm seemed to be tolerant against deviations from these assumptions.

There have also been first attempts for image segmentation in standard resolution OCT. Rogowska et al. developed a semiautomatic algorithm using edge detection followed by edge linking by graph searching for the detection of cartilage boundaries [152, 153]. In ophthalmic OCT adaptive thresholding was applied [154] as a straight forward technique, since the retina is a layered, stratified organ with a regular structure. Koozekanani et al. used a one-dimensional edge detection followed by a Markov model [155]. Nonlinear complex diffusion is a natural regularized edge-detector [156], where the zero-crossings of the imagi-

nary part indicate edges, similar to the derivation of the filtered signal. It has been shown that complex diffusion is able to segment the layered structure of the retina [157]. Chan et al. used anisotropic noise suppression and deformable splines for measuring the NFL thickness in ultrahigh resolution FDOCT volumes [28]. In pathologic cases, however, these algorithms often fail. Gregori *et al.* presented results with segmentation algorithms on Stratus OCT1 data [158].

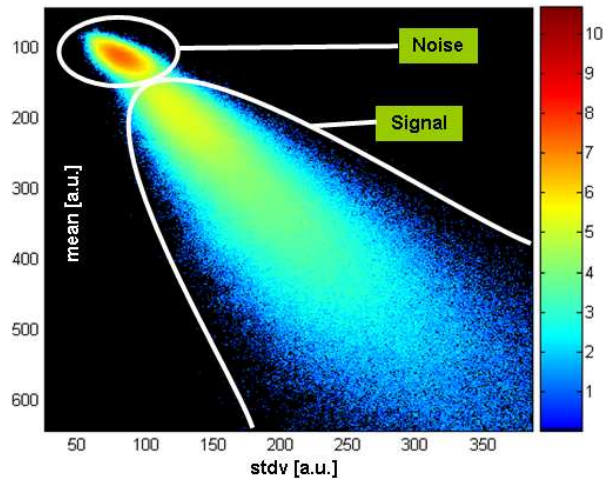


Figure 5.1: Histogram of local mean and standard deviation (stdv). Two nearly distinct areas can be distinguished: low mean and low stdv assignable to noise in the absence of high signals, and an area of the appropriate signal itself.

Algorithm. The classification of different layers just by looking at a tomogram seems to be a mixture of statistics (how many scatterers, mean distance between similar scatterers) and signal height. Because of that the first approach was

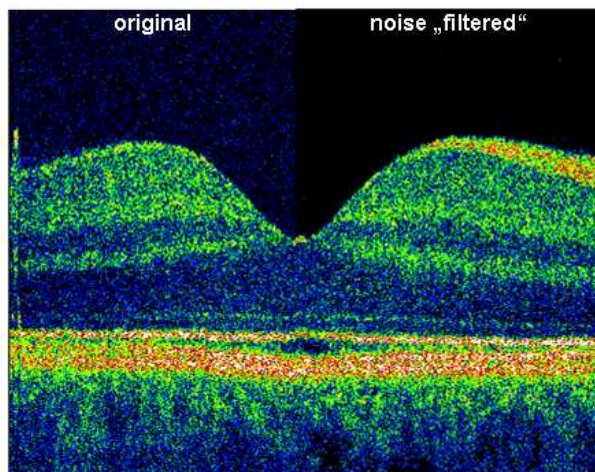


Figure 5.2: Unfiltered and filtered tomogram. Histogram filtering only reduces noise in the absence of signals, i.e. in regions of low mean value.

to quantify local mean values and local standard deviation (stdv) in an OCT image. Figure 5.1 shows an histogram of the calculated local mean and standard deviation. A relatively small area of small mean and small stdv indicates the noise floor in the vitreous, where high signals are absent. The comet-like tail indicates the signal-region with a variety of mean and stdv. The different layers with their different local mean and stdv distribution are not distinguishable. This finding

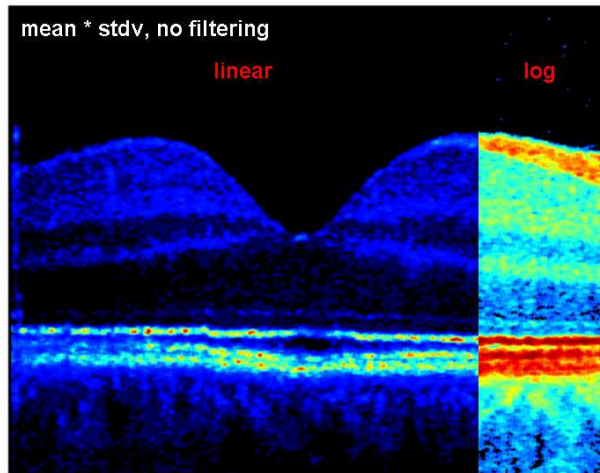


Figure 5.3: Tomogram produced by multiplication of the local mean and the local standard deviation. The different layers are better distinguishable than in the tomogram (fig. 5.2).

is supported by fig. 5.2, which indicates on the left side the original tomogram, on the right side the noise-reduced tomogram after suppression of points which belong to the smaller “noise-area” in the histogram (fig. 5.1). The difference to thresholding is the preservation of small signal in the vicinity of high signals, while small signals “alone” are suppressed.

Multiplication of the local mean and the local stdv lead to figure 5.3, where the local structural differences of the distinct layers are enhanced compared to the intensity tomogram (fig. 5.2), comparable to a smoothing filter.

5.1 2–dimensional segmentation in a glaucoma monkey model

Glaucoma is a disease, where the intraocular pressure is increased. The long term consequence is an irreversible thinning of the nerve fiber layer, which manifests in a progressive limitation of the field of view, followed by blindness. Glaucoma is, together with age-related macular degeneration, the major cause for blindness in the western civilization.

A matlab based user interface for thickness determination of the retina and the nerve fiber layer was developed for a glaucoma study on a monkey eye model. The implemented segmentation first detects the internal limiting membrane (ILM), and a approximation to the retinal pigmented epithelium (RPE). After peak detection in the filtered filtered image the extremal values are calculated and used for final detection of the RPE layer and the nerve fiber layer (NFL). The user interface offers the possibility to correct for false detected layers and to save the calculated boundaries. One of the main sources of segmentation errors in ultrahigh resolution OCT images is the disruption of the layers due to shadowing from blood vessels (see fig. 5.4). The algorithm uses a vessel detection based on the idea, that the mean value of an single A-scan is much smaller in the presence of a vessel. With this vessel detection segmentation errors were minimized.

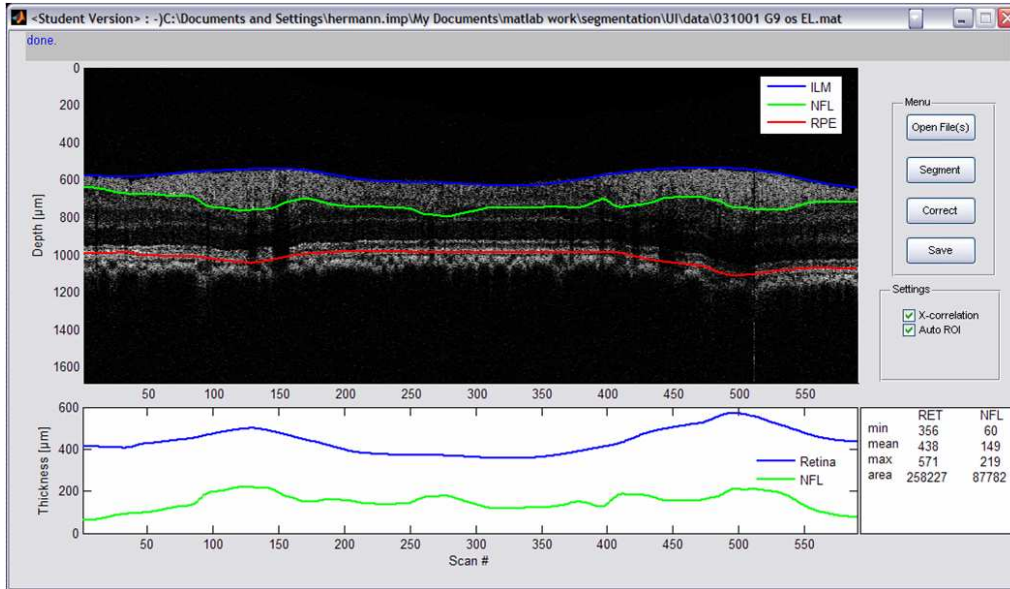


Figure 5.4: User interface. On the top the tomogram is overlaid with the boundaries found by the algorithm; on the bottom the retinal thickness and the nerve fiber layer thickness are indicated.

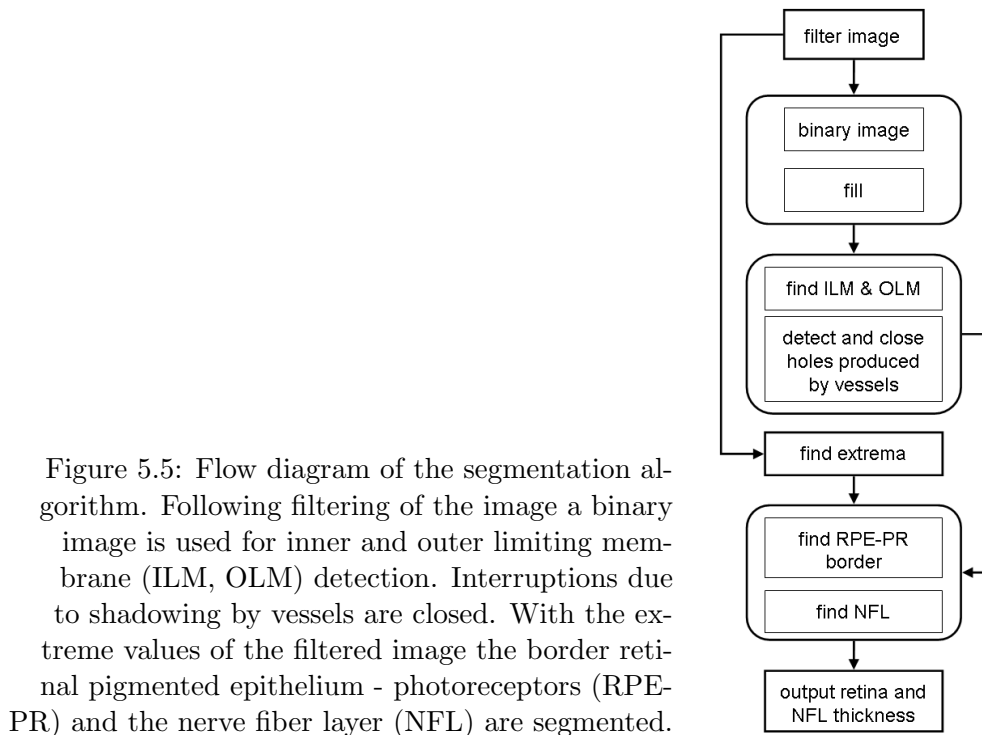


Figure 5.5: Flow diagram of the segmentation algorithm. Following filtering of the image a binary image is used for inner and outer limiting membrane (ILM, OLM) detection. Interruptions due to shadowing by vessels are closed. With the extreme values of the filtered image the border retinal pigmented epithelium - photoreceptors (RPE-PR) and the nerve fiber layer (NFL) are segmented.

5.2 3–dimensional segmentation of photoreceptors in humans

The photoreceptors (PR) are responsible for the light detection in the eye. Nutrition is supported by the retinal pigmented epithelium (RPE), where the PRs are anchored. In many vision related diseases the PRL is affected, like in age–related macular degeneration or serous chorioretinopathy for instance. Segmentation and succeeding quantification of the PR could help in diagnosis and during treatment.

The segmentation of the photoreceptor layer, which includes the ELM, the junction of the inner and outer segments, and the PR–RPE boundary, are very challenging for automated segmentation. The signal originating from the ELM is usually very weak and disrupted. Hence a semi–automatic segmentation approach was applied.

Segmentation of two dimensional data The distance between the RPE and the ELM indicates the thickness of the photoreceptors and is about 48–50 μm in the parafoveal region, with about 17–21 μm distributed to the outer (OS) and about 30 μm to the inner (IS) photoreceptor segment. As in the horizontal direction, the thickness of the PR layer significantly increases in the central foveal region, consistent with the well-known increase in length of the outer cone segments in this region to about 90 μm , approximately equally distributed to the inner (IS: 47 μm) and the outer (OS: 43 μm) photoreceptor segment.

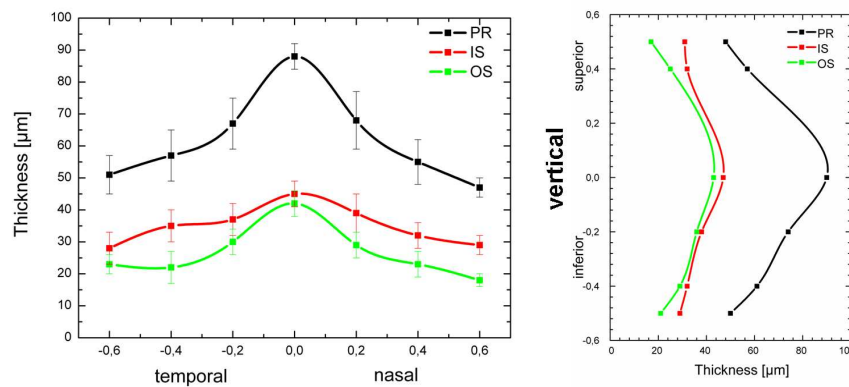


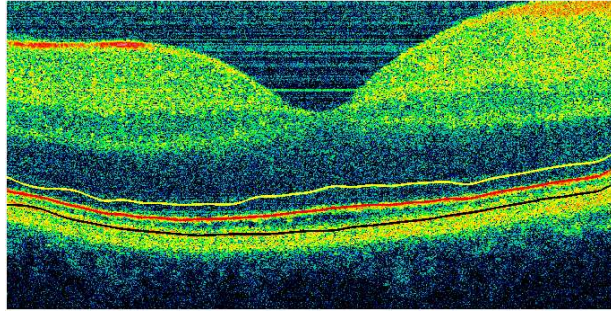
Figure 5.6: Segmentation of two dimensional UHR data. The graphs represent thickness maps in horizontal (left) and vertical (right) direction for the total photoreceptor layer (PR, black), inner segment (IS, red) and outer segment (OS, green). In the central foveal region the total thickness of the PR is maximal ($\sim 90 \mu\text{m}$), approximately equally distributed between the inner and outer segments. Parafoveal the total thickness is about 50 μm , with the inner segment slightly larger ($\sim 30 \mu\text{m}$) than the outer segment ($\sim 20 \mu\text{m}$).

Semi-automatic segmentation algorithm for three–dimensional data.

From a given starting point at one transversal end of the tomogram a rotating

averaging kernel (16x32 pixel, axial x transversal) maximizes the transversal average value and steps through the hole tomogram (stepsize 30 pixel). The direction vector of the highest mean value, the mean value itself and its position

Figure 5.7: Representative averaged scan. Note that the layers appear more prominent than in the tomogram due to the directional averaging kernel.



is stored and taken as starting point for the next position. After successful segmentation of the inner/outer segment junction the algorithm tries to find the RPE and the ELM distal and proximal to the IS/OS junction, using the same kernel and the obtained vectors.

Results. The in fig. 5.8 presented graphs represent thickness maps for the inner segment (top) and outer segment (middle) photoreceptors (PR), as well as the combined total PR-thickness (bottom) as a mean for 5 healthy subjects. In the central foveal region the total thickness of the PR is maximal ($\sim 90 \mu\text{m}$), approximately equally distributed between the inner and outer segments, which is consistent with the well-known increase in length of the outer cone segments in this region. Parafoveal the total thickness is about $50 \mu\text{m}$, with the inner segment slightly larger ($\sim 30 \mu\text{m}$) than the outer segment ($\sim 20 \mu\text{m}$).

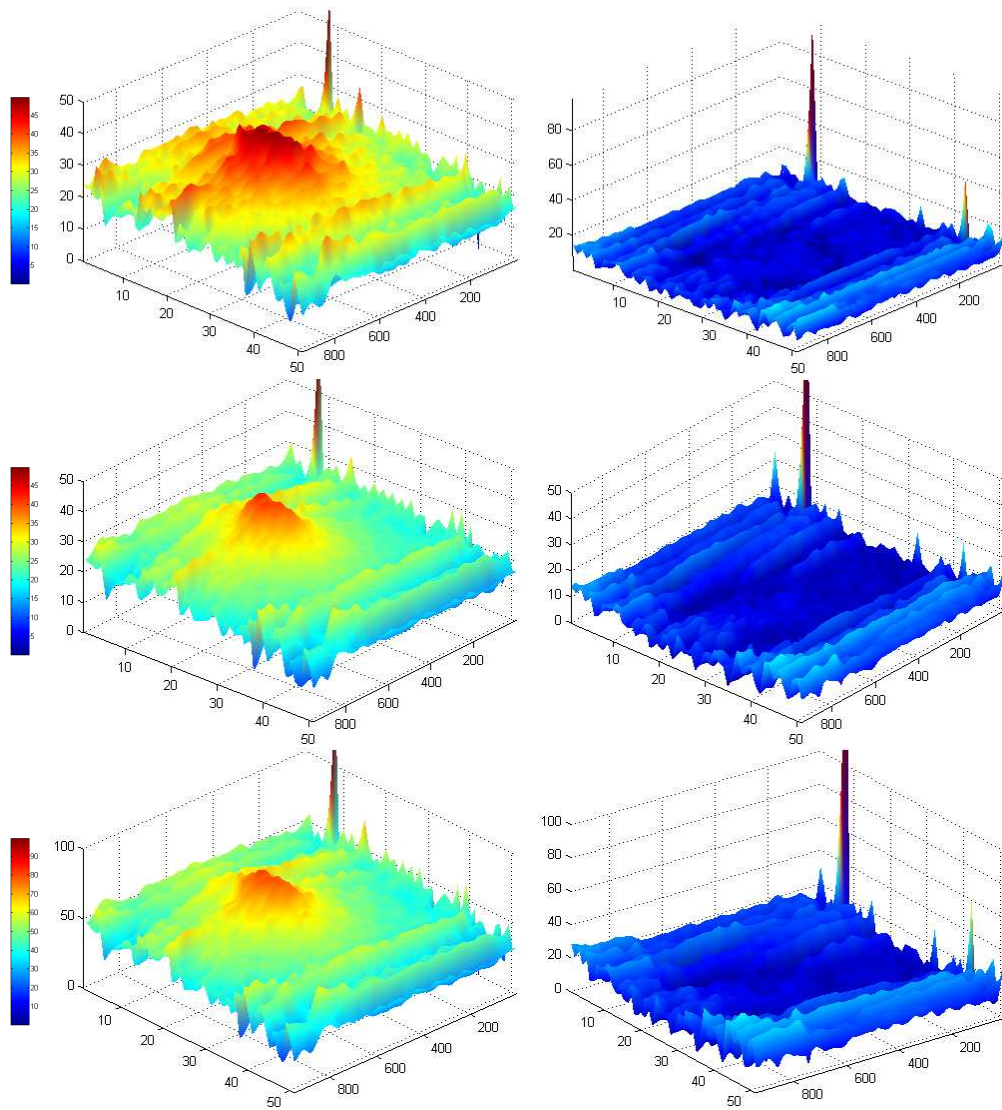


Figure 5.8: Three dimensional photoreceptor thickness maps. Top: Inner Segment; middle: Outer Segment; bottom: IS+OS; all axes in μm . Left graphs show the averaged photoreceptor thickness, right graphs show the standard deviation. The thickness maps are averages from 5 healthy subjects.

Part III

Functional Extensions of Ophthalmic Ultrahigh Resolution OCT

Chapter 6

Extraction of Depth Resolved Spectroscopic Information

6.1 Precision of extraction using spectroscopic OCT

6.1.1 Introduction

Optical coherence tomography enables non-invasive, high resolution *in vivo* imaging in transparent and non-transparent tissue [18, 26, 100]. The possibility of extracting spatially resolved spectroscopic information simultaneously with the generation of high resolution images can significantly extend the range of biomedical applications of OCT. The first qualitative, proof-of-principle spectroscopic OCT studies were conducted using narrow bandwidth (~ 50 nm) light sources centered at 1300 nm [159] (time - domain OCT) and 830 nm [39] (frequency-domain). In other studies a combination of two narrow band sources centered at 1.3 μm and 1.5 μm , and a differential absorption method were used to quantify water content in phantoms at a single wavelength [37, 160]. Utilization of a single broadband light source for quantitative, depth-resolved SOCT offers many advantages: it permits better spatial localization of the absorbing object, reduces the complexity of the instrument as well as the data acquisition and processing algorithm, eliminates the additional noise associated with the use of multiple narrow bandwidth, mutually incoherent light sources, and most importantly, permits extraction of absorption profiles $\mu_a(\lambda)$ over a broad wavelength range with a single measurement. Commercially available femtosecond Ti:Al₂O₃ lasers can generate a spectrum centered around 800 nm with a bandwidth larger than 100 nm at FWHM (full width at half maximum) [99], which overlaps with the so-called therapeutic window, covering the absorption profiles of several biological chromophores, such as melanin, oxy- and deoxyhemoglobin [161]. It was demonstrated in the past that qualitative spectroscopic information acquired with ultrahigh resolution SOCT in biological tissue can be used as a type of “spectroscopic staining”, in analogy to histological staining, thus enhancing the OCT image contrast [38]. In addition, it was lately shown that spectroscopic low coherence interferometry can aid measurements of dye diffusion constants in gels [162]. Recently, an *in vitro* quantitative SOCT measurement of blood oxygenation by use of a broad

bandwidth ($\Delta\lambda = 125 \text{ nm}$) Ti:Al₂O₃ laser has been published [163]. So far only preliminary results have been reported on the precision of the SOCT method utilizing a single broad bandwidth source for quantitative measurement of chromophores imbedded in weakly scattering media [164]. In this work we present a thorough theoretical and experimental evaluation of the effect of various factors related to the performance of the TD-OCT (time-domain) instrument, the measurement procedure or the data processing algorithm on the precision of SOCT for extracting absorption profiles $\mu_a(\lambda)$ from weakly scattering phantoms.

6.1.2 Theory

As described in detail in [37] and [163], the signal detected with an OCT system is proportional to the cross-correlation between the electrical fields backscattered from the imaged object and the reference mirror. Assuming that the mirror reflectivity is spectrally flat over the emission bandwidth of the light source, the reference field can be represented as a Doppler shifted version of the light source field. However, the field backreflected from the imaged object is a convolution of the incident source field and the depth-dependent spectral reflectivity profile of the imaged object. In the frequency domain the convolution can be expressed as a product of the light source spectrum $S(\omega)$ and the spectral reflectivity of the object $H(\omega)$:

$$I(\omega) = S(\omega)H(\omega),$$

where $I(\omega)$ is the amplitude spectrum measured at the detector of the TD-OCT system. The magnitude of the spectral reflectivity $H(\omega)$ is a measure of the frequency (wavelength) dependent attenuation, $\mu(z, \lambda) = \mu_a(z, \lambda) + \mu_s(z, \lambda)$, of light in the imaged object resulting from scattering (μ_s) and absorption (μ_a) and is depends in general on the depth z . The magnitude of $H(\omega)$ can be obtained from the OCT fringe pattern by applying a frequency analysis to it such as Fourier- (FT) or wavelet transform (WT). Assuming that the sample has spatially and temporally homogeneous attenuation properties, $\mu(z, \lambda) \equiv \mu(\lambda)$, that comply with Beer-Lambert law, the magnitude of $H(\omega)$ expressed in wavelength units can be written as a function of the depth z in the sample:

$$H(\lambda, z) = e^{-2z\cdot\mu(\lambda)} \quad (6.1)$$

Here $\mu(\lambda)$ is the wavelength dependent attenuation coefficient of the imaged object. In very weakly scattering media where the attenuation of light is dominated by absorption, the attenuation coefficient can be substituted, within certain precision limits, with the corresponding absorption coefficient $\mu_a(\lambda)$. In SOCT $\mu_a(\lambda)$ can be obtained by extracting the amplitude spectra I_0 and I_1 at two depths within a weakly or non-scattering sample separated by distance d :

$$\mu_a(\lambda) = \frac{1}{2d} \ln \frac{I_0}{I_1} \quad (6.2)$$

The factor of 2 in the denominator of (6.2) designates a bidirectional pass of the optical beam through an absorbing region in the sample with thickness d , since

OCT detects backreflected light. In addition, (6.2) can be used to evaluate the expected error in measuring $\mu_a(\lambda)$ with SOCT:

$$\frac{\Delta\mu_a(\lambda)}{\mu_a(\lambda)} = \left\{ \left(\frac{\Delta d}{d} \right)^2 + \left[\ln \left(1 - \frac{\delta I_0(\lambda)}{I_0(\lambda)} \right) \right]^{-2} \cdot \left[\left(\frac{\Delta I_0(\lambda)}{I_0(\lambda)} \right)^2 + \left(\frac{\Delta I(\lambda)}{I(\lambda)} \right)^2 \right] \right\}^{1/2} \quad (6.3)$$

Here $\Delta d/d$, $\Delta I_0/I_0$ and $\Delta I/I$ are the statistical errors in measuring the sample thickness d and the amplitude spectra I_0 and I obtained at the front and rear interface of the absorbing sample, while $\delta I_0/I_0 := 1 - I/I_0$ is the differential change in the incident amplitude spectrum I_0 resulting, in an ideal case, only from light absorption in a phantom with thickness d and absorption coefficient μ_a .

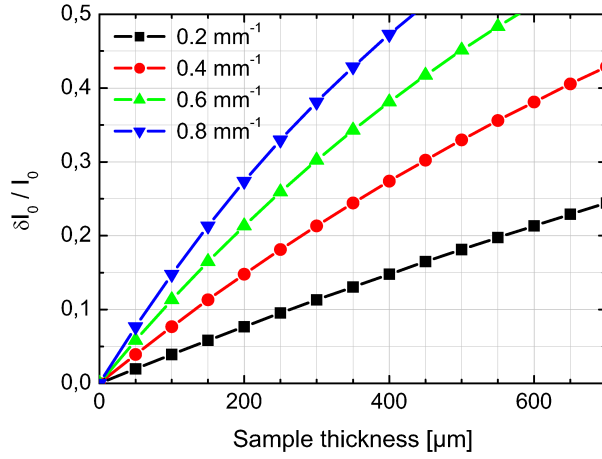


Figure 6.1: Differential changes in the incident amplitude spectrum $\delta I_0/I_0$ as a function of the sample thickness d calculated for different absorption coefficients; ($\mu_a = 0.4 \text{ mm}^{-1}$ is equal to the absorption coefficient of whole blood at the isosbestic point, $\lambda = 800 \text{ nm}$).

Since SOCT was developed with the intention to be used for quantitative measurement of absorption profiles $\mu_a(\lambda)$ of various biological chromophores, it may be useful to provide an initial theoretical estimate of the sensitivity of the method to weak and small size absorbers. For example, the absorption coefficient of blood ranges from 0.2 mm^{-1} to 2 mm^{-1} in the wavelength range of 650 nm to 950 nm depending on various physiological conditions such as blood oxygenation level, hematocrit content and osmolarity, and is $\sim 0.4 \text{ mm}^{-1}$ at the isosbestic point ($\lambda = 800 \text{ nm}$) [165]. The size of blood vessels varies significantly in the human body. However, in the retina the largest arteries rarely exceed $300 \mu\text{m}$ in diameter. Figure 6.1 shows the expected effect of blood absorption with $\mu_a = 0.2, 0.4, 0.6$ and 0.8 mm^{-1} on the differential change $\delta I_0/I_0$ as a function of the size of the blood vessel. The graph clearly shows that at the isosbestic point where $\mu_a \sim 0.4 \text{ mm}^{-1}$, light absorption in arterioles $\sim 50 \mu\text{m}$ in diameter would result only in $\sim 4\%$ differential change in the attenuated amplitude spectrum, while absorption of light in vessels the size of $300 \mu\text{m}$ could produce a change $\delta I_0/I_0 \sim 20\%$.

Figure 6.2 is a graphical representation of (6.3) and demonstrates that the relative error $\Delta\mu_a/\mu_a$ is very sensitive to the magnitude of the differential change in the incident amplitude spectrum $\delta I_0/I_0$ produced by the presence of an absorber,

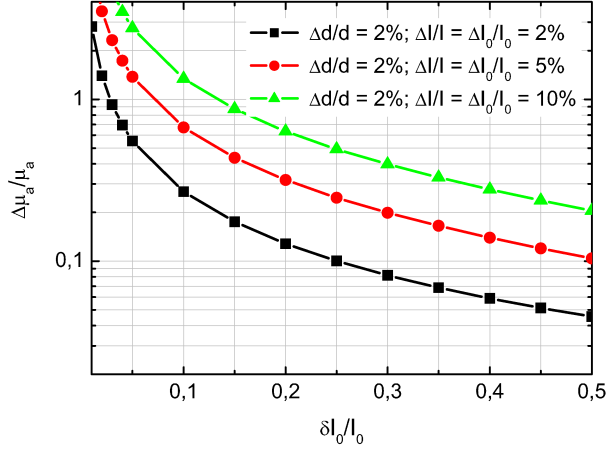


Figure 6.2: Relative error in the extracted absorption coefficient, $\Delta\mu_a/\mu_a$, as a function of the differential changes in the incident amplitude spectrum $\delta I_0/I_0$.

i.e. the weaker and smaller the absorber, the larger the error in the extracted μ_a . It also shows that $\Delta\mu_a/\mu_a$ is strongly dependent on the relative errors in the amplitude spectra, $\Delta I_0/I_0$ and $\Delta I/I$, measured at the boundaries of the absorbing sample. For the case of an absorber with $\mu_a = 0.4 \text{ mm}^{-1}$ (close to absorption of whole blood at $\lambda = 800 \text{ nm}$) and thickness $d = 50 \mu\text{m}$, and assuming that the $\delta I_0/I_0$ is solely due to absorption in the object, that $\Delta d/d = 2\%$ and that $\Delta I_0/I_0 = \Delta I/I = 2\%$ (spectrally flat over the examined wavelength region), the expected $\Delta\mu_a/\mu_a \sim 70\%$. If the size of the absorbing object increases to $300 \mu\text{m}$, the relative error in extracted μ_a is reduced to $\sim 12\%$.

The theoretical evaluation presented above shows that if SOCT is used for quantitative evaluation of blood oxygenation, care has to be taken about the experimental errors, since the overall error $\Delta\mu_a/\mu_a$ is very sensitive on them. In an SOCT measurement, the errors $\Delta I_0/I_0$ and $\Delta I/I$ are sensitive to both the intensity noise and spectral noise of the light source. In addition, the differential change $\delta I_0/I_0$ may be influenced by presence of chromatic aberrations, dispersion mismatch, angle and wavelength dependent specular and / or diffuse reflections, as well as artifacts in the extracted spectra, generated by the processing algorithm (dependent on parameters such as the size and shape of the window in the windowed FT), the effects of which on $\delta I_0/I_0$ may be falsely interpreted as induced by presence of absorbers within the imaged object. The following sections will discuss the experimental evaluation of various factors that primarily affect the precision of SOCT for extraction of absorption profiles, as well as different strategies that can be applied to minimize the experimental errors.

6.1.3 Experiments

For the purpose of this study an ultra-broad bandwidth, state-of-the-art Ti:Al₂O₃ laser [166] (Femtolasers GmbH, $\lambda_c = 800$, $\Delta\lambda = 260 \text{ nm}$, $P_{out} = 120 \text{ mW}$ ex-fiber, see fig. 6.3, black line) was interfaced to a free-space OCT system, described in detail in [164], and modified in this case for optimal performance in the 600–1000 nm wavelength range. The system's optical components were selected to support propagation of broadband light and to compensate for

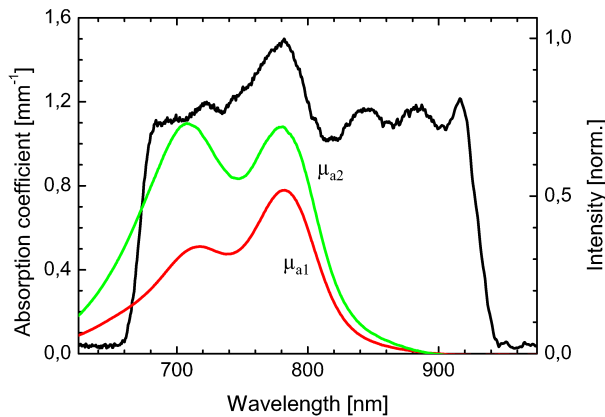


Figure 6.3: Emission spectrum of the $\text{Ti:Al}_2\text{O}_3$ laser (black line) as measured with SOCT from a mirror reflection. Absorption profiles measured with a spectrometer from two gel samples with different concentration of ICG (green and red lines).

any polarization and dispersion mismatch between the two arms of the interferometer. Custom designed achromat lenses ($D = 5 \text{ mm}$, $f = 10 \text{ mm}$) were used in the sample and reference arms of the interferometer to minimize the effect of chromatic aberrations and dispersion mismatch on the precision of the measurement. The system utilized dynamic focus tracking to closely match the position of the coherence gate with the focal plane of the imaging lens within the samples. Nonlinearities in the voice coil (VC) scanning rate were accounted for by acquiring a reference fringe pattern from an additional interferometer powered by a He-Ne laser, simultaneously with the actual data acquisition and subsequently applying a data correction algorithm. The OCT system provided $1.3 \mu\text{m}$ axial and $3 \mu\text{m}$ lateral resolution in air with 107 dB sensitivity of for 5 mW incident power.

All phantoms used in the SOCT measurements were prepared by bounding single or multiple gel layers (4 g/l agar in distilled water) doped with ICG (Indocyanine Green dye, initial concentration of $50 \mu\text{M/l}$ solution in distilled water) between thin ($\sim 150 \mu\text{m}$) glass coverslips. One of the reasons for using ICG dye as an absorbing agent in this SOCT study was the fact that its absorption profile overlaps partially with the emission spectrum of the $\text{Ti:Al}_2\text{O}_3$ laser (see fig. 6.3), which facilitated data normalization. The ICG dye was mixed very well with the gel to produce homogeneous mixture and the ICG:gel ratio was varied to result in absorption profiles $\mu_a(\lambda)$ with various shapes and peak absorption magnitude. As a base-line reference, the attenuation properties of pure (undoped with ICG) gel were measured with a spectrometer (Ocean Optics, USB2000). The attenuation coefficient $\mu(\lambda)$ of pure gel appeared almost flat over the wavelength range of 550-950 nm, with magnitude ~ 2 orders smaller than the absorption peak of the smallest concentration of ICG used in experiments described here.

To evaluate the sensitivity of SOCT to the size of the absorbing object, phantoms with various thickness of the ICG-gel layer were prepared. Since the absorption profile of the ICG dye is dependent on time, chromophore concentration and light illumination [167], the absorption spectrum of each phantom was measured with the spectrometer immediately before and after an SOCT measurement in order to account for any time or exposure to $\text{Ti:Al}_2\text{O}_3$ light related changes in the spectrum. Furthermore, to minimize the effect of high power radiation on the

ICG spectrum, all samples were imaged with incident power lower than 1 mW.

For each phantom 50 A-scans were acquired at a single position. Prior to the data acquisition the OCT system was aligned so that the imaging beam was focused on the first glass-gel interface and the reference arm coherence gate overlapped with the focal plane. Similar measurements were performed in pure undoped gel samples to be used as reference and correction factors. The dispersion in the system was matched at the first glass-gel interface. The OCT fringe data was digitized with a 16 bit, 10 Ms/s A/D converter and filtered with a band-pass filter centered at 195 kHz (corresponding to VC velocity of ~ 38 mm/s). Windowed Fourier transform (WFT) was used to extract power density spectra from the fringe patterns corresponding to reflections from the glass-gel and gel-glass interfaces in a sample.

The size of the window is a critical parameter: a small window leads to a good spatial localization with poor spectral information, i.e. the density of points on the wavelength scale of the extracted spectra. A large window leads to a good spectral resolution at the expense of the spatial resolution, since the spectroscopic information is averaged over the window size. However, in tissue samples a time-frequency-decomposition, i.e. sliding WFT or wavelet transform, can lead to a better spatial localization. In this experiment a super-gaussian window with a width of $8 \times \text{FWHM}$ (FWHM is the full width at half maximum of the fringe envelope) was found to provide spectra which were in in very good agreement with spectrometer measurements. Since the FWHM changes with depth due to dispersion, but the same wavelength scale for spectra obtained from different depth is needed for the calculation of the absorption, each data set was expanded to the size of 1024 points by zero-padding. The extracted spectra were averaged over the 50 scans and the mean spectra corresponding to the front and the back surface of the examined gel layer were used to calculate the absorption coefficient $\mu_a(\lambda)$ of ICG using Beer-Lambert's law (6.2). The standard deviation for the averaging of the 50 scans is a measure for the repeatability of the obtained spectra, and does not include systematic errors.

6.1.4 Results and discussion

To evaluate the overall performance of the SOCT system, a reflection from a mirror was repeatedly measured (50 A-scans acquired at one location) and the corresponding spectra were extracted by using the windowed FT algorithm described above. Care was taken to precisely match the dispersion of the two arms of the interferometer before the measurements. The acquired data was statistically averaged and the standard deviation for the series of measurements was evaluated to be below 3% for a wavelength range corresponding to the FWHM of the Ti:Al₂O₃ laser emission spectrum ($\Delta\lambda = 260$ nm). The spectral fluctuations of the light source alone, which constitute a part of the total SOCT measurement error, were measured separately and were determined to be below 2% for the same wavelength range.

Since in this study we used a spectrometer as a 'golden standard' to evaluate the performance of the SOCT method, the precision of the spectrometer was

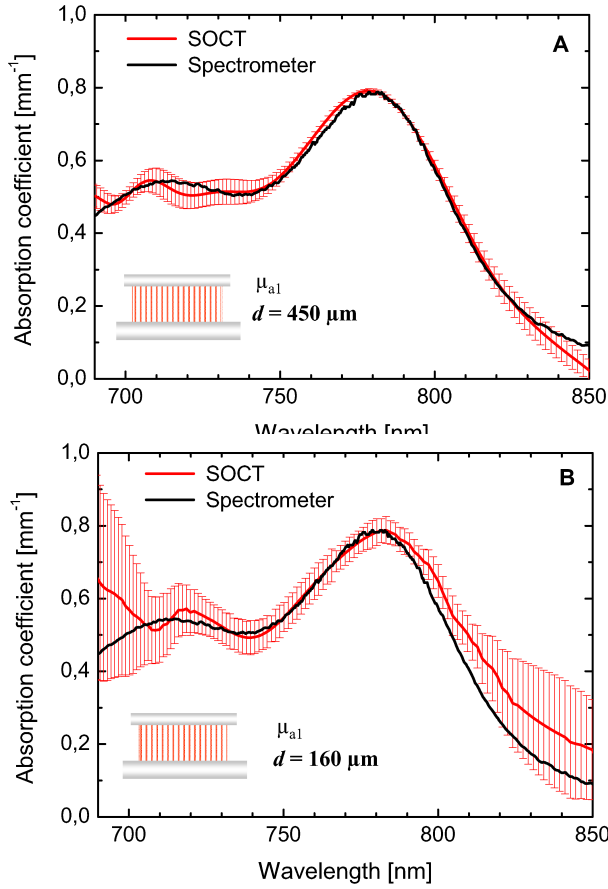


Figure 6.4: Absorption profiles measured from 450 μm thick (A) and 180 μm thick (B) single layered gel:ICG phantoms with SOCT (red line) and with the spectrometer (black line). The insets show schematics of the sample; light is incident from the top.

also tested by measuring the absorption profile of a neutral density (ND) filter. The uncertainty in this case was evaluated to be $\sim 2\%$ for the wavelength range 550–950 nm for a series of 10 measurements.

To examine the reproducibility of OCT for measuring distances, the thickness of a glass coverslip was measured multiple times at different locations. The experimental error was found to be less than 1.5%.

To evaluate the effect of dispersion mismatch on the precision of SOCT, power spectra were extracted from the front and back boundaries of a 160 μm thick glass coverslip and a 1050 μm thick microscope glass slide. In both cases comparison of the two spectra (corresponding to the front and back air-glass interfaces) showed that they matched within 3% of each other for the entire wavelength range corresponding to the FWHM of the Ti:Al₂O₃ emission spectrum, signifying that dispersion mismatch has a negligible effect on the precision of SOCT.

The use of a broad bandwidth light source in an OCT system that utilizes refractive optics is inevitably accompanied by chromatic aberrations. In this experiment custom designed achromat doublets were used to provide optimal correction in the wavelength range 600–1000 nm. The chromatic focal length aberrations were evaluated to be less than 0.25% of the focal length of the lens ($f = 10$ mm), corresponding to ~ 25 μm spectral spread in air which is comparable to the depth of focus of the lenses (~ 50 μm in air).

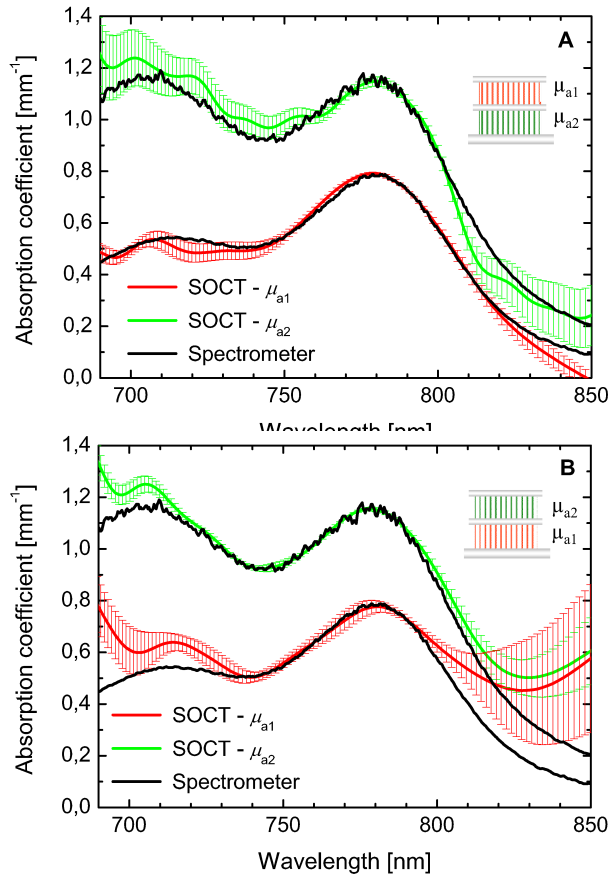


Figure 6.5: Absorption profiles measured from double layered gel:ICG samples with SOCT (red and green lines) and with the spectrometer (black line). The insets shows schematics of the phantoms, light is incident from the top. (A) Low absorption layer on top ($\sim 490\mu\text{m}$), high absorption layer below ($\sim 530\mu\text{m}$). (B) High absorption layer ($\sim 560\mu\text{m}$) on top of a low absorption layer ($\sim 510\mu\text{m}$).

The use of a $\text{Ti:Al}_2\text{O}_3$ laser with a spectral width $\Delta\lambda = 260\text{ nm}$ resulted in $\sim 1.3\mu\text{m}$ coherence gate length in air. Translation of the coherence gate along the optical axis within the depth of focus will change the power spectral density of the OCT-signal. Since in this study the spectral spread in the focal region was ~ 25 times larger than the coherence gate width, variations in the shape and magnitude of the spectra extracted at various positions of the $1.3\mu\text{m}$ wide coherence gate within the beam depth of focus were expected. This fact was confirmed experimentally by focusing the imaging beam onto a mirror and translating the coherence gate within the depth of focus of the beam. The spectra measured at different locations of the coherence gate thereby exhibited significant variations in shape and magnitude. This experiment demonstrates that changes in the overlap during scanning between the focal volume of the imaging beam and the coherence gate within the sample is by far the largest source of error in extraction of absorption profiles from weakly scattering, absorbing media.

Currently, OCT system designs utilize either static focusing (the imaging beam is focused at one location and the coherence gate is swept through it), or dynamic focusing, where in theory the coherence gate can be centered in the focal region and its position relative to the focal plane is kept the same as the imaging beam is focused deeper into the sample. Dynamic focus tracking techniques that utilize a retroreflector and a scanner to expand simultaneously the beam

paths in the sample and reference arms of the interferometer [37] (similar to the voice coil used in the SOCT system) operate perfectly only in sample media with refractive index $n = \sqrt{2}$. In a medium with a different refractive index there is an immanent mismatch between the positions of the focal plane and the coherence gate. As a result, the detected interferometric signal will correspond to an intensity distribution located in front or behind the focal plane of the imaging lens, depending on whether the refractive index is larger or smaller than $\sqrt{2}$. The mismatch, ΔL , between the coherence gate and the focal plane increases with the depth within the sample: $\Delta L = L_R - L_S = (2 - n^2) \cdot d$, where L_R is the pathlength in the reference arm, and L_S the sample arm length, and d is the change of L_S in air. For the case of gel phantoms ($n = 1.34$) the mismatch constituted $\sim 20\%$ of the distance d , and in combination with the present chromatic aberrations caused changes in the incident spectrum larger than the changes expected purely from absorption.

To compensate for the combined effect of chromatic aberrations and the focal plane - coherence gate mismatch, we have developed a data correction procedure: reference measurements were performed in phantoms containing pure (without ICG-doping) gel with approximately the same layer thickness as the phantoms with the ICG doped gel layers. In all cases the coherence gate was overlapped with the focal plane of the imaging lens, which in turn was positioned at the first glass-gel interface in the phantoms. The spectra extracted at the different gel-glass interfaces in the pure gel phantoms were used as correction factors for the spectra obtained at the corresponding glass-gel interfaces in the ICG doped gel phantoms. Not using this correction would result in a systematic error in the order of 100%–200% at the edges of the wavelength range.

Figure 6.3 shows the spectrum extracted with SOCT from a mirror reflection (black line), and the absorption profiles of ICG doped gels for two different dye concentrations (red and green lines) as measured with the spectrometer. Due to the partial overlap between the ICG absorption spectra and the light source emission spectrum, the relative error $\Delta\mu_a/\mu_a$ was expected to be minimal in the wavelength region of 675 nm–840 nm.

Figure 6.4(a) shows the mean ICG absorption profile $\mu_a(\lambda)$ extracted from a 450 μm thick sample (red line) and the standard deviation of 4 measurements (50 scans each). Comparison with a reference ICG spectrum measured with the spectrometer from the same phantom (black line) demonstrates excellent agreement to within 2% in the central region and 8% at the edges of the 690 nm - 810 nm wavelength range. Note that the statistical error quickly becomes larger for wavelengths shorter than 690 nm and longer than 810 nm. Similar measurements were obtained from an 180 μm thick phantom with the same ICG:gel ratio in the doped gel layer (see fig. 6.4(b)). As expected, the measurement error in this case was higher - the agreement between the absorption profiles measured with OCT and the spectrometer was within 10% in the central region and larger than 50% at the edges of the examined wavelength range.

To evaluate the ability of SOCT to discriminate between regions in the sample with different absorption properties, measurements were performed in multilayered phantoms. Figure 6.5 shows absorption spectra extracted from two-layered

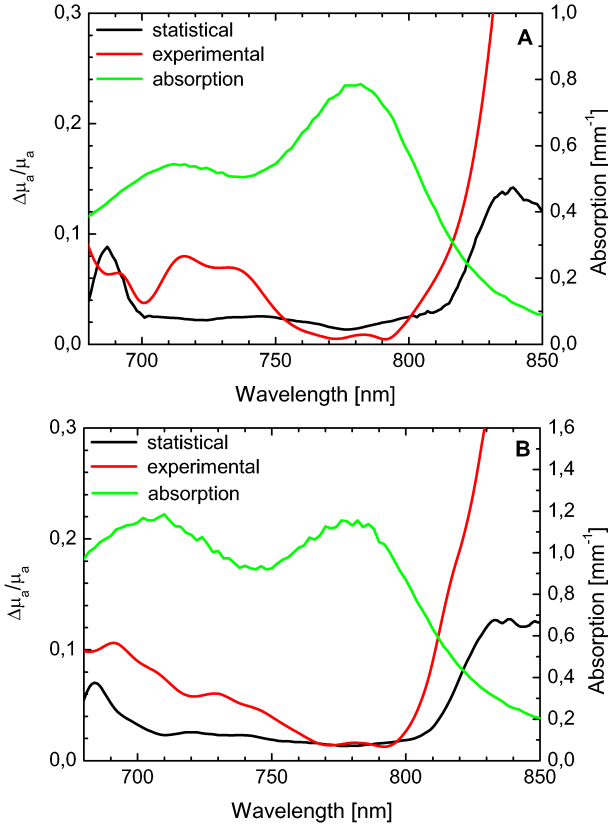


Figure 6.6: Comparison between the due to Eq. (6.3) expected error (black line) and the statistical error (red line) $\Delta\mu_a/\mu_a(\lambda)$ (average of 4 profiles, 50 A-scans each) determined for a double layered phantom corresponding to fig. 6.5(a). Absorption profiles measured from the top (A) and the bottom (B) layer of the phantom (green line).

samples using SOCT (red and green lines) and the spectrometer (black line). The insets in fig. 6.5(a) and 6.5(b) show schematics of the multilayered gel-glass samples. In fig. 6.5(a) a low absorptive layer ($\sim 490 \mu\text{m}$) is positioned on top of a high absorptive layer ($\sim 530 \mu\text{m}$). The SOCT precision in the wavelength range 690 nm - 810 nm for the $\mu_a(\lambda)$ extracted from the top layer (average over 4 measurements, 50 scans each) appears similar to the precision achieved in single layered samples. Although the magnitude of the absorption profile of the bottom layer was ~ 1.5 to 2 times larger than the absorption of the top layer, the precision in this case was worse. In the reverse situation, shown in fig. 6.5(b), when the low absorption layer ($\sim 510 \mu\text{m}$) was below the high absorptive layer ($\sim 560 \mu\text{m}$), the statistical error in the extracted absorption profile was greater than 80% at the edges of the examined wavelength range. The larger errors in fig. 6.5(b) compared to fig. 6.5(a) might be due to a different focal position within the samples. In fig. 6.5(b) the larger systematic errors below 740 nm show that the correction procedure in this case was not optimized, because the pure gel phantom used for correction did not match the thickness.

The results obtained after correction from both the single and double layered gel samples (presented in fig. 6.4 and fig. 6.5) still exhibited significant variations in the extracted absorption profiles, larger at the edges and smaller in the central part of the wavelength region 690-850 nm. To investigate the error's dependence on the wavelength, we calculated the expected error $\Delta\mu_a/\mu_a$ by as-

suming a perfectly matched coherence gate, lack of chromatic aberrations and total differential change $\delta I_0/I_0$ due to absorption $2d\mu_a$. This was accomplished by substituting in Eq.(6.3) the experimentally determined errors $\Delta d = 0.7 \mu\text{m}$, $\Delta I_0/I_0(\lambda)$, $\Delta I/I(\lambda)$ and the absorption profile $\mu_a(\lambda)$ as measured with the spectrometer. The expected errors calculated for the top and bottom layers of a double layered sample and compared with the corresponding measurement errors (red line) are shown in fig. 6.6(a) and 6.6(b). The figures show that the expected error is always smaller than the measurement error at the edges of the selected wavelength region. This result is most probably due to imperfect data correction procedure related to possible discrepancies between the thickness of the undoped and ICG-doped gel phantoms, as well as local absorption density variations. The increase in the error at wavelengths longer than 810 nm can be partially explained with the expected rise in imprecision resulting from the decreasing ICG absorption.

The results presented so far demonstrate that with proper optimization of the data acquisition and processing procedures SOCT is capable of extracting absorption profiles of weak and small absorbers imbedded in very weakly scattering media with fairly high precision. Development of better focus tracking techniques along with methods for better compensation of chromatic aberrations can significantly improve the precision of the method in weakly or non-scattering media. However in turbid media such as biological tissue where scattering of light can be orders of magnitude larger than absorption and where spatial variations in the refractive index can be significant on a micrometer scale, precise alignment between the focal plane and the coherence gate may be challenging. Therefore extraction of absorption spectra from biological samples will necessitate development of novel data processing algorithms that are able to separately estimate the absorption and scattering properties of tissue.

6.1.5 Conclusion

The results presented in this study demonstrate the feasibility of SOCT to extract spatially resolved, quantitative absorption profiles of weak and small absorbers imbedded in weakly scattering media with fairly high precision over a wavelength region equivalent to the FWHM of the light source. This result is very promising, considering the fact that the Ti:Al₂O₃ spectrum covers the absorption peak of deoxy-hemoglobin at 760 nm as well as the hemoglobin isosbestic point at around 800 nm providing an opportunity for evaluation of blood oxygenation. However, development of better focus tracking techniques and data processing algorithms that can overcome the limitations of the currently existing methods will be essential for the achievement of high precision $\mu_a(\lambda)$ measurements with SOCT. In addition, since light scattering in biological tissues is orders of magnitude larger than the absorption of blood, development of strategies how to differentiate absorption from scattering in highly scattering media will be necessary.

6.2 Water absorption measured by spectroscopic OCT

As a demonstration of the potential of SOCT the water absorption in the near infrared (1150–1550 nm) was measured with a free space interferometer. The optics were selected to support the bandwidth in this wavelength region. Water filled containers with a thickness of $\sim 500 \mu\text{m}$ were measured with SOCT. The transfer function of the system was measured separately with empty containers and used for correction of the obtained spectra. Figure 6.7 shows the results: the spectral progression is well determined at relatively high absorptivities of $\sim 10 \text{ cm}^{-1}$ (fig. 6.7, top, blue line). At lower absorptivities the extracted spectrum appears modulated. This behavior might be due to window artifacts of the extraction algorithm.

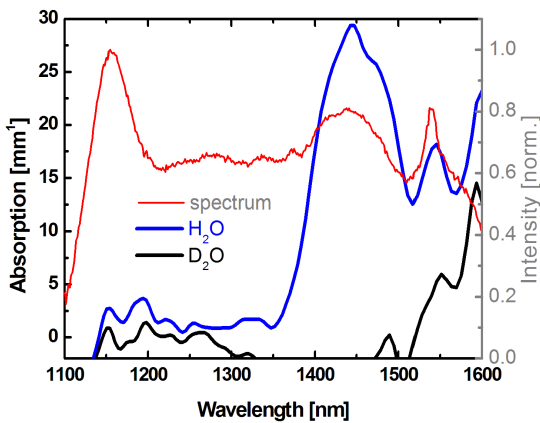
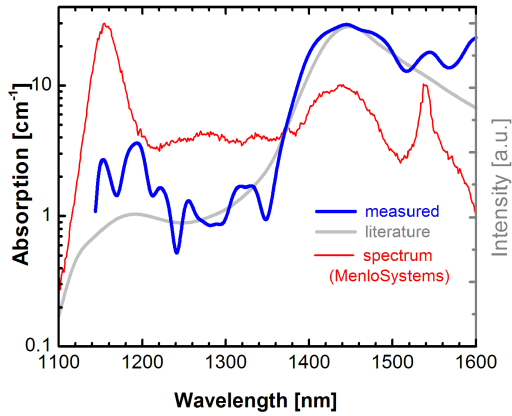


Figure 6.7: Water absorption. The top graph shows the with SOCT measured water absorption (blue) in comparison with the literature value (gray) in a logarithmic scale. The optical spectrum of the light source is indicated in red. The bottom graph compares absorption profiles of normal water (H_2O , blue) with heavy water (D_2O , black). Heavy water has nearly no absorption at 1450 nm and was used to validate the SOCT measurement.

6.3 In vivo qualitative spectroscopic OCT

A morlet wavelet transformation, which is essentially a windowed Fourier transformation with a Gaussian window, was applied to the full fringe data of an UHR TDOCT tomogram (fig. 6.8). In fig. 6.9 the intensity is given by the amplitude

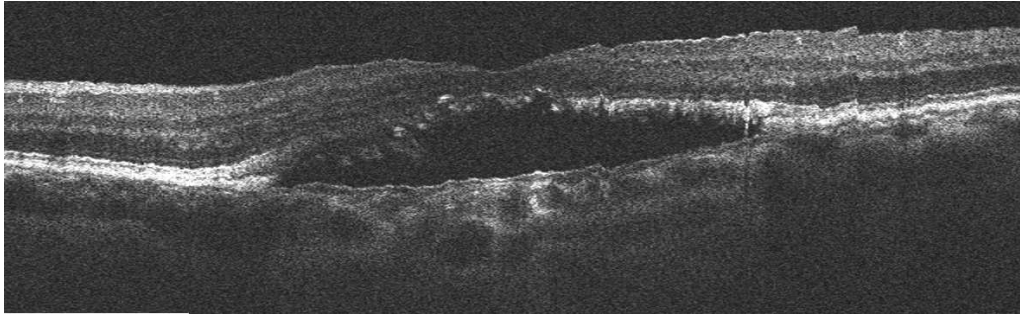


Figure 6.8: Grayscale amplitude tomogram of a foveomacular dystrophy.

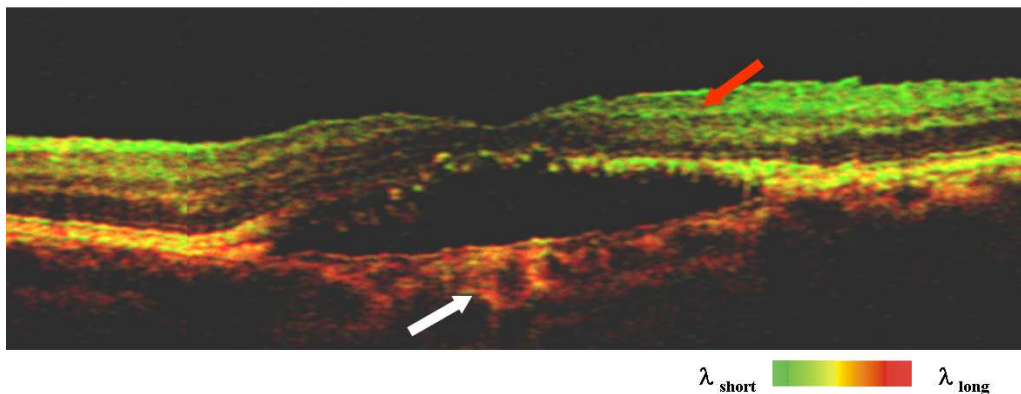


Figure 6.9: In vivo qualitative SOCT. Tomogram of a foveomacular dystrophy. Red color indicates spectral shift to longer wavelengths, green color indicates spectral shift to shorter wavelengths. Better contrast compared to amplitude tomogram is achieved (red arrow). The white arrow indicates a region in the choroid with less red shift compared to the surrounding tissue.

of the OCT signal. The color is encoded corresponding to the spectral shift of the central wavelength. There is a clear gradient from green (top of the retina) to red (bottom of the retina). This behavior is based on the fact that for shorter wavelength the scattering is higher than for longer wavelength, resulting in a higher attenuation of shorter wavelength compared to longer wavelength. The contrast between layers in spectroscopic OCT is enhanced (see fig. 6.9, red arrow) compared to the amplitude tomogram (fig. 6.8). In addition, in the central fovea, scattering is reduced compared to parafoveal scattering, indicated by a central wavelength shift towards lower wavelength (white arrow, fig. 6.9). This might be related to a loss of melanin due to the atrophy.

Chapter 7

Extraction of Depth Resolved Physiologic Information

7.1 Optophysiology: depth resolved probing of retinal physiology

The basic idea of optophysiology is the simultaneous, non-invasive probing of both retinal morphology and function, which could significantly improve the early diagnosis of various ophthalmic pathologies and could lead to better understanding of pathogenesis. This project was realized in cooperation with P. Ahnelt, R. Pflug, and H. Reitsamer from the Department of Physiology, Medical University of Vienna.

The vertebrate retina consists of several distinct layers: nuclear layers containing cell bodies can be differentiated from plexiform layers with axons and dendrites forming the neuronal network that pre-processes light evoked signals before transmission to the brain. Early stages of retinal disorders are often confined to one of these layers and are manifested by both morphological abnormalities and impaired physiological responses. Detection of such pathologies requires high resolution imaging methods. Various imaging modalities such as fundus photography, ultrasound imaging and optical coherence tomography (OCT) are clinically used for imaging retinal morphology. OCT is an emerging imaging technique that allows for non-contact, in-vivo visualization of biological tissue morphology with micrometer-scale resolution at imaging depths of 1-2 mm. Currently electrophysiological tests such as electroretinography (ERG) [168], multifocal ERG (mfERG) [169] are used for clinical assessment of retinal function.

More than 25 years ago it has been observed that the isolated retina at stimulation with visible light changes the amount of transmitted near infrared light (NIR) [170,171] Photoreceptors were determined as the main source of this effect and in the following years this method has been used for investigation and quantitative evaluation of the activation of the photoreceptor G-protein transducin and the time course of transduction events [172–175]. In the last years other physiological processes at the cellular and subcellular level such as membrane depolarization [176], cell swelling [177] and altered metabolism have been found

to cause small changes in the local optical properties of neuronal tissue that are detectable by measurement of light scattering signals. In studies carried out in isolated retinas [178] and retinal slice preparations [179] changes of NIR-light transmission and scattering have been recorded from retinal layers including the inner retina before and after light stimulation.

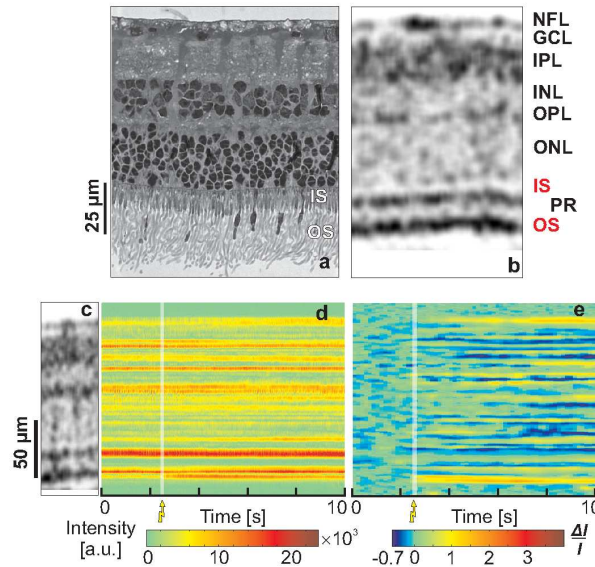


Figure 7.1: (a) Morphological and functional retinal imaging with UHROCT. Comparison between a histological cross-section; an OCT morphological tomogram (b) of the isolated retina demonstrates the ability of UHROCT to visualize the layered retinal structure. (d) OCT M-scan; optical signal measured at one position over time) and differential M-scan (e; produced from d by subtracting the background signal, calculated as a time average of the preactivation depth scans from the entire M-scan) are compared with a morphological UHROCT tomogram (c) of the location where the OCT M-scan was acquired. The white strips mark the onset and duration of the white light flash.

Recently, a novel study on in-vivo imaging of light triggered physiological responses recorded at the surface of the retina (changes of local blood flow and metabolism) was published [180]. Advances in laser technology have allowed the improvement of the OCT technique and the acquisition of depth profiles in biological tissue with an axial resolution below $3 \mu\text{m}$ [21, 23, 99, 164, 181–183]. Clinical studies in ophthalmology have demonstrated that UHROCT (ultra-high resolution OCT) is capable of non-contact, real-time, visualization of retinal morphology both in healthy and pathological retinas with sub $3 \mu\text{m}$ axial resolution [22, 85, 96]. Furthermore, the large sensitivity of OCT (~ 100 dB) allows for detection of very weak optical signals. Preliminary results on using standard axial ($\sim 20 \mu\text{m}$) resolution OCT for imaging brain function [184] in animal models and propagation of action potentials in isolated nerve fibres [185] have been reported.

Here we focus on physiological responses and demonstrate for the first time that functional UHROCT (fUHROCT) can be successfully utilized for non-contact, spatially-resolved probing of physiological responses from light-

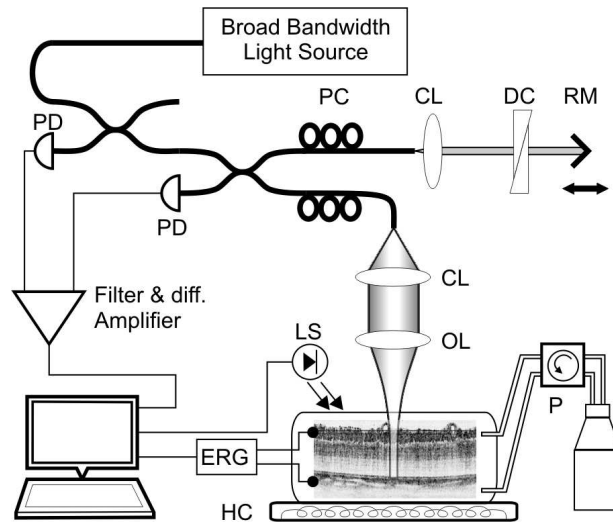


Figure 7.2: Schematic of the fUHROCT set up. Isolated, living retinas were kept in a heated chamber (HC) connected to a perfusion system (P). The UHROCT system provided a $3.5 \times 10\text{-}\mu\text{m}$ (axial \times lateral) spatial resolution and a 4.5-ms time resolution. The optical data acquisition was synchronized with the white light stimulus and the ERG recordings. CL, collimation lens; OL, objective lens; DC, dispersion compensation; RM, reference mirror; PC, polarization controllers; PD, photodiodes; LS, light stimulus.

stimulated retinal sublayers.

7.1.1 UHR OCT system

A schematic of the experimental set-up is presented in fig. 7.2. Optical recordings from isolated, living rabbit retinas were acquired by using an UHROCT system designed for optimal performance in the 1100- to 1500-nm wavelength range. The system was illuminated by a state-of-the-art fiber laser with emission spectrum centred at 1250 nm, a spectral bandwidth of 150 nm and output power of 250 mW. A light source with longer central wavelength than visible was chosen for the current study in order to avoid unwanted light stimulation of the dark-adapted retinas during the optical recordings. The UHROCT system provided $3.5\ \mu\text{m} \times 10\ \mu\text{m}$ (axial \times lateral) resolution in biological tissue, and sensitivity of 100 dB for 2 mW incident power at the sample. The time resolution achieved, 4.5 ms, was limited by the scan rate of the galvanometric scanner used in the reference arm of the UHROCT system. To prevent local heating of the retinal tissue in the vicinity of the optical beam focus the optical beam was blocked at all times except during acquisition of morphological or functional UHROCT tomograms.

7.1.2 Isolated retina sample preparation

Eyes from anesthetized rabbits were enucleated, retinas were isolated and positioned in a superfusion chamber under a nylon mesh and maintained at constant temperature of $33\ \text{°C}$ in oxygenated buffered Ames medium. The retinal pigmented epithelium was removed to allow for better perfusion of and for easy

administration of pharmacological drugs to the isolated retina. The viability of the isolated retinal samples was tested by acquiring ERG recordings during SF light stimulation. All animal procedures were approved by the Institutional Animal Care and Use Committee and conducted in accordance with the ARVO statement for the Use of Animals in Ophthalmic and Vision Research.

7.1.3 Data acquisition and processing

Since removal of the RPE can damage the outer segment (OS) of the photoreceptors (PR) and render them dysfunctional, morphological 2D UHROCT tomograms were acquired from chosen locations in the living retina prior to the functional recordings to ensure the morphological intactness of the PR layer. The chosen locations were carefully marked for subsequent histological analysis, intended to verify that none of the photoreceptors were damaged at the specified areas.

During the functional experiments the isolated retinas were stimulated with single, 200 ms long white light flashes. The brightness of the light stimulus was varied over two orders of magnitude. During the functional experiments the isolated retinas were stimulated with single, 200 ms long white light flashes. The brightness of the light stimulus was varied over two orders of magnitude. Assuming $2 \mu\text{m}^2$ collection area per rod the average number of photons per flash per PR, calibrated to the maximum sensitivity at 505 nm were set to approximately 27, 370 and 2300 photons/rod/flash, thus staying well beneath the bleaching limit and allowing for recovery within the 2-3 min inter-scan period [186]. The time course of the light stimulus consisted of 2.5 s pre-stimulation, 0.2 s single white light flash and 7.3 s post-stimulation periods followed by intensity dependent adaptation time of up to 3 min. The UHROCT depth-scans were combined to form two-dimensional raw data M-scans presenting the retinal reflectivity profile as a function of time (similar to M-scans in ultrasound imaging).

The processing of the optical data involved application of a cross-correlation algorithm to account for any movement of the retina caused by the solution flow; calculation of the optical background (average over the pre-stimulation depth-scans for each individual M-scan) and generation of differential M-scans showing $\Delta I/I$, where I is the total average optical signal intensity within an depth-scan, and ΔI is the difference between the signal and the time averaged optical background determined from the pre-stimulation depth-scans of the raw data M-scans. Fast variations in the optical speckle pattern were suppressed by applying band pass filter.

7.1.4 Results

Fig. 7.1 shows a histological cross-section (a) and the corresponding morphological UHROCT tomogram (b) acquired from a location in the retina where functional measurements were performed. Retinal layers with high optical reflectivity, such as the nerve fiber layer and the plexiform layers appear dark in UHROCT tomograms because of increased light scattering. Direct comparison between

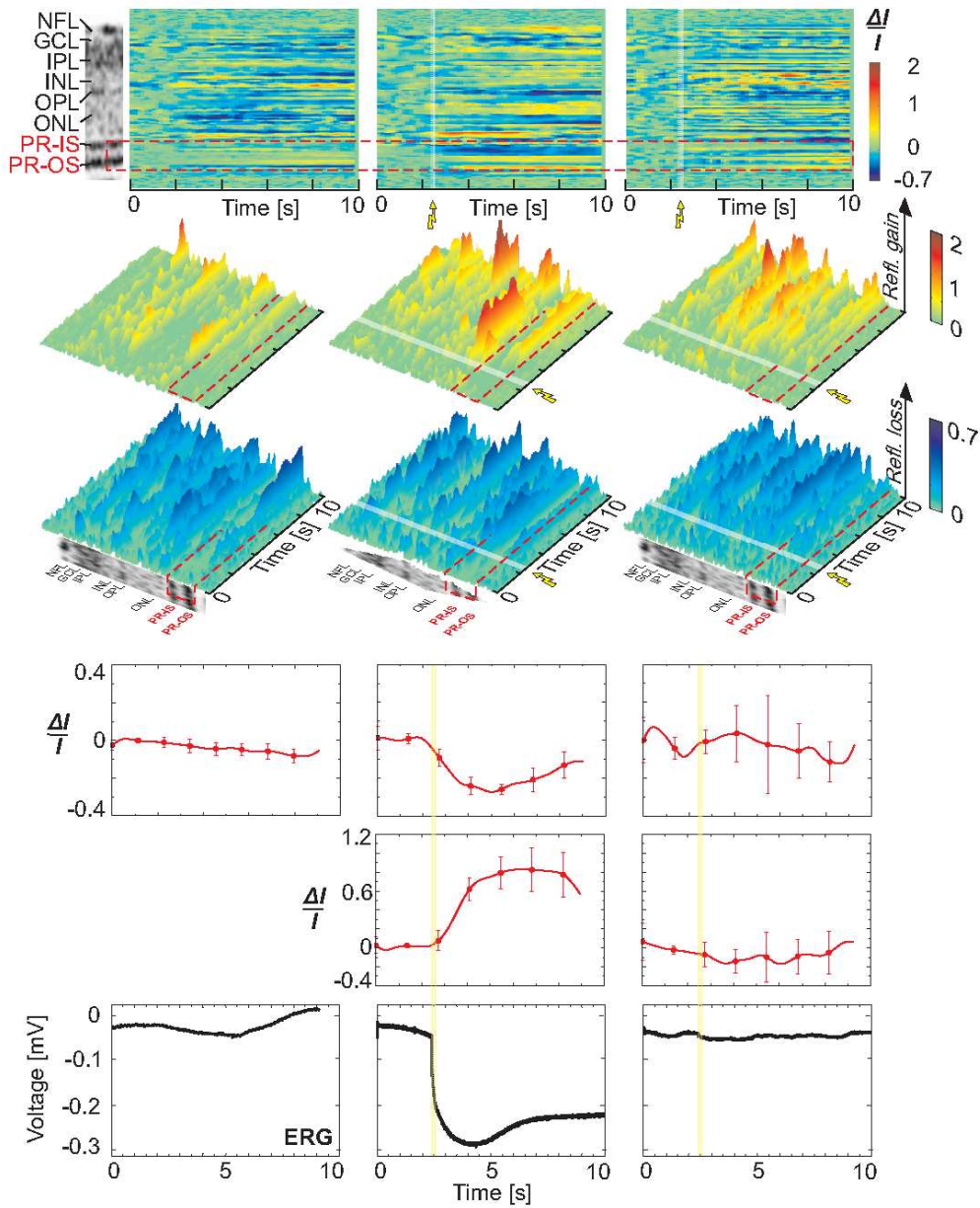


Figure 7.3: fUHROCT data: the PR response. (a) A morphological retinal image compared with differential M-scans corresponding to DS (no light stimulus; Left), an SF scan in normal retina (Middle), and an SF scan in retina with inhibited PR function (Right). The red dashed line marks the location of the PR layer in all M-scans. (b and c) Visualization of the differential M-scans in 3D, emphasizing the positive and negative optical signals, respectively, is shown. (d and e) The time course of the optical signals extracted from the IS (d) and OS (e) of the PR, respectively. The error bars show the SD computed by averaging 10 differential M-scans. (f) The ERG recordings acquired simultaneously with the fUHROCT M-scans. The white (a-c) and yellow (d-f) strips in the M-scans and the extracted time courses mark the onset and time duration of the SF light stimulus.

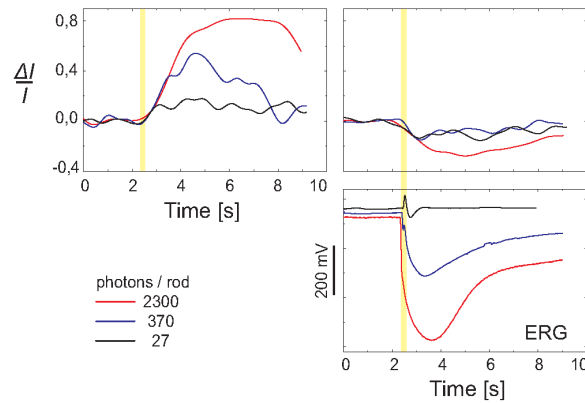
fig. 7.1a and 7.1b demonstrates that the spatial resolution of UHROCT is sufficient to clearly visualize all retinal layers. The histological cross-section and the UHROCT tomogram exhibit an intact outer segment (OS) of the photoreceptor (PR) layer - indicating morphological completeness for signal transduction.

To test if UHROCT is capable of detecting changes in the retina reflectivity triggered by light stimulation, a dark-adapted, isolated living retina was exposed to a single flash (SF) of white light at 3 different intensities while fUHROCT data was acquired synchronously with ERG recordings. Fig. 7.1d presents a raw data fUHROCT M-scan that shows the retinal depth reflectivity profile as a function of time. Comparison of the M-scan with a 2D morphological UHROCT image (fig. 7.1c) allows correlation to the morphological origin of the optical reflectivity changes observed in the fUHROCT images. To improve the visibility of the stimulus-induced optical changes, the raw data M-scan (fig. 7.1d) was normalized to the optical background (see methods section) and a differential M-scan (fig. 7.1e) was generated. The white strips on fig. 7.1d and 7.1e indicate the onset and duration of the light flash. The differential M-scan exhibited pronounced increase in the optical reflectivity in the area corresponding to the PR outer segment for the time period immediately following the light flash. Both positive and negative changes in the tissue reflectivity were observed in the inner retina.

To rule out the possibility that the observed optical changes are imaging artifacts, three types of control experiments were carried out. Each type was designed to alter the normal physiological state of a specific group of retinal neurons by utilizing either dark adaptation versus light stimulation or pharmacological inhibition. During the first type of experiments dark scans (DS) - 10 second lasting fUHROCT recordings in dark-adapted retinas without light stimulus were alternated with SF measurements of the same duration after an intensity dependent dark adaptation time of up to 3 min at a fixed location in the retina. In the second type of experiments SF recordings were acquired from preparations where the normal response of the photoreceptors to light stimulation was inhibited by superfusing the retina with 44 mM potassium solution corresponding to a potassium equilibrium potential at the level of the photoreceptor dark membrane potential. In the third type of experiments pharmacological drugs (30 μ M solutions of L-2-amino-4-phosphono butyric acid (APB) and 2,3 dihydroxy-6-nitro-7-sulfamoyl-benzo-f-quinoline (NBQX) [187, 188] were used to block inner retina function, specifically, the normal response of the ON- and OFF- bipolar cells.

Fig. 7.3 summarizes results from the first and second type of experiments. The top row compares differential M-scans acquired during DS, SF and SF + PR inhibition with a morphological scan (top left). The red dashed line marks the boundaries of the PR layer. The second and third rows show the same M-scans in 3D for better visualization of the time course and magnitude of the positive and negative optical changes. The next two rows present traces extracted from the differential M-scans at locations corresponding to the inner (IS) and outer segments (OS) of the photoreceptor layer. These show the average retinal response and the standard deviation for 10 selected consecutive measurements. The last row in fig. 7.3 shows the corresponding traces from the ERG recordings.

Figure 7.4: fUHROCT data: the stimulus-dependent PR response. (a and b) Time course of ensemble averages of 10 consecutive differential optical signals extracted from a 5- to 6- μm -wide strip of the IS and OS reflexes of the PR, respectively. The illumination corresponds to 27 (black), 370 (blue), and 2300 (red) photons/rod/flash. The flash is indicated by a yellow stripe. (c) Corresponding ERG.



As expected, during DS (no light stimulus) neither the optical reflectivity of the PR layer, nor the ERG signals changed significantly with time. In the first and second type of experiments during SF recordings conducted in normal dark adapted retinas, the reflectivity of the IS and OS of the PR layer exhibited significant intensity dependent negative and positive changes respectively after application of the light stimulus. The ERG recordings showed a large negative response since the absence of pigment epithelium and application of a bright light stimulus reduced the ERG to its PIII component, in respect to the normal function of the photoreceptors. The onset of both the optical and the ERG signals correlated well with the onset of the light flash. In the case of K^+ inhibited PR function, the optical changes observed in the IS and OS of the PR layer appeared close to the optical background level and showed no correlation to the onset of the light stimulus. Similar signals were observed in the ERG recording.

Fig. 7.4 depicts stimulus dependent photoreceptor responses detected by fUHROCT. The positive (left) and negative (mid) responses are time courses of ensemble averages of ten consecutive differential optical signals extracted from a 5–6 μm wide strip of the inner (IS) and outer segment (OS) reflexes of the PR respectively. The illumination corresponds to 27 (black), 370 (blue) and 2300 (red) photons/rod/flash. The flash is indicated by a yellow stripe. Corresponding ERG recordings are also presented (right).

Fig. 7.5 summarizes results from the first and third type of experiments. The top row compares differential M-scans acquired during DS, SF and SF+APB+NBQX inhibition with a morphological scan (top left). The red dashed line shows the borders of the retinal inner plexiform layer (IPL). Considering that the IPL does not have clearly defined sub-layered morphology and appears fairly homogeneous within the axial resolution limits of this experiment, the optical traces extracted from each differential M-scan were spatially averaged over the full width of the IPL. The small amplitudes obtained from the inner plexiform layer did not allow getting significantly different responses at different light intensities. The second and third rows show the same M-scans in 3D for better visualization of the time course and the magnitude of the observed

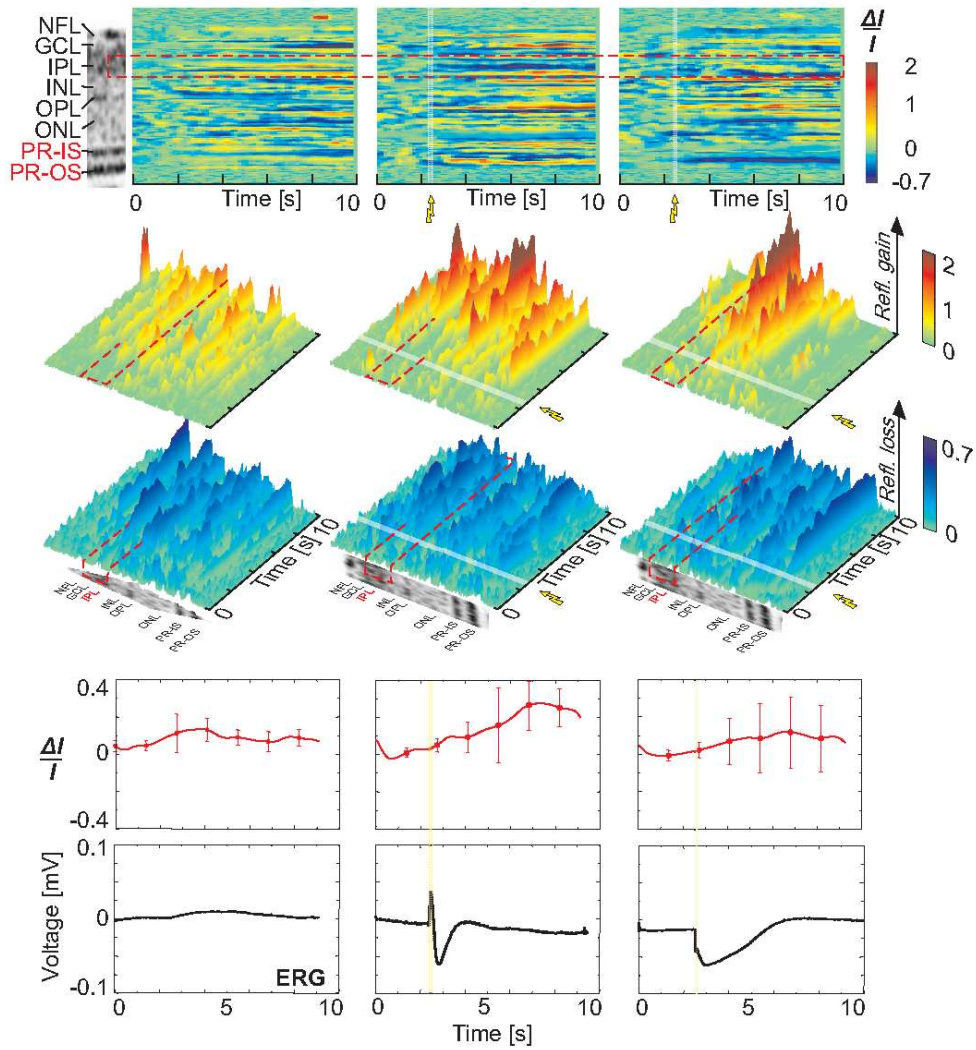


Figure 7.5: fUHROCT data: the IPL response. (a) A morphological retinal image compared with differential M-scans corresponding to a DS (no light stimulus) (Left), an SF scan in normal retina (Middle), and an SF scan in retina with inhibited bipolar cell function in the IPL (Right). The red dashed line marks the boundaries of the IPL in all M-scans. (b and c) A 3D visualization of the positive and negative optical signals in differential M-scans. (d) The time course of the optical signals (average across the width of the IPL) extracted from the IPL. The error bars show the standard deviation computed by averaging 10 differential M-scans. (e) The ERG recordings acquired simultaneously with the fUHROCT M-scans. The white (a-c) and yellow (d-e) strips in the M-scans mark the onset and time duration of the SF light stimulus.

positive and negative optical changes. Rows 4 and 5 show the averaged optical signals and the corresponding traces from the ERG recordings. The white strips in the differential M-scans and the yellow strips in the optical and ERG traces mark the activation of the light stimulus.

During DS both the average optical reflectivity of the IPL, as well as the ERG traces, exhibited slow, small magnitude changes close to the measured physiological noise level. During SF recordings conducted in normal dark-adapted retinas, the averaged IPL reflectivity exhibited changes over time that correlated with the light stimulus onset. In this case the brightness of the light stimulus was adapted to result in a pronounced b-wave in the ERG recording - an indication for proper function of the inner retina - the ERG trace showed both a positive b-wave and a negative PIII potential, corresponding to properly functioning visual pathway from the PR layer to the nerve fiber layer. Changes in the optical reflectivity, correlated with the light stimulus were also observed in the outer plexiform layer (OPL). The application of APB and NBQX drugs during the SF experiments resulted in altered reflectivity of the IPL and OPL. In this case, the average optical traces extracted from the IPL exhibited low magnitude changes, uncorrelated with the onset of the light stimulus. As expected, blocking the photoreceptor/bipolar cell synapses caused disappearance of the b-wave in the corresponding ERG recording, while the PIII negative response reappeared. As reported in [188], the presence of the PIII potential corresponds to normal function of the photoreceptors, while the loss of the b-wave is generally attributed to blocked transmission from the photoreceptors to the bipolar cells.

7.1.5 Discussion

The results described above clearly demonstrate that fUHROCT is capable of detecting small changes in the optical reflectivity of living retinas, caused by external stimuli with high spatial resolution. The control experiments certify that the observed signals appear because of statistically significant changes in the retinal reflectivity, due to the altered physiological state triggered by light-stimuli. Functional UHROCT experiments were carried out on 14 isolated, non-inhibited retinas and more than 370 SF M-scans were acquired at 30 different locations. Experiments with pharmacological inhibition were carried out in 6 retinas. Optical signals extracted from the IS/OS of the PR layer exhibited excellent correlation with the ERG recordings and the light stimulus onset, as well as very high reproducibility ($\approx 72\%$). Averaged optical traces extracted from the IPL were well correlated with the light stimulus onset and the ERG, but exhibited fairly low reproducibility in terms of the shape and sign of the optical changes at different transversal locations.

The differential magnitudes (i.e. the signals initiated by the stimulus compared to the dark adapted ones) of the observed positive and negative optical changes were time dependent and varied between 5% and 80% depending on the location within the retina (PR or IPL) and the type of experiment. Statistical analysis performed on sets of 10 consecutive M-scans showed that in the case of SF recordings from normal dark-adapted retinas, the optical traces in

the PR and the IPL after the light flash were statistically different ($p = 0$) from the optical background (pre-stimulation). In the case of DS recordings or the KCL and APB+NBQX inhibited retinas, there was no statistical difference ($0.93 < p < 0.98$) between the pre-stimulus and post-stimulus recorded data.

UHROCT is sensitive to local variations in the reflectivity of the imaged object, which can be related to changes in its shape, size and refractive index of different morphological features. Although the exact mechanism that causes the observed optical signals is currently not known, a number of physiological processes occurring during and immediately after light stimulation may result in time-dependent changes of the retinal reflectivity.

Origin of the optical signals in the PR layer. Changes in light transmission and scattering in the photoreceptor outer segment layer have been reported by various groups. NIR scattering signals have been extensively investigated in bovine rod outer segments in a number of studies. Their origin was described [170, 171] and subsequently NIR optical measurements were used to investigate the activation and/or effector interaction of the G-protein transducin [172–174]. Dawis and Rossetto [179] observed a relatively slow increase in light transmission of light activated rod outer segments of unknown origin in the anuran retina. Yao et al. [178] used a modified standard resolution OCT system with fixed depth selection to record a light evoked decrease of NIR scattering in the photoreceptor and an increase in the ganglion cell layer. Their work suggested that cell swelling and shrinkage and membrane depolarisation resulting from the ionic fluxes are the most probably cause for the observed optical changes. The hypothesis was supported by the swelling and shrinking of cells produced by ionic fluxes associated with membrane polarization as a possible cause for these effects which is supported by the voltage dependence of the amount of light scattered by *Aplysia* axons during action potentials [176].

Photoreceptors hyperpolarize during light stimulation which may result in a temporary modulation of the optical reflectivity of the cell membrane. However scattering changes observed in our study are relatively slow and correspond more to the time course of ion shifts involved in ERG generation than to the rapid hyperpolarization of the photoreceptor membrane evoked by light stimuli. In addition we observe two different scattering signals, one at the level of the OS and the other at the level of the IS. While the OS are packed with thousands of densely stacked discs that contain the photosensitive agent rhodopsin and the G-protein that mediates phototransduction, the inner segment ellipsoids of the PR consist of mitochondria tightly packed in parallel [189]. Altered metabolic rates during light stimulation could cause changes in the mitochondrial refractive index, which in turn may result in decrease of the PR inner segment reflectivity. Actin-dependent retinomotor activity is a general phenomenon of the non-mammalian vertebrate photoreceptors and pigment epithelial processes [190]. Currently there is no evidence for this phenomenon in mammalian retinas. However adaptive alignment and realignment towards the direction of highest light intensity (pupil) has been described and attributed to the activity of inner segment cytoskeletal elements, actin fibers and microtubuli [191, 192]. We cannot

exclude that minute light-induced motor responses could contribute to the optical reflectivity changes observed in the inner-outer segments of the PR.

The cross-section of the imaging fUHROCT beam was $\sim 10\text{--}20\ \mu\text{m}$ in diameter, which, considering the size of a single photoreceptor ($\sim 2\ \mu\text{m}$ in diameter), was sufficient to illuminate $\sim 15\text{--}50$ photoreceptors, assuming a fill factor of 0.5 of the photoreceptor matrix. The large number of simultaneously probed photoreceptors may account for the relatively large magnitude and the high reproducibility rate of the optical signals detected by fUHROCT. Since the functional experiments were conducted in isolated retinas, the RPE was removed, which prevented normal regeneration of the visual pigment rhodopsin. Temporary and later permanent bleaching of the photoreceptors resulted in gradual decrease in signal magnitude, followed by complete loss of the optical signals over time, when multiple SF recordings were acquired. If fUHROCT experiments are conducted in-vivo, the photoreceptor bleaching would be temporary, which should improve the reproducibility rate of the detected optical signals significantly.

Origin of the optical signals in the IPL/OPL. The neuropil of the retinal inner and outer plexiform layers has a very complex microstructure; the OPL contains the dendritic extensions of photoreceptors, horizontal and bipolar cells; in the IPL interactions of a variety of specialized amacrine cells, axonal terminals of ON- and OFF- bipolar cells and ganglion cells takes place. All synapses contain a large number of dynamically cycled micro-vesicles, while the dendrites are packed with round mitochondria, ribosomes and neurofilaments. Exposure of a dark-adapted retina to light causes transmission of electrical potentials through the axonal and dendritic extensions of the different cells, which in turn polarize the cell membranes and change both the synaptic states and the mitochondrial metabolism. It was expected that these processes would cause positive changes in the IPL and OPL reflectivity after onset of the light stimulus, with some spatial variation over the thickness of each layer, as well as time-dependent variations in the optical signal magnitude resulting from differences in the time course of the transmitted electrical signals generated by the different cells. Such changes were indeed observed in most of the SF experiments. However, on few occasions the M-scans exhibited slow decrease in the IPL and OPL reflectivity immediately following the single flash. A possible cause for the decrease in the IPL and OPL reflectivity could be the swelling of Müller cells that more or less follows the transmission of electrical signals within the retina. Müller cells are Glia cells that extend vertically through the entire thickness of the retina. If the body of a swollen Müller cell partially overlaps with the fUHROCT imaging beam, light would propagate through the Müller cell with very little scattering, which in turn would locally reduce the reflectivity of both plexiform layers.

The **current manuscript** focused on optical changes observed only in selected retinal layers - PR and IPL. The reason was that in general, retinal nuclear layers such as the inner nuclear, outer nuclear and the ganglion cell layers have low optical reflectivity, which would render detection of small optical signals related to retinal physiology very difficult. The retinal nerve fiber layer (NFL) is comprised of the axonal extensions of ganglion cells and is highly reflective.

Therefore it would be of interest to investigate the optical response of the NFL during propagation of action potentials related to SF light stimulation of the retina. However, in our case fUHROCT recordings were acquired mostly from the mid ventral part of the rabbit retina, where the NFL was very thin, which impeded the extraction of optical traces.

The complex morphology and physiology of the retinal plexiform layers accounts for the short time scale variations in the IPL and OPL reflectivity observed in the functional SF M-scans, as well as the fairly low reproducibility rate of the optical signals in terms of shape and sign. Future experiments and technological development may allow for separation of the contributions from different types of cells and their physiological state to the total optical response of the retinal plexiform layers to SF stimulation. In conclusion, we have demonstrated for the first time that fUHROCT can be used successfully to probe light-induced retinal response non-invasively and with high depth resolution. Provided that better understanding of the relation between retinal optical reflectivity and physiology is gained by future experiments, fUHROCT could potentially develop as a clinical method for simultaneous high resolution imaging of the morphology and physiology of the human retina.

Chapter 8

Future Perspectives of Ophthalmic Ultrahigh Resolution OCT

Adaptive Optics A 3D adaptive optics UHR OCT system is already under development. First results of correcting the aberrations and demonstrating $5\ \mu\text{m}$ transversal resolution in a human eye has been shown in frequency domain UHR OCT [193] (see fig. 8.1).

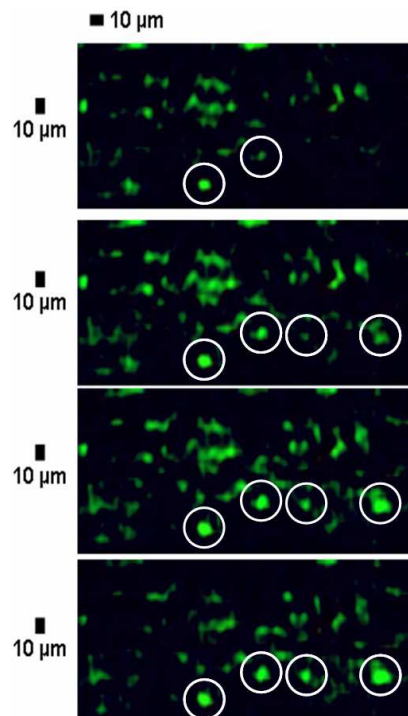


Figure 8.1: Groups of highly scattering small dots in the external limiting membrane (RPE), are apparent in consecutive en-face images and belong to groups of terminal bars of photoreceptors.

Contrast enhancement. Contrast agents are widely used in biomedical imaging. Microspheres with special designed absorption behaviour [194] and their ability to bind to designated biomolecules can be used as contrast agents for spectroscopic OCT. Different time-frequency analysis methods could be applied to obtain spectral information with UHR OCT. Quantitative spectroscopic UHR OCT will provide a possibility to evaluate physiological processes *in vivo*, as blood oxygenation, blood flow, and be a useful tool for early cancer diagnosis.

Technological progress. Faster cameras with improved read out rates and more pixels will lead to an increase in speed and resolution for three-dimensional UHR OCT. Rendering on the graphic chip (GPU) will considerably increase the speed of 3D-rendering. Complex signal processing computations can be ported to dedicated digital signal processing units (DSP).

In segmentation statistical methods could be helpful. Algorithms combining different methods like principal component analysis (PCA) and neuronal networks could be a possible solution for segmentation. Time-consuming algorithms can be calculated with distributed computing.

Signal processing & segmentation. Signal processing algorithms for modeling of the UHR OCT signal followed by extraction of signal parameters as absorption, scattering, refractive index, need to be applied. Segmentation remains challenging, but a combination of different methods such as principal component analysis, neuronal networks and genetic algorithm could be an important step toward the solution.

In vivo optophysiology. First preliminary data was conducted in *in vivo* optophysiology measurements (see fig. 8.2). A less invasive simultaneous electroretinogram should be used during the measurements employing different electrodes, e.g. gold foil electrodes. Data should also be analyzed with statistical methods, as peak finding or principal component analysis.

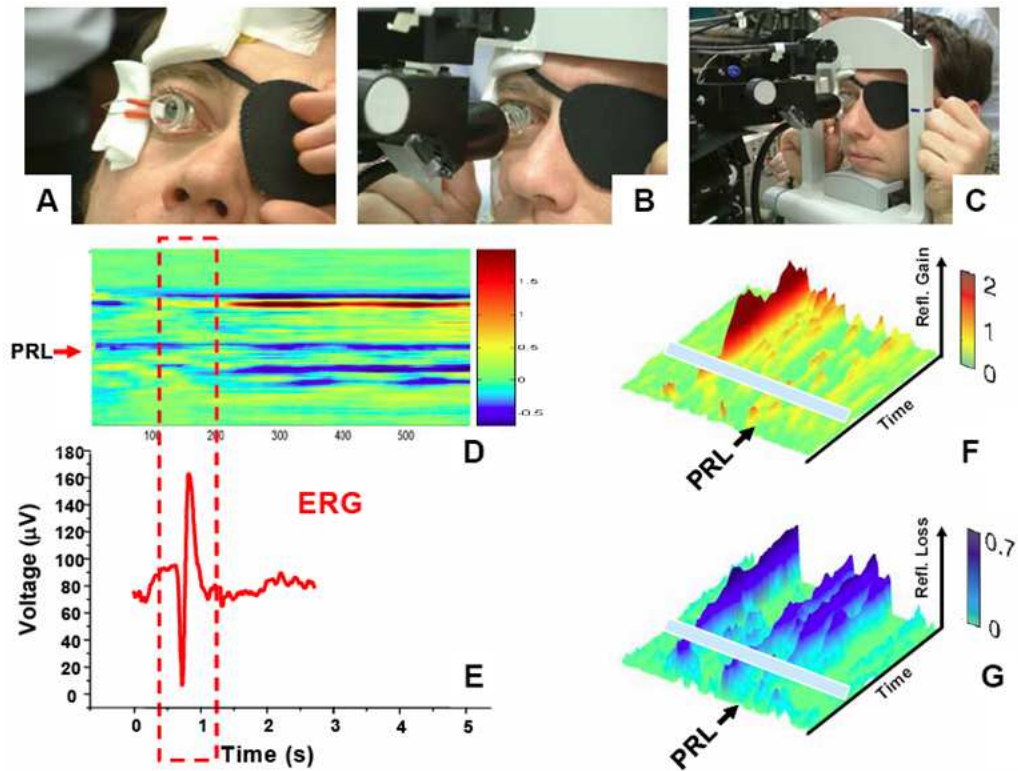


Figure 8.2: Preliminary results of in vivo human optophysiology in a normal human subject slightly parafoveal. A-C: in vivo OCT system with ERG contact electrode for simultaneous ERG measurements. D: morphological M-scan; E: corresponding ERG; F-G: three-dimensional representation of and differential M-scan indicated in D. PRL: photo receptor layer; red dashed box indicates time point and length of the white light stimulus.

Bibliography

- [1] J. Ambrose and G. Hounsfield. Computerized transverse axial tomography. *Br. J. Radiol.*, 46:148–149, 1973.
- [2] P. C. Lauterbur. Image formation by induced local interactions: Examples employing nuclear magnetic resonance. *Nature*, 242:190–191, March 1973.
- [3] G. H. Mundt and W. F. Hughes. Ultrasonics in ocular diagnosis. *Am. J. Ophthalmol.*, 41(3):488–498, Mar 1956.
- [4] Frederic L. Lizzi and D. Jackson Coleman. History of ophthalmic ultrasound. *J. Ultrasound Med.*, 23(10):1255–1266, October 2004.
- [5] T. Olsen. The accuracy of ultrasonic determination of axial length in pseudophakic eyes. *Acta Ophthalmol (Copenh.)*, 67(2):141–144, April 1989.
- [6] JC Bamber and M Trstam. *The Physics of Medical Imaging*, chapter Diagnostic ultrasound, pages 319–388. Adam Hilger Bristol and Philadelphia, PA, 1988.
- [7] CJ Pavlin, JA McWhae, HD McGowan, and FS Foster. Ultrasound biomicroscopy of anterior segment tumors. *Ophthalmology*, 99(8):1220–1228, August 1992.
- [8] D. Z. Reinstein, R. H. Silverman, M. J. Rondeau, and D. J. Coleman. Epithelial and corneal thickness measurements by high-frequency ultrasound digital signal processing. *Ophthalmology*, 101(1):140–146, Jan 1994.
- [9] D. J. Coleman, R. H. Silverman, M. J. Rondeau, and F. L. Lizzi. New perspectives: 3-D volume rendering of ocular tumors. *Acta Ophthalmol Suppl*, 204:22, 1992.
- [10] R. H. Webb, G. W. Hughes, and O. Pomerantzeff. Flying spot tv ophthalmoscope. *Appl. Opt.*, 19:2991–2997, 1980.
- [11] R. H. Webb, G. W. Hughes, and F. C. Delori. Confocal scanning laser ophthalmoscope. *Appl. Opt.*, 26:1492–1499, 1987.
- [12] J.F. Bille, A.W. Dreher, and G. Zinser. *Noninvasive Diagnostic Techniques in Ophthalmology*, chapter Scanning laser tomography of the living human eye, pages 528–547. Springer-Verlag, New York, 1990.
- [13] B. R. Masters and A. A. Thaer. Real-time scanning slit confocal microscopy of the in vivo human cornea. *Appl. Opt.*, 33(4):695–701, 1994.
- [14] B. R. Masters. Three-dimensional confocal microscopy of the living in situ rabbit cornea. *Opt. Express*, 3(9):351–355, 1998.
- [15] R. C. Youngquist, S. Carr, and D. E. N. Davies. Optical coherence-domain reflectometry: a new optical evaluation technique. *Opt. Lett.*, 12(3):158–160, March 1987.

- [16] K. Takada, I. Yokohama, K. Chida, and J. Noda. New measurement system for fault location in optical waveguide devices based on an interferometric technique. *Appl. Opt.*, 26(9):1603–1606, May 1987.
- [17] A.F. Fercher and E. Roth. Ophthalmic laser interferometer. In *Proc. SPIE*, volume 658, pages 48–51, 1986.
- [18] D. Huang, E.A. Swanson, C.P. Lin, J.S. Schuman, W.G. Stinson, W. Chang, M.R. Hee, T. Flotte, K. Gregory, C.A. Puliafito, and J.G. Fujimoto. Optical coherence tomography. *Science*, 254:1178–1181, 1991.
- [19] J. G. Fujimoto, S. De Silvestri, E. P. Ippen, C. A. Puliafito, R. Margolis, and A. Oseroff. Femtosecond optical ranging in biological systems. *Opt. Lett.*, 11(3):150–152, March 1986.
- [20] A. F. Fercher, C. K. Hitzenberger, W. Drexler, G. Kamp, and H. Sattmann. In vivo optical coherence tomography. *Am J Ophthalmol*, 116(1):113–114, Jul 1993.
- [21] W. Drexler, U. Morgner, F. X. Kärtner, C. Pitris, S. A. Boppart, X. D. Li, E. P. Ippen, , and J. G. Fujimoto. In vivo ultrahigh-resolution optical coherence tomography. *Opt. Lett.*, 24(17):1221–1223, September 1 1999.
- [22] W. Drexler, U. Morgner, R.i K. Ghanta, F. X. Kärntner, J. S. Schuman, and J. G. Fujimoto. Ultrahigh-resolution ophthalmic optical coherence tomography. *Nat. Med.*, 7(4):10–15, April 2001.
- [23] B. Považay, K. Bizheva, A. Unterhuber, B. Hermann, H. Sattmann, A. F. Fercher, W. Drexler, A. Apolonski, W. J. Wadsworth, J. C. Knight, P. St. J. Russell, M. Vetterlein, and E. Scherzer. Submicrometer axial resolution optical coherence tomography. *Opt. Lett.*, 27(20):1800–1802, October 2002.
- [24] A. F. Fercher. Optical coherence tomography. *J. Biomed. Opt.*, 1(2):157–173, April 1996.
- [25] A. F. Fercher and C. K. Hitzenberger. *Progress in Optics*, chapter Optical Coherence Tomography, pages 215–301. Progress in Optics. Elsevier Science B. V., 2002.
- [26] A.F. Fercher, W. Drexler, C.K. Hitzenberger, and T. Lasser. Optical coherence tomography – principles and applications. *Rep. Prog. Phys*, 66:239–303, 2003.
- [27] M. R. Hee, D. Huang, E. A. Swanson, and J. G. Fujimoto. Polarization-sensitive low-coherence reflectometer for birefringence characterization and ranging. *J. Opt. Soc. Am. B*, 9(6):903–908, June 1992.
- [28] M. Mujat, R. C. Chan, B. Cense, B. H. Park, C. Joo, T. Akkin, T. C. Chen, and J. F. de Boer. Retinal nerve fiber layer thickness map determined from optical coherence tomography images. *Optics Express*, 13(23):9480–9491, Nov 14 2005.
- [29] E. Götzinger, M. Pircher, and C. K. Hitzenberger. High speed spectral domain polarization sensitive optical coherence tomography of the human retina. *Opt. Express*, 13:10217–10229, 2005.
- [30] J. A. Izatt, M. D. Kulkarni, S. Yazdanfar, J. K. Barton, and A. J. Welch. In vivo bidirectional color doppler flow imaging of picoliter blood volumes using optical coherence tomography. *Opt. Lett.*, 22(18):1439–1441, September 15 1997.
- [31] Z. Chen, Y. Zhao, S. M. Srinivas, J. S. Nelson, N. Prakash, and R. D. Frostig. Optical doppler tomography. *IEEE J. Sel. Top. Quantum Electron.*, 5(4):1134–1142, July/August 1999.

- [32] Yoshihisa Aizu and Toshimitsu Asakura. Coherent optical techniques for diagnostics of retinal blood flow. *J. Biomed. Opt.*, 4(1):61–75, 1999.
- [33] R. A. Leitgeb, L. Schmetterer, W. Drexler, A. F. Fercher, R. J. Zawadzki, and T. Bajraszewski. Real-time assessment of retinal blood flow with ultrafast acquisition by color doppler fourier domain optical coherence tomography. *Opt. Express*, 11(23):3116–3121, November 17 2003.
- [34] B. R. White, M. C. Pierce, N. Nassif, B. Cense, B. Hyle Park, G. J. Tearney, B. E. Bouma, T. C. Chen, and J. F. de Boer. In vivo dynamic human retinal blood flow imaging using ultra-high-speed spectral domain optical doppler tomography. *Opt. Express*, 11(25):3490–3497, December 15 2003.
- [35] Michael A. Choma, Siavash Yazdanfar, and Joseph A. Izatt. Wavelet and model-based spectral analysis of color doppler optical coherence tomography. *Opt. Commun.*, In Press, 00 2006.
- [36] Y. Pan, E. Lankenau, J. Welzel, R. Birngruber, and R. Engelhardt. Optical coherence-gated imaging of biological tissues. *IEEE J. Sel. Top. Quantum Electron.*, 2:1029–1034, 1996.
- [37] J. M. Schmitt, S. H. Xiang, and K. M. Yung. Differential absorption imaging with optical coherence tomography. *J. Opt. Soc. Am. A*, 15(9):2288–2296, September 1998.
- [38] U. Morgner, W. Drexler, F.X. Kärtner, X.D. Li, C. Pitris, E.P. Ippen, and J.G. Fujimoto. Spectroscopic optical coherence tomography. *Opt. Lett.*, 2(2):111–113, January 15 2000.
- [39] R. Leitgeb, M. Wojtkowski, A. Kowalczyk, C.K. Hitzenberger, M. Sticker, and A.F. Fercher. Spectral measurement of absorption by frequency domain optical coherence tomography. *Opt. Lett.*, 25:820–822, 2000.
- [40] D. J. Faber, F. J. van der Meer, M. C.G. Aalders, and T. G. van Leeuwen. Quantitative measurement of attenuation coefficients of weakly scattering media using optical coherence tomography. *Opt. Express*, 12(19):4353–4365, 2004.
- [41] M. D. Kulkarni, C. W. Thomas, and J. A. Izatt. Image enhancement in optical coherence tomography using deconvolution. *Electronics Letters*, 33(16):1365–1367, Jul 31 1997.
- [42] D. Marks, P. S. Carney, and S. A. Boppart. Adaptive spectral apodization for sidelobe reduction in optical coherence tomography images. *Journal of Biomedical Optics*, 9(6):1281–1287, Nov-Dec 2004.
- [43] A. F. Fercher, C. K. Hitzenberger, M. Sticker, R. Zawadzki, B. Karamata, and T. Lasser. Numerical dispersion compensation for partial coherence interferometry and optical coherence tomography. *Optics Express*, 9(12):610–615, Dec 3 2001.
- [44] D. L. Marks, A. L. Oldenburg, J. J. Reynolds, and S. A. Boppart. Digital algorithm for dispersion correction in optical coherence tomography for homogeneous and stratified media. *Appl. Opt.*, 42(2):204–217, January 10 2003.
- [45] M. Wojtkowski, V. J. Srinivasan, T. H. Ko, J. G. Fujimoto, A. Kowalczyk, and J. S. Duker. Ultrahigh-resolution, high-speed, fourier domain optical coherence tomography and methods for dispersion compensation. *Opt. Express*, 12(11):2404–2422, May 31 2004.

- [46] D. C. Adler, T. H. Ko, and J. G. Fujimoto. Speckle reduction in optical coherence tomography images by use of a spatially adaptive wavelet filter. *Optics Letters*, 29(24):2878–2880, Dec 15 2004.
- [47] D. L. Marks, T. S. Ralston, and S. A. Boppart. Speckle reduction by i-divergence regularization in optical coherence tomography. *J. Opt. Soc. Am. A*, 22(11):2366–2371, Oct 2005.
- [48] Georg A. Reider. *Photonik - Eine Einführung in die Grundlagen*. Springer-Verlag, 1997.
- [49] A.F. Fercher, C.K. Hitzenberger, M. Sticker, R. Zawadzki, B. Karamata, and T. Lasser. Dispersion compensation for optical coherence tomography depth-scan signals by a numerical technique. *Opt. Commun.*, 204:67–74, 2002.
- [50] Claudio Vinegoni, Jeremy Bredfeldt, Daniel Marks, and Stephen Boppart. Nonlinear optical contrast enhancement for optical coherence tomography. *Opt. Express*, 12(2):331–341, January 26 2004.
- [51] Richard Phillips Feynman, Robert B Leighton, and Matthew L Sands. *The Feynman Lectures on Physics*. Redwood City, Calif., 1989.
- [52] Scott Prahl. Scott prahl's database. Internet, <http://omlc.ogi.edu/spectra/>.
- [53] M. V. Klein and T. E. Furtak. *Optik*, chapter 2.2 - Reflexion und Transmission an Grenzflächen, pages 56–68. Springer, 1988.
- [54] E. A. Swanson, D. Huang, M. R. Hee, J. G. Fujimoto, C. P. Lin, and C. A. Puli-afito. High-speed optical coherence domain reflectometry. *Opt. Lett.*, 17(2):151–153, January 1992.
- [55] E. A. Swanson, D. Huang, M. R. Hee, J. G. Fujimoto, C. P. Lin, and C. A. Puli-afito. High-speed optical coherence domain reflectometry: erratum. *Opt. Lett.*, 17(7):547–549, April 1992.
- [56] W S Boyle and G E Smith. Charge coupled semiconductor devices. *Bell Syst. Tech. J.*, 49:587–593, 1970.
- [57] G. L. Abbas, V. W. S. Chan, and T. K. Yee. Local-oscillator excess-noise suppression for homodyne and heterodyne detection. *Opt. Lett.*, 8(8):419–421, August 1983.
- [58] R. A. Leitgeb, L. Schmetterer, C. K. Hitzenberger, , and A. F. Fercher. Real-time measurement of in vitro flow by fourier-domain color doppler optical coherence tomography. *Opt. Lett.*, 29(2):171–173, January 15 2004.
- [59] Marinko V. Sarunic, Brian E. Applegate, and Joseph A. Izatt. Spectral domain second-harmonic optical coherence tomography. *Opt. Lett.*, 30:2391–2393, 2005.
- [60] R. Leitgeb, C. K. Hitzenberger, and A. F. Fercher. Performance of fourier domain vs. time domain optical coherence tomography. *Opt. Express*, 11(8):889–894, April 21 2003.
- [61] Johannes F. de Boer, Barry Cense, B. Hyle Park, Mark C. Pierce, Guillermo J. Tearney, and Brett E. Bouma. Improved signal-to-noise ratio in spectral-domain compared with time-domain optical coherence tomography. *Opt. Lett.*, 28:2067–2069, 2003.
- [62] S. H. Yun, G. J. Tearney, J. F. de Boer, N. Iftimia, and B. E. Bouma. High-speed optical frequency-domain imaging. *Optics Express*, 11(22):2953–2963, Nov 3 2003.

- [63] Susana Martinez-Conde, Stephen L. Macknik, and David H. Hubel. The role of fixational eye movements in visual perception. *Nat. Neurosci.*, 5:229–240, 2004.
- [64] Michael Richard Hee. *Optical Coherence Tomography of the Eye*. PhD thesis, Massachusetts Institute of Technology, 1996.
- [65] C. A. Toth, D. G. Narayan, S. A. Boppart, M. R. Hee, J. G. Fujimoto, R. Birngruber, C. P. Cain, C. D. DiCarlo, and W. P. Roach. A comparison of retinal morphology viewed by optical coherence tomography and by light microscopy. *Arch Ophthalmol*, 115(11):1425–1428, Nov 1997.
- [66] Y. Huang, A. V. Cideciyan, G. I. Papastergiou, E. Banin, S. L. Semple-Rowland, A. H. Milam, and S. G. Jacobson. Relation of optical coherence tomography to microanatomy in normal and rd chickens. *Invest Ophthalmol Vis Sci*, 39(12):2405–2416, Nov 1998.
- [67] D. S. Chauhan and J. Marshall. The interpretation of optical coherence tomography images of the retina. *Invest Ophthalmol Vis Sci*, 40(10):2332–2342, Sep 1999.
- [68] W. Drexler, U. Morgner, R. K. Ghanta, J. S. Schuman, F. X. Kärtner, M. R. Hee, E. P. Ippen, and J. G. Fujimoto. *The Shape of Glaucoma; Objective Neural Imaging Techniques*, chapter New technology for ultrahigh resolution optical coherence tomography of the retina, pages 75–104. The Netherlands: Kugler Publications, 2000.
- [69] M. D. Sherar, M. B. Noss, and F. S. Foster. Ultrasound backscatter microscopy images the internal structure of living tumour spheroids. *Nature*, 330(6147):493–495, 1987.
- [70] W. Lange, P. Debbage, and P. Trudrung. Lectin-binding sites in the retina of the pig, baboon and cat. *Fortschr Ophthalmol*, 87(2):214–217, 1990.
- [71] R. Hebel. Distribution of retinal ganglion cells in five mammalian species (pig, sheep, ox, horse, dog). *Anat Embryol (Berl)*, 150(1):45–51, Dec 1976.
- [72] P.K. Ahmelt, A. Küber-Heiss, C. Schubert, and M. Glösmann. Two peaks in cone topographies of the domestic pig and the european wild hog retina. In *XV. Int Cong Eye Res Geneva*, volume 72, 2002.
- [73] Anita Hendrickson and David Hicks. Distribution and density of medium- and short-wavelength selective cones in the domestic pig retina. *Exp Eye Res*, 74(4):435–444, Apr 2002.
- [74] P. Simoens, L. De Schaepdrijver, and H. Lauwers. Morphologic and clinical study of the retinal circulation in the miniature pig. A: Morphology of the retinal microvasculature. *Exp Eye Res*, 54(6):965–973, Jun 1992.
- [75] C. R. Braekevelt. Fine structure of the retinal rods and cones in the domestic pig. *Graefes Arch Clin Exp Ophthalmol*, 220(6):273–278, 1983.
- [76] W. H. Miller and A. W. Snyder. The tiered vertebrate retina. *Vision Res*, 17(2):239–255, Feb 1977.
- [77] W. H. Miller and A. W. Snyder. Optical function of human peripheral cones. *Vision Res*, 13(12):2185–2194, Dec 1973.
- [78] R. Winston and J. M. Enoch. Retinal cone receptor as an ideal light collector. *J Opt Soc Am*, 61(8):1120–1122, Aug 1971.

- [79] R. L. Sidman. The structure and concentration of solids in photoreceptor cells studied by refractometry and interference microscopy. *J Biophys Biochem Cytol*, 3(1):15–30, Jan 1957.
- [80] M. W. Rana and S. R. Taraszka. Monkey photoreceptor calycal processes and interphotoreceptor matrix as observed by scanning electron microscopy. *Am J Anat*, 192(4):472–477, Dec 1991.
- [81] B. Borwein, D. Borwein, J. Medeiros, and J. W. McGowan. The ultrastructure of monkey foveal photoreceptors, with special reference to the structure, shape, size, and spacing of the foveal cones. *Am J Anat*, 159(2):125–146, Oct 1980.
- [82] J. M. Enoch. Vertebrate receptor optics and orientation. *Doc Ophthalmol*, 48(2):373–388, Apr 1980.
- [83] A. Stacey and C. Pask. Spatial-frequency response of a photoreceptor and its wavelength dependence. I. Coherent sources. *J. Opt. Soc. Am. A*, 11(4):1193–1198, Apr 1994.
- [84] B. Považay, K. Bizheva, B. Hermann, A. Unterhuber, H. Sattmann, A. Fercher, W. Drexler, C. Schubert, P. Ahnelt, M. Mei, R. Holzwarth, W. Wadsworth, J. Knight, and P. St. J. Russell. Enhanced visualization of choroidal vessels using ultrahigh resolution ophthalmic OCT at 1050 nm. *Opt. Express*, 11(17):1980–1986, August 2003.
- [85] M. Glösmann, B. Hermann, C. Schubert, H. Sattmann, P. K. Ahnelt, and W. Drexler. Histologic correlation of pig retina radial stratification with ultrahigh-resolution optical coherence tomography. *Invest Ophthalmol Vis Sci*, 44(4):1696–1703, Apr 2003.
- [86] V. H. Perry and A. Cowey. The lengths of the fibres of Henle in the retina of macaque monkeys: implications for vision. *Neuroscience*, 25(1):225–236, Apr 1988.
- [87] S. J. Schein. Anatomy of macaque fovea and spatial densities of neurons in foveal representation. *J Comp Neurol*, 269(4):479–505, Mar 1988.
- [88] P. K. Ahnelt. The photoreceptor mosaic. *Eye*, 12 (Pt 3b):531–540, 1998.
- [89] H. Wässle, U. Grünert, J. Röhrenbeck, and B. B. Boycott. Retinal ganglion cell density and cortical magnification factor in the primate. *Vision Res*, 30(11):1897–1911, 1990.
- [90] A. Hsu, Y. Tsukamoto, R. G. Smith, and P. Sterling. Functional architecture of primate cone and rod axons. *Vision Res*, 38(17):2539–2549, Sep 1998.
- [91] J. Sjöstrand, Z. Popovic, N. Conradi, and J. Marshall. Morphometric study of the displacement of retinal ganglion cells subserving cones within the human fovea. *Graefes Arch Clin Exp Ophthalmol*, 237(12):1014–1023, Dec 1999.
- [92] M. P. Rowe, J. M. Corless, N. Engheta, , and Jr. E. N. Pugh. Scanning interferometry of sunfish cones. i. longitudinal variation in single-cone refractive index. *J. Opt. Soc. Am. A*, 13:2141–2150, 1996.
- [93] Q. V. Hoang, R. A. Linsenmeier, C. K. Chung, and C. A. Curcio. Photoreceptor inner segments in monkey and human retina: mitochondrial density, optics, and regional variation. *Vis Neurosci*, 19(4):395–407, 2002.
- [94] Austin Roorda and David R Williams. Optical fiber properties of individual human cones. *J Vis*, 2(5):404–412, 2002.

- [95] Alexander I. Kholodnykh, Irina Y. Petrova, Kirill V. Larin, Massoud Motamedi, and Rinat O. Esenaliev. Precision of measurement of tissue optical properties with optical coherence tomography. *Appl. Opt.*, 42(16):3027–3037, 2003.
- [96] W. Drexler, H. Sattmann, B. Hermann, T. H. Ko, M. Stur, A. Unterhuber, C. Scholda, O. Findl, M. Wirtitsch, J. G. Fujimoto, and A. F. Fercher. Enhanced visualization of macular pathology with the use of ultrahigh-resolution optical coherence tomography. *Arch Ophthalmol*, 121(5):695–706, May 2003.
- [97] American national standards institute safe use of lasers., 1993.
- [98] R. Leitgeb, W. Drexler, A. Unterhuber, B. Hermann, T. Bajraszewski, T. Le, A. Stingl, and A. Fercher. Ultrahigh resolution fourier domain optical coherence tomography. *Opt. Express*, 12(10):2156–2165, May 2004.
- [99] A. Unterhuber, B. Považay, B. Hermann, H. Sattmann, W. Drexler, V. Yakovlev, G. Tempea, C. Schubert, E. M. Anger, P. K. Ahnelt, M. Stur, J. E. Morgan, A. Cowey, G. Jung, T. Le, and A. Stingl. Compact, low-cost Ti:Al₂O₃ laser for in vivo ultrahigh-resolution optical coherence tomography. *Opt. Lett.*, 28(11):905–907, Jun 2003.
- [100] J.G. Fujimoto, M.E. Brezinski, G.J. Tearney, S.A. Boppart, B. Bouma, M.R. Hee, J.F. Southern, and E.A. Swanson. Optical biopsy and imaging using optical coherence tomography. *Nature Medicine*, 1:970–972, 1995.
- [101] RS Ramrattan, TL van der Schaft, CM Mooy, WC de Bruijn, PG Mulder, and PT de Jong. Morphometric analysis of bruch’s membrane, the choriocapillaris, and the choroid in aging. *Invest. Ophthalmol. Vis. Sci.*, 35(6):2857–2864, May 1994.
- [102] D. J. Coleman and F. L. Lizzi. In vivo choroidal thickness measurement. *Am J Ophthalmol*, 88(3 Pt 1):369–375, Sep 1979.
- [103] R. N. Johnson and J. D. Gass. Idiopathic macular holes. Observations, stages of formation, and implications for surgical intervention. *Ophthalmology*, 95(7):917–924, Jul 1988.
- [104] J. D. Gass. Reappraisal of biomicroscopic classification of stages of development of a macular hole. *Am J Ophthalmol*, 119(6):752–759, Jun 1995.
- [105] K. Stargardt. über familiäre progressive degenerationen im kindesalter. *Graefes Arch Clin Exp Ophthalmol.*, 71:534–550, 1909.
- [106] T. M. Aaberg. Stargardt’s disease and fundus flavimaculatus: evaluation of morphologic progression and intrafamilial co-existence. *Trans Am Ophthalmol Soc*, 84:453–487, 1986.
- [107] A. Franchescetti and J. Francois. Fundus flavimaculatus: a clinical classification. *Arch Ophthalmol.*, 24:505–530, 1965.
- [108] Y. Isashiki and N. Ohba. Fundus flavimaculatus: polymorphic retinal change in sibilings. *Br J Ophthalmol*, 69(7):522–524, Jul 1985.
- [109] K. G. Noble and R. E. Carr. Stargardt’s disease and fundus flavimaculatus. *Arch Ophthalmol*, 97(7):1281–1285, Jul 1979.
- [110] Ygal Rotenstreich, Gerald A Fishman, and Robert J Anderson. Visual acuity loss and clinical observations in a large series of patients with Stargardt disease. *Ophthalmology*, 110(6):1151–1158, Jun 2003.

- [111] J. D. Armstrong, D. Meyer, S. Xu, and J. L. Elfervig. Long-term follow-up of Stargardt's disease and fundus flavimaculatus. *Ophthalmology*, 105(3):448–57; discussion 457–8, Mar 1998.
- [112] G. A. Fishman, M. Farber, B. S. Patel, and D. J. Derlacki. Visual acuity loss in patients with Stargardt's macular dystrophy. *Ophthalmology*, 94(7):809–814, Jul 1987.
- [113] A. R. Irvine and F. L. Wergeland. Stargardt's hereditary progressive macular degeneration. *Br J Ophthalmol*, 56(11):817–826, Nov 1972.
- [114] O. B. Hadden and J. D. Gass. Fundus flavimaculatus and Stargardt's disease. *Am J Ophthalmol*, 82(4):527–539, Oct 1976.
- [115] S. B. Bressler. Health maintenance issues of the elderly. Vision: age-related macular degeneration. *Md Med J*, 38(2):135–137, Feb 1989.
- [116] F. G. Holz. [Autofluorescence imaging of the macula]. *Ophthalmologe*, 98(1):10–18, Jan 2001.
- [117] A. von Ruckmann, F. W. Fitzke, and A. C. Bird. In vivo fundus autofluorescence in macular dystrophies. *Arch Ophthalmol*, 115(5):609–615, May 1997.
- [118] C. Bellmann, F. G. Holz, O. Schapp, H. E. Völcker, and T. P. Otto. [Topography of fundus autofluorescence with a new confocal scanning laser ophthalmoscope]. *Ophthalmologe*, 94(6):385–391, Jun 1997.
- [119] W. Hammerstein and E. Leide. [The importance of fluorescein angiography in the diagnosis of Stargardt's macular degeneration (author's transl)]. *Klin Monatsbl Augenheilkd*, 178(1):20–23, Jan 1981.
- [120] P. E. Stanga, S. M. Downes, R. M. Ahuja, N. H. Chong, R. Antcliff, A. C. Reck, and A. C. Bird. Comparison of optical coherence tomography and fluorescein angiography in assessing macular edema in retinal dystrophies: preliminary results. *Int Ophthalmol*, 23(4-6):321–325, 2001.
- [121] P. Lachapelle, J. M. Little, and M. S. Roy. The electroretinogram in Stargardt's disease and fundus flavimaculatus. *Doc Ophthalmol*, 73(4):395–404, Dec 1989.
- [122] P. Stavrou, P. A. Good, G. P. Misson, and E. E. Kritzinger. Electrophysiological findings in Stargardt's-fundus flavimaculatus disease. *Eye*, 12 (Pt 6):953–958, 1998.
- [123] R. Itabashi, O. Katsumi, M. C. Mehta, R. Wajima, M. Tamai, and T. Hirose. Stargardt's disease/fundus flavimaculatus: psychophysical and electrophysiologic results. *Graefes Arch Clin Exp Ophthalmol*, 231(10):555–562, Oct 1993.
- [124] F. Mori, S. Ishiko, N. Kitaya, A. Takamiya, E. Sato, T. Hikichi, and A. Yoshida. Scotoma and fixation patterns using scanning laser ophthalmoscope microperimetry in patients with macular dystrophy. *Am J Ophthalmol*, 132(6):897–902, Dec 2001.
- [125] Michael J Pianta, Tomas S Aleman, Artur V Cideciyan, Janet S Sunness, Yuanyuan Li, Betsy A Campochiaro, Peter A Campochiaro, Donald J Zack, Edwin M Stone, and Samuel G Jacobson. In vivo micropathology of Best macular dystrophy with optical coherence tomography. *Exp Eye Res*, 76(2):203–211, Feb 2003.
- [126] Mineo Kondo, Yasuki Ito, Shinji Ueno, Chang-Hua Piao, Hiroko Terasaki, and Yozo Miyake. Foveal thickness in occult macular dystrophy. *Am J Ophthalmol*, 135(5):725–728, May 2003.

- [127] Nathanael Benhamou, Eric H Souied, Ricky Zolf, Florence Coscas, Gabriel Coscas, and Gisele Soubrane. Adult-onset foveomacular vitelliform dystrophy: a study by optical coherence tomography. *Am J Ophthalmol*, 135(3):362–367, Mar 2003.
- [128] Luisa Pierro, Gemma Tremolada, Ugo Introini, Giliola Calori, and Rosario Brancato. Optical coherence tomography findings in adult-onset foveomacular vitelliform dystrophy. *Am J Ophthalmol*, 134(5):675–680, Nov 2002.
- [129] E. M. Anger, A. Unterhuber, B. Hermann, H. Sattmann, C. Schubert, J. E Morgan, A. Cowey, P. K. Ahnelt, and W. Drexler. Ultrahigh resolution optical coherence tomography of the monkey fovea. Identification of retinal sublayers by correlation with semithin histology sections. *Exp. Eye Res.*, 78(6):1117–1125, Jun 2004.
- [130] M. Stur and S. Ansari-Shahrezaei. The effect of axial length on laser spot size. *Arch Ophthalmol.*, 119:1323–1328, 2001.
- [131] Y. Ligier, O. Ratib, M. Logean, and C. Girard. Osiris: A medical image manipulation system. *MD Comput J.*, 11:212–218, 1994.
- [132] Christina Gerth, Monika Andrassi-Darida, Markus Bock, Markus N Preising, Bernhard H F Weber, and Birgit Lorenz. Phenotypes of 16 Stargardt macular dystrophy/fundus flavimaculatus patients with known ABCA4 mutations and evaluation of genotype-phenotype correlation. *Graefes Arch Clin Exp Ophthalmol*, 240(8):628–638, Aug 2002.
- [133] K. Zhang, M. Kniazeva, A. Hutchinson, M. Han, M. Dean, and R. Allikmets. The ABCR gene in recessive and dominant Stargardt diseases: a genetic pathway in macular degeneration. *Genomics*, 60(2):234–237, Sep 1999.
- [134] B. Jeroen Klevering, Alessandra Maugeri, Anja Wagner, Sioe Lie Go, Carolien Vink, Frans P M Cremers, and Carel B Hoyng. Three families displaying the combination of Stargardt’s disease with cone-rod dystrophy or retinitis pigmentosa. *Ophthalmology*, 111(3):546–553, Mar 2004.
- [135] Gerald A. Fishman, Edwin M. Stone, Sandeep Grover, Deborah J. Derlacki, Heidi L. Haines, and Robin R. Hockey. Variation of clinical expression in patients with stargardt dystrophy and sequence variations in the abcr gene. *Arch Ophthalmol*, 117(4):504–510, April 1999.
- [136] Pablo Artal, Antonio Guirao, Esther Berrio, and David R. Williams. Compensation of corneal aberrations by the internal optics in the human eye. *J. Vis.*, 1(1):1–8, May 2001.
- [137] P. Artal and R. Navarro. High-resolution imaging of the living human fovea: measurement of the intercenter cone distance by speckle interferometry. *Opt. Lett.*, 14:1098–1100, 1989.
- [138] J. Liang and D. R. Williams. Aberrations and retinal image quality of the normal human eye. *J. Opt. Soc. Am. A*, 14(11):2873–2883, November 1997.
- [139] F. Vargas-Martín, P. M. Prieto, and P. Artal. Correction of the aberrations in the human eye with a liquid-crystal spatial light modulator: limits to performance. *J. Opt. Soc. Am. A*, 15:2552–2562, 1998.
- [140] Enrique J. Fernández, Ignacio Iglesias, and Pablo Artal. Closed-loop adaptive optics in the human eye. *Opt. Lett.*, 26(10):746–748, May 2001.
- [141] A. Roorda, F. Romero-Borja, III W. Donnelly, H. Queener, T. Hebert, and M. Campbell. Adaptive optics scanning laser ophthalmoscopy. *Opt. Express*, 10:405–412, 2002.

- [142] Ben C. Platt and Roland Shack. History and principles of shack-hartmann wavefront sensing. *Journal of Refractive Surgery*, 17:S573–S577, September 2001.
- [143] J. C. Wyant and K. Creath. *Applied Optics and Optical Engineering, Vol. XI*, chapter Basic Wavefront Aberration Theory for Optical Metrology, Zernike Polynomials, pages 28–39. Academic Press, Inc., 1992.
- [144] Enrique Fernandez and Pablo Artal. Membrane deformable mirror for adaptive optics: performance limits in visual optics. *Opt. Express*, 11:1056–1069, 2003.
- [145] L. N. Thibos, R. A. Applegate, J. T. Schwiegerling, and R. Webb. *OSA Trends in Optics OSA Trends in Optics and Photonics Series*, chapter Vision Science and Its Applications, pages 232–244. Optical Society of America, Washington, D.C., 2000.
- [146] U. Schmidt-Erfurth, R. A. Leitgeb, S. Michels, B. Považay, S. Sacu, B. Hermann, C. Ahlers, H. Sattmann, C. Scholda, A. F. Fercher, and W. Drexler. Three-dimensional ultrahigh-resolution optical coherence tomography of macular diseases. *Invest Ophthalmol Vis Sci*, 46(9):3393–3402, Sep 2005.
- [147] Kai Huang and Robert F. Murphy. From quantitative microscopy to automated image understanding. *J. Biomed. Opt.*, 9(5):893–912, September 2004.
- [148] T. M. Lehmann, J. Bredno, and K. Spitzer. On the design of active contours for medical image segmentation - a scheme for classification and construction. *Methods Inf Med*, 42(1):89–98, 2003.
- [149] Yan Li, Peng Wen, David Powers, and C. Richard Clark. Lsb neural network based segmentation of mr brain images. In *Proc. 1999 IEEE Systems, Man and Cybernetics Conference*, October 1999. nothing.
- [150] Zümray Dokur and Tamer Ölmez. Segmentation of ultrasound images by using a hybrid neural network. *Pattern Recognition Letters*, 23:1825–1836, 2002.
- [151] Edward A. Ashton and Kevin J. Parker. Multiple resolution bayesian segmentation of ultrasound images. *Ultrasonic Imaging*, 17(4):291–304, October 1995.
- [152] J. Rogowska and M. Brezinski. Image processing techniques for noise removal, enhancement and segmentation of cartilage oct images. *Phys. Med. Biol.*, 47:641–655, 2002.
- [153] J. Rogowska, C. M. Bryant, and M. E. Brezinski. Cartilage thickness measurements from optical coherence tomography. *J. Opt. Soc. Am. A*, 20(2):357–367, Feb 2003.
- [154] Hiroshi Ishikawa, Daniel M. Stein, Gadi Wollstein, Siobahn Beaton, James G. Fujimoto, and Joel S. Schuman. Macular segmentation with optical coherence tomography. *Invest. Ophthalmol. Vis. Sci.*, 46(6):2012–2017, June 2005.
- [155] D. Koozekanani, K. Boyer, and C. Roberts. Retinal thickness measurements from optical coherence tomography using a markov boundary model. *Ieee Transactions on Medical Imaging*, 20(9):900–916, Sep 2001.
- [156] Guy Gilboa, Nirr Sochen, and Yehoshua Y. Zeevi. Image enhancement and denoising complex diffusion process. *IEEE Trans. PAMI*, 25:1020–1036, 2004.
- [157] Delia Cabrera Fernandez, Harry M. Salinas, and Carmen A. Puliafito. Automated detection of retinal layer structures on optical coherence tomography images. *Opt. Express*, 13:10200–10216, 2005.
- [158] G. Gregori and R.W. Knighton. A robust algorithm for retinal thickness measurements using optical coherence tomography (stratus oct). *Invest. Ophthalmol. Vis. Sci.*, 45(5):3007–, May 2004.

- [159] M.D. Kulkarni and J.A. Izatt. Summaries of papers presented at the conference on lasers and electro optics 9, 1996.
- [160] Ujwal S. Sathyam, Bill W. Colston, Jr., Luiz B. Da Silva, and Matthew J. Everett. Evaluation of optical coherence quantitation of analytes in turbid media by use of two wavelengths. *Appl. Opt.*, 38(10):2097–2104, April 1 1999.
- [161] J.L. Boulnois and A. Morfino. Photo–biomolecular effects of laser radiation. *Minerva Med.*, 74:1669–1673, 1983.
- [162] T. Støren, A. Simonsen, O. Løkberg, T. Lindmo, L. Svaasand, and A. Røyset. Measurement of dye diffusion in agar gel by use of low coherence interferometry. *Optics Letters*, 28:1215–1217, 2003.
- [163] D.J. Faber, E.G. Mik, M.C.G. Alders, and T.G. van Leeuwen. Light absorption of (oxy-)hemoglobin assessed by spectroscopic optical coherence tomography. *Opt. Lett.*, 28:1437–1439, 2003.
- [164] K. Bizheva, B. Považay, B. Hermann, H. Sattmann, W. Drexler, M. Mei, R. Holzwarth, T. Hoelzenbein, V. Wacheck, and H. Pehamberger. Compact, broadband fiber laser for sub-2-microm axial resolution optical coherence tomography in the 1300-nm wavelength region. *Opt. Lett.*, 28(9):707–709, May 2003.
- [165] A. Roggan, M. Friebel, K. Dörschel, A. Hahn, and G. Müller. Optical properties of circulating human blood in the wavelength range 400 - 2500 nm. *J. Biomed. Opt.*, 4(1):36–46, January 1999.
- [166] T. Fuji, A. Unterhuber, V.S. Yakovlev, G. Tempea, F. Krausz, and W. Drexler. Generation of smooth, ultra-broadband spectra directly from a prism-less ti:sapphire laser. *Appl. Phys. B: Lasers Opt.*, 77:125–128, 2003.
- [167] M.J.L. Landsman, G. Kwant, G.A. Mook, and W.G. Zijlstra. Light absorbing properties, stability, and spectral stabilization of indocyanine green. *Opt. Comm.*, 40:575–583, 1976.
- [168] H. P. Scholl and E. Zrenner. Electrophysiology in the investigation of acquired retinal disorders. *Surv Ophthalmol*, 45(1):29–47, 2000.
- [169] Donald C Hood, Jeffrey G Odel, Candice S Chen, and Bryan J Winn. The multifocal electroretinogram. *J Neuroophthalmol*, 23(3):225–235, Sep 2003.
- [170] H. H. Harary, J. E. Brown, and L. H. Pinto. Rapid light-induced changes in near infrared transmission of rods in *Bufo marinus*. *Science*, 202(4372):1083–1085, Dec 1978.
- [171] K. P. Hofmann, R. Uhl, W. Hoffmann, and W. Kreutz. Measurements on fast light-induced light-scattering and -absorption changes in outer segments of vertebrate light sensitive rod cells. *Biophys Struct Mech*, 2(1):61–77, Apr 1976.
- [172] M. Kahlert, D. R. Pepperberg, and K. P. Hofmann. Effect of bleached rhodopsin on signal amplification in rod visual receptors. *Nature*, 345(6275):537–539, Jun 1990.
- [173] M. Kahlert and K. P. Hofmann. Reaction rate and collisional efficiency of the rhodopsin-transducin system in intact retinal rods. *Biophys J*, 59(2):375–386, Feb 1991.
- [174] D. R. Pepperberg, M. Kahlert, A. Krause, and K. P. Hofmann. Photic modulation of a highly sensitive, near-infrared light-scattering signal recorded from intact retinal photoreceptors. *Proc. Natl. Acad. Sci. U. S. A.*, 85(15):5531–5535, Aug 1988.

- [175] Vadim Y Arshavsky, Trevor D Lamb, and Edward N Pugh. G proteins and phototransduction. *Annu Rev Physiol*, 64:153–187, 2002.
- [176] R. A. Stepanoski, A. LaPorta, F. Raccaia-Behling, G. E. Blonder, R. E. Slusher, and D. Kleinfeld. Noninvasive detection of changes in membrane potential in cultured neurons by light scattering. *Proc. Natl. Acad. Sci. U. S. A.*, 88(21):9382–9386, Nov 1991.
- [177] S. P. Srinivas, Joseph A Bonanno, Els Larivière, Danny Jans, and Willy Van Driessche. Measurement of rapid changes in cell volume by forward light scattering. *Pflugers Arch*, 447(1):97–108, Oct 2003.
- [178] Xin-Cheng Yao, Angela Yamauchi, Beth Perry, and John S George. Rapid optical coherence tomography and recording functional scattering changes from activated frog retina. *Appl Opt*, 44(11):2019–2023, Apr 2005.
- [179] S. M. Dawis and M. Rossetto. Light-evoked changes in near-infrared transmission by the ON and OFF channels of the anuran retina. *Vis Neurosci*, 10(4):687–692, 1993.
- [180] Darin A Nelson, Sara Krupsky, Ayala Pollack, Eyal Aloni, Michael Belkin, Ivo Vanzetta, Mordechai Rosner, and Amiram Grinvald. Special report: Noninvasive multi-parameter functional optical imaging of the eye. *Ophthalmic Surg Lasers Imaging*, 36(1):57–66, 2005.
- [181] L. Vabre, A. Dubois, and A. C. Boccara. Thermal-light full-field optical coherence tomography. *Opt. Lett.*, 27(7):530–532, April 1 2002.
- [182] I. Hartl, X. D. Li, C. Chudoba, R. K. Ghanta, T. H. Ko, J. G. Fujimoto, J. K. Ranka, and R. S. Windeler. Ultrahigh-resolution optical coherence tomography using continuum generation in an air-silica microstructure optical fiber. *Opt. Lett.*, 26(9):608–610, May 1 2001.
- [183] Wolfgang Drexler. Ultrahigh-resolution optical coherence tomography. *J. Biomed. Opt.*, 9(1):47–74, January/February 2004.
- [184] R. Uma Maheswari, H. Takaoka, R. Homma, H. Kadono, and M. Tanifuji. Implementation of optical coherence tomography (oct) in visualization of functional structures of cat visual cortex. *Optics Communications*, 202(1-3):47–54, February 2002.
- [185] Mariya Lazebnik, Daniel L. Marks, Kurt Potgieter, Rhanor Gillette, and Stephen A. Boppart. Functional optical coherence tomography for detecting neural activity through scattering changes. *Opt. Lett.*, 28(14):1218–1220, July 15 2003.
- [186] M. E. Breton, A. W. Schueller, T. D. Lamb, and E. N. Pugh. Analysis of ERG a-wave amplification and kinetics in terms of the G-protein cascade of phototransduction. *Invest Ophthalmol Vis Sci*, 35(1):295–309, Jan 1994.
- [187] E. D. Cohen and R. F. Miller. The network-selective actions of quinoxalines on the neurocircuitry operations of the rabbit retina. *Brain Res*, 831(1-2):206–228, Jun 1999.
- [188] R. A. Shiells and G. Falk. Contribution of rod, on-bipolar, and horizontal cell light responses to the ERG of dogfish retina. *Vis Neurosci*, 16(3):503–511, 1999.
- [189] Roland Thar and Michael Köhl. Propagation of electromagnetic radiation in mitochondria? *J Theor Biol*, 230(2):261–270, Sep 2004.

- [190] B. Burnside. Light and circadian regulation of retinomotor movement. *Prog Brain Res*, 131:477–485, 2001.
- [191] M. S Marion S Eckmiller. Defective cone photoreceptor cytoskeleton, alignment, feedback, and energetics can lead to energy depletion in macular degeneration. *Prog Retin Eye Res*, 23(5):495–522, Sep 2004.
- [192] J. M. Enoch and D. G. Birch. Inferred positive phototropic activity in human photoreceptors. *Philos Trans R Soc Lond B Biol Sci*, 291(1051):323–351, Mar 1981.
- [193] J. Fernandez and W. Drexler. Three dimensional adaptive optics uhr oct. In *Proc. SPIE*, 2006.
- [194] Brian Stout, Christine Andraud, Sophie Stout, and Jacques Lafait. Absorption in multiple-scattering systems of coated spheres. *J. Opt. Soc. Am. A*, 20(6):1050–1059, 2003.

Publication List

of peer reviewed papers

- [1] C. Scholda, M. Wirtitsch, B. Hermann, A. Unterhuber, E. Ergun, H. Sattmann, T. H. Ko, J. G. Fujimoto, A. F. Fercher, M. Stur, and W. Drexler. Ultrahigh resolution optical coherence tomography of macular holes. *Retina*, In Press, 2006.
- [2] K. Bizheva, R. Pflug, B. Hermann, B. Považay, H. Sattmann, P. Qiu, E. Anger, H. Reitsamer, S. Popov, J. R. Taylor, A. Unterhuber, P. Ahnelt, and W. Drexler. Optophysiology: Depth-resolved probing of retinal physiology with functional ultrahigh-resolution optical coherence tomography. *Proc. Natl. Acad. Sci. U. S. A.*, 103(13):5066–5071, March 21 2006.
- [3] K. Bizheva, A. Unterhuber, B. Hermann, B. Považay, H. Sattmann, A. F. Fercher, W. Drexler, M. Preusser, H. Budka, A. Stingl, and T. Le. Imaging ex vivo healthy and pathological human brain tissue with ultra-high-resolution optical coherence tomography. *J. Biomed. Opt.*, 10(1):11006, 2005.
- [4] U. Schmidt-Erfurth, R. A. Leitgeb, S. Michels, B. Považay, S. Sacu, B. Hermann, C. Ahlers, H. Sattmann, C. Scholda, A. F. Fercher, and W. Drexler. Three-dimensional ultrahigh-resolution optical coherence tomography of macular diseases. *Invest Ophthalmol Vis Sci*, 46(9):3393–3402, Sep 2005.
- [5] E. Ergun, B. Hermann, M. Wirtitsch, A. Unterhuber, T. H. Ko, H. Sattmann, C. Scholda, J. G. Fujimoto, M. Stur, and W. Drexler. Assessment of central visual function in Stargardt’s disease/fundus flavimaculatus with ultrahigh-resolution optical coherence tomography. *Invest Ophthalmol Vis Sci*, 46(1):310–316, Jan 2005.
- [6] A. Unterhuber, B. Považay, B. Hermann, H. Sattmann, A. Chavez-Pirson, and W. Drexler. In vivo retinal optical coherence tomography at 1040 nm - enhanced penetration into the choroid. *Opt. Express*, 13:3252–3258, 2005.
- [7] E. J. Fernández, B. Považay, B. Hermann, A. Unterhuber, H. Sattmann, P. M. Prieto, R. Leitgeb, P. Ahnelt, P. Artal, and W. Drexler. Three-dimensional adaptive optics ultrahigh-resolution optical coherence tomography using a liquid crystal spatial light modulator. *Vision Res*, 45(28):3432–3444, Dec 2005.
- [8] E. J. Fernández, A. Unterhuber, P. M. Prieto, B. Hermann, W. Drexler, and P. Artal. Ocular aberrations as a function of wavelength in the near infrared measured with a femtosecond laser. *Opt. Express*, 13:400–409, 2005.
- [9] M. G. Wirtitsch, E. Ergun, B. Hermann, A. Unterhuber, M. Stur, C. Scholda, H. Sattmann, T. H. Ko, J. G. Fujimoto, and W. Drexler. Ultrahigh resolution optical coherence tomography in macular dystrophy. *Am J Ophthalmol*, 140(6):976–983, Dec 2005.
- [10] R. J. Linnola, O. Findl, B. Hermann, H. Sattmann, A. Unterhuber, Risto-Pekka Happonen, and W. Drexler. Intraocular lens-capsular bag imaging with ultrahigh-resolution optical coherence tomography Pseudophakic human autopsy eyes. *J Cataract Refract Surg*, 31(4):818–823, Apr 2005.

- [11] K. Bizheva, A. Unterhuber, B. Hermann, B. Považay, H. Sattmann, W. Drexler, A. Stingl, T. Le, M. Mei, R. Holzwarth, H. A. Reitsamer, J. E. Morgan, and A. Cowey. Imaging ex vivo and in vitro brain morphology in animal models with ultrahigh resolution optical coherence tomography. *J. Biomed. Opt.*, 9(4):719–724, 2004.
- [12] E. M. Anger, A. Unterhuber, B. Hermann, H. Sattmann, C. Schubert, J. E. Morgan, A. Cowey, P. K. Ahnelt, and W. Drexler. Ultrahigh resolution optical coherence tomography of the monkey fovea. Identification of retinal sublayers by correlation with semithin histology sections. *Exp. Eye Res.*, 78(6):1117–1125, Jun 2004.
- [13] A. Unterhuber, B. Považay, K. Bizheva, B. Hermann, H. Sattmann, A. Stingl, T. Le, M. Seefeld, R. Menzel, M. Preusser, H. Budka, Ch Schubert, H. Reitsamer, P. K. Ahnelt, J. E. Morgan, A. Cowey, and W. Drexler. Advances in broad bandwidth light sources for ultrahigh resolution optical coherence tomography. *Phys Med Biol*, 49(7):1235–1246, Apr 2004.
- [14] B. Hermann, E. J. Fernández, A. Unterhuber, H. Sattmann, A. F. Fercher, W. Drexler, P. M. Prieto, and P. Artal. Adaptive-optics ultrahigh-resolution optical coherence tomography. *Opt. Lett.*, 29(18):2142–2144, Sep 2004.
- [15] B. Hermann, K. Bizheva, A. Unterhuber, B. Považay, H. Sattmann, L. Schmetterer, A. Fercher, and W. Drexler. Precision of extracting absorption profiles from weakly scattering media with spectroscopic time-domain optical coherence tomography. *Opt. Express*, 12(8):1677–1688, 19 April 2004.
- [16] R. Leitgeb, W. Drexler, A. Unterhuber, B. Hermann, T. Bajraszewski, T. Le, A. Stingl, and A. Fercher. Ultrahigh resolution fourier domain optical coherence tomography. *Opt. Express*, 12(10):2156–2165, May 2004.
- [17] K. Bizheva, B. Považay, B. Hermann, H. Sattmann, W. Drexler, M. Mei, R. Holzwarth, T. Hoelzenbein, V. Wacheck, and H. Pehamberger. Compact, broad-bandwidth fiber laser for sub-2-microm axial resolution optical coherence tomography in the 1300-nm wavelength region. *Opt. Lett.*, 28(9):707–709, May 2003.
- [18] B. Považay, K. Bizheva, B. Hermann, A. Unterhuber, H. Sattmann, A. Fercher, W. Drexler, C. Schubert, P. Ahnelt, M. Mei, R. Holzwarth, W. Wadsworth, J. Knight, and P. St. J. Russell. Enhanced visualization of choroidal vessels using ultrahigh resolution ophthalmic oct at 1050 nm. *Opt. Express*, 11(17):1980–1986, August 2003.
- [19] W. Drexler, H. Sattmann, B. Hermann, T. H. Ko, M. Stur, A. Unterhuber, C. Scholda, O. Findl, M. Wirtitsch, J. G. Fujimoto, and A. F. Fercher. Enhanced visualization of macular pathology with the use of ultrahigh-resolution optical coherence tomography. *Arch Ophthalmol*, 121(5):695–706, May 2003.
- [20] A. Unterhuber, B. Považay, B. Hermann, H. Sattmann, W. Drexler, V. Yakovlev, G. Tempea, C. Schubert, E. M. Anger, P. K. Ahnelt, M. Stur, J. E. Morgan, A. Cowey, G. Jung, T. Le, and A. Stingl. Compact, low-cost Ti:Al₂O₃ laser for in vivo ultrahigh-resolution optical coherence tomography. *Opt. Lett.*, 28(11):905–907, Jun 2003.
- [21] M. Glösmann, B. Hermann, C. Schubert, H. Sattmann, P. K. Ahnelt, and W. Drexler. Histologic correlation of pig retina radial stratification with ultrahigh-resolution optical coherence tomography. *Invest Ophthalmol Vis Sci*, 44(4):1696–1703, Apr 2003.

- [22] B. Považay, K. Bizheva, A. Unterhuber, B. Hermann, H. Sattmann, A. F. Fercher, W. Drexler, A. Apolonski, W. J. Wadsworth, J. C. Knight, P. St. J. Russell, M. Vetterlein, and E. Scherzer. Submicrometer axial resolution optical coherence tomography. *Opt. Lett.*, 27(20):1800–1802, October 2002.

Book Chapters

- [1] Wolfgang Drexler, Boris Hermann, Angelika Unterhuber, Harald Sattmann, Mathias Wirtitsch, Michael Stur, Christoph Scholda, Erdem Ergun, Elzbieta Polska, Arno Doelemeyer, Tony H. Ko, James G. Fujimoto, and Adolf F. Fercher. *Optical Coherence Tomography in Retinal Diseases*, chapter Ultrahigh Resolution Optical Coherence Tomography in Macular Diseases. Jaypee Brothers, Medical Publishers LTD, 2004.

Conference Contributions

- [1] B. M. Hermann, B. Povazay, S. Michels, S. Sacu, C. Glittenberg, C. Ahlers, H. Sattmann, C. Scholda, R. A. Leitgeb, U. Schmidt-Erfurth, and W. Drexler. Three-dimensional ultrahigh resolution oct. In *Photonics West - Biomedical Imaging Conference BIOS*, 2006.
- [2] B. Hermann, B. Povazay, C. Glittenberg, S. Michels, S. Sacu, C. Ahlers, H. Sattmann, C. Scholda, U. Schmidt-Erfurth, R. A. Leitgeb, and W. Drexler. Virtual optical biopsy of retinal pathologies. In *Photonics West - Biomedical Imaging Conference BIOS*, 2006.
- [3] B. Hermann, S. Michels, R. Leitgeb, C. Ahlers, B. Povazay, S. Sacu, H. Sattmann, A. Unterhuber, U. Schmidt-Erfurth, and W. Drexler. Thickness mapping of photoreceptors of the foveal region in normals using three-dimensional optical coherence tomography. In *ARVO Poster*, 2005.
- [4] B. M. Hermann, H. Sattmann, A. Unterhuber, B. Povazay, M. Wirtitsch, M. Stur, C. Scholda, E. Ergun, T. H. Ko, J. G. Fujimoto, and W. Drexler. Quantification of intraretinal layers in normals: a baseline for objective diagnosis of retinal pathologies. In *Photonics West - Biomedical Imaging Conference BIOS*, 2005.
- [5] B. Hermann, S. Michels, B. Povazay, R. A. Leitgeb, S. Sacu, C. Ahlers, H. Sattmann, C. Scholda, U. Schmidt-Erfurth, A. F. Fercher, and W. Drexler. Three-dimensional ultrahigh resolution optical coherence tomography of retinal pathologies. In Wolfgang Drexler, editor, *Proc. SPIE*, volume 5861 of *Optical Coherence Tomography and Coherence Techniques II*, pages 31–34. SPIE–The International Society for Optical Engineering., August 2005.
- [6] B. Hermann, K. Bizheva, A. Unterhuber, H. Sattmann, B. Povazay, A. F. Fercher, and W. Drexler. Extraction of absorption and scattering properties with spectroscopic optical coherence tomography. In *Photonics West - LASE - Commercial and Biomedical Applications of Ultrafast Lasers VI - Imaging Using Ultrashort Laser Pulses*, 2004.
- [7] B. Hermann, A. Unterhuber, H. Sattmann, M. Wirtitsch, M. Stur, E. Ergun, C. Scholda, E.M. Anger, T.H. Ko, P.K. Ahnelt, J.S. Schuman, J.G. Fujimoto, A.F. Fercher, and W. Drexler. Quantification of photoreceptor layer thickness using ultrahigh resolution optical coherence tomography. In *ARVO Poster*, 2004.
- [8] B. Hermann, K. Bizheva, H. Sattmann, A. Unterhuber, B. Povazay, A.F. Fercher, and W. Drexler. Precision of quantitative absorption measurement with spectroscopic optical coherence tomography. In *European Conference on Biomedical Optics*. SPIE, 2003.
- [9] B. Hermann, K. K. Bizheva, A. Unterhuber, H. Sattmann, B. Povazay, A. F. Fercher, and W. Drexler. Precision of quantitative absorption measurement with spectroscopic

- optical coherence tomography. In Wolfgang Drexler, editor, *Proc. SPIE*, volume 5140 of *Optical Coherence Tomography and Coherence Techniques*, pages 84–86, October 2003.
- [10] B. Hermann, H. Sattmann, K. K. Bizheva, B. Považay, A. Unterhuber, R. Leitgeb, L. F. Schmetterer, F. Krausz, A. F. Fercher, and W. Drexler. Sensitivity estimation of spectroscopic optical coherence tomography. In Valery V. Tuchin, Joseph A. Izatt, and James G. Fujimoto, editors, *Proc. SPIE*, volume 4619 of *Coherence Domain Optical Methods in Biomedical Science and Clinical Applications VI*, pages 145–148, 2002.

Part IV
Appendix

Appendix A

Envelope generation - matlab code

```
function out = envelope_fft2(data, S, ef, dwmsmpl)
% data: input fringe data
% S: time for one sampling interval (in seconds)
% S:= 1/f, f: sampling frequency: f = 1e7 => S = 1e-7 in the normal case
% ef: electronic frequency, i.e. 550 kHz or 1 MHz - depends on the galvo
% speed
% dwmsmpl: downsample factor, i.e. 5

%tic;

N = length(data);
NumScans = size(data,2);
%disp([num2str(S / 1e-3) ' ms; ' num2str(1/S/1e6) ' MHz'])

t = [0:S:S*(N-1)];
f = [0:N-1] / (N*S);
if dwmsmpl < 1
    dwmsmpl=1;
end

% calculate the position of the zero frequency (n_ef) according to the electronic
% frequency ef
n_ef = double(int32(ef *N/2 * 2*S));
if mod(n_ef,2) ~= 0
    n_ef = n_ef + 1;
end

dwnScanLength = double(int32(N / dwmsmpl));
if dwnScanLength < 3/2*n_ef + 1
    error('Downsample factor for envelope_fft too high.')
end

% Zero point correction
% loop is faster than using matrix representation which does the same:
% data = data - repmat(mean(data),N,1);
for i = 1:NumScans
    data(:,i) = data(:,i) - mean(data(:,i));
end

spectrum = fft(data);

% calculate new length according to downsample factor
% use even number
if mod(dwnScanLength,2) ~= 0
    dwnScanLength = dwnScanLength+1;
```

```
end

% shift center frequency to zero
shifted = zeros(dwnScanLength,NumScans);
from = int32(dwnScanLength/2-n_ef/2);
to = int32(dwnScanLength/2+n_ef/2);
shifted(from:to,:) = ...
    spectrum(n_ef/2:n_ef/2+to-from,:);

% generate envelope by inverse fft of the zero-shifted spectrum
out = abs(ifft(shifted)/dwnsmpl*2);
%toc;
```

Appendix B

Cross-correlation – matlab code

```
function [B, maxcorrpos, maxcorr] = ...
    crosscorr3c(A, mode, maxlags, xcorrnum, weight, offset, sigma)
%
% usage: [B, maxcorrpos, maxcorr] = crosscorr(A, mode, columns2correlate, weight, offset)
% where
%
%         A: Matrix to correlate
%         mode: 0: Start correlation from beginn
%              1: start from xcorrnum+1 and don't shift the first
%              xcorrnum files. Returns only the scans xcorrnum+1:end.
% columns2correlate: number of neighboured columns to correlate
%         weight: weighting for the correlation coefficient of these columns
%              Should be a string 'rectangular', 'triangular' or ' gaussian
%              If empty rectangular is used by default.
%         offset : offset for shift - all column are shifted by that value
%              in addition. empty value is treated as zero.
%         sigma : used for crosscorr. cut-off for filtering maxcorrpos.
%              in percent of numscans. used in function myfilt
%
% For rectangular weight each column has the same impact to the overall
% correlation. For triangular weight the most left cloumn has the smallest
% weight. The column with distance clmns2correlate+1 to the actual column
% has weight zero.
%
% Correlates for matrix A a number of columns and returns correlated
% matrix B and array of size A with the correlation coefficients in maxcorrpos.
% maxcorr is unused yet.
% Uses the matlab funtion xcorr.
%
% Boris Hermann, 15.08.2003

sz = size(A);
if size(sz) ~= 2 | sz(2) == 1 | isempty(xcorrnum)
    disp(' ');
    disp('ERROR in crosscorr3: PLEASE CHECK INPUT VARIABLES');
    help crosscorr3;
    B = [];
    maxcorrpos = [];
    maxcorr = [];
    return;
end
ScanLength = sz(1);
NofPoints = sz(2);
```

```

out = zeros(ScanLength*2-1, NofPoints-1);
maxcorrpos = zeros(NofPoints,1);
maxcorr = 'not implemented yet';
if xcorrnum < 1
    B = A;
    return;
end

progressbar;
% X-correlation
% first step: copy first column from A to B
B = zeros(size(A));
if mode == 0 % start from the beginning
    if offset == 0
        B(:,1) = A(:,1);
    else
        B(:,1) = shifted(A(:,1), offset);
        maxcorrpos(1) = -offset;
    end

    % first x-corr loop
% calculates x-correlation for the first xcorrnum columns
% i is the actual column to correlate
for i = 2:xcorrnum
    % TODO: calculate weight coefficients
    n = 0;
    xcorrcoeff = zeros(2*maxlags+1, 1);
    % this is for rectangular weighting
    w = 1;
    column = shifted(A(:,i), -maxcorrpos(i-1));
    for j = i-1:-1:1
        xcorrcoeff = xcorrcoeff + w * xcorr(B(:,j), column, maxlags, 'coeff');
        %xcorrcoeff = xcorrcoeff + w * xcorr(B(:,1), A(:,i), maxlags, 'coeff');
        n = n + 1 * w;
    end
    xcorrcoeff = xcorrcoeff/n;
    [maxcorr, maxcorridx] = max(xcorrcoeff);
    maxcorrpos(i) = maxcorridx - maxlags-1 + maxcorrpos(i-1);
    B(:,i) = shifted(A(:,i), -maxcorrpos(i));
    progressbar(i/NofPoints);
end
end % for mode == 0

if mode == 1
    B(:,1:xcorrnum) = A(:,1:xcorrnum);
    maxcorrpos(xcorrnum) = -offset;
end

% second x-correlation loop
% calculates the correlation for xcorrnum left-hand neighbours of scan i
for i = xcorrnum + 1:NofPoints
    % TODO: calculate weight coefficients
    n = 0;
    xcorrcoeff = zeros(2*maxlags+1, 1);
% this is for rectangular weighting
    w = 1;
    column = shifted(A(:,i), -maxcorrpos(i-1));

```

```

    for j = i-1:-1:i-xcorrnum
        xcorrcoeff = xcorrcoeff + w * xcorr(B(:,j), column, maxlags, 'coeff');
    n = n + 1 * w;
    end
    if n > 0
        xcorrcoeff = xcorrcoeff/n;
    end
    [maxcorr, maxcorridx] = max(xcorrcoeff);
    maxcorrpos(i) = maxcorridx - maxlags-1 + maxcorrpos(i-1);
    B(:,i) = shifted(A(:,i), -maxcorrpos(i));
    progressbar(i/NofPoints);
end
% maxcorrpos(end) contains the last shift and should be used if not the
% whole data set is processed at once
% lastshift = maxcorridx;
% for i = 2:NofPoints
%   out(:,i-1) = xcorr(A(:,i-1), A(:,i), 'coeff');
% end
% [maxcorr, maxcorrpos] = max(out);
% maxcorrpos = maxcorrpos - ScanLength;
if mode == 1
    B(:,1:xcorrnum) = [];
    maxcorrpos(1:xcorrnum) = [];
    % maxcorridx(1:xcorrnum,:) = [];
end
filt_maxcorrpos = myfilter(maxcorrpos, sigma);
B = shift(A, -filt_maxcorrpos);
progressbar(1);
end

% function out = myfilter(in, sigma)
% % expand data to 3x the original length
% fin = [flipud(in); in; flipud(in)];
% fin = fft(fin);
% l = length(fin);
% fsigma = sigma * l / 100; % transform from percent to points
% ffilt = exp(-((l/2-[1:l]).^2/(2*fsigma^2)).^2);
% ffilt = fftshift(ffilt);
% out = abs(ifft(fin.*ffilt'));
% % reduce data to original length
% out = out(l/3+1:2*l/3);
% end

```

Acknowledgements

I would like to thank my adviser Wolfgang Drexler for giving me the opportunity of working in his group. For me the last years were really exciting in a scientific as well as in a personal respect. I also thank the group members Boris Považay, Angelika Unterhuber, Joshua Fernández, Bernd Hofer, and the former group member Dida Bizheva for being patient with me and providing a familiar atmosphere, especially during the time before conferences.

I thank Rainer Leitgeb and Harald Sattmann for interesting discussions and support, and all the colleagues of the former Institute for Medical Physics, especially A.F. Fercher and Leo Schmetterer.

Supported by Austrian Science Fund Grants FWF-P14218PSY, FWF-Y159PAT, and CRAF-199970549; the Christian Doppler Society and the European Community Grant QLK6CT200100279. Partially supported by Carl Zeiss Meditec Inc. (Dublin, CA, USA) and Femtolasers Produktions GmbH (Vienna, Austria).

Curriculum Vitae

PERSONAL DETAILS	
name	Hermann
surname	Boris
date of birth	25.07.1966
nationality	german
marital status	unmarried
EDUCATION	
2001 – 2006	PhD student at the Technical University & Medical University of Vienna, Center for Biomedical Engineering and Physics
06/2000	Graduation in Physics, degree “Diplom-Physiker” (master in physics), Free University Berlin
1992 – 2000	during studies different jobs for different companies: <ul style="list-style-type: none"> • archive at Axel-Springer-Verlag (german newspaper publisher) • GfU - Association for environmental measurement engineering, Potsdam
09/1998 – 02/2000	master thesis in the Hahn-Meitner-Institute, Prof. v. Oertzen, Berlin: “Nachweis von Wasserstoff in dünnen Schichten mit ERDA”, (detection of hydrogen in thin layers using ERDA; ion beam analytics)
1994 – 2000	Physics studies at Free University Berlin, minor subjects: informatics (foundation course), mineralogy and crystallography (main course)
1994	Abitur (diploma from German secondary school qualifying for university admission or matriculation)
1991 – 1994	Berlin-Kolleg (school for adult’s education)
1986 – 1991	work as physics laboratory assistant in the quality control and -assurance, electrical engineering, Auergesellschaft, Berlin
1982 – 1986	apprenticeship as physics laboratory assistant at BAM (Federal Institute for Material Research and Testing, Berlin)
1972 – 1982	elementary school, comprehensive School (secondary school level)